UNIVERSIDAD AUTÓNOMA DE MADRID

FACULTAD DE CIENCIAS

DEPARTAMENTO DE QUÍMICA-FÍSICA APLICADA

Optimisation of a non-chromium-containing tartaric acid/sulphuric acid anodising bath for aluminium alloys for aerospace industry application

Memoria para optar al grado de doctor presentada por

MANUEL GARCÍA RUBIO

Dirigida por los doctores

PILAR OCÓN ESTEBAN e IGNACIO MANUEL GARCÍA DIEGO

Madrid, octubre 2009

Departamento de tecnología de superficies. Airbus Spain

AIRBUS

A mis padres,

Manuel y Rosa María.

A mis hermanas, Rosa María y Raquel

Agradecimientos

En este pequeño espacio, me gustaría recordar y agradecer a todas esas personas sin las que esta tesis no podría haberse realizado o sin cuya ayuda habría sido mucho más difícil:

A la Dra. Pilar Ocón Esteban por confiar en mí desde el primer momento y por sus ánimos durante estos tres años, por sus buenos consejos, su acertada dirección y por su preocupación tanto profesional como personal por mi presente y mi futuro.

Al Dr. Ignacio Manuel García Diego, gracias a su dedicación diaria, su codirección y su estimulante visión crítica de las cosas, que han enriquecido y mejorado esta tesis.

Al proyecto Airbus-FUAM, y a todas las personas involucradas en él por facilitar este trabajo desde el siempre imprescindible punto de vista económico.

A todas las personas que han formado o forman parte del departamento de tecnología de superficies de I+D de Airbus España: a Ángeles, Alex, Vero y Manuel Calahorro. Mi más sincero agradecimiento a Laura por su ayuda desinteresada, por su cómo lo pasemos y por su variado repertorio de fiestas populares. Un desagradecimiento especial a Paco y a Marisa, porque ellos siempre lo han querido así, aunque sabéis que me habéis ayudado mucho y lo hemos pasado bárbaro.

A Begoña y Mari Carmen del departamento de materiales metálicos de I+D de Airbus España por enseñarme a manejar el SEM y otros muchos aparatos. A Julio, Santos y Ballesteros por su rápida ayuda en el corte y mecanizado de piezas. A María por sus tentativas con el AFM y por su amistad.

A todos los compañeros de I+D de Airbus España con los que he compartido el "Airbus way".

Al Dr. Richard Smith y al Dr. Aurelio Climent por su aportación y sus enseñanzas con el RBS, así como al personal técnico del CMAM de la UAM.

Al profesor George. E. Thompson, director del "Corrosion and Protection Centre" de la Universidad de Manchester por acogerme en su grupo de investigación durante mis dos estancias en Manchester, así como al Dr. Michele Curioni por su ayuda y colaboración con el ultramicrotomo y el TEM.

A todos mis compañeros de los cursos de doctorado, perros viejos de la electroquímica, por ser mi familia en Córdoba y por los buenos ratos en los congresos. Especialmente a Patricia por su ayuda con el XPS y por su amistad.

A mis amigos: Pelos, Rober, Danito, Makea, Melero, Perla, Candao… y muchos otros, porque siempre están ahí, aunque yo no me deje ver.

A mi familia, a mis hermanas Rosa María y Raquel a mis padres, Rosa María y Manuel, por su sacrificio durante su vida para darme esta oportunidad y por su apoyo constante sin el cual no estaría terminando de escribir estas líneas.

A Clara, por cuidarme y ser mi punto de apoyo en los mejores y en los peores momentos. Aquí no cabe todo lo que te tengo agradecer, pero espero poder hacerlo cada día.

Abstract

In this thesis, a new chromate-free process was tested for anodising aluminium alloys in the semi-industrial scale. Anodising consists of the growth of an aluminium oxide film on an aluminium alloy acting as an anode in an electrolytic bath. The anodic film confers to the alloys two important properties of especial interest in the aircraft industry: corrosion resistance and paint adherence.

The materials utilised were aluminium alloys of the 2xxx, the 6xxx and the 7xxx series. Such materials were anodised in a semi-industrial tartaric acid/sulphuric acid electrolytic bath.

The characterisation of the anodic films included the determination of the morphology by scanning and transmission electron microscopies, chemical composition by means of glow discharge optical emission spectroscopy, Rutherford backscattering spectroscopy and X-ray photoelectron spectroscopy and corrosion resistance by potentiodynamic techniques, electrochemical impedance spectroscopy and salt spray tests.

The thickness of the anodic films grown in the tartaric acid/sulphuric acid bath ranged from 1 to 5 μm, depending on the anodising conditions and the alloy. Such anodic films presented a porous morphology that was highly influenced by the alloying elements of the aluminium alloys. Besides, the presence of species in the anodic films incorporated both, from the bath and from the alloy was also detected. The corrosion resistance of the anodic films was mainly dependant on the anodising conditions and the copper content of the alloys.

The compatibility of the anodic films with various postreatments was also tested. This postreatments included new chromate-free treatments and typical aircraft industry chromate-loaded treatments. Namely, these postreatments were: sealing of the porous film in the presence and the absence of chromates, application of Cr (VI)-free and Cr (VI)-loaded chemical conversion coatings and painting with different coating systems including Cr (VI)-loaded epoxy solvent-based primers, and Cr (VI)-loaded and Cr (VI)-free water-based primers. In general, all the postreatments improved the corrosion resistance of the anodic films,

Another relevant issue was the development of a new anodising bath containing tartaric acid/sulphuric acid and sodium molybdate. The anodic films obtained in this bath were morphologically similar to that obtained in the tartaric acid/sulphuric acid bath, but residual Mo^{6+} species in the pores of the anodic films improved the corrosion resistance.

Finally, some accelerated corrosion tests were undertaken. These test revealed good behaviour of the anodic films to in-service temperatures (RT-45 °C) inside an aircraft and high corrosion rates over 60 °C.

Resumen

En esta tesis, se ha probado un proceso libre de cromatos a escala semi-industrial para anodizar aleaciones de aluminio. El proceso de anodizado consiste en crecer una capa de óxido de aluminio sobre la aleación de aluminio, que actúa como ánodo en un baño electrolítico. La película anódica confiere a las aleaciones dos importantes propiedades de especial interés en la industria aeroespacial: resistencia a la corrosión y adherencia de pintura.

Los materiales utilizados fueron aleaciones de aluminio de las series 2xxx, 6xxx y 7xxx. Estos materiales fueron anodizados en un baño semi-industrial de ácido tartárico/ácido sulfúrico.

La caracterización de las capas anódicas incluyó la determinación de la morfología mediante microscopias de emisión y transmisión electrónicas, la composición química por medio de espectroscopía óptica de emisión de descarga de brillo, espectroscopía de retrodispersión de Rutherford y espectroscopía fotoelectrónica de rayos-X, la resistencia a la corrosión mediante técnicas potenciodinámicas, espectroscopía de impedancia electroquímica y test de niebla salina.

Los espesores de las capas anódicas crecidas en el baño de ácido tartárico/ácido sulfúrico estaban comprendidos entre 1 y 5 mm, dependiendo de las condiciones de anodizado y de la aleación. Además, se detectó la presencia de especies en la capa anódica, incorporadas desde el baño y la aleación. La resistencia frente a la corrosión de las películas anódicas dependía principalmente de las condiciones de anodizado y del contenido en cobre de las aleaciones.

También se comprobó la compatibilidad de las capas anódicas con varios postratamientos. Tales postratamientos incluyeron tratamientos libres de cromatos y los tratamientos con cromatos típicos de la industria aeroespacial. Concretamente, estos postratamientos fueron: el sellado de la capa porosa en presencia y en ausencia de cromatos, la aplicación de capas de conversión químicas con y sin cromatos y pinturas con distintos sistemas de protección, incluyendo imprimaciones epoxy de base disolvente con cromatos e imprimaciones de base agua con y sin cromatos. En general, todos los postratamientos mejoraron la resistencia de las películas anódicas frente a la corrosión.

Otro tema relevante es el desarrollo de un nuevo baño de anodizado que contiene ácido tartárico/ácido sulfúrico y molibdato sódico. Las películas anódicas obtenidas en este baño son morfológicamente similares a las obtenidas en el baño ácido tartárico/ácido sulfúrico, pero las especies de Mo^{6+} en los poros de las capas anódicas mejoraron la resistencia frente a la corrosión.

Finalmente, se llevaron a cabo algunos test de corrosión acelerada. Estos experimentos mostraron un buen comportamiento de las películas anódicas a las temperaturas normales en servicio (RT-45 °C) dentro de un avión y altas velocidades de corrosión por encima de los 60 °C.

Thesis Index

1. State of the art

1. State of the art

Chromium (VI) compounds (also known as chromates) have been utilised over the last 60 years in the aircraft industry as corrosion inhibitors and are present in most of the treatments for metallic materials, from aluminium surface treatments to hard chromium coatings. However, such compounds present several drawbacks: they are toxic and dangerous for the environment [1] and carcinogenic activity of chromates has been demonstrated [2]. Besides, new legislation will affect the industrial use of Cr (VI) compounds in the European Community.

REACH is a new European Community Regulation on chemicals and their safe use [3]. It deals with the **R**egistration, **E**valuation, **A**uthorisation and Restriction of **Ch**emical substances. The new law entered into force on 1 June 2007, whit different deadlines for subsequent requirements for the European industries until 2018.

The aim of REACH is to improve the protection of human health and the environment through the better and earlier identification of the intrinsic properties of chemical substances. At the same time, innovative capability and competitiveness of the EU chemicals industry should be enhanced. The benefits of the REACH system will come gradually, as more and more substances are phased into REACH.

The REACH considers all the chromium (VI) compounds (well known IARC category 2 carcinogenic) as Very high Concern Substances and therefore the use of such compounds in any specific application must to be previously evaluated and authorised for that specific application.

Unfortunately, substitution of chromium (VI) compounds in the aircraft industry is a laborious work. In the particular case of the substitution of Cr (VI) for anodising aluminium alloys, Airbus has participated in several research projects in collaboration with leading European research centres and universities [4]. Such projects evaluated potential substitutes for the anodising in chromic acid leading to suggest tartaric sulphuric acid anodising as the most promising candidate.

The anodising process in the aircraft industry has to fulfil three main requirements (fig. 1), firstly, it has to confer corrosion protection to the aluminium alloy, secondly, it has to confer adhesion to primers and thirdly, it has to present minimal impact in the fatigue life of the alloy.

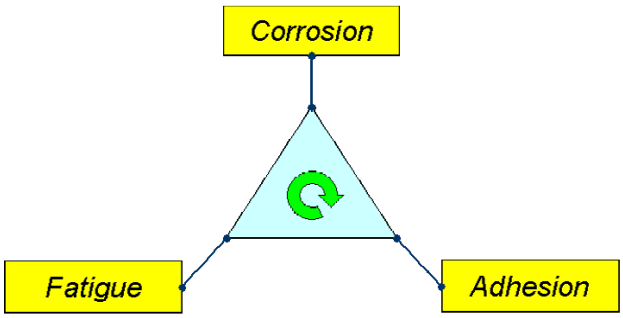

Figure 1. Technical requirements in the aircraft industry for anodising processes

Tartaric acid/sulphuric acid (TSA) anodising has been selected as that process providing the best compromise between technical and industrial performance with respect to the Airbus

requirements. Table 1 compares the parameters for anodising in chromic acid bath (CAA) and in TSA bath.

Table 1. Parameters for the CAA and the TSA anodising processes

Parameter	CAA	TSA
Film thickness	3-5 µm	3-5 µm
Temperature	40 °C	37-43 °C
Process time	45 min	20-25 min
Voltage	40 V or 21 V	13-15 V
Concentration	30-100 g L^{-1} chromic acid	80 g L^{-1} tartaric acid 40 g L^{-1} sulphuric acid

From and industrial and economical viewpoint, the TSA process present several advantages compared to the CAA process: the anodising time needed for obtaining film thicknesses appropriate for the aircraft industry is halved, the voltage is lower and the maintenance operations and replenishment of reagents are reduced. Besides, the disposal treatment costs are also reduced due to the low environmental impact of the TSA components.

Another important factor that makes attractive the TSA process is that the installations currently used for CAA anodising are easily adaptable to the TSA process with minimal modifications.

Table 2 shows the state-of-the art of the Cr (VI) replacement in the aircraft industry.

Table 2. State-of-the-art of the chromium substitution in the anodising processes of aluminium alloys in the aircraft industry.

	Pretreatment	Anodising	Postreatment	Primer
Past	Cr (VI)	Cr (VI)	Cr (VI)	Solvent-based Cr (VI)
Present	Cr (VI)-free	Cr (VI)	Cr (VI)	Solvent-based Cr (VI)
Implement phase	-	Cr (VI)-free	-	Water-based Cr (VI)
Research phase	Improved Cr (VI)-free	Modified Cr (VI)-free	Cr (VI)-free	Water-based Cr (VI)-free

Currently, aircraft industry is replacing the CAA by Cr-free anodising alternatives as is the case of TSA. At the same time the solvent-based primers and paints are being replaced by low VOC (volatile organic compound) water-based formulations, both with chromates inhibitors. Therefore TSA is now in the central point of the effort of the industry to avoid the use of chromates and at the same time subjected to intense research. The reason is that corrosion protection systems with TSA must fulfil the same strict requirement that the CAA current systems. Besides, the progressive replacement of other components of the system (solvent-based by water-based chemistry for the paints, chromate-based by chromate-free inhibitor component of the primers of CAA) makes necessary for the TSA to be compatible with all of them (current and future). Moreover, at the same time TSA is being implemented in the industry in combination with Cr-loaded paints, more development and optimization is needed to be able to provide the same level of corrosion resistance when the new Cr-free paints will be available.

2. Objectives

2. Objectives

The main objective of this thesis is the optimisation of a chromate free tartaric acid/sulphuric acid (TSA) anodising bath for aluminium alloys. This objective can be divided in partial objectives as follows:

- The starting-up of a pilot plant for surface treatments, specifically for up-scaling of Cr-free anodising of aluminium and aluminium alloys.
- Assessment of the reliability and robustness of a tartaric acid/ sulphuric acid anodising bath in semi-industrial scale for the main aerospace aluminium alloys.
- The study of the variation of key anodising parameters like bath temperature, parts layout, stirring, anodising time, anodising potential and currentless remaining time in the bath.
- Multidisciplinary characterisation of the TSA anodic layers morphology by means of electron-optical techniques (scanning and transmission electron microscopies), composition by surface analysis techniques (glow discharge optical emission spectroscopy, X-Ray photoelectron spectroscopy and Rutherford backscattering spectroscopy) , and functionally by means of corrosion test methods (salt spray test, potentiodynamic polarisation and electrochemical impedance spectroscopy) and paint adhesion (cross cut test).
- Compatibility validation of the TSA anodic films with the conventional hot sealing postreatments and development of new cold postreatments, including a chromate free one.
- Appraisal of the TSA anodic layer as pretreatment for conventional solvent-based chromate loaded paints and new water-based chromate loaded and chromate free corrosion inhibiting paints.
- Improvement of the corrosion resistance of TSA anodic films by means of addition of molybdate salts to the anodising bath.
- Development of new accelerated corrosion test for the long term assessment of anodic layers.

2. Objetivos

El principal objetivo de esta tesis es la optimización de un baño de anodizado de ácido tartárico/ácido sulfúrico libre de cromatos para aleaciones de aluminio. Este objetivo se puede dividir en objetivos parciales como se indica a continuación:

- La puesta en marcha de una planta piloto para tratamientos superficiales, específicamente para el escalado de un proceso de anodizado libre de cromatos para el aluminio y las aleaciones de aluminio.
- Evaluación de la fiabilidad y la robustez de un baño de ácido tartárico/ácido sulfúrico a escala semi-industrial para las principales aleaciones de aluminio.
- El estudio de la variación de los parámetros de anodizado clave, como la temperatura del baño, la disposición de las piezas en el baño, agitación, tiempo de anodizado y tiempo de permanencia sin corriente en el baño.
- Caracterización multidisciplinar de la morfología de las capas anódicas de TSA por medio de técnicas electrón-ópticas (microscopías de emisión y de transmisión electrónicas), la composición mediante técnicas de análisis superficial (espectroscopía óptica de emisión de descarga de brillo, espectroscopía de retrodispersión de Rutherford y espectroscopía fotoelectrónica de rayos-X) y la funcionalidad por medio de test de corrosión (test de niebla salina, polarización potenciodinámica y espectroscopía de impedancia electroquímica) y adherencia de pinturas (test de “cross cut”).
- Validación de la compatibilidad de las películas anódicas de TSA con postratamientos convencionales de sellado en caliente y desarrollo de nuevos postratamientos en frío, incluyendo no libre de cromatos.
- Valoración de las capas anódicas de TSA como pretratamiento para pinturas convencionales de base disolvente con cromo y de nuevas pinturas base agua con cromatos y sin cromatos pero con otros inhibidores.
- Mejora de la resistencia a la corrosión de las capas anódicas de TSA por medio de la adición de sales de molibdato al baño de anodizado.
- Desarrollo de nuevos test de corrosión acelerados para la evaluación a largo plazo de las capas anódicas.

3. Introduction

3. Introduction

3.1. Aluminium and its alloys

3.1.1. Aluminium

Aluminium is the third most abundant element comprising about 8 % of the Earth's crust [5]. Because of its chemical reactivity, aluminium is never found in nature as an element but always in its oxidised form, as one of a selection of about 250 different minerals. The most prominent groups of such minerals are the silicates, and the products of their weathering, the clays. Other important compounds include the hydroxides, a group which includes bauxite, the base raw material for primary aluminium production.

Bauxite is generally extracted by open cast mining from strata, typically some 4-6 metres thick under a shallow covering of topsoil and vegetation.

Eighty percent of world bauxite production, mainly from large blanket type deposits is from surface mines, with the rest, mainly from Southern Europe and Hungary, from underground excavations. The major bauxite deposits are to be found in the tropics and in the Caribbean and Mediterranean regions. Today most bauxite mines (fig. 2) are in the Caribbean area, South America, Australia and Africa.

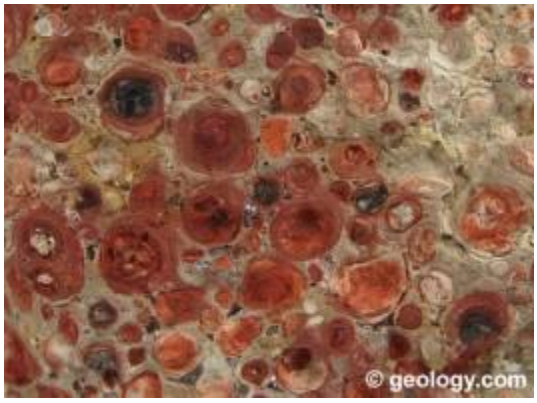

Figure 2. Pisolitic structure of bauxite mineral from Little Rock, Arkansas [6]

Despite its abundance, aluminium was not isolated until well into the eighteenth century. Sir Humphrey Dave made the first unsuccessful attempts in 1807, but it was not until 1825 when Oersted succeeded in preparing aluminium powder by the reduction of anhydrous aluminium chloride with sodium amalgam. Modern production of aluminium begins from the mineral bauxite (aprox. 40-60% Al_2O_3, 10-30% Fe_2O_3). Alumina (Al_2O_3) is extracted from bauxite with sodium hydroxide by means of the Bayer process. Then alumina is reduced in an electrolytic bath to aluminium metal at a large economical cost.

Aluminium is the most utilised metal in the aircraft industry due to its low density (2.7 g cm^{-3}), the relatively high corrosion resistance of the pure metal, but especially because of a high mechanical strength that can be achieved by suitable alloying and heat treatments. However, the main alloying elements are heavy metals that decrease the corrosion resistance. There

does not exist an alloy performing high mechanical strength and high corrosion resistance hitherto. Therefore, the development of a range of protective finishes for these high strength alloys is of great importance for the industry.

3.1.2. Aluminium alloys.

3.1.2.1. Classification of aluminium alloys

There exist a number of aluminium alloys that can be classified according to their fabrication process, the chemical composition or the heat treatment.

Fabrication process

The main two routes of producing are: casting alloys melted and then casted in an appropriate mould, and wrought alloys which are subjected to plastic deformation by hot working or cold working (such as rolling, extruding...) without being remelted.

Chemical composition

Historically, different countries have had different designations for the aluminium alloys. Nowadays, there exists a numerical designation used in America and Europe for its simplicity. This type of nomenclature, which is used for wrought and casting aluminium alloys, is represented by a number of four figures. A first figure of 1 denotes those alloys in which the aluminium is greater than 99%. A first figure from 2 to 8 denotes the other alloys identifying the main alloying element (see table 3).

Table 3. Numerical designation of the aluminium alloys.

Series	Wrought alloys	Series	Casting alloys
1xxx	-	1xx.x	-
2xxx	Cu	2xx.x	Cu
3xxx	Mn	3xx.x	Si plus Cu and/or Mg
4xxx	Si	4xx.x	Si
5xxx	Mg	5xx.x	Mg
6xxx	Mg and Si	6xx.x	Unused series
7xxx	Zn	7xx.x	Zn
8xxx	Other elements	8xx.x	Sn
9xxx	Unused series	9xx.x	Other elements

For the wrought alloys, in the 1xxx series the third and fourth figures indicate the percentage of aluminium above 99% e.g. 1070 alloy has aluminium content of 99.70%. The second figure represents the level of impurities. It is equal to zero if the impurities are uncontrolled, and it can vary between 1 and 9 depending upon the level which the impurity content is not to exceed.

In the other groups, the second figure is equal to zero for the main alloy and varies between 1 and 9 for its modifications. The third and fourth figures identify together the specific alloy within each group.

In the case of the cast alloys, the first figure indicates the group as for the wrought alloys. The second and third figures for the 1xx.x series indicate purity whereas the last figure denotes the product form; 1xx.0 indicates casting and 1xx.1 indicates ingot. For the rest of the series the second and third figure identify the alloy in the group and the fourth figure indicates the product form as for the 1xx.x series.

Thermal treatment

Heat-treatable alloys are those that can be hardened by a controlled cycle of heating and cooling. During this cycle, the alloying elements dissolve into solid solution and precipitate as coherent submicroscopic particles). The heat-treatable alloys include the 2xxx, 6xxx and 7xxx series. The heat treating can be separated into the following phases:

Heating (up to 450-530 °C depending upon the alloy).

Tempering with water or air

Ageing at room temperature (natural ageing)

Ageing at a temperature varying between 120 and 180 °C (artificial ageing).

Non-heat treatable alloys, also called work-hardenable alloys, include alloys from the 3xxx and 5xxx series. The strength is increased by dispersion of second phase constituents or elements in solid solution and cold work the alloy.

The temper designation system is based on the sequences of mechanical or thermal treatments. The temper designation follows the alloy designation. Basic tempers consist of individual capital letters and one or more digits following the letter indicate major subdivisions of them.

Table 4. Classification of the metallurgical stage [7]

<table>
<tr><th>Basic treatment</th><th colspan="4">Secondary treatments</th><th>Symbol</th></tr>
<tr><td>As fabricated</td><td colspan="4"></td><td>F</td></tr>
<tr><td>Annealed (only wrought)</td><td colspan="4"></td><td>O</td></tr>
<tr><td rowspan="3">Cold Worked (H)</td><td colspan="4">Cold worked only</td><td>H1</td></tr>
<tr><td colspan="4">Cold worked and partially annealed</td><td>H2</td></tr>
<tr><td colspan="4">Cold worked and stabilised</td><td>H3</td></tr>
<tr><td rowspan="8">Heat treatment (T)</td><td rowspan="4">Separate solution</td><td colspan="2" rowspan="2">Without work hardening</td><td>Naturally aged</td><td>T4</td></tr>
<tr><td>Artificially aged</td><td>T6</td></tr>
<tr><td rowspan="2">With work hardening</td><td>Work hardened</td><td>Naturally aged</td><td>T3</td></tr>
<tr><td>Artificially aged</td><td>T8</td></tr>
<tr><td>Artificially aged</td><td>Work hardened</td><td>T9</td></tr>
<tr><td rowspan="4">Without separate solution</td><td colspan="2" rowspan="2">Without work hardening</td><td>Naturally aged</td><td>T1</td></tr>
<tr><td>Artificially aged</td><td>T5</td></tr>
<tr><td rowspan="2">With work hardening</td><td>Work hardened</td><td>Naturally aged</td><td>T11</td></tr>
<tr><td>Artificially aged</td><td>T12</td></tr>
<tr><td>Artificially aged</td><td>Work hardened</td><td>T10</td></tr>
</table>

3.1.2.2. Alloying elements

There are five major alloying elements—copper, manganese, silicon, magnesium, and zinc—that significantly influence the properties of aluminium alloys. For those elements in concentration below their solubility limits, the alloying elements are essentially in solid solution and constitute a single phase. However, no element is known to have complete miscibility with aluminium in the solid state.

Magnesium reduces the melting point; it increases work-hardening ability and corrosion resistance to salted water.

Copper gives great strength increase and allows cold precipitation hardening, but reduces corrosion resistance, weldability and ductility.

Manganese increases strength either in solid solution or as finely precipitated intermetallic phase. It has no adverse effect on corrosion resistance.

Silicon increases strength and ductility and reduces the melting point. If combined with magnesium it allows precipitation hardening.

Zinc drastically increases strength and allows hot or cold precipitation hardening.

Other alloying components that are less significant from a corrosion-resistance standpoint are frequently included to improve mechanical and other physical properties. These are iron (increases the strength of pure aluminium if a low percentage is used), chromium (increases resistance to stress corrosion), titanium (decrease grain size), zirconium (a stabilizer element which influences temperability), lithium (reduces the alloy density), and nickel (increases strength under high-temperature conditions).

3.1.3. Aluminium in the aircraft industry

A commercial airplane is designed and operated for maximum yield, i.e., capacity to deliver (e. g., expressed as passenger km) as a function of operating and capital costs. Among attributes contributing to an aircraft's yield are its size, shape, speed, mass, and fuel efficiency. Some of these are constrained by aerodynamic considerations and external factors but mass and fuel efficiency are strongly influenced by the selection and application of the materials of construction [8].

Figure 3. Airbus 380 landing at "Internationalen Luftfahrtausstellung. Berlin 2006"

The aluminium is the major material used in the aircraft construction, although its presence has partially dropped by the appearance of new composite materials in the last years. In the new Airbus A380 (fig. 3), the biggest commercial aircraft hitherto, the aluminium alloys supposes the 60% wt. of the aircraft (fig. 4).

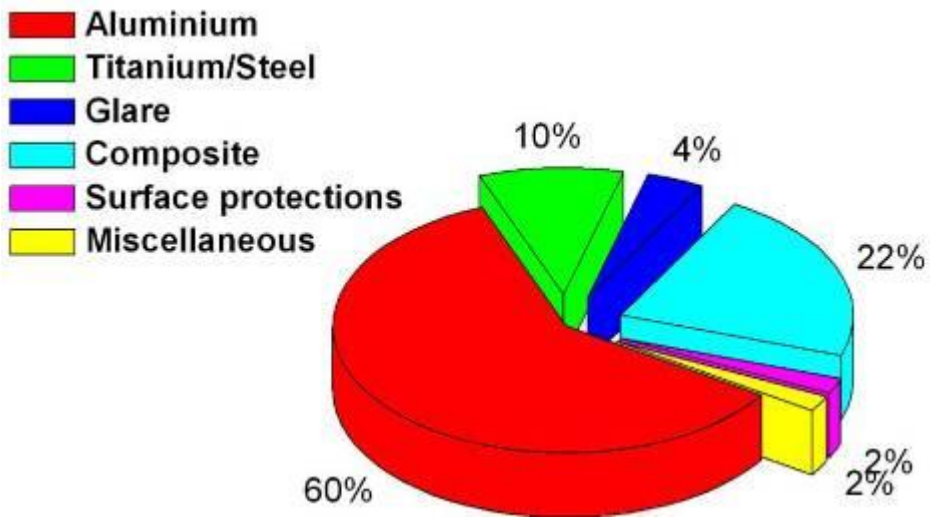

Figure 4. Material distribution (% wt.) on Airbus A380 aircraft.

Metal sections and thicknesses are the reasonable minima needed to carry the maximum anticipated stresses safely and excessive structural reserves to compensate for avoidable corrosion are unacceptable. Even protective coatings, such as paints, contribute some mass and must be applied with discrimination.

The aluminium alloys are present in the fuselage of the aircraft (fig. 4), in the upper part, the most resistant aluminium alloys (6xxx series) are in the bottom part of the aircraft because such areas are prone to accumulation of fluids and liquids. However, the alloys with higher mechanical properties (2xxx and 7xxx series) are in the upper and middle part of the fuselage.

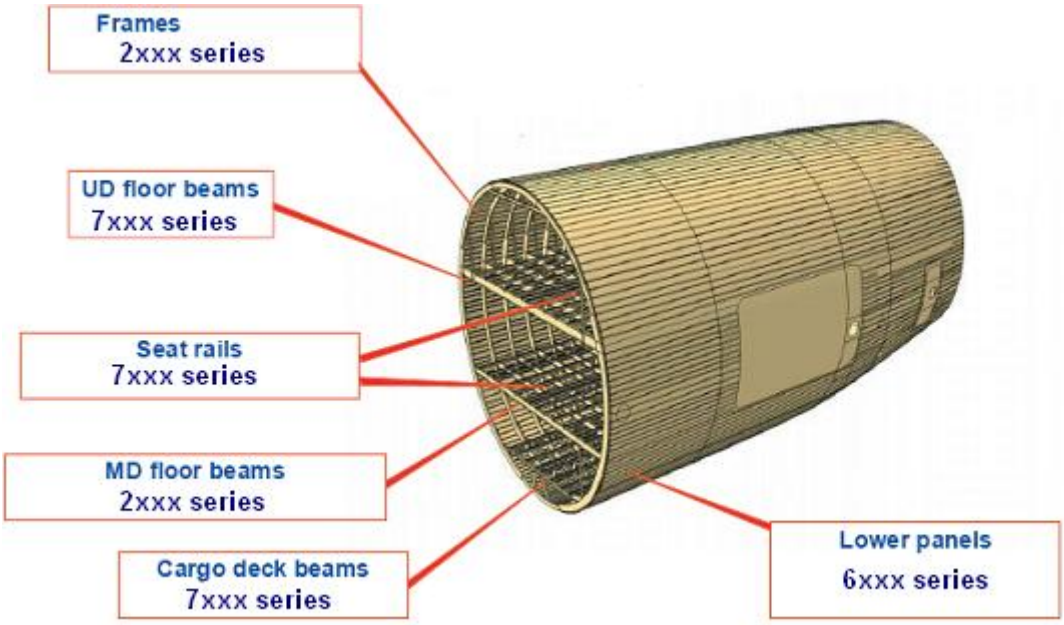

Figure 5. Typical materials on Airbus A380 fuselage

The wings (fig. 5) are made of aluminium alloys of the 2xxx and the 7xxx series due to the high mechanical strength of the alloys in these series.

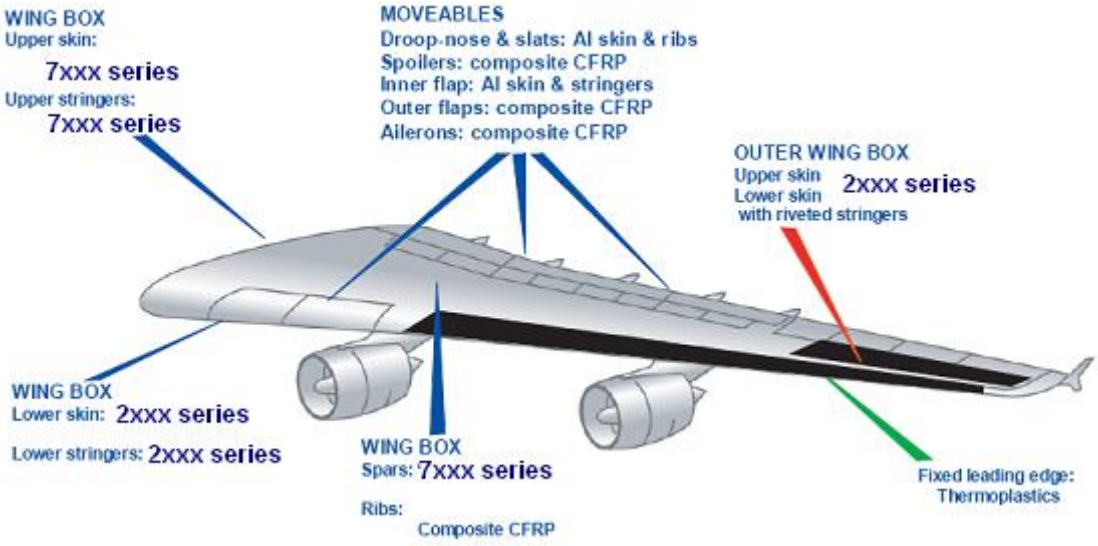

Figure 6. Typical materials on Airbus A380 wings

3.2. Corrosion of aluminium

3.2.1. Uniform corrosion

This type of corrosion develops as pits of very small diameter, in the order of a micrometer, and results in a uniform and continuous decrease in thickness over the entire surface area of the metal.

In aluminium this type of corrosion is observed especially in highly acidic or alkaline media, in which the solubility of the nature oxide film is high. The solution rate of the film is greater than its rate of formation; however, the ratio of both rates can change over time.

The conditions for thermodynamic stability of the oxide film are expressed by the Pourbaix (potential versus pH) diagram shown in Fig. 7.

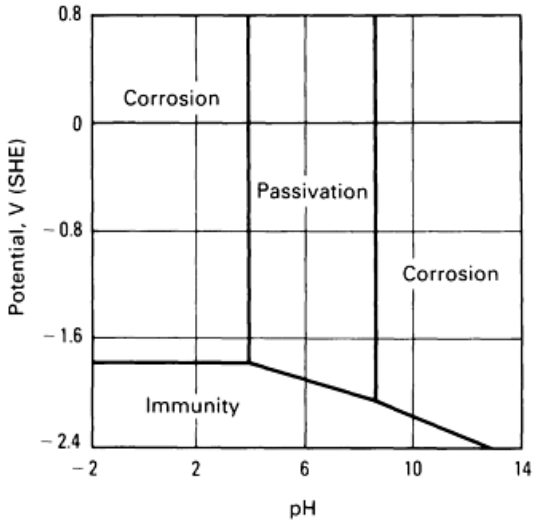

Figure 7. Pourbaix diagram for aluminum with an $Al_2O_3 \cdot 3H_2O$ film at 25 °C. Potential values are for the standard hydrogen electrode (SHE) scale. [9]

As shown by this diagram, aluminium is passive (is protected by its oxide film) in the pH range of about 4 to 8.5. The limits of this range, however, vary somewhat with temperature, with the specific form of oxide film present, and with the presence of substances that can form soluble complexes or insoluble salts with aluminium.

Beyond the limits of it passive range, aluminium corrodes in aqueous solutions because its oxides are soluble in many acids and bases, yielding Al^{3+} ions in the former and (aluminate) ions in the latter. There are, however, instances when corrosion does not occur outside the passive range, for example, when the oxide film is not soluble or when the film is maintained by the oxidizing nature of the solution. [10].

3.2.2. Localised corrosion

3.2.2.1. Pitting corrosion

This localised form of corrosion is characterised by the formation of irregularly shaped cavities on the surface of the metal [11]. Their diameter and depth depend on several parameters related to the metal, the medium and service conditions.

Pitting corrosion occurs when the metal is exposed to permanent or intermittent contact with aqueous media: water, seawater, rain water and humidity. Experience shows that when pitting corrosion occurs, it will always develop during the first weeks of exposure.

The electrochemical mechanisms of pitting corrosion are very complex. Pitting corrosion shows two distinct stages: initiation and propagation.

Initiation stage

Initially, chloride ions are adsorbed on the natural oxide film, followed by the rupture of the film at weak points with formation of microcracks that are a few nanometres wide. Many pits are initiated within a very short time. The pit density depends on the alloy: from 10^4 cm^{-2} on AA1199 to 10^{10} cm^{-2} on an alloy containing 4% copper. However, most pits will stop after a few days. Polarisation studies have demonstrated that when pits stop growing, they will be repassivated. When the metal is polarised once again, these passivated pits will not be reinitiated again, but pitting will start on fresh sites. Aluminium will oxidise rapidly where the film cracks; and a complex intermediate chloride $AlCl_4^-$ will be formed.

On the other hand, oxygen will be reduced slowly in cathodic areas. These areas seem to be intermetallics phases underneath the oxide layer that more or less covers them.

Propagation stage

Only a minute fraction of initiated pits will continue to propagate according to the two electrochemical reactions:

Oxidation at the anode formed at the pit's bottom:

$$Al \rightarrow Al^{3+} + 3e^-$$

Reduction at the cathode outside the cavity:

$$3/2\ O_2 + 3H_2O + 6e^- \rightarrow 6OH^- \qquad \text{Neutral and basic media}$$

$$6H^+ + 6e^- \rightarrow 3\ H_2 \qquad \text{Acid media}$$

If the anode is stable and localised, corrosion will dig a cavity, that is to say a pit (fig. 8). The formation of OH^- ions or the consumption of H^+ ions will locally lead to an excess of OH^- ions and, thus to an alkaline pH.

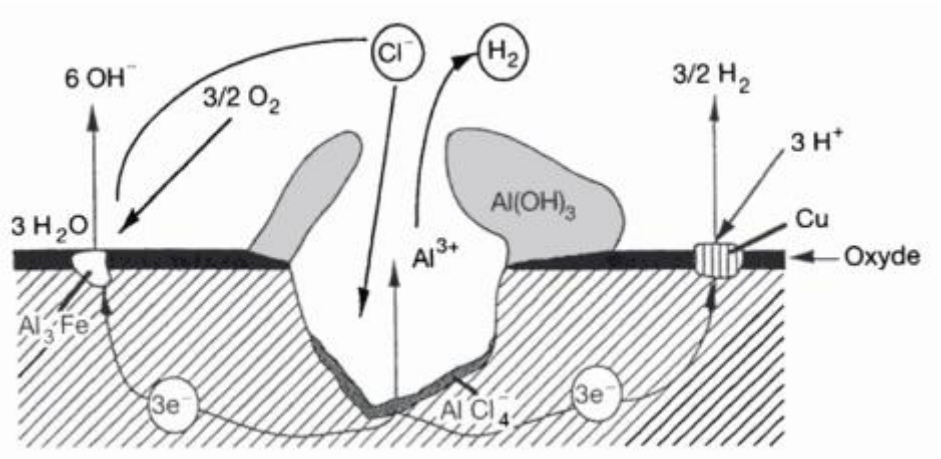

Figure 8. Mechanism of pitting corrosion of aluminium

The overall reaction of pitting corrosion on aluminium is

$$2Al + 3H_2O + 3/2\ O_2 \rightarrow 2\ Al(OH)_3$$

The dissolution of aluminium by formation of Al^{3+} ions at the bottom of the pit creates an electrical field that shifts Cl^- ions towards the pit's bottom, chemically neutralising the solution and forming aluminium chlorides. Cl^- ions are the most mobile of all ions that participate in these reactions.

The hydrolysis of aluminium chlorides according to

$$Al^{3+} + 3H_2O \rightarrow Al(OH)_3 + 3H^+$$

Will lead to the acidification of the pit's bottom up to a pH<3. The medium becomes very aggressive, leading to autopropagation of the pit.

Al^{3+} ions being highly concentrated at the pit's bottom, they will diffuse towards the pit's opening, where they will meet a medium that is more and more alkaline, especially on the lateral surfaces, where the cathodic reaction leads to alkalinisation. Then, alumina precipitates as a membrane.

3.2.2.2. Intercrystalline corrosion

Intercrystalline corrosion is the process of preferential attack either at grain boundaries or within the immediately adjacent regions. It results from the segregation and/or precipitation of alloying elements along the boundaries and this have the effect of altering the electrochemical stability at these points. Most of the heat-treatable alloys have some susceptibility to intercrystalline corrosion but normally this does not pose a serious practical problem.

This form of corrosion consumes only a very small amount of metal. However, when penetrating into the bulk of the metal, intercrystalline corrosion may lead to a reduction of mechanical properties, especially of elongation, and may even lead to the rupture of components.

The propagation of intercrystalline corrosion starts at pits. Nevertheless, there is not relationship between the penetration depth of intercrystalline corrosion and the diameter of corrosion pits. This means that intercrystalline corrosion may also propagate from minute, superficial pits.

3.2.2.3. Stress-assisted corrosion

Essentially, the stress-assisted corrosion is the propagation of the intergranular cracking of the material whilst elastically loaded at stress concentrations well below the fracture toughness of the material. Stress corrosion requires a combination of a residual or applied tensile stress, a corrosive environment particularly containing chloride ions, and a directional microstructure allowing easy crack propagation. Al-Cu, Al-Mg, Al-Zn-Mg and Al-Li alloys are all sensitive to stress corrosion cracking.

3.2.2.4. Filiform corrosion

Filiform corrosion only occurs on coated substrates and growth proceeds in a linear manner producing a characteristic worm-like trace. Filiform corrosion is initiated at a break or defect in a coating, and this enable a corrosive environment to react with the underlying aluminium substrate.

It is now widely accepted that filiform corrosion is driven by a differential aeration cell between the anodic filament head and the cathodic tail. [12]

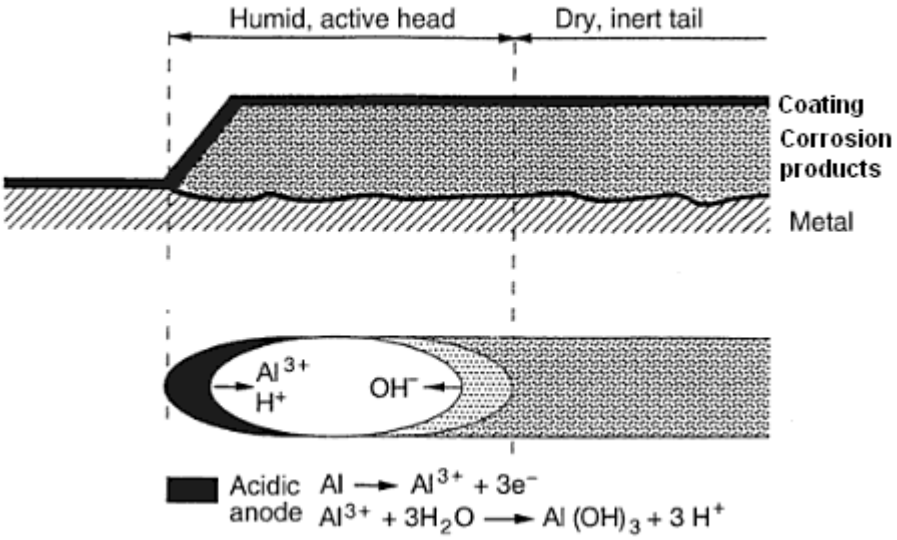

Figure 9. Scheme of filiform corrosion [13]

Aluminium dissolution occurs at the active anodic head of the cell, and the passive trailing area oxygen and water are reduced to produce hydroxyl ions. When the cell electrolyte is saturated with dissolved aluminium ions, aluminium hydroxide is precipitated as pseudoboehmite. Aluminium both dissolves in the cell electrolyte and reacts directly with water to evolve hydrogen.

Both water and oxygen must be continuously supplied to the cell or growth stops, and chloride ions are essential to provide electrical conductivity and to stimulate the initiation of corrosion. These ions migrate with the filament head electrolyte and growth stops once they have been consumed by incorporation in the corrosion product. Growth proceeds by anodic undermining of the coating and the voluminous corrosion products precipitated behind the active head provide the pressure to cause delamination and lifting of the coating [14].

3.2.3. Galvanic corrosion

This type of corrosion occurs when dissimilar conductor materials are in direct electrical contact in corrosive solutions or atmospheres.

Attack by bi-metallic contacts can be as damaging as stress corrosion, since, once initiated, it continues to propagate. In general terms the two main contributory factors are the severity of the environment and the electrochemical separation between the respective metals as given

in the Galvanic Series. The more aggressive the environment and the larger the potential difference, then the greater is the attack likely to be. The effect occurs when two dissimilar metals are in contact, the nobler being cathodically protected by the less noble metal, which becomes a sacrificial anode. If the area of the anodic metal is small compared to that of the cathodic metal, corrosion will be accelerated, whereas if the ratio of areas is reversed the overall corrosion rate is lesser. The situation occurs most commonly when dissimilar materials are used in fastener combinations e.g. a steel bolt through aluminium sheet.

3.2.4. Corrosion characteristic by aluminium alloy series

The following paragraphs succinctly describe the corrosion behaviour of each general alloy class. While this discussion is specifically focused on wrought product forms, castings of similar compositions generally behave similarly [15].

1xxx Series. The alloys in this series are at least 99% pure aluminium. These materials are really not alloys but rather pure aluminium with various levels of impurities. The major impurities are iron and silicon. These materials are relatively corrosion resistant. Nevertheless, in compositions with higher iron impurities, there is a tendency toward pitting corrosion, especially in aqueous chloride solutions.

2xxx Series. The alloys in this series contain primarily copper, up to 7%. Several also contain magnesium and/or manganese. The alloys in this series are strengthened by thermal treatment to attain high strengths and are used in sheet, plate, and extruded forms, primarily in aerospace applications. However, copper in aluminium alloys generally decreases the resistance to general corrosion and pitting. With proper heat treatment, quenching, and aging, these alloys can achieve moderately good resistance to stress-corrosion cracking and other forms of intergranular corrosion. Therefore, the resistance to general and pitting corrosion is strongly influenced by the copper content in these alloys, regardless of thermal processing control. Several of the alloys in this series contain lithium (<2.5%), and a few also contain silver (<1%). The corrosion resistance of these low-density alloys is similar to other alloys in this series. A special group of alloys in this series contains nickel (<2.5%), which imparts high-temperature corrosion resistance for applications such as internal combustion engine pistons.

3xxx Series. The alloys in this series contain primarily manganese, up to 1.5%. Several also contain magnesium, up to 1.5%. The alloys in this series are strengthened by work hardening and are produced in extruded, sheet, and plate forms. Manganese has minimal impact on the corrosion resistance of aluminium alloys. These alloys have only moderate strengths and good corrosion resistance. Alloys in this series find use in beverage and food containers, building products, heat-exchanger tubing, and other general uses requiring good corrosion resistance.

4xxx Series. The alloys in this series contain primarily silicon, up to 14%. Because of their low melting points, these alloys are used primarily for braze and weld filler applications. These alloys are usually produced as sheet or wire and are found in the as-cast condition following a thermal joining process. The silicon in these alloys generally does not promote corrosion of the alloy itself. However, when used in a thermal joining process, there have been cases where the silicon has diffused into the grain boundaries of the materials being joined, causing decreased corrosion resistance.

5xxx Series. The alloys in this series contain primarily magnesium, up to 6%. Several of the alloys also contain manganese. Alloys in this series are strengthened by work hardening and

are produced primarily as sheet and plate. Several of the alloys that are produced as drawn wire are used in the production of window screens and as weld filler. The magnesium additions generally improve the corrosion resistance of these alloys, especially in seawater. The 5xxx series of alloys can be divided into two groups: low magnesium (under 3%) and high magnesium (3 to 6%). The low-magnesium alloys have very good corrosion resistance in a broad range of environments. The high-magnesium alloys have greater strength than the low-magnesium alloys, and they have outstanding corrosion resistance in saltwater environments. The only drawback to the high-magnesium alloys is that they can be susceptible to intergranular forms of corrosion, including exfoliation and stress-corrosion cracking. Such corrosion susceptibility can be avoided by using particular tempers and by limiting the maximum service temperatures to 65 °C. The high-magnesium alloys are used extensively in marine vessels and structures.

6xxx Series. The alloys in this series contain primarily magnesium (<2%) and silicon (<2%), which form a strengthening constituent, magnesium silicide. Several of the alloys in this series also contain copper (<1.2%) and/or manganese (<1.2%). The alloys in this series are strengthened by thermal processing to have moderate strength. They generally have good corrosion resistance but those that contain copper have somewhat poorer corrosion resistance than those without copper. The range of alloys in this series is very broad. Some of the alloys are produced only as sheet products for applications such as automotive body panels; others are produced only as extrusions for use as structural shapes. Still others are produced as extrusions and sheet.

7xxx Series. The alloys in this series all contain zinc, up to 9%. In addition, nearly all of these alloys contain magnesium (<4%), and many of them contain copper (<3%). The alloys in this series are strengthened by thermal processing, resulting in several that are among the strongest commercially available aluminium alloys. Most of the alloys in this series are produced in both sheet and plate products; several of the alloys are also produced as extrusions. Because of their significant copper content, most of these alloys have only moderate resistance to general corrosion and pitting. When overaged tempers are used, these alloys have good-to excellent exfoliation and stress-corrosion-cracking resistance. A few of the alloys in this series have very little copper and are used for special corrosion-related applications, such as sacrificial cladding on cladded sheet products.

8xxx Series. The alloys in this series do not fit into any of the previous series. Most of these alloys contain significant quantities of iron (<10%). A number of these alloys are produced as foils for consumer and commercial food wraps. In these applications, the alloys have very good corrosion resistance. Also, several of these alloys contain copper (<2%), magnesium (<2%), and lithium (<3%), with little or no iron. The lithium is added to reduce the density of the alloys for weight-critical aerospace applications. These low-density alloys are produced as sheet and plate that are thermally processed to develop strength. These alloys have corrosion resistance similar to many of the 7xxx alloys.

3.3. Corrosion protection of aluminium alloys

In order to improve the corrosion performance of the aluminium alloys to be usable in the aircraft industry, the alloys must be surface treated and usually coated. There exist a number of industrial processes, but most of them involve basically a pretreatment of the parts (cleaning and etching), a chemical conversion treatment (electrochemical or chemical

treatment) and a postreatment (sealing or primer). The general scheme of one of the classical protective system for aluminium alloys in an aircraft is shown in fig. 10.

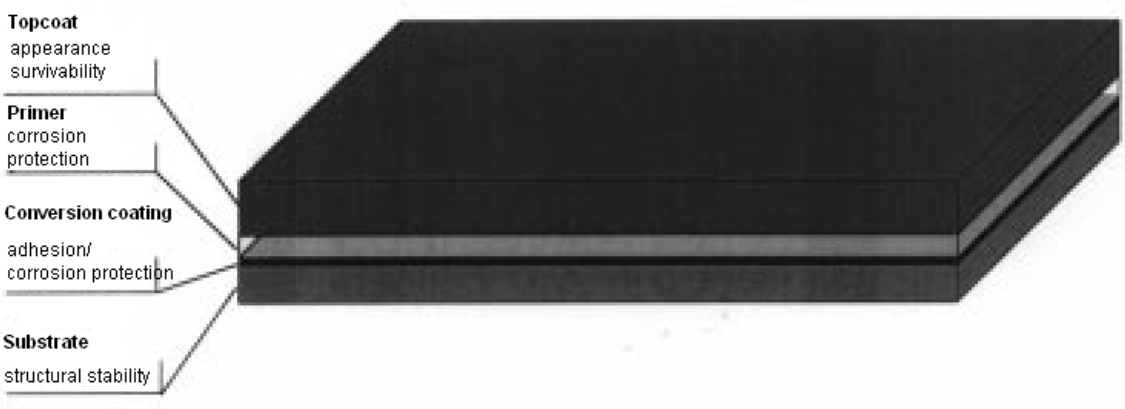

Figure 10. Schematic of the components of an aircraft protection system [16]

Following, a summary of these processes is described.

3.3.1. Pretreatment

The pretreatment of the pieces prior to anodising or other chemical conversion processes should not be underestimated; if this is not carried out correctly all subsequent processes effectiveness are endangered.

3.3.1.1. Cleaning

The functions of a cleaning cycle involve removal of at least one of a variety of undesired by-products of the manufacturing route, such as: protective oils and greases, polishing compounds, surface oxides or corrosion products, handling grease, finger marks, dust, metal chips, solid dirt, foreign matter, welding or brazing fluxes, corrosive salts and welding or annealing scales after welding, moisture, faulty organic coatings or organic coatings applied for corrosion protection during storage, faulty electrodeposits for refinishing, oxide films or faulty anodic or chemical coatings.

Cleaning methods

Vapour degreasing

This cleaning process removes oils and greases as well as solid dirt particles from metal surfaces. However, it will not produce a chemically clean surface and is usually supplemented by alkaline cleaners.

The solvents employed are non-inflammable chlorinated hydrocarbons; the most common of them was trichloroethylene (B.P. 87 °C). Nevertheless, the use of these chemicals is restricted due to the strong evidence that chlorofluorocarbons were depleting the ozone layer in the

atmosphere. Nowadays, new low temperatures and environmentally compliant solvents have also been developed.

Ultrasonic cleaning

Ultrasonic cleaning is increasingly used for difficult cleaning jobs where simple immersion is unsatisfactory. The value of the ultrasonic cleaning lies in the mechanical scrubbing action that occurs as the fluid is ruptured and then reformed and this takes place at a rate equal to the frequency of the energy input. However, ultrasonic cleaning requires expensive equipment and is normally feasible only for relatively small parts.

Alkaline cleaning

This is the most important of all the cleaning processes. There exist lots of commercial alkaline cleaners that are basically compounded of sodium hydroxide, corrosion inhibitors and wetting agents. The alkaline cleaners need to be strictly controlled. The ideal cleaner should satisfy the following conditions: The salts should be completely and easily soluble and the cleaner should be stable and possess good rinsing properties. Its alkalinity should be suited to the metal, for aluminium preferably between pH 9 and pH 11. It should also be buffered to help maintain constant activity of the cleaner. It should possess good wetting power. It should have a high emulsifying power to break up and disperse such oils and greases as can form soluble soaps. It should be able to deflocculate dirt particles and disperse them throughout the solution by colloidal action. The cleaner should be inhibited to minimise attack on the basis metal. It must be non-irritant to the skin, and should be preferably be non-toxic. The cleaner should act as a water softener and so prevent precipitation of hard-water salts on the metal surface. Finally, the cleaner must be economical.

The compounds commonly used as inhibitors are silicates, chromates, phosphates, fluorides, silicofluorides or organic materials. These compounds provide a protective film that is formed by reaction of the inhibitor with the aluminium or the oxide surface, or, in the case of silicates, a mono-molecular layer of hydrated silica may be formed superficially. The inhibitors should allow a minimum of visible etching and at the same time allow a mild chemical attack.

Rinsing

The rinsing operations in a cleaning cycle are as important as the cleaning operation itself and the work of the most effective cleaners may be undone by contaminated rinses. It is important not allow any delay between the cleaner and the rinse, as a cleaner which has dried on to the metal surface may be very difficult to remove in the rinse. Alkaline materials such as sodium hydroxide are difficult to remove from metal surfaces, so that, agitation of the rinse water is recommended to accelerate the dilution of the sodium hydroxide film.

3.3.1.2. Etching

Alkaline etching

The most frequently used method for etching aluminium is in aqueous solution of sodium hydroxide with or without other additives.

Aluminium dissolves in sodium hydroxide with the release of hydrogen to form the compound aluminate that exists only in alkaline solution:

$$2Al + 2NaOH + 2H_2O \rightarrow 2NaAlO_2 + 3H_2$$

The available sodium hydroxide decreases as this reaction proceeds and with the consumption of such free sodium hydroxide the etching rate drops, the electrical conductivity of the solution decreases and the viscosity increases. If no sodium hydroxide is added the bath action become very sluggish, but eventually the clear or brownish solution will turn to a milky white and at this point the etching rate will suddenly increase again to a value which may not be very far below the initial etching rate. The main reaction at this point becomes:

$$NaAlO_2 + 2H_2O \leftrightarrows \downarrow Al(OH)_3 + NaOH$$

It has been found that a sodium hydroxide solution in continuous use will take aluminium into solution until the uncombined sodium hydroxide is approximately one quarter of the original total sodium hydroxide, and thereafter it will continue etching with the uncombined sodium hydroxide fluctuating about this level with and amplitude which depends on the temperature, rate of usage and resting periods. The hydrate will slowly settle or crystallise at the tank bottom and sides forming a very hard rock hydrate; this represent a third reaction, dehydration of the aluminium hydroxide to form alumina:

$$2Al(OH)_3 \rightarrow Al_2O_3 + 3H_2O$$

Another important effect of aluminium is that increasing aluminium content decreases the etch rate very significantly. In practice, this means that if a constant etch rate is required, the free caustic content of the solution needs to be increased as the aluminium content of the bath rises.

The main method to prevent or slow down the rate of deposition of alumina is the use of chelating agents. Tartrates or citrates were commonly used for this purpose, but the introduction of sodium gluconate and sodium heptonate has provided much more effective agents for retaining aluminium in alkaline solution.

When high copper containing aluminium alloys alkaline are etched, a characteristic smut is deposited on the surface of such parts. Smut is a gray-to-black residual film formed by alloying elements (principally copper, iron or silicon) that are insoluble in alkaline media and thus is reduced to metal form on the aluminium surface.

The alkaline etching of aluminium alloys, especially those containing copper, always needs a subsequent treatment in nitric acid, therefore for the aircraft industry, it is more efficient to have a one-step etching process and usually acid etching baths are utilised. Especially, when the part is processed by machining and the surface does not present heavy oxide due to other manufacturing processes or thermal treatments.

Acid etching

Several commercial acid etching products exist; in the aircraft industry are used for different purposes that include:

- Cleaning with little or not etching prior to the application of a suitable chemical conversion coating prior to the application of organic coatings or electroplated coatings. This kind of solutions usually contain nitric acid or chromic acid, the former attacking aluminium only very slowly, while chromic acid both passivates aluminium and tends to confer a passivating action on any other solution to which it is added.

- As a desmutting bath or neutralising rinse after alkaline etching. In this category, nitric acid is principally employed as a desmutting bath after alkaline etching to remove the insoluble products generated during the alkaline etching (mainly copper oxides).

- Removal of oxide, mill scale, corrosion products, heat treatment scale or welding fixtures. Mixtures of chromic and phosphoric acids at 98-100 °C are used for removing oxides with little effect on aluminium of most alloys. Other mixtures are compounded of sulphuric and hydrofluoric acids or sulphuric and chromic acids.

Environmental concerns are putting pressure on the use of products containing chromium or fluoride ions and this has resulted in a number of formulations that are acid based but chromium and fluoride free, e.g. aqueous acid cleaners based on phosphoric and sulphuric acids and containing various additives.

One of the most promising formulations for the aircraft industry is a mixture of sulphuric acid, nitric acid and ferric sulphate.

Hot concentrated sulphuric acid acts as an acid and as an oxidising agent. It reacts with tin, zinc and copper to produce the salt, water and sulphur dioxide.

$$Cu(s) + 2\ H_2SO_4\ (aq) \rightarrow CuSO_4\ (aq) + 2\ H_2O\ (l) + SO_2\ (g)$$

The action of nitric acid on a metal usually results in reduction of the acid (a decrease in the oxidation state of the nitrogen). The products of the reaction are determined by the concentration of nitric acid, the reactivity of the metal involved, and the temperature. In most cases, a mixture of nitrogen oxides, nitrates, and other reduction products is formed. Relatively unreactive metals such as copper reduce nitric acid primarily to NO_2.

$$Cu\ (s) + 2\ H^+ + 2\ HNO_3 \rightarrow Cu^{2+} + 2\ NO_2\ (g) + 2\ H_2O\ (l)$$

The nitric acid reacts as an acid only with magnesium, magnesium and calcium

$$Mg\ (s) + 2\ HNO_3\ (aq) \rightarrow Mg(NO_3)_2\ (aq) + H_2\ (g)$$

Ferric sulphate also acts as an oxidising agent

$$Fe_2(SO_4)_3 + Cu \rightarrow 2\ FeSO_4 + CuSO_4$$

3.3.2. Conversion coatings of aluminium

3.3.2.1. Electrochemical conversion coatings: anodising of aluminium

Aluminium anodising is an electrochemical method to form protective non-conductive aluminium oxide (Al_2O_3) surface films. This aluminium oxide is adhered to the substrate forming a film, generally of several nm. Anodising increases corrosion resistance and wear resistance of the aluminium alloys, providing also improved adhesion for organic coatings comparing with the bare metal.

As all electrochemical methods, aluminium anodising must be undertaken in an electrochemical cell. This electrochemical cell consists of an anode and a cathode, an electrolyte and a current rectifier.

The anode is aluminium or aluminium alloy part being anodised; the main reaction taking place in its surface is the oxidation of aluminium

$$Al \rightarrow Al^{3+} + 3e^-$$

Side reactions are possible such as oxidation of water.

$$2\ H_2O \rightarrow O_2 + 4H^+ + 4e^- \text{ In acid media}$$

$$4\ OH^- \rightarrow O_2 + 2H_2O + 4e^- \text{ in alkaline media}$$

The cathode can be of different materials, widespread lead is not longer used due to its health and environmental drawback and now usually stainless steel is used. In the cathode, the main reaction is hydrogen evolution

$$2H^+ + 2e^- \rightarrow H_2 \text{ in acid media}$$

$$2H_2O + 2e^- \rightarrow H_2 + 2OH^- \text{ in alkaline media}$$

Side reaction usually occurs during the anodising of aluminium alloys, namely the deposition of metals previously dissolved from the alloys i.e. copper deposition.

$$Cu^{2+} + 2e^- \rightarrow Cu$$

Anodic film structure

The morphology of the anodic film will mainly depend on the anodising conditions and the electrolyte. The structure of the anodic films can be classified in two major groups: barrier-type films and porous type films.

Barrier-type films

Barrier type films are those anodic layers that grow uniformly on the aluminium or aluminium alloy substrate. The electrolytes for obtaining such barrier films are near neutral pH, in the region where Al is passivated (see Pourbaix diagram in Fig. 7). Some examples of those electrolytes are diluted aqueous solutions of ammonium tartrate, ammonium borate/boric acid and ammonium pentaborate (fig. 11).

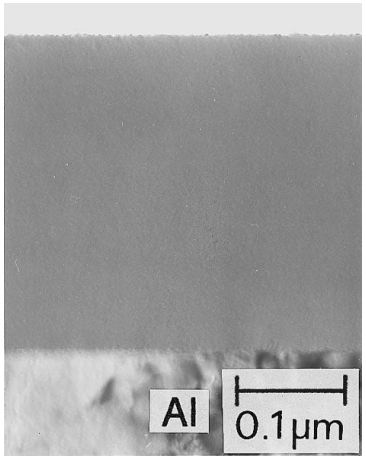

Figure 11. Transmission electron micrograph of an ultramicrotomed section of a 300 V film formed in 0.1 M ammonium pentaborate solution at 20 °C [17].

These films are of considerable technological importance, for example, in the fabrication of electrolytic capacitors [18], TFT in liquid crystal display devices, MIM cathodes for electron beam lithography systems [19], vacuum micro-transistors [20] and display devices [21].

Porous-type films

Porous type films are those anodic films obtained by anodisation of aluminium or aluminium alloy in aqueous electrolytes at a pH region where corrosion of aluminium takes place (see Pourbaix diagram in fig. 7). As a result of this, during anodising process there is a balance between aluminium oxide formation and aluminium dissolution. If the current density efficiency is high enough (See fig. 12), the aluminium oxide formation is the predominant process and the anodic film will present a barrier-type structure. However, if the current density efficiency is low enough, the formation/dissolution balance results in a porous-type film.

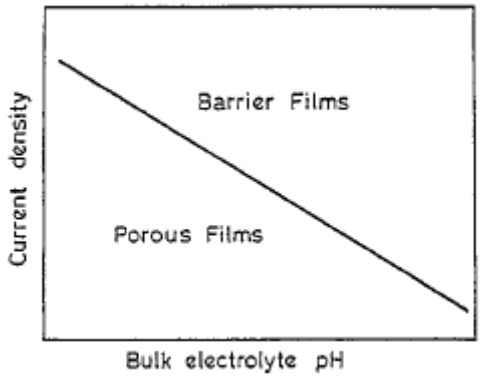

Figure 12. Schematic diagram showing the relationship between solution pH and current density for barrier or porous-type anodic alumina formation. The current densities are typically in the mA range over a pH range between 0 and 7. [22]

The porous structure consist of a duplex structure, on the aluminium or aluminium alloy surface, a continuous barrier layer of some nm thick; on the barrier layer and normal to the substrate there is an array of columnar hexagonal cells with a pore in the centre [23], this porous layer is some µm thick.

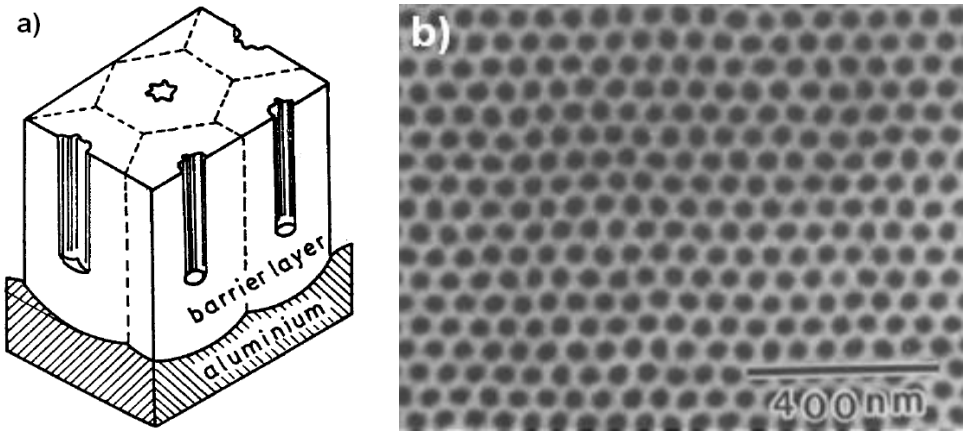

Figure 13. (a) schematic structure of the porous anodic film (b) Scanning electron micrograph of the surface of an anodic film grown on electropolished 99.99% Al in 0.5 M H_2SO_4 at 25 V and 10 °C [24]

The thickness of both, the barrier and the porous layers as well as the cell dimensions will be given by the anodising conditions and the electrolyte. On the other hand, second phase particles and intermetallics in the alloys generate distortion of the structure.

Electrolytes

Electrolytes are usually strong inorganic acids, or mixtures of weak organic acids and a strong inorganic acid, although anodising in alkaline media is also possible. The following section will describe the most common electrolytes and anodising conditions for obtaining porous anodic films.

Sulphuric acid

The sulphuric acid (SA) anodising process is the most widely used type of anodising bath and has many desirable benefits. First, because it has a fairly hard surface, it can be used in situations that require light-to-moderate wear resistance. Applications included lubricated sliding assemblies and items subject to handling wear, such as front panels. Second, because it is the most aesthetically pleasing type of anodise, it should be used where final appearance is important. It can be dyed almost any colour and produces deep, rich shades that make the item appear to be made of a material bearing a colour throughout, rather than an applied coating. Finally, because the corrosion resistance is fairly high for most of the aluminium applications. Besides sulphuric anodise is the least costly and most widely available type of anodise.

However, the sulphuric acid anodising process is not convenient for the aircraft industry because of the low paint adherence and the reduced resistance to fatigue of the anodised parts.

The recommended operating parameters for a good quality of the anodising are [25]:

Electrolyte temperatures: 18-20 °C controlled to within ± 1 °C. Higher temperatures will lead to excessive film attack and temperatures below 17 °C will necessitate the use of high anodising voltages.

Electrolyte concentration: 1.63-1.84 M (160-180 g L^{-1}) controlled to within 10 g L^{-1}. Higher electrolyte concentrations lead to increased film attack, particularly in combination with high

electrolyte temperatures, whereas low electrolyte concentrations will necessitate the use of high anodising voltages.

Anodising current density: 1.4-2.0 A dm^{-2}. Low anodising current densities mean a slow rate of film formation, hence increased attack on the film. On the contrary, the use of high current densities mean fast rates of film formation, but film thickness variation is increased and contact problems may be experienced.

Electrolyte agitation: even and effective. This is essential in order to take heat away from the surface of the anodic coating and should be sufficient to give uniform temperature distribution throughout the anodising electrolyte.

Anodising voltage: a range of 17-21 V is required.

A special process carried about in SA under specific anodising conditions is the hard sulphuric acid anodising. This process produces a coating that is normally 50 µm thick, although other thicknesses can be specified. The coating is extremely hard.

Hardcoat penetrates the base metal for one-half of its thickness and builds above the original base metal dimension for one-half of its thickness. Thus, for a thickness of 50 µm per side, the dimensional change of the workpiece would be 25 µm per side. Commercially available coating thickness tolerances are the greater of ± 5 µm or ± 10% of the total targeted thickness. The corrosion resistance of the unsealed coating is very good and comparable to the other types of anodise. When the hardcoat anodise is sealed, it becomes the most corrosion-resistant type of anodise.

Hardcoat anodising, because of its variety of desirable properties, has found widespread use in manufactured products. Its extreme hardness makes it suitable in situations in which wear resistance is required. Applications include valve/piston assemblies, drive belt pulleys, tool holders and fixtures, and many other items requiring wear resistance.

Hardcoat has excellent resistance to corrosion and is used on aluminium components in harsh environments. These include outside exposure in salt air, marine components, automobile wash equipment, components for the aircraft and aerospace industries, and food preparation machines.

Besides, hardcoat is an excellent electrical resistor. It can be used to insulate heat sinks for direct mounting of electrical or electronic equipment. Also, it is used in welding fixtures where some areas may need to be insulated from work.

Hardcoat is a naturally porous substance, it is used in many areas in which the bonding or impregnation of other materials to aluminium is needed. This coating bonds very well with paints and adhesives. Also, it can be impregnated with Teflon (polytetrafluoroethylene, or PTFE) and many dry film lubricants to impart lubricating properties to the coating.

Lastly, because of its desirable properties and also because it produces a buildup of coating, it is widely accepted as a salvage coating to restore worn or improperly machined parts to usable dimensions. Coating thicknesses in excess of 250 µm per side are possible on some alloys with certain proprietary hardcoat processes.

Hardcoat anodising is the most expensive type of anodising. It is generally twice the cost of H_2SO_4 anodising and 50% more than CrO_3 anodising.

Chromic acid

CrO_3 anodising is the least used of the three main types of anodising. However, it is the most used in the aircraft industry because of several advantages that make its use desirable. First, because CrO_3 is much less aggressive toward aluminium than H_2SO_4 and it should be used whenever part design makes the bath electrolyte rinsing is difficult. This includes welded assemblies, riveted assemblies, and porous castings. Second, a typical CrO_3 anodic film is 0.7 µm per side with good repeatability. Therefore, it is a very good coating to use when it is necessary to coat a precise dimension to size. Third, CrO_3 anodising produces the least reduction in fatigue strength of the anodic coatings; it should be used where fatigue strength is a critical factor. Fourth, the colour of CrO_3 anodising will change with different alloy compositions and heat-treat conditions; this makes it useful as a test of the homogeneity of structural components or overheating during machining. Lastly, when properly applied, CrO_3 anodising can be used as a mask for subsequent hard coat anodising operations.

From an economical viewpoint, chromic anodising costs more than H_2SO_4 but less than hardcoat anodising.

A summary of the typical operating parameters for a good quality of the chromic acid anodising for the aerospace industry are [26]:

Electrolyte temperatures: 38-42 °C

Electrolyte concentration: 30-100 g L^{-1} the purity of the chromic acid shall be no less than 99.5%.

Anodising voltage: The voltage across the bath should be increased in steps of not more than 5 V from 0-40 V in the first 10 min, maintained at 40 V for 20 min, gradually raised to 50 V in the next 5 min and maintained at 50 V for 5 min.

Anodising current density: The average current density over the 40 min is approximately 0.3-0.4 A dm^{-2}.

The cathode shall be mild steal or stainless steal. The anode:cathode area ratio is not critical, but less chromic acid is consumed at the higher ratios. Values varying from 5:1 to 10:1 are generally suitable.

Oxalic acid

The oxalic acid processes are more expensive than the sulphuric acid processes both in chemicals and power consumption, but thicker coatings of up to 60 um may be obtained without the use of special techniques. Hence oxalic acid has been used to some extent in hard anodising.

There have been described several operating parameters that results in small differences in the colour, thickness and porosity of the anodised pieces, most of them are presented in the following [27]:

Electrolyte temperatures: 18-35 °C

Electrolyte concentration: 3-5% Electrolyte purity is probably of grater importance in the oxalic than in the sulphuric acid process, and pitting occurs more readily.

Anodising voltage: 20-60 V

Anodising current density: 1-3 A dm^{-2}.

Anodising time: 20-60 min

Weak organic acids

These kinds of electrolytes are usually two or three components mixtures utilised with the aim of obtaining coloured anodic films. Kape [28,29] formulated the proposition that all satisfactory acid for anodising are dibasic (two –COOH or SO_3H groups, or one of each) with a dissociation constant of at least 10^{-4} for the second hydrogen ion and at least 1% solubility in water at 20 °C. Some organic acids fulfilling these conditions are: maleic acid, succinic acid, citric acid, formic acid, propionic acid or tartaric acid.

Tartaric acid/sulphuric acid

Tartaric acid/sulphuric acid (TSA) process is the most promising anodising bath for substituting the CAA process in the aircraft industry.

L-Tartaric acid is an organic diacid naturally found in fruits and is one of the principal acids in wine, the first constant of dissociation is -1.50 10^{-3} and the second 4.57 10^{-5}.

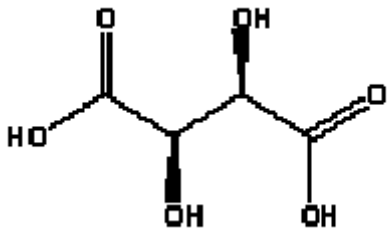

Figure 14.Structure of L-tartaric acid ($C_4H_6O_6$)

The anodising conditions are [30]:

Electrolyte temperatures: 37 ± 1 °C

Electrolyte concentration: 40 ± 10 g L^{-1} H_2SO_4 80 ± 10 g L^{-1} $C_4H_6O_6$

Anodising voltage: 14 ± 1 V

Anodising current density: 0.5-1.0 A dm^{-2}.

Anodising time: 25 ± 1 min

The addition of L-tartaric-acid to a SA bath results in a decrease of conductivity, although the action of the tartaric acid in the bath is not well understood. Iglesias-Rubianes et al. [31] claimed the addition of tartaric acid to the SA anodising bath does not result in significant changes on the film morphology, whereas Curioni et al. [32] suggested the tartaric acid is incorporated residually in the pores of the anodic film, such residual tartaric acid decreases the solution rate of the anodic film generated on AA2024-T3 in the acidic environment.

Boric acid/ sulphuric acid

The boric acid/sulphuric acid anodising bath (BSA) [33] has been proposed as a potential replacer of the chromic acid bath by Boeing, the anodising conditions are:

Electrolyte temperatures: 22 °C

Electrolyte concentration: 45 g L^{-1} H_2SO_4 and 10-50 g L^{-1} HBO_3

Anodising voltage: 15 V

Anodising time: 15-30 min

Corrosion test of BSA anodised AA7075-T6 specimens passed the same requirements as the CAA anodised samples. [34]

Domingues et al. tested small additions of Na_2BO_4 to the BSA anodising bath [35], AA2024-T3 resulted in corrosion and fatigue resistance comparable to those obtained by the CAA process.

From an industrial viewpoint, these processes are more expensive than the SA anodising bath.

Phosphoric acid

Phosphoric acid anodising is not used for protective finishing; its main application is a preparative treatment for subsequent application of organic coatings or adhesive bonding. The anodising conditions are [36]:

Electrolyte temperatures: 21-24 °C

Electrolyte concentration: 10-12 % wt.

Anodising voltage: 10-15 V

Anodising time: 20-25 min

Some two-step anodising processes have been developed with the aim of obtaining bonding properties and corrosion resistance: the anodising in phosphoric acid is the common first step for all these kind of anodising, then is followed by anodising in a BSA bath [37] or a TSA bath [38].

Growth of the film

As previously mentioned, morphology of the film, and therefore growth of the film will be dependant on the electrolyte, the anodising conditions and the purity of the substrate.

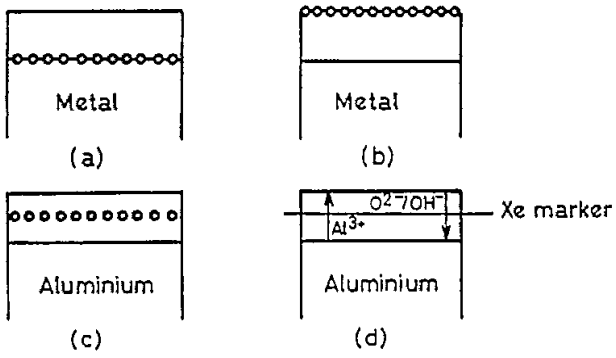

Figure 15. Schematic diagram of sections of films, revealing location of marker for film growth by (a) cation transport, (b) anion transport (c) cation and anion transport and (d) mobile ions for aluminium anodising process [39].

Fig. 15 summarises the position of a marker after the film growth due to transport by cation egress (Fig. 15a), anion ingress (Fig. 15b) and combines cation egress and anion ingress (Fig. 15c). In the particular case of high current efficiency anodising of aluminium (Fig. 15d), Xe markers studies revealed that Al^{3+} transport number is about 0.4. The cation transport number is determined from the ratio of the film thickness developed above the marker to the total film thickness.

Tracer studies utilising mobile ^{16}O and ^{18}O during the anodising process [40,41] and outwardly mobile cations suggested a cooperative transport mechanism of Al^{3+} and O^{2-}/OH^- [42,43]. Such cooperative mechanism consists of the penetration of the anion to the metal/oxide interface, reacting with the aluminium to form aluminium oxide:

$$2\ Al + 3\ O^{2-} \rightarrow Al_2O_3 + 6e^-$$

And the outwardly mobile aluminium cations reacting in the oxide/interface electrolyte to form alumina:

$$2\ Al^{3+} + 3\ H_2O \rightarrow Al_2O_3 + 6\ H^+$$

Effect of the electrolyte on the composition of the anodic film

Apart from the anodic film formation, the incorporation and distribution of the specimens in the electrolyte across the anodic film has been also studied with the help of xenon markers. Fig. 16 shows such distribution on alumina films formed in borate, phosphate and tungstate electrolytes.

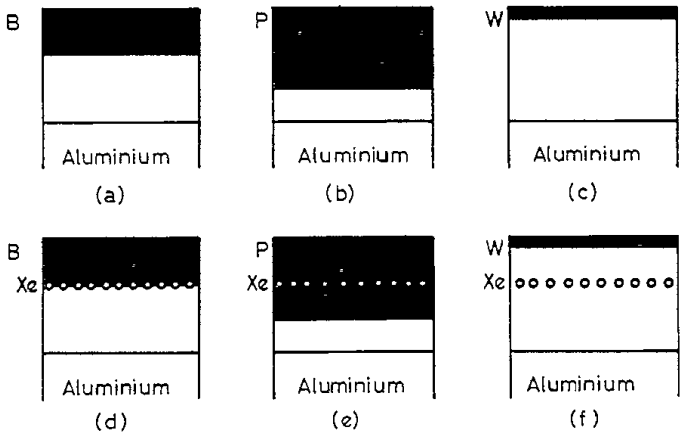

Figure 16. Schematic diagrams of sections of barrier films formed on aluminium in: (a) borate, (b) phosphate and (c) tungstate electrolytes. The location of xenon markers are revealed in (d-f) [44].

For highly efficient film growth and with reference to the xenon inert marker, B species (fig. 16d) are present in the outer part of the film thickness, specifically in the outer film region developed by Al^{3+} egress (about 0.4) This result suggest that B species are immobile in anodic alumina. P specimens are present in the outer film region and have passed below the marker into the film region developed by O^{2-}/OH^- ingress (fig. 16e), showing inward mobility. W species are present in the very outer film region (fig. 16f) therefore outwardly mobile. The fate of the adsorbed/incorporated specimens in the film depends on the consequences of the action of the electric field on the incorporated species. Thus, it is suggested that B_2O_3 units are incorporated with the electric field strength being insufficient to break B-O bonds. Conversely, the field strips oxygen atoms from WO_3, resulting in the generation of W^{6+} cations, which move

outwards at a slower rate than that of Al^{3+} under the field. For PO_4^{3-} anions, these remain unaffected by the high field and migrate inwards, at a rate less than that of O^{2-}/OH^- anions.

Effect of the alloying element on the composition of the anodic film

The alloying elements fall into several categories:

- Alloying elements oxidise immediately at the alloy-film interface (Li, Mg) and moves outwardly.
- Alloying elements enrich at the alloy film interface (Zn, Cu) during the initial oxidation of aluminium. This enrichment is over 1-5 nm immediately below the anodic film. Once a critical concentration is achieved, the alloying element will oxidise and migrate outwardly.
- Alloying elements without subsequent oxidation and incorporation into the anodic film (Au). These elements enriches at the alloy-film interface without eventual oxidation and incorporation into the anodic film.

Porous film growth

In the particular case of the growth of the alumina film at reduced current efficiency, no contribution to solid film growth is evident at the film-electrolyte interface. Besides, the film developed at the metal-film interface interacts with the electrolyte. Such interaction results in dissolution of the anodic film assisted by the electric field, and the development of penetration paths from the outer film surface will take place. Fig. 17. schematically illustrates the development of penetration paths for CAA.

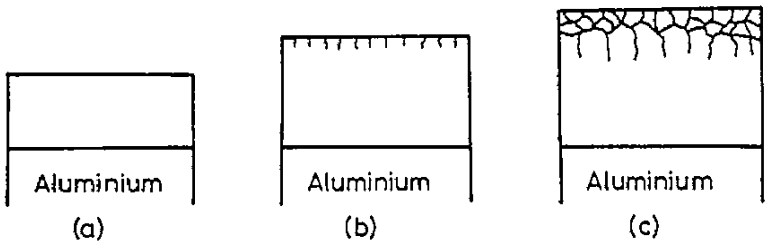

Figure 17. Schematic diagram illustrating the development of penetration paths, the precursors top ores, during anodising in chromic acid [44].

The initial uniform potential distribution (fig. 17a) will change [45] and concentrate beneath the paths, locally increasing the field strength (fig. 17b). Further penetration of the paths (fig. 17c) consequently increases the field-assisted dissolution. The relatively strong lateral component of the field beneath the tip of the penetration path causes a development of an embryo pore with the characteristic inversely funnelled sectional appearance.

As the voltage rises, the development of the anodic film is not uniform [46]. Protuberances extend from the outer surface of the anodic film (fig. 18).

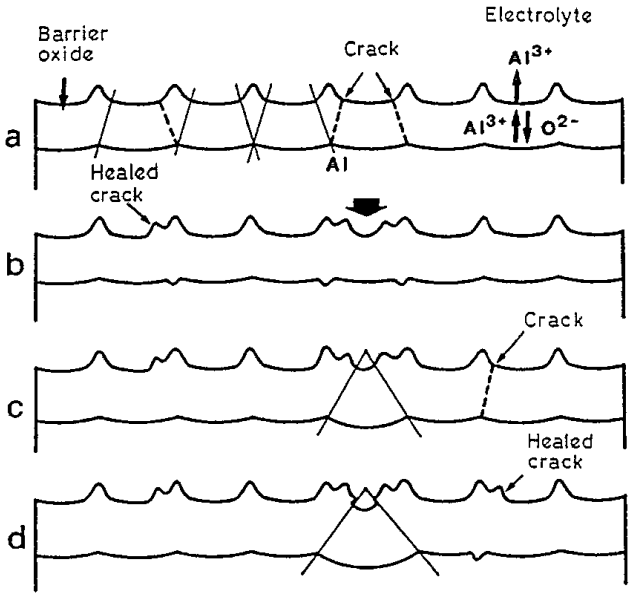

Figure 18. Schematic diagram showing pore development during anodising of aluminium in phosporic acid [44].

During the crack-heal events, the curvature of the cracks increases, increasing the field in the previous thinner film regions to a level where the field-assisted dissolution rate is equal to the rate of thickening of the oxide at the metal-film interface. This results in the development of major pores.

3.3.2.2. Chemical conversion coatings on aluminium

Chemical conversion coatings (CCC) are adherent surface layers of low-solubility oxide, produced by oxidation/reduction reaction of suitable reagents with the metallic surface. These coatings affect the appearance, electrochemical potential, electrical resistivity, surface hardness and absorption.

Although chemical conversion coatings offer a lower corrosion protection than anodic layers, they are widely used for improving the adhesion of organic finishes on aluminium parts. They are also used as spot treatment for the repair of damaged areas in anodic coatings or where the anodisation is not possible or very difficult, e.g. interior of pipes. There are various types of CCC, which are following described.

Chromate conversion coatings.

The formation of a film of mixed chromium oxide/hydroxide on an aluminium surface is a result of an electrochemical reaction that involves the oxidation of aluminium and the reduction of chromate species:

$$Al \rightarrow Al^{3+} + 3e^{-} \quad (1)$$

$$HCrO_4^{-} + 7H^{+} + 3e^{-} \rightarrow Cr^{3+} + 4H_2O \quad (2)$$

$$Cr_2O_7^{2-} + 14H^{+} + 6e^{-} \rightarrow 2Cr^{3+} + 7H_2O \quad (3)$$

With the evolution of reactions (2) and (3), and the reduction of hydrogen ions as a secondary cathodic reaction, the pH of the chromate bath in proximity to the aluminium surface rises to a value high enough to enable the precipitation of a solid conversion coating consisting of chromium hydroxide [47]:

$$Cr^{3+} + 3H_2O \rightarrow Cr(OH)_3 + 3H^+$$

Zhang et al. [48] studied the influence of coating time of pure aluminium on breakdown potential by anodic polarisation, concluding that increasing coating time increases anodic inhibition. Most of the improvement in inhibition occurs in the first 30 s of coating time, and then such inhibition slightly improves up to 2 min of coating time. At this point, longer coating time up to 5 min does not have any beneficial effect on the anodic inhibition.

It has been stated that the real corrosion protection depends strongly on the Cr (VI) traces present in the chromium hydroxide coating [49]. Insoluble Cr (III) has many surface hydroxyl groups available for formation of Cr(III)-O-Cr(VI) bonds. These hydroxyl groups act as sites for adsorption of Cr(VI), accompanied by the addition of a hydrogen ion to produce water. The reaction may be represented by [50]:

$$Cr(III)\text{-}OH + Cr\ (VI) + H_+ \leftrightarrows Cr(III)\text{-}O\text{-}Cr(VI)\ (ad) + H_2O$$

Recently, a conversion coating process named trivalent chromium process (TCP) patented by NAVAIR [51,52] claims that there are not Cr^{6+} containing.

Yu et al. [53] coated AA6063 in a 20 g L^{-1} $KCr(SO_4)_2$, 20 g L^{-1} H_3PO_4 bath at pH = 2.1, the surface analysis by XPS showed only presence of Cr^{3+} compounds. The corrosion inhibition of the conversion coating compared to the bare alloy was clear, however, further insight into the corrosion inhibition mechanism as well as testing the coating on low corrosion resistance (high copper content) aluminium alloys is necessary in order to confirm such coatings as a real alternative to Cr (VI) conversion coatings.

Phosphate conversion coatings

The phosphate conversion coatings contain about ⅔ $NH_4H_2PO_4$, but also NH_4HF_2 and $K_2Cr_2O_7$. The phosphate-chromate conversion coatings are used on aluminium parts or assemblies to provide galvanic protection from components of different kinds of materials.

There exist a variety of other combinations of heavy metals + phosphate conversion coatings (iron, zinc or manganese phosphates), however the corrosion resistance of this coatings is very poor [54], and are only utilised for enhancing adhesion on materials on which corrosion is not a determining factor.

3.3.3. Postreatments for aluminium anodic films

3.3.3.1. Sealing

Sealing process is the conversion of aluminium oxide into one of its hydrates, this process is accompanied by an increase in volume which bridges over and closes up the porous structure. Therefore, it gives a coating that is both impervious to liquids and more resistant than the

unsealed coating to most chemical environments by virtue of its inherent stability and greater resistance to chemical attack [55].

Hot water sealing

The simplest technique for achieving the previous is named hot water sealing (HWS); such technique consist of the immersion of the anodised part in distilled or deionised water at or near its boiling point. The mechanism of HWS has been broadly studied: impedance studies of SA anodic films on pure aluminium sealed in a variety of media by Hoar and Wood [56] concluded that the pores become filled by inward movement from their sides at the same time as they are plugged at the surface until the pore volume is about 99% filled. This initial mechanism has been the base for further insight into the sealing water process [57-62]. The accepted sealing mechanism was described by Thompson and Wood [63], the schematic mechanism is shown in fig. 19.

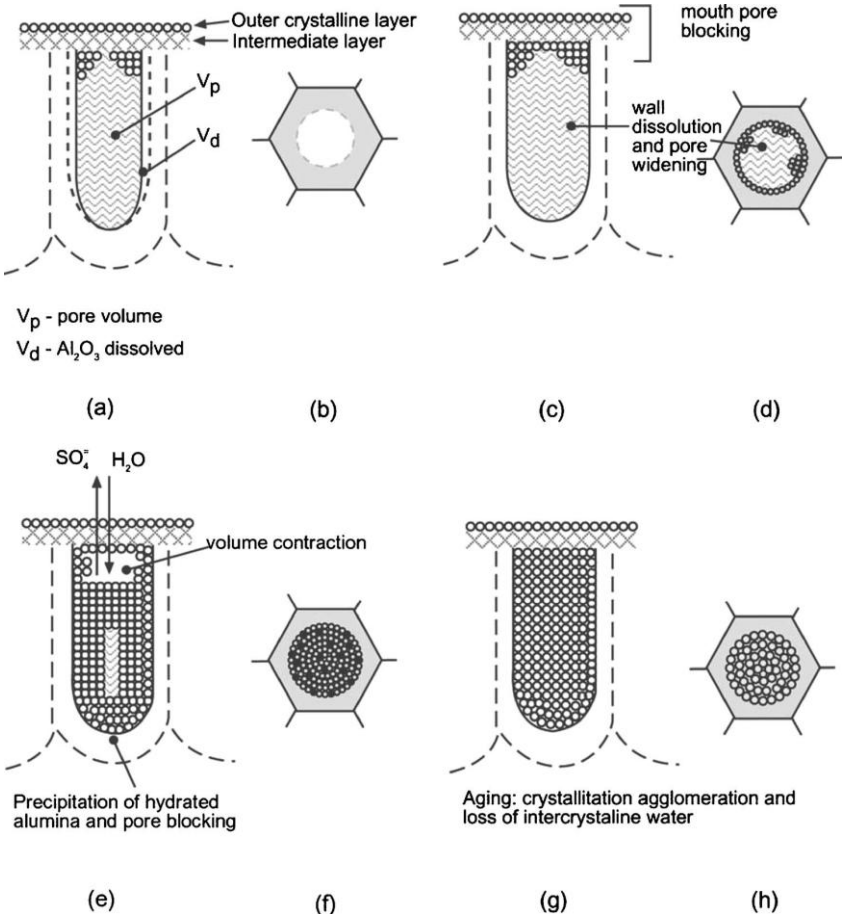

Figure 19. Sealing mechanism (a,b) Filling of the pores with the sealing solution, plugging of the pore mouths, and formation of a surface layer of acicular pseudobohemite crystals and a compact intermediate layer, (c,d) dissolution of the pore walls and widening of the pores, (e,f) saturation of the solution with alumina hydrates and precipitation of hydrated alumina, progressively plugging the entire length of the pores and (g,h) agglomeration and growth of hydrated alumina crystals during aging [64].

Hot water penetrates in the pores very rapidly, the relatively high pH in the pores tends to precipitate hydrated alumina (probably pseudoboehmite) and at the same time there is an outward diffusion of acidic solution containing aluminium ions from the pores. Dissolution of

the pore walls and barrier layer adjacent to the pore renders the cell material surrounding the pore irregular, and the pores become largely plugged by the solid product deposited via this dissolution/precipitation process (Fig. 19a,b).

Then the dissolution of the macroscopic film surface occurs and precipitation of pseudoboehmite or boehmite takes place, obliterating the outer pore structure and often possessing a platelike or needlelike form, to a thickness of about 1 µm (Fig. 19c,d).

An intermediate layer of featureless morphology develops beneath the surface crystallites and grows progressively in depth, until it is up to several µm thick (Fig. 19e,f).

Over periods of many hours more subtle changes take place within the cell walls and the precipitated material in the pores. Agglomeration apparently occurs, with larger particles tending to grow at the expense of smaller ones by dissolution/precipitation processes. Such processes redistribute the porosity but wit no significant change in the macroscopic film volume (Fig. 19g,h).

The hydrothermal treatment limits the removal and access of molecular water from the pores and intercrystalline regions and apparently increases progressively the hydroxyl content of the film.

López et. at [64] observed the mechanism of sealing of anodic films generated in SA on pure aluminium by SEM, TEM and EIS, concluding that during HWS process only the first step was completed, whereas the rest steps were completed during atmospheric exposure.

The processes described above occur at different rates for films formed in different acids with the acid anion from the anodising bath playing a distinct role in the process. A well known phenomenon is the inhibitive effect of phosphate on the sealing process [65].

From the industrial viewpoint, hot water sealing is an expensive method; HWS is used in the aircraft industry mainly in non-structural applications as in cabin structure. However, this HWS is still used as a quality check of the anodised parts.

The sealing rate is strongly dependant on temperature. HWS should be carried out at between 98 and 100 °C, the sealing rate is perceptively slower at 95 °C and is substantially reduced below 90 °C. [65]

Studies of the sealing time at 100 °C [66] reveals that 20-30 min is enough time to obtain a good quality seal. The sealing water should be in a stable pH region for the alumina, preferably between 5.5 and 7, the acidification of the bath due to the electrolyte from the anodising bath can be neutralised by additions of ammonia or buffering the seal bath with ammonium acetate. However, there are limitations in the water characteristics, since impurities in the water can affect negatively to the sealing process: removal of $Ca^{2+}$and Mg^{2+} from hard water is recommended. Especially harmful are PO^{3-}_4, SiO_2 and F^-; these last anions can act as suppression sites. SiO_2 from the interchange columns for deionised water can pose a problem since the silica tolerance is very low.

Dichromate sealing

Dichromate sealing (DS) is a combination of two processes: the absorption of chromate and the closing of the pores by normal hot water sealing, which also locks the Cr^{6+} into the pores.

Tomashov and Tyukina [67] studied the sealing of SA anodic films in boiling 10 % $K_2Cr_2O_7$ in a pH range between 3.7 and 8.5. Complete sealing was achieved after 5-10 min at pH next to 7.

The absorption mechanism was an anion exchange forming aluminium oxychromate in more acidic solutions:

$$OAl\text{-}OH + KHCrO_4 \leftrightarrows OAl\text{-}HCrO_4 + KOH$$

And aluminium dioxychromate in the higher pH ranges;

$$2\ OAl\text{-}OH + KHCrO_4 \leftrightarrows (OAl)_2\text{-}CrO_4 + KOH + H_2O$$

The chromate incorporated gives corrosion inhibiting properties, such inhibition effect is a function of the closing of the pores and the resistance of the absorbed chromate to leaching.

From an industrial viewpoint, the working pH is between 6 and 7.5, pH control is necessary due to the alkalinisation of the bath during DS. The harmful effect of impurities [68] is similar to that observed in the HWS bath.

3.3.3.2. Organic coating

Typical aerospace coating systems consist of a conversion coating on the aluminium alloy surface, a chromate-containing primer, and a topcoat. The application of an organic coating has a double role: on the one hand it has to act as a barrier to water, ions and oxygen. On the other hand it has to act as a corrosion inhibitor reservoir when some of the former aggressive agents penetrate through the coating. The conversion coating (either anodic film or chemical conversion coating) provides a good adhesion between the metal and the organic coatings. It also affords some corrosion protection. The topcoat prevents mechanical damage and contains UV absorbers to prevent coating photodegradation [69]. However, the main active corrosion protection comes from the primer, which can contain up to 25% chromate inhibitor by weight [70].

The most used corrosion inhibitor is strontium dichromate. It is incorporated in the paint formulation as a pigment because of its solubility in water: it is soluble enough to be transported from the primer to the location where corrosion takes place but not so much enough to avoid leaching out from the primer and produce blistering [71]. Other dichromate salts does not fulfil the required solubility, i.e $PbCrO_4$ is so insoluble in water that it has not electrochemical action, at the other extreme Na_2CrO_4 is a poor passivating pigment because it is very soluble in water an it would be rapidly leached out of a film an would probably cause massive blistering.

The mechanism of corrosion protection is similar to that described for the chromate conversion coatings, the main difference is that the organic primer has a reservoir of chromates that will be leached to the solution only when required [72].

All commercial corrosion inhibitor pigments belong to a few generic families of inorganic salts of $A_m^{n+}B_n^{m-}$ or basic salts of $A_m^{n+}B_{n-z}^{m-}OH_z^-$ general formula, where n, m = 2 or 3, and A^{n+} is Zn(II), Ca(II), Sr(II), Al(III), Ba(II), Mg(II), while B^{m-} is CrO_4^{2-}, PO_4^{3-}, MoO_4^{2-}, BO_2^-, $(SiO_3^{2-})_{n,n>1}$, HPO_3^{2-}, $P_3O_{10}^{5-}$, NCN^{2-} [73,74], CO_3^{2-} or various combinations of the same. Additionally, OH^- is a constituent of basic salts [75]. According to Sinko review, there is no other practical inorganic pigment that can match the performance of $SrCrO_4$. However, new hybrid inorganic-organic pigments, such as $Zn(NCN)_2$/Zn(2-mercaptobenzothiazole), can equal or excel its performance on aluminium [76,77].

4. Experimental procedure

4. Experimental procedure

4.1. Description of the pilot plant

The pilot plant where most of the treatments described in this thesis (fig. 20) have been undertaken belongs to the Surface Technology department of Airbus Spain in Getafe, Madrid.

Figure 20. Baths line of the pilot plant of Airbus Spain.

Such pilot plant consists of 10 tanks of about 220 L of capacity each and designed to be able to hold different surface treatments of aluminium and titanium alloys as well as corrosion resistant steels. The tanks are polyethylene (PE) made, except one of PVC for alkaline treatments and one of steel for bearing high temperature treatments. Those tanks designed for treatments are equipped with at least one heating resistance and agitation mechanisms: air stirring (blower) or mechanical stirring (recirculation pump). Three of these tanks are equipped with cathodes to perform electrolytic processes connected to a 30 A DC power supply with automatic potential control. The rinsing tanks have a shower system for a more effective rinse of the samples and a drain to renew continuously the water. The whole bath line is provided with an air and fumes extraction system with water tramp.

The drained water is conducted to a deposit where is treated with NaOH to maintain the pH between 4 and 9, this water can be conducted to an evaporator to recycle it into distilled water and subsequently passed through ionic exchange resins to obtain deionised water. The properties of these two classes of water are as follows.

Table 5. Minimal requirements for the different water qualities in the pilot plant.

Property	Deionised water	Distilled water
Resistivity (20 °C)	> 100000 Ω cm	> 2500 Ω cm
Solids	< 20 ppm	< 400 ppm
Cl^-	≤ 1 ppm	≤ 30 ppm
pH	5 - 7	5 - 8.5

4.2. Materials

The materials utilised in this research are four aerospace quality wrought aluminium alloys used by Airbus. They are representative of the 2xxx, the 6xxx and the 7xxx series, specifically AA2024-T3, clad AA2024-T3, AA6061-T6 and AA7475-T6. The chemical composition (wt. %) of these alloys is detailed in table 6.

Table 6. Chemical composition of the aluminium alloys (wt. %)

Alloy	Cu	Mg	Zn	Mn	Si	Fe	Ti	Cr
AA2024-T3	4.50	1.44	0.02	0.60	0.06	0.13	0.03	0.10
AA1230	0.10	0.05	0.10	0.05	0.70 (Si + Fe)		0.03	-
AA6061-T6	0.18	0.97	0.01	0.10	0.65	0.15	0.02	0.19
AA7475-T6	1.45	2.29	5.78	0.02	0.02	0.09	0.02	0.21

The term “clad” is used for describing a duplex product in which a thin surface layer of one aluminium alloy (usually 5 to 10% of the total thickness) is metallurgically bonded to the main core alloy selected for strength. In order to ensure effective sacrificial cathodic protection of the core alloy, the clad alloy is usually selected to be at least 100 mV anodic to the core [15].

The surface layer is normally 1xxx for 2xxx cores, or 7072 for 3xxx, 5xxx, 6xxx, and 7xxx cores. In the case of the clad AA2024-T3 alloy, the clad layer is AA1230 (Al min 99.30%), with a cladding nominal thickness per side of 5%.

The alclad aluminium alloys provide resistance to perforation by pitting corrosion. Pits do not penetrate into the core alloy, so loss of mechanical properties on long-term exposure to corrosive atmospheres is minimized.

The heat treatments of the studied alloys were:

T3 solution heat-treated, cold worked, and naturally aged to a substantial stable condition. This treatment improves strength after solution heat treatment and for which mechanical properties have been stabilized by room temperature aging.

T6 solution heat-treated and artificially aged. This treatment substantially improves the mechanical properties and dimensional stability.

The possible phases in these alloys depend on the alloy composition and the treatment. For the wrought alloys, the following phases have been described [78]:

AA1230 (2024 clad layer) $FeAl_3$, Fe_3SiAl_{12}

AA2024-T3 $(Fe,Mn)SiAl_{12}$, Mg_2Si, $CuMgAl_2$, Cu_2FeAl_7

AA6061-T6 $(Fe,Cr)_3SiAl_{12}$, Mg_2Si

AA7475-T6 $(Fe,Cr)_3SiAl_{12}$, Cu_2FeAl_7, Mg_2Si, $CuMgAl_2$, $Mg(Zn_2AlCu)$

For the sake of simplicity, the alloys will be named only by its chemical composition (e.g. AA2024), without reference to the thermal process (AA2024-T3).

The dimensions of the samples used are of 150 mm x 100 mm x 2 mm otherwise indicated.

The racks for supporting the samples on the anode are made of Ti (fig. 21).

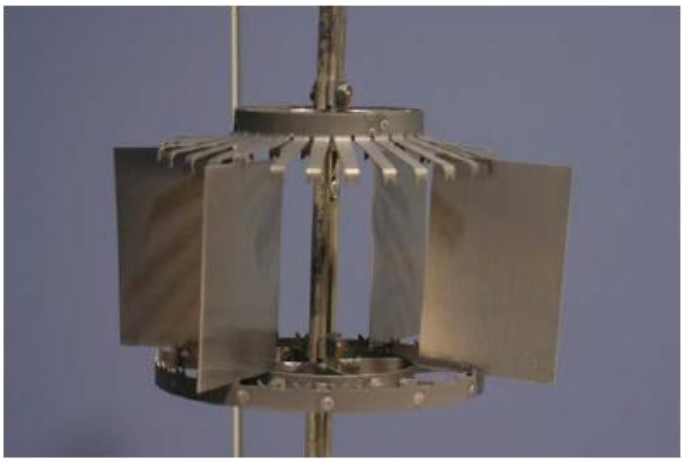

Figure 21. Ti rack holding four 150 x 100 x 2 mm AA2024 specimens.

This material has been utilised because it is relatively inert to the variously treatments in the process. The main advantage is that the Ti rack is electrical conductor in spite of the Ti oxidation during the anodising process. Such phenomenon occurs because the TiO formed on the Ti occupies less volume than the Ti alloy, (Pilling-Bedworth ratio 0.81 [ref]). The racks are designed for a good drainage, minimal gassing effects and air entrapment and good current distribution.

4.3. Processes for specimen preparation

4.3.1. Pretreatment

4.3.1.1. Degrease

The surface conditioning of the samples before anodising is a very important step in the process, as a bad pretreatment may compromise the characteristics of the final anodic film.

The pretreatment comprises several steps. The first one is degreasing with a cotton cloth impregnated with butanone (methylethylketone or MEK). The main purpose of this is the removal of inks, oils and greases from the surface of the alloys. This step is not fundamental but prolongs the service life of the next bath.

The second step is immersion in an alkaline degrease bath. This bath is an aqueous solution of Turco® 4215 NC-LT manufactured by Henkel. The composition of this non-silicated, non-chromated, mildly cleaner is as follows:

Table 7. Chemical composition of the Turco® 4215 NC-LT

Component	Percent
Sodium tetraborate	30-60
Sodium tripolyphospate	30-60
Nonylphenoxypoly (ethylenoxy) ethanol	1-10
Sodium nitrate	1-10
Sodium silico fluoride	1-10
Diethylene glycol butyl ether	1-10

The nominal concentration in the bath is 50 g L^{-1}. Working conditions are 50 ± 10 g L^{-1}. According to the manufacturer, immersion of the work for 10 min at 50 °C with continuous stirring is enough to provide clean surfaces.

The pH of the bath is slightly alkaline (next to 9); the attack to the aluminium in the alloy is very slow. The bath removes inks, oils and greases.

The concentration of the product was controlled periodically by determination of the alkalinity of the bath an acid/base titration with 1 M HCl. New product was added when needed.

After the immersion in the alkaline cleaning bath, the samples were always kept wet until the end of the treatment, the unique exception is between anodisation and primer application.

Water rinse following the alkaline cleaning was undertaken for 5 min in distilled water. After the rinse, the work was then rinsed with showers for 1 min, paying especial attention to the complete removal of foam on the surface of the specimens.

4.3.1.2. Etching

The following step of the pretreatment is the immersion of the batch in an acid etching bath. This bath is an aqueous dilution of Ardrox® 295 GD manufactured by Chemetall, a Cr-free liquid deoxidiser and desmutter for use on aluminium alloys following cleaning or alkaline etching. The composition is a mixture of H_2SO_4, HNO_3, and Fe_2O_3.

Etching time and temperature conditions were adjusted to remove a determined superficial thickness. The attack factor of the bath was calculated by the gravimetric method. Table n indicates the amount of material removed in terms of µm $surface^{-1}$ for the four studied alloys under the selected conditions (10 min at 40 °C with stirring).

Table 8. Mass loss for the aluminium alloys after immersion in the etching bath for 10 min at 40 °C.

Alloy	Mass loss (µm $surface^{-1}$ h^{-1})	Mass loss after 10 min of immersion (µm $surface^{-1}$)
AA2024	5.12	0.85
Clad AA2024	3.71	0.61
AA6061	6.10	0.75
AA7475	4.52	1.02

In order to maintain the etching properties of the bath, a concentration between 20-25% of Ardrox® 295 GD was kept according to manufacturer instructions. Apart from the attack factor, two periodical controls were established, the acidity of the bath and the oxidising power.

The acidity of the bath was controlled by determination of the acidity of the bath an acid/base titration with 1 M NaOH.

The oxidising power of the solution was controlled by redox titration with 0.1 M $Na_2S_2O_3$ and starch solution as indicator.

The objective of the acid etching bath is the removal of intermetallics particles and the mechanically deformed layer produced during the rolling process of the aluminium alloy.

Water rinse was undertaken for 5 min followed by shower rinse for 1 min to ensure the removal of the remaining rests of the etching bath.

4.3.2. Anodising

The pilot plant has two different anodising baths which are following described

4.3.2.1. Tartaric/sulphuric acid anodising bath

The first anodising bath studied in this work is a tartaric acid/sulphuric acid (TSA) solution (fig. 22). The nominal composition of the bath is 0.46 M (40 g L^{-1}) H_2SO_4 and 0.53 M (80 g L^{-1}) $C_4H_6O_6$. The anodising bath was be maintained within 40 ± 10 g L^{-1} of H_2SO_4 and 80 ± 10 g L^{-1} of $C_4H_6O_6$.

Figure 22. TSA bath with two AISI 321 stainless steel cathodes.

This was controlled by acidity of the bath in organic media, and the total acidity. Besides, some parameters are important, such as the Al^{3+} and the Cu^{2+} concentration.

High concentrations of Al^{3+} can affect the bath. Although some efforts were directed towards a quick, inexpensive, precise determination of Al^{3+} in the bath by titration, the only methods for

determining was atomic absorption and ICP-MS. The last technique revealed an Al^{3+} accumulation about 1 g L^{-1} in the TSA bath after 3 years of service life.

Copper is incorporated to the bath by dissolution of the alloys in acid media and outward migration of the Cu^{2+} ions during the anodising process. As a result, copper deposition occurs as a side cathodic reaction. A maintenance operation was periodical withdrawal of the AISI 316 cathodes from the bath and removal of the deposited copper by polishing. Cu was in the ppm range (last control 158 ppm of Cu).

The basic anodising cycle is shown in fig. 23. All the anodised specimens described in this work were anodised following these parameters, unless other conditions are indicated.

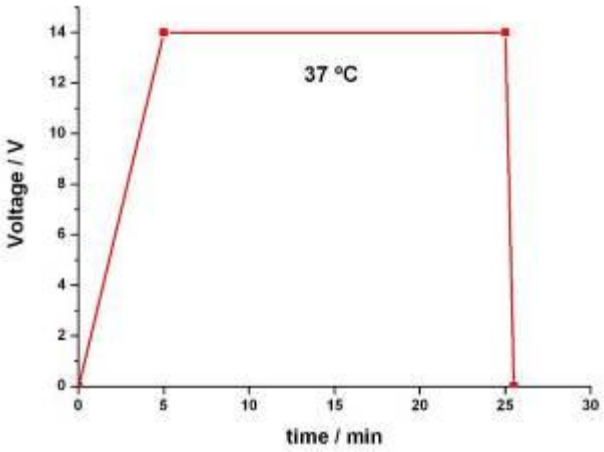

Figure 23. Anodising program

The anodising program consist of a potential ramp from open circuit potential (OCP) to 14 V for 5 min, this ramp is for avoid current peaks, then there is a plateau of 14 V for 20 min and finally, a 30 s descendent ramp from 14 V to OCP'.

The rectifier controls the anodising voltage, it is designed for controlling a maximum current of 30 A, therefore for a 14 V anodising cycle, obtaining current densities between 0.5-1 A dm^{-2} depending on the alloy, the maximum work load is 30 dm^{-2} per anodising cycle.

4.3.2.2. Molybdenum modified Tartaric/sulphuric acid anodising bath

The second bath was developed during this work, such bath consists of a TSA bath with 0.25 M $Na_2MoO_4 \cdot 2H_2O$, named as MoTSA. This bath has been patented by Airbus [79]. Detailed description of the optimisation of the Na_2MoO_4 concentration will be described in chapter 5.4.

The methods of control previously described for the TSA bath were also valid for the determination of H_2SO_4, $C_4H_6O_6$, Al and Cu in the bath. Besides, Mo determination was difficult due to the complex chemistry of Mo in acidic solutions and therefore, Mo concentration was controlled by ICP MS. After one year of, the concentrations of Al and Cu in the MoTSA bath were 54 and 14 ppm, respectively.

4.3.3. Postreatments

The racks with each specimen batch were withdrawn from the anodising bath immediately after the end of the anodising cycle and immersed in a deionised water rinse bath for 5 min followed by shower rinse for 1 min. This operation is crucial as the anodic film can be attacked by the electrolyte in the absence of imposed current.

The anodised samples not followed by painting or any other postreatment were dried in an air furnace at 60 °C for 5 min and stored in a controlled environment. In other case, one of the following postreatments was applied without drying the anodised samples.

4.3.3.1. Chemical conversion coatings

The chemical conversion coatings (CCC) are usually applied on the bare alloys without anodising. However, in this work, chemical conversion coatings were applied by immersion of the anodised samples in the CCC solutions at RT for 1 min to evaluate the possible use as anodising postreatments.

Two different CCC were used. The first one is a commercial Cr (VI)-containing chemical Alodine 1200 (pH=1.8) manufactured by Henkel. Composition is given in table n.

Table 9. Alodine 1200 composition

Component	Percent (wt.)
CrO_3	50-60
KBF_4	20-30
$K_3Fe(CN)_6$	10-15
K_2ZrF_6	5-10
NaF	5-10

The other CCC was a Cr (VI)-free product described in the patent of Navair [51]. According to the manufacturer, such product is based on trivalent chromium salts.

After application of CCC, the specimens were water rinsed for 3 min and dried at 60 °C.

4.3.3.2. Sealing

Sealing postreatment was undertaken in one of the following sealing baths.

The first sealing bath is a 10 L boiling distilled water (min 95°C) beaker. The sealing was performed by immersion in the sealing bath immediately after water rinse of the anodised pieces.

The second sealing bath is a 10 L boiling aqueous 30 mM $K_2Cr_2O_7$ solution. This sealing is undertaken at a minimal temperature of 95 °C for 20 min.

After the sealing postreatment, the specimen were rinsed in distilled water for 3 min and dried at 60 °C.

4.3.3.3. Primers

Different organic primers were applied on the treated aluminium alloys. In general, such organic primers were applied by conventional air spray gun, passing as many crossed hands as needed for obtaining the desired coating thickness.

A primer Cr (VI)-loaded epoxy organic solvent currently in use by Airbus was utilised on anodised specimens to test the compatibility of this postreatment with the anodic films generated in the TSA bath.

Besides, some new water based primers were tested on variously treated AA2024 specimens. Such water based primers were of two kinds, a Cr (VI)-loaded water based primer and a Cr (VI)-free water based primer with inhibitors.

All the primed specimens were dried in an oven at 60 °C for 2 h. Some of these samples were subsequently coated with a polyurethane topcoat impermeable to fluids that provides mechanical strength. When this topcoat was applied, a second dry process (60 °C for 2 h) was necessary.

In all cases the minimal curing time after the application of the last coating layer was 7 days prior to any test.

4.4. Characterisation techniques

4.4.1. Morphology

4.4.1.1. Eddy currents

Objective

The eddy current test is a non destructive test for measuring the total anodic film thickness and the coating system thickness in the case of primed specimens.

Methodology

Anodic layer film thicknesses were determined employing a Fischerscope MMR with an ETA 3.3 sensor specific for non ferric materials. Prior to measuring, the equipment was calibrated on several locations of a bare piece of the corresponding aluminium alloy. The measures were taken at a minimum of 10 locations on the surface of the anodised or primed specimens.

4.4.1.2. Scanning electron microscopy

Objective

Scanning electron microscopy is used for determining the morphology of the surface of the aluminium alloys.

Fundamentals

Electrons from a thermionic or field emission cathode are accelerated through a voltage difference between cathode and anode that may be between 0.1 keV and 50 keV.

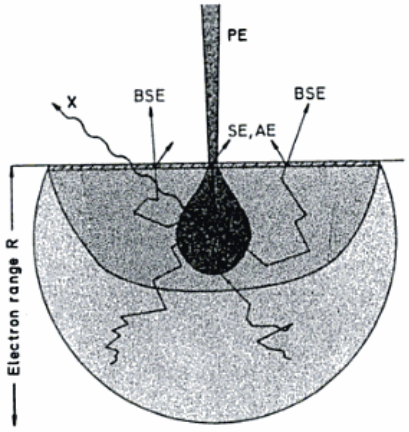

Figure 24. Origin and information depth of secondary electrons (SE), backscattered electrons (BSE), Auger electrons (AE) and X-ray quanta (X) in the diffusion cloud of electron range R for normal incidence of the primary electrons (PE).

In the scanning mode the electron beam is focused on a small spot of the sample (roughly 10 nm). Detected are either the electrons or the X-rays or gamma rays, which escape from the sample (either forward or backward emission). Imaging is obtained by scanning the electron beam line by line over the sample surface and detecting the number of emitted secondary electrons or the beam intensity. As the detection probability of secondary electrons is high, a weak primary electron beam can be used, which prevents destruction of the sample. As the secondary electron yield depends on the sample material, different phases (e.g. of alloys) or crystallographic orientations can be distinguished. The probability of the emission of secondary electrons on edges is higher than the emission from planes thus causing a stereoscopic effect of the images [ref].

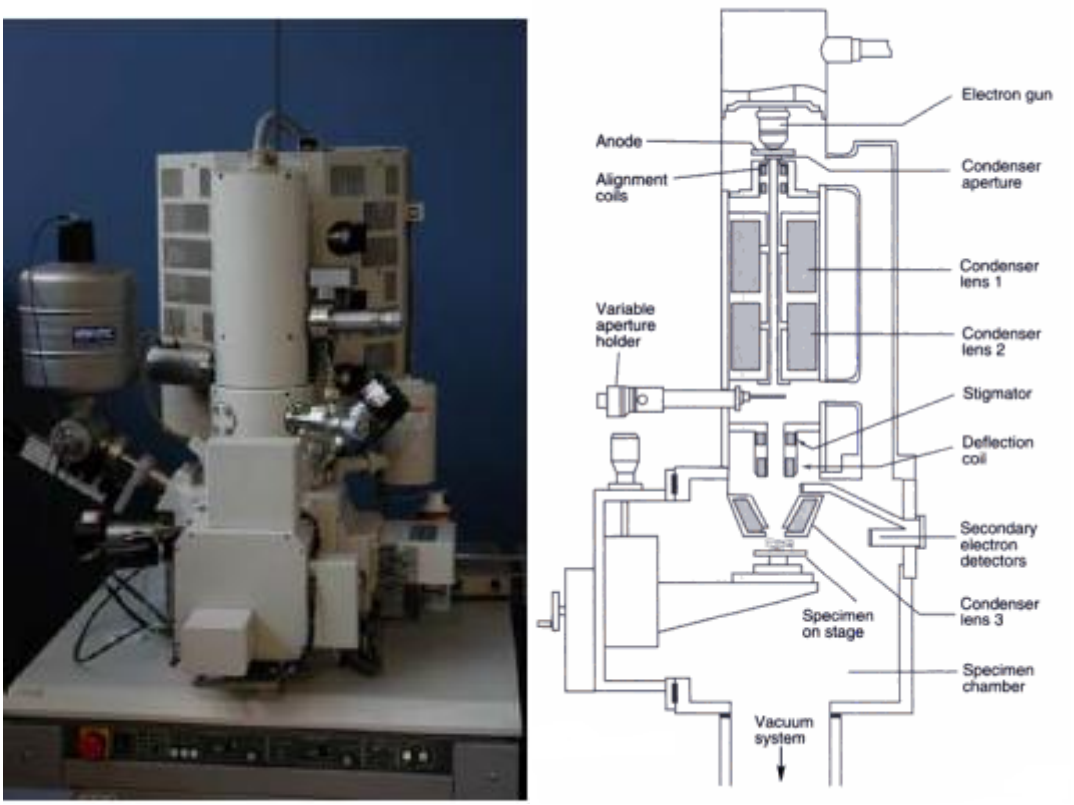

Figure 25. (a) column of a standard SEM and (b) Detailed diagram of the column of standard SEM showing major components [81].

Methodology

The specimens were cut to dimension less than 3 cm x 3 cm, not electrical conductor specimens were coated with a Physical vapour deposition of Cr. In order to obtain a thin Cr film that does not modify the surface of the specimen, the sputtering of the coating was undertaken at 125 mA for 10 s.

The specimens were introduced in the chamber of a Hitachi S470 FEG-SEM (fig. na) operated at 5-10 kV with a working distance of 4 mm and observation between 500x and 50000x magnification.

4.4.1.3. Transmission electron microscopy

Objective

The transmission electron microscopy (TEM) technique shows the morphology of the cross section of the treated alloys.

Fundamentals

In the transmission mode an electron beam of 100 - 400 kV passes through the sample. The transmitted electrons form a two dimensional projection of the sample which is further magnified by an electromagnetic lens system. The resulting image is a so-called bright-field image. In addition diffraction of the electron beam while passing through the sample is observed. By analysis of these electrons a diffraction image, a so-called dark field image, is

obtained which is used for collecting crystallographic information. Electron transmission is dependent on the density and thickness of the material. As the penetration depth of electrons is usually low, thin sample layers have to be prepared [80].

Methodology

The specimen preparation consists of cutting very thin slices (15-50 nm) of the cross section of the anodic film by ultramicrotomy [82] Initial cutting was made with a glass knife and final cut with a diamond knife.

The equipment is a JEOL 2000 FX II instrument of the corrosion and protection centre of the University of Manchester, and was operated at 120 kV.

4.4.2. Chemical composition

4.4.2.1. Glow discharge optical emission spectroscopy

Objective

The applications of GD-OES spectroscopy are mainly bulk analysis of solid metals and alloys (DC) and the analysis of non conductive materials such as polymers, ceramics and glasses (RF)) Because the GD sputtering process removes uniform layers of materials from the sample surface, it can be used to examine coatings and multilayered materials [83].

Fundamentals

The glow discharge (GD) is a reduced pressure gas discharge generated between two electrodes in a tube filled with an inert gas such as argon. The sputtered atom cloud in a glow discharge source consists of excited atoms, neutral atoms and ions. In the 1990s, a new GD source based on radio-frequency (RF) excitation was developed. This RF GD source permits the sputtering and excitation of non conductive materials. The sample is subjected to an RF frequency of 13.56 MHz (fig. 26).

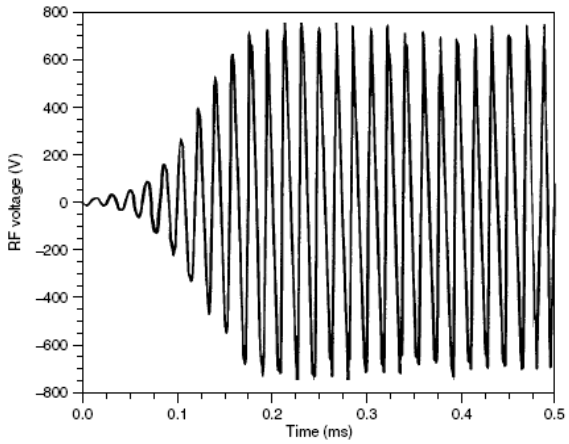

Figure 26. Transient signals recorded on an oscilloscope for the application of an rf potential to the back of a 2 nm thick ceramic specimen which illustrates the establishment of a dc-bias potential at the surface of the sample.

The sample acts as a capacitor with respect to the alternating RF voltage. This results an alternating charge on the sample surface through each cycle. When the sample surface is negatively charged, the positive Ar^+ ions are accelerated to the negative surface and the sample material is sputtered into the glow discharge. The charge alternates very rapidly, so the sputtering process is very efficient, Excitation and emission occur as described for the DC source.

Methodology

The elemental depth profiles were recorded with a Jobin Yvon 5000 RF instrument. Such instrument belongs to the corrosion and protection centre, in the University of Manchester.

4.4.2.2. Rutherford backscattering spectroscopy

Objective

Rutherford backscattering spectroscopy (RBS) provides quantitative depth composition profiles of anodic films of appropriate thickness, with a depth resolution of 20-30 nm.

Fundamentals

A beam of monoenergetic particles in the MeV energy range, generally being $^4He^+$ or $^1H^+$ ions issuing from an accelerator, impinges on the sample. In the solid, the projectiles will be progressively stopped, but a small fraction will also undergo close collisions with nuclei of single atoms, producing large changes in energy and direction. Still fewer incident projectiles ($<10^{-4}$) are scattered backwards and escape from the target. By measuring the energy of these particles at a well defined angle, it is possible to obtain information on the nature and concentration of the target atoms as well as on their depth distribution [84].

The major effects arising in RBS can be explained on the basis of four physical principles.

- Two body collision between an incident particle (projectile) and an atom of the solid sample (target), leading to the possibility of mass separation through a kinematic factor.
- The probability of such collisions is described in terms of the scattering cross section and allows quantitative analysis of the target composition.
- The energy loss of the projectiles in the target is given by the stopping cross section, allowing analysis of the target as a function of depth.
- The statistical dispersion in energy loss or energy straggling constitutes a limitation on the mass and depth resolution.

Methodology

Rutherford backscattering spectrometry (RBS) spectra were acquired using the 5 MeV tandem accelerator at CMAM, with an ion beam of 2.0 MeV $^4He^+$ ions. The backscattered ions were detected at 170° and quantification of the spectra was undertaken using the SINMRA software code [85].

4.4.2.3. X-ray photoelectron spectroscopy

Objective

The objective of the X-ray photoelectron spectroscopy (XPS) is the analysis of the surface of the specimens. This technique detects the oxidation state of the surface elements.

Fundamentals

A magnesium or aluminium target is bombarded by an electron beam of several kiloelectron volts of kinetic energy. Such metals emit X-ray radiation of a given energy. These X-rays penetrate down in the solid specimen. On the way, the X-rays cause electrons to be emitted from the atoms or molecules that they meet. The electrons belonging to the atoms close to the surface escape into the vacuum of the equipment. The detector finds out the energies of the electrons being emitted. Since these energies are characteristics of the atoms from which they are emitted, it is possible to identify the elements of the surface region of the material examined.

Methodology

The XPS analysis was undertaken in the ICP facilities with a VG Escalab 200 R. The XPS spectra were analysed with XPS peak 4.1. software.

4.4.3. Electrochemical methods

4.4.3.1. Linear polarisation

Objective

This technique allows to obtain corrosion parameters such as the corrosion potential (E_{corr}), which gives information about the thermodynamics of the corrosion processes, and the corrosion current density (i_{corr}) that informs about the kinetics of the corrosion processes.

Fundamentals

Linear polarisation consists of the imposition of a potential slope on the working electrode, obtaining a current density response [86]. The relation between the signal and the response is given by the Butler-Volmer equation.

$$i = i_0 \left[e^{\frac{-\alpha n F \eta}{RT}} - e^{\frac{(1-\alpha) n F \eta}{RT}} \right]$$

Where io is the exchange current density, α is the electron transference coefficient, n is the number of electrons involved in the reaction, F is the Faraday constant and η is the overpotential.

The Butler-Volmer equation is usually plotted as E_{corr} vs. logarithm i (fig. 27)

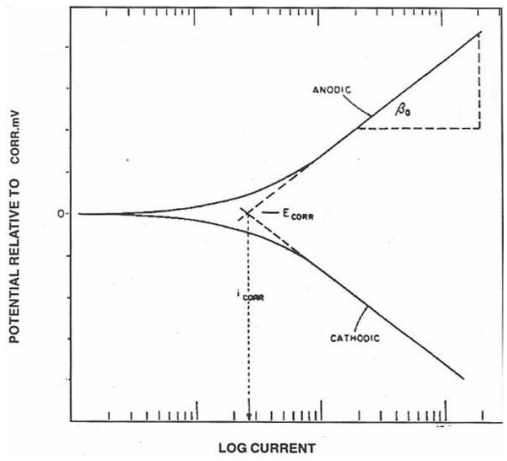

Figure 27. i-E curve

Such plots are commonly known as i-E curves.

Methodology

The electrochemical measurements were made with a Gamry PCI4-750 potentiostat-frequency analyser, using a three-electrode cell containing naturally aerated 0.5 M NaCl solution at room temperature. The alloy specimen (3.8 cm2) was the working electrode of the cell, with a saturated calomel electrode (SCE) reference electrode and a graphite rod counter-electrode.

Polarisation measurements were carried out after monitoring the open circuit potential (OCP) for approximately 1 h until steady values were achieved; potentiodynamic polarisation used a scan rate of 0.17 mV s^{-1}, starting from -200 mV below the OCP and finishing once the pitting potential was reached.

4.4.3.2. Cyclic voltammetry

Objective

Cyclic voltammetry allows to obtain valuable information about the redox reactions taking place on the working electrode and the reversibility or irreversibility of such reactions.

Fundamentals

Cyclic voltammetry describes the imposition of a triangular potential time waveform on the working electrode. The working electrode potential is varied periodically between the lower turning potential E_{t1} and the upper turning potential E_{t2} with a constant scan rate v = dE/dt as shown in fig. 28..

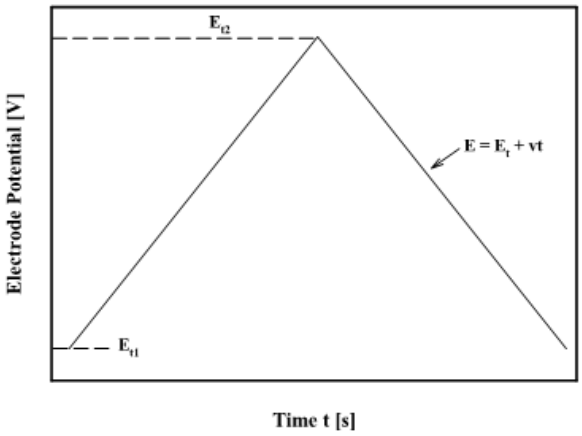

Figure 28. Potential-time behaviour of the working electrode typical for the cyclic voltammetry.

The thus obtained current-potential values are recorded and displayed as cyclic voltammogram. By definition anodic currents are plotted in positive and cathodic currents in negative direction

Methodology

The electrochemical measurements were made with an Autolab instrument in a classical three electrode cell with gold working and auxiliary electrodes, and SCE reference electrode. The solutions were deaerated passing nitrogen for 15 min prior to each measurement.

4.4.3.3. Electrochemical impedance spectroscopy

Objective

The electrochemical impedance spectroscopy (EIS) gives reliable information about the structure of the anodic films, the electrical properties and the reactions taking place on the surface of the samples during the experiment.

Fundamentals

The impedance is the resistance of a circuit to the alternating current (AC) [87-89]. The Electrochemical impedance is usually measured by applying an AC potential to an electrochemical cell and measuring the current response of the cell. Assuming the applied signal is a sinusoidal potential excitation, the response to this potential is an AC current signal. This current signal can be analysed thus as a sum of sinusoidal functions (a Fourier series).

Electrochemical Impedance is normally measured using a small excitation signal. This is done so that the cell's response is pseudo-linear. In a linear (or pseudolinear) system, the current response to a sinusoidal potential will be a sinusoid at the same frequency but shifted in phase (fig. 29).

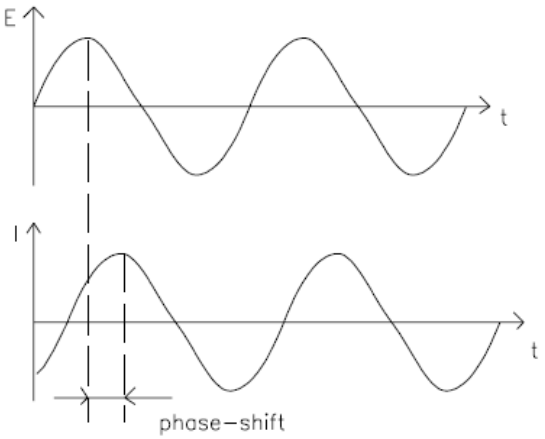

Figure 29. Sinusoidal potential excitation signal and sinusoidal current response in a linear system.

The excitation signal, expressed as a function of time, has the form

$$E_t = E_0 \sin(\omega t)$$

E_t is the potential at time t, E_0 is the amplitude of the signal, and ω is the radial frequency. The relationship between radial frequency ω (expressed in radians/second) and frequency f (expressed in hertz) is:

$$\omega = 2\pi f$$

The response signal, I_t, is shifted in phase and has different amplitude I_o

$$I_t = I_o \sin(\omega t + \phi)$$

An expression analogous to Ohm's law (R = E / I), where R is resistance, allows to calculate the impedance of the system.

$$Z = E_t / I_t = E_o \sin(\omega t) / I_o \sin(\omega t + \phi) = Z_o \sin(\omega t) / \sin(\omega t + \phi)$$

The impedance is therefore expressed in terms of a magnitude Z_o and a phase shift, ϕ.

The plot of the applied sinusoidal signal E(t) on the X-axis of a graph and the sinusoidal response signal I(t) on the Y-axis, the result is an oval known as a Lissajous figure (fig. 30).

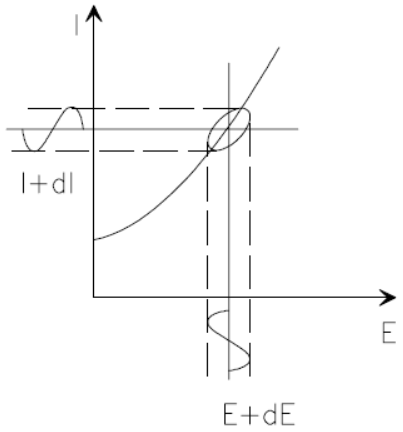

Figure 30. Lissajous figure

With Euler's relationship

$$\exp(j\phi) = \cos(\phi) + j\sin(\phi)$$

It is possible to express the impedance as a complex function. The potential is described as

$$E_t = E_0 \exp(j\omega t)$$

And the current response as

$$I_t = I_o \exp(j\omega t - \phi)$$

The impedance is then represented as a complex number,

$$Z(\omega) = E/I = Z_0 \exp(j\phi) = Z_0(\cos\phi + j\sin\phi)$$

There exist several ways of plotting the impedance; if the real part is plotted on the X-axis and the imaginary part is plotted in the Y-axis of a chart, the graph obtained is called a Nyquist plot (fig. 31).

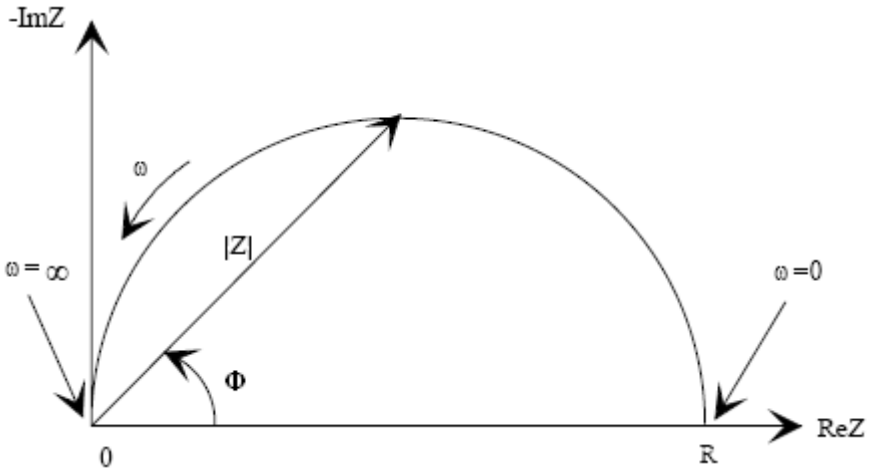

Figure 31. Nyquist plot.

On the Nyquist plot, the impedance at one frequency can be represented as a vector of length $|Z|$. The angle between this vector and the X-axis represents the phase angle (ϕ).

Another representation is the Bode plot (fig. 32). In this case, the logarithm of absolute values of the impedance and the phase angle in are plotted the Y-axis and the log frequency on the X-axis.

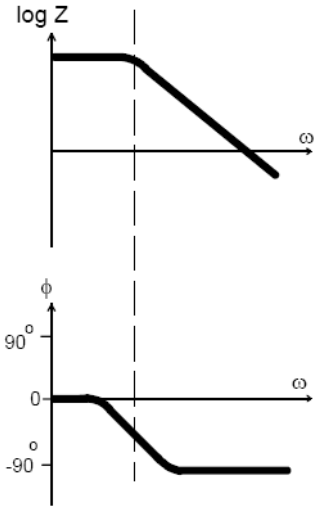

Figure 32. Bode plot.

Often, EIS data is analysed by fitting it to an equivalent electrical circuit model that includes common electrical elements such as resistors or capacitors. For example the Nyquist plot in fig. 31 and the Bode plot in fig. 32 are equivalent to a composed of a resistor and a capacitor in parallel (fig.33).

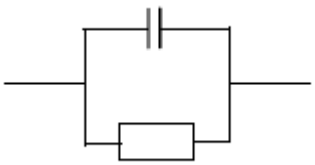

Figure 33. Simple equivalent circuit with one time constant

To be useful, the model should have a basis in the physical electrochemistry of the system. The different elements in the equivalent circuit result in characteristic responses. The impedance of a resistor is independent of frequency and has no imaginary component ($Z = R$), whereas the impedance of a capacitor decreases as frequency is raised. Capacitors only have an imaginary impedance component ($Z = 1/j\omega C$). The elements of different circuits can be combined in series and parallel (fig. 34).

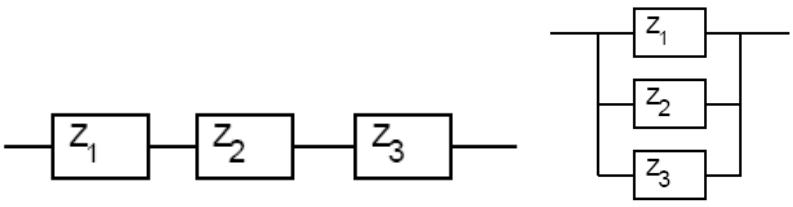

Figure 34. Combination of serial and parallel elements.

The equivalent impedance (Z_{eq}) of the series elements is

$$Z_{eq} = Z_1 + Z_2 + Z_3$$

The equivalent impedance of the parallel elements is

$$1/Z_{eq} = 1/Z_1 + 1/Z_2 + 1/Z_3$$

The equivalent circuits utilised in this research work will be described following in the methodology of the technique.

Methodology

The electrochemical cell is the same described in the methodology of the lineal polarisation, the EIS measurements were undertaken over the frequency range from 10^5 to 10^{-1} or 10^{-2} Hz, with 10 points per decade, using a 3 mV root mean square (8.5 mV) sinusoidal potential perturbation.

The small sinusoidal potential perturbation of 3 rms, was selected to maintain the linearity of the system. Electrochemical cells are not linear, however, if a small portion of the i-V curve is observed, it appears to be linear (fig. 35).

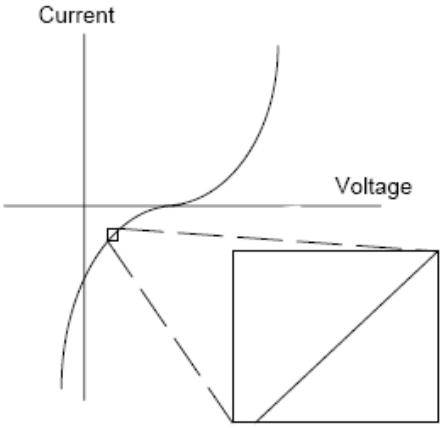

Figure 35. i-V curve showing pseudo-linearity.

The selected frequency range starts at 10^5 Hz. The measures take about 10-15 min measuring 10 points per decade until 10^{-1} Hz; whereas measures up to 10^{-2} Hz measures takes longer, about 30-45 min. During the experiment, it is assumed that the system is at a steady state through the time required to measure the EIS spectrum. However, a steady state is difficult to achieve in practise as the cell can change. So that, most of the EIS measures, and especially of those specimens that demonstrate rapid changes were undertaken up to 10^{-1} Hz.

Equivalent circuits

The following discussion will consider different equivalent circuits (EC) that match with the different morphological features and electrochemical processes occurring on the surface of the different treated samples during the immersion of such samples in 0.5 M NaCl or 0.5 M Na_2SO_4 solutions.

A general component of all these EC is the resistance of the electrolyte, named as R_{sol} or R_Ω. The contribution of the resistance to the overall impedance is small, and generally appears at frequencies above 10^4 Hz. According to the experimental results in this work, R_{sol} of both utilised electrolytes is about 25 Ω cm^2, therefore, it can be considered as a constant parameter.

Equivalent circuits for anodised specimens

The equivalent circuits proposed for fitting EIS spectra of the porous anodic film generated on aluminium, without further postreatments have been discussed by several authors.

Hoar and Wood [90] proposed some equivalent circuits (EC) based on their experimental results for sealing of porous anodic oxide films on Al (Fig. 36).

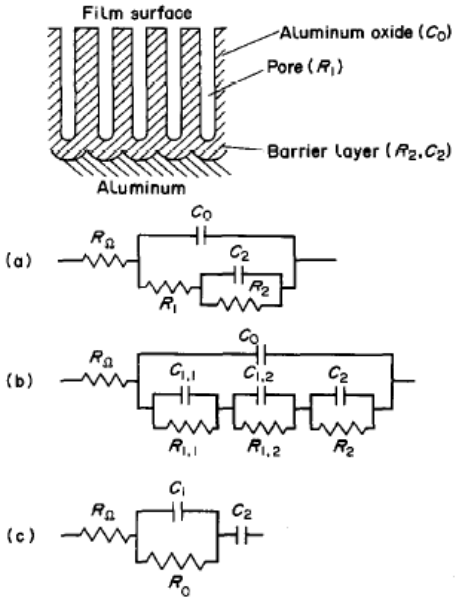

Figure 36. Model and equivalent circuits for anodised aluminium alloys.

The EC in Fig. 36a applies for the unsealed oxide. C_o is the capacitance of the solid alumina in the film, R_1, is the resistance of the sealing solution in the pores of the film, R_2 is the resistance of the barrier layer between the bottom of the pores and the metal, and C_2 is the capacitance of this layer.

The EC in Fig. 36b is derived for the partially sealed oxide. It is important to note that Hoar and Wood assumed in the analysis of their experimental impedance data that C_o, C_2, and R_2 remained constant during sealing. The changes of the spectra with sealing time are due to pronounced decreases of $C_{1,1}$ and $C_{1,2}$ and increases of $R_{1,1}$ and $R_{1,2}$.

The EC in Fig. 36c was used by Koda et al. [91] who investigated the changes of the impedance during sealing in hot water for Al which was anodized in 2% oxalic acid. In this case C_1 and R_1 correspond to the hydrous oxide formed in the pores of the oxide. Hitzig et al. [92] have used the model in Fig. 36c to interpret their results for pure Al which was anodised in sulphuric acid and sealed in hot water. In this case R_0 and C_1 were taken as representative values for the properties of the outer porous oxide layer.

In a latter paper, Hitzig et. al [93] described the aluminium oxide layer consisting of a very thin nonporous barrier layer and a thick porous, partially hydrated layer on top (fig. 37a).

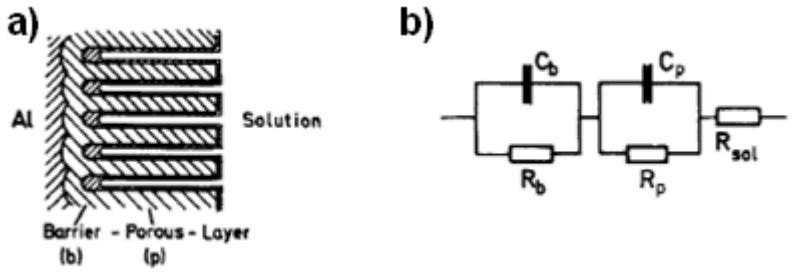

Figure 37. Model and equivalent circuit for anodised aluminium alloys

Considering both oxide layers as separate quasi-homogeneous oxide phases, the physical properties of each layer can be characterized by mean values of a capacitance, C, and a resistance, R, in parallel describing their dielectric and electronic behaviour. In the circuit in fig. 37b, C_b, C_p, denote the capacitance and R_b, R_p, the resistances of the barrier (b) and porous (p) layer, respectively.

Besides, they take into account the inhomogeneities of the freshly anodised aluminium surface or localised corrosion and aging effects for long-time exposure of the anodic films to natural environmental conditions. When surface inhomogeneities are produced by localised corrosion, two cases may be distinguished: the first case is the formation of passive pits with still existing barrier layer in a non aggressive medium (fig. 38a)

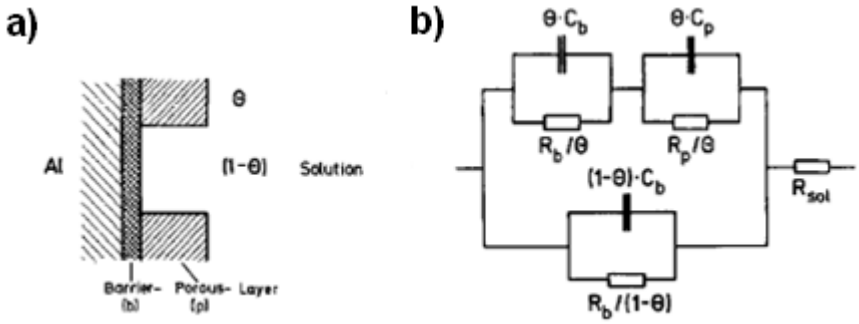

Figure 38. Model and equivalent circuit for inhomogeneous oxide film with passive pits on aluminium alloys.

The modification of the model consists of the introduction of a surface parameter (Θ) representing the fraction of the surface covered with the perfect oxide layer (fig. 38b). When Θ = 1 the model corresponds to a perfect oxide layer, simplifying the circuit to that observed in fig. 37. When Θ = 0, the surface is covered by a homogeneous barrier layer.

The second case is the formation of active pits with active aluminium corrosion in the presence of an aggressive medium (fig. 39a).

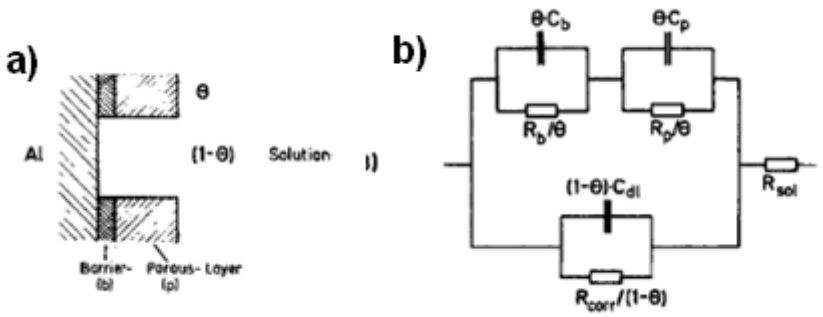

Figure 39. Model and equivalent circuit for inhomogeneous oxide film with active pits on aluminium alloys.

The model described for this second case (Fig. 39b) is similar to the previous but as the corrosion is reaching the aluminium, the double layer capacitance and the corrosion resistance must be taken into account.

These two models are good approaches; however some considerations may be taken into account when fitting EIS spectra. In a corrosive environment (i.e. 0.5 M NaCl solution) the localised corrosion, namely pitting corrosion, can either partially attack the barrier layer (passive pitting) or extend the attack to the base metal (active pitting). So that, the surface parameter (Θ) will be the sum of three different surfaces: the pristine oxide film, the passive pits and the active pits. Therefore, it is very difficult to determine Θ experimentally.

In the solid electrolytes, contamination, surface roughness or inhomogeneities can interfere in the electrochemical behaviour of such electrolytes. In those cases, the capacitance of the circuits is substituted by the so called constant phase elements (CPE). The CPE is generally believed to originate from a distribution in the current density along the electrode surface as a result of surface inhomogeneity [94].

The general expression for the CPE is [95]

$$CPE=1/C(j\omega)^{n}$$

Where n is the frequency dispersion factor and varies from 0 to 1.When n = 1 the CPE can be considered as a capacitance, whereas n = 0 represents a resistance.

In the case of the anodised samples described in this thesis, the selected equivalent circuit for fitting unsealed anodised samples is a simplification of the EC previously described. The EIS spectra show only one time constant; such time constant is attributed to the capacitance (C_b) and the resistance (R_b) of the barrier layer. Evidently, other physical elements (pore capacitances and resistances associated with the pores and the pore walls, flawed areas) and processes (passive and active pitting, general corrosion, absorption of specimens...) are present in this electrochemical system. However, the contribution of such elements to the overall impedance is small. The capacitance is substituted by a CPE to obtain better fitting results. The EC is shown in fig. 40a, jointly with an example of the fitting of an anodised specimen.

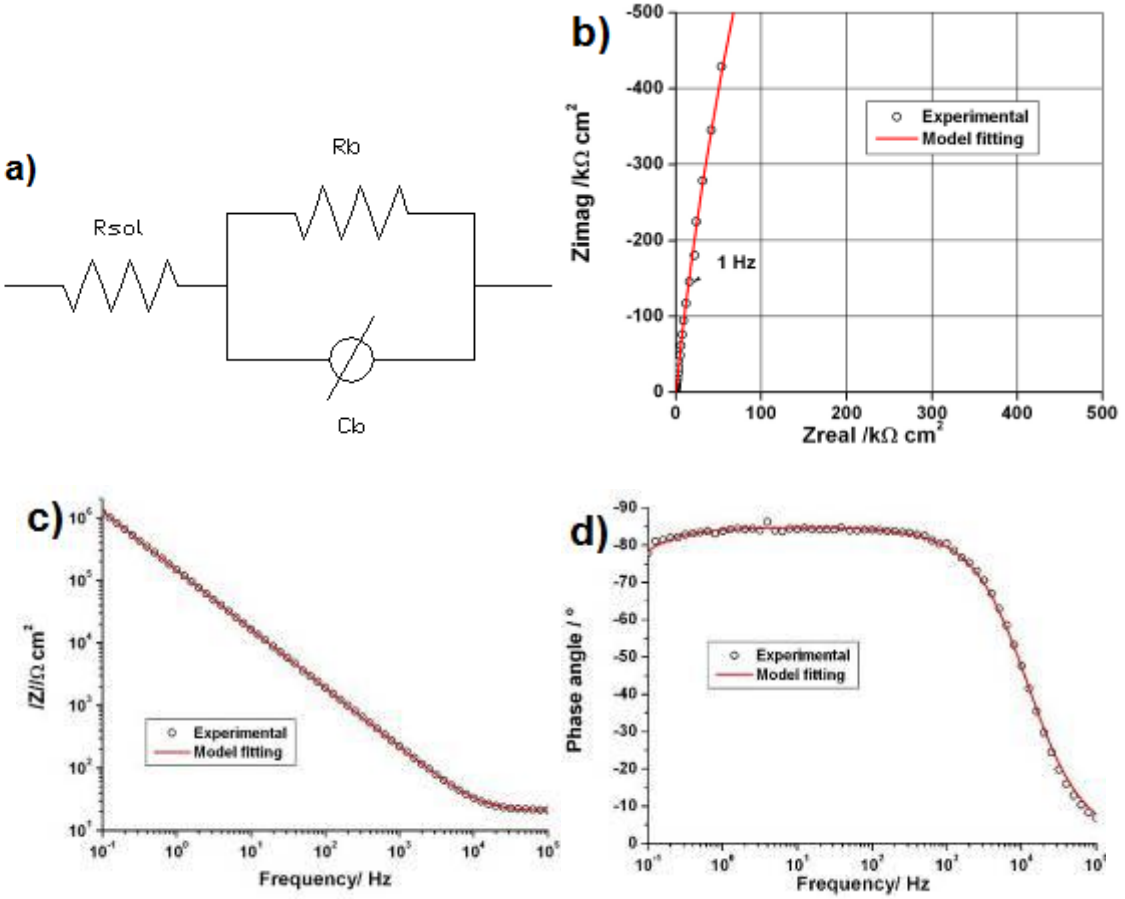

Figure 40. (a) Equivalent circuit proposed for fitting anodised samples. Experimental and EIS spectra after 1 h of immersion in a 0.5 M NaCl solution of a AA2024 TSA anodised sample (37 °C, 5min + 20min) and fitting with the proposed EC: (b) Nyquist plot, (c,d) Bode plots.

This model gives satisfactory fitting for most of the anodised films described in this thesis. However, sometimes the proposed EC is not enough for giving a satisfactory fitting matched with a physical meaning. Eventually, during the degradation of the anodic films, evidences of two different time constants appear. The proposed model is in fig. 41a.

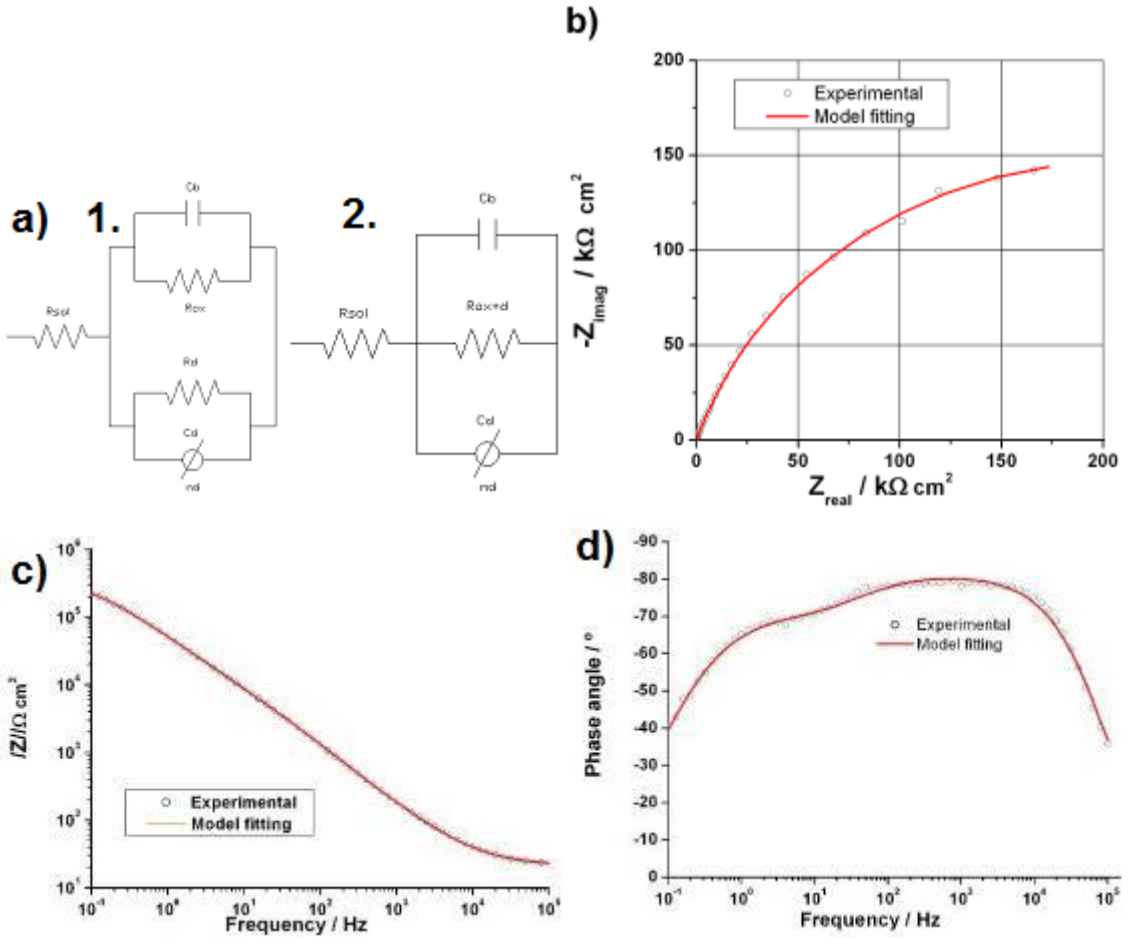

Figure 41. (a) Equivalent circuit proposed for fitting anodised samples partially degraded. Experimental and EIS spectra after 168 h of immersion in a 0.5 M NaCl solution of a AA2024 MoTSA anodised sample and coated with a water based Cr-loaded primer and fitting with the proposed EC: (b) Nyquist plot, (c,d) Bode plots.

This EC was chosen to simulate the conditions expected on the alloy surface, with regions covered by porous anodic oxide and exposed regions were localized corrosion proceeds. In the EC in fig. na1, the capacitance and resistance of the barrier at the base of the porous anodic film are represented by C_b and R_{ox}, respectively, while the resistance and capacitance associated with the areas where the alloy is directly exposed to the electrolyte are expressed by R_d and C_d, respectively. This model does not allow separation of the individual contributions of R_{ox} and R_d, because the two resistors are in parallel and, for this reason, the parameter R_{ox+d} is used for the fitting of the EIS data (circuit 2). R_{ox+d} is the inverse of the sum of the inverses of R_{ox} and R_d.

$$1/R_{ox+d} = 1/R_{ox} + 1/R_d.$$

Conversely, the individual contributions to the impedance behaviour of the capacitances C_b and C_d can be separated if it is assumed that the intact area of the barrier layer behaves as a capacitor, while the damaged area displays behaviour represented by a constant phase element.

Separation of the components is possible by fitting the data using the following procedure:

i) The model of Fig. 42 is used to fit the data from frequencies of 100 Hz upward for all the specimens (neglecting R_{ox} which is very high compared with R_d).

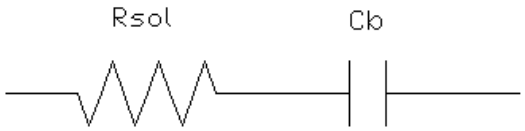

Figure 42. EC proposed for fitting in the high frequency range

ii) the value of C_b is used as a fixed parameter in the model circuit of Fig. 41, performing the final fit over all the frequency range available.

The barrier layer thickness (d) can be estimated from the following equation, considering that the barrier layer can be simulated as a coplanar capacitor of thickness *d*:

$$C_b = \varepsilon_0 \times \varepsilon_r \times A / d$$

where C_b is the capacitance of barrier layer, determined by the fitting of EIS spectra, ε_0 is the vacuum dielectric constant ($\varepsilon_0 = 8.854\times10^{-14}$ Fcm^{-1}), ε_r is the permittivity of the alumina and *A* is the geometrical area.

The permittivity value for pure alumina is considered to be 10 [ref], however, some authors consider that incorporation of sulphur from the anodising bath to the alumina structure influence such value, and calculate values of 17[96] or 20 [97]. In this work, ε_r value will be taken as 10.

Equivalent circuits for anodised and sealed specimens.

The fig. 43 shows the schematic structure of a sealed anodic film with the selected EC superposed.

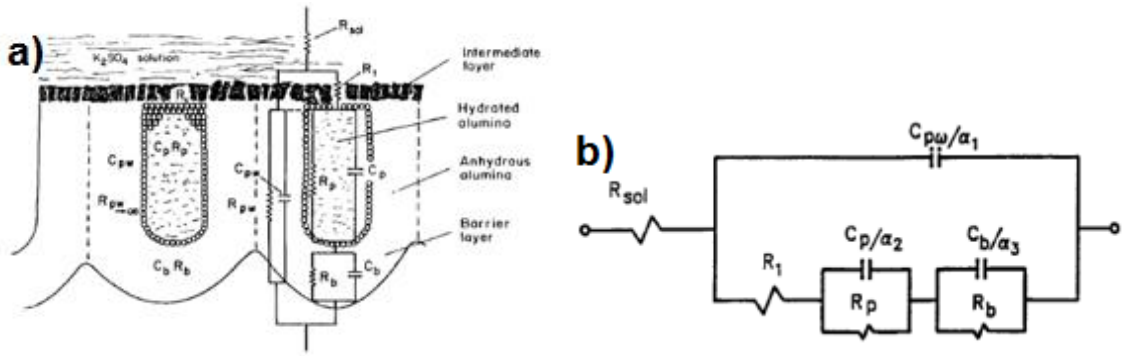

Figure 43. (a) Scheme of an anodised and sealed anodic film and (b) EC for sealed anodic films [97].

As observed in the fig. 43a, there exist multiple interfaces in the complex anodic film structure: the pore wall, the porous oxide film and the barrier layer film. C_{pw} and R_{pw} are the capacitance and the resistance of the pore wall, respectively. Assuming R_{pw} is very high, this can be eliminated from the EC (fig. 43b). R_1 is the resistance of the electrolyte penetrating through the pores. The electrochemical parameters of the pore filling are C_p and R_p whereas those for the barrier layer are C_b and R_b.

According to the experimental data obtained for the sealed samples in this thesis, only two time constants are evident for the sealed specimens. Therefore, a simplification of the previous EC was used (fig. 44a). The time constant appearing in the low frequency range in the Bode plot (fig. 44c,d) is matched with the electrochemical behaviour of the barrier layer and the one appearing in the high frequency range is attributed to the electrochemical properties of the porous layer.

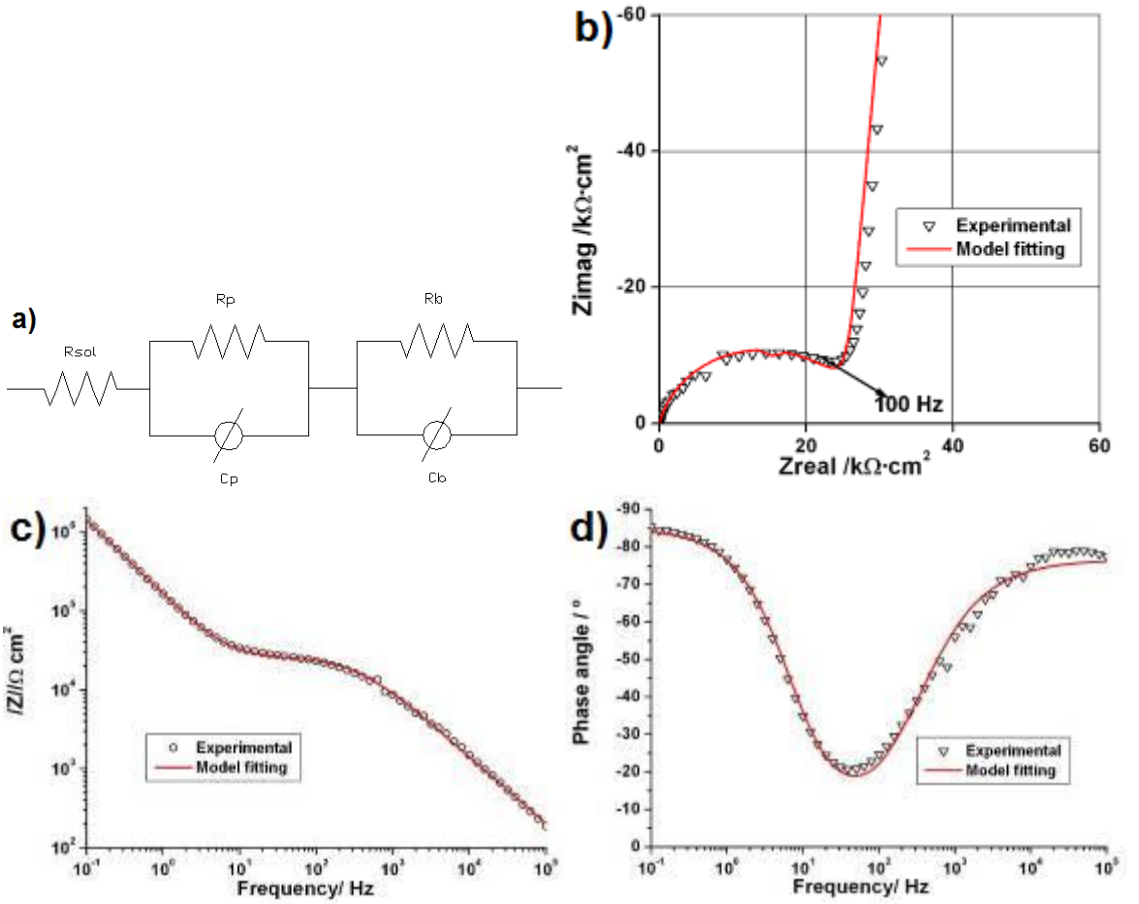

Figure 44. (a) Equivalent circuit proposed for fitting anodised and sealed samples. Experimental and EIS spectra after 1 h of immersion in a 0.5 M NaCl solution of a AA2024 TSA anodised sample (37 °C, 5min + 20min) and subsequently sealed in HWS bath for 40 minand fitting with the proposed EC: (b) Nyquist plot, (c,d) Bode plots.

In the proposed EC, C_b and R_b correspond to the capacitance and the resistance of the barrier layer, respectively; whereas C_p is the capacitance associated to the porous layer and R_p is the resistance of the electrolyte to penetrate through the pores of the anodic film.

Equivalent circuit for organic coatings on metal substrates

The model selected for organic coatings is generally accepted for flawed organic coatings, this model considers the coating as a porous film with its respective capacitance (C_c) and the resistance of the electrolyte to penetrate through the pores (R_p). Besides, it considers the underlying interface between the aluminium substrate and the electrolyte reaching the surface of the aluminium as a RC parallel circuit (fig. 45).

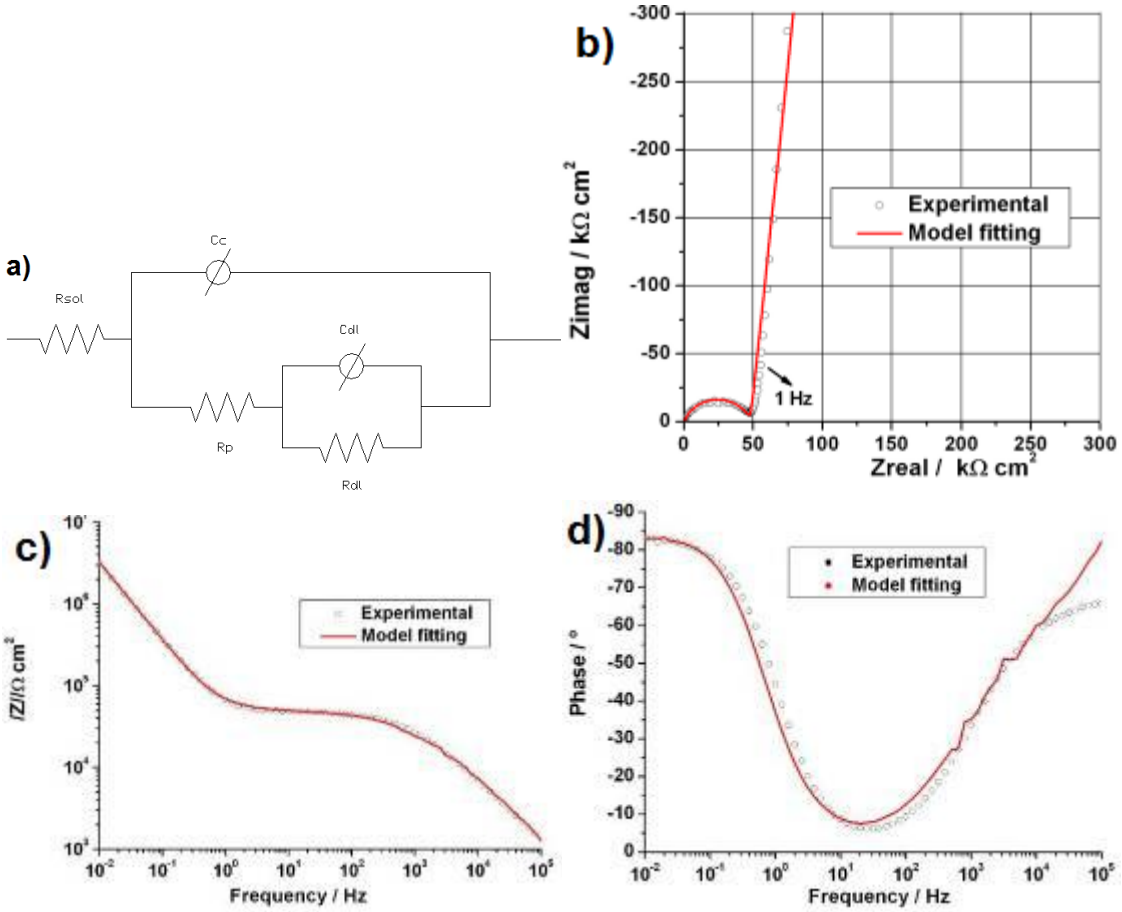

Figure 45. (a) Equivalent circuit proposed for fitting organic coatings on metal substrates. Experimental and EIS spectra after 720 h of immersion in a 0.5 M NaCl solution of a AA2024 TSA pickled sample and coated with a water based Cr-loaded primer and fitting with the proposed EC: (b) Nyquist plot, (c,d) Bode plots.

This circuit has been broadly utilised in the evaluation of the corrosion behaviour of polymer coated metals. Kendig and Mansfield [98-101] suggested that the observed decrease of R_p with exposure time is due to damage to the coating and the formation of conductive paths. Haruyama et al. [101] have proposed that the decrease of R_p is due to an increase of the delaminated area under the coating. Some authors have assumed a constant value of C_{dl} and have calculated the corroding area based on the observed increases of the value of C_{dl}.[102].

In order to make the discussion of the results easier to follow, the EC proposed for fitting the specimens described in this thesis will be named as follow:

Table 10. Models and nomenclature of the EC used in the thesis

Model	Nomenclature
Anodised samples	EC1
Anodised samples partially degraded	EC2
Sealed samples	EC3
Organic coated samples	EC4

4.4.4. Neutral salt spray test

Objective

The objective of the salt spray test is assessing the corrosion resistance to pitting of the exposed specimens.

Methodology

The neutral salt spray test was performed according to ISO 9227. At least three specimens of 150 x 100 x 2mm of each condition were tested.

4.4.5. Paint adherence test

Objective

The objective of this test is assessing the resistance of paint coatings to separation from substrates.

Methodology

The paint adherence was tested by the cross-cut test according to ISO 2409.

5. Results and discussion

5. Results and discussion

5.1. TSA. Determination of a robust range of conditions

The anodic films obtained in the TSA bath will be described in this chapter beginning with some previous technical considerations such as the layout of the electrodes and the bath stirring effects.

Secondly, a thorough study of the changes in the morphology of the surface during the process at different parameters values was observed by means of SEM for all the aerospace alloys. Besides, the anodic films generated in the TSA bath were morphologically characterized by means of TEM and their qualitative chemical composition was studied with GDOES.

Thirdly, from a point of view of corrosion resistance, the different bare alloys were electrochemically characterised using potentiodynamic polarisation and EIS to establish their initial differences. After that, the anodic films were generated under different anodising parameters and electrochemically evaluated in order to find a robust range of the variously anodising parameters such as bath temperature, anodising time and anodising potential.

The baseline presented in this chapter for the TSA process and the anodic film properties will be the starting point for the further development of a modified TSA bath as will be seen in chapter 4.2.

5.1.1. Geometrical effects of the bath on the anodic films

It is well known that the layout of the electrodes in the bath during acid anodising of aluminium may affect both the quality and the properties of the growth anodic films. One obvious idea to homogenise the field lines is to use circular cathodes but this solution is not applicable at industrial scale. Therefore, the work was limited to the usual industrial electrodes setup and the first study was evaluating the homogeneity of such current distribution using two AISI 321 stainless steel cathodes.

Anodising process (37 °C, 14 V, 5+20 min) was undertaken in a TSA bath, with a cathode consisting of two parallel 300 mm x 300 mm AISI 321 stainless steel sheets. The anode was a titanium holder equipped with clips for holding the samples. In this experiment four 150 mm x 100 mm samples were introduced in the bath as shown in fig. 46. Two of them (samples 1 and 3) were in parallel to the cathodes so there was a constant distance of 26 cm between the surface of the samples and the cathodes. The other two (samples 2 and 4) were normal to the cathodes, in this case, the distance between the surface of the samples and the cathodes ranged from 9 cm to 19 cm.

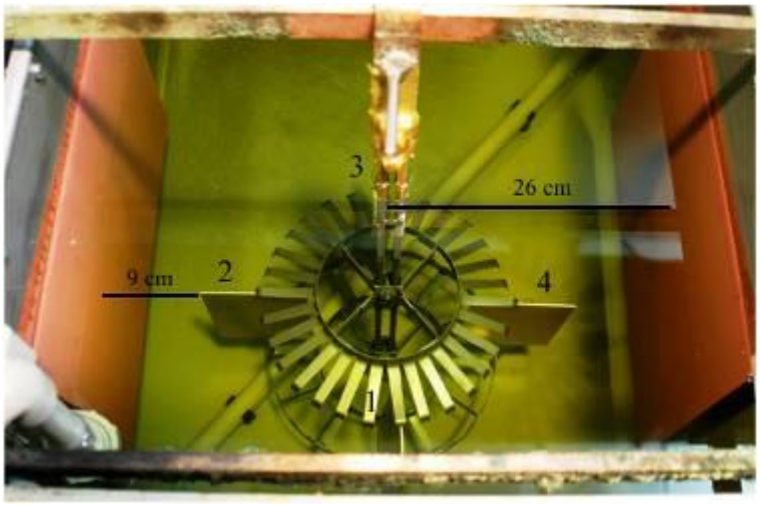

Figure 46. Layout of the samples in the TSA anodising bath

The purpose of this experiment was to find out a possible relation between the electrodes distance during the anodising process and the anodic film thickness obtained. After anodising, the film thickness was measured by means of eddy currents in 10 points along the horizontal axis of both sides of the four samples, these results are shown in the table 11:

Table 11. Anodic film thicknesses measured by eddy currents for the AA7475 specimens anodised in different locations inside the TSA bath.

Sample	Mean thickness (µm)	Thicknesses (µm) for a constant anode-cathode distance of 26,0 cm									
1	**5.0 ± 0.5**	4.7	5.1	4.8	4.6	4.6	5.4	5.0	4.1	5.6	3.8
		4.8	5.6	5.0	5.0	5.4	5.0	5.0	5.3	5.8	5.1
3	**4.8 ± 0.5**	5.4	5.1	5.3	5.7	4.1	4.7	4.8	4.8	4.6	4.8
		5.4	4.3	5.0	5.0	4.5	4.1	5.2	4.2	4.0	4.6
Sample	**Mean thickness (µm)**	**Thicknesses (µm) for different anode-cathode distances (cm)**									
		9.5	**10.5**	**11.5**	**12.5**	**13.5**	**14.5**	**15.5**	**16.5**	**17.5**	**18.5**
2	**4.8 ± 0.5**	5.5	4.7	4.8	3.9	4.4	5.1	4.4	3.7	5.1	4.3
		4.5	5.4	5.2	4.9	5.0	4.7	5.2	4.6	5.4	5.0
4	**5.0 ± 0.3**	5.2	4.9	5.3	4.9	5.1	4.6	4.7	5.2	4.9	4.8
		4.7	5.5	5.2	5.7	4.4	5.2	5.1	4.9	5.0	4.9

The mean values obtained are similar for the samples 1 and 3, besides the thickness of the samples 2 and 4 are in the same range than the previous and there is not a remarkable influence of the distance to the cathodes on the thickness of the anodic film.

This experiment showed that there is a high throwing power and homogeneous distribution of the current distribution lines in the bath and therefore the effect of the ohmic drop due to the electrolyte resistance is negligible.

5.1.2. Stirring effects on the anodic films

The second parameter tested in the pilot plant bath is the influence of the bath stirring on the anodic film thickness. The anodising tank is equipped with two stirring mechanisms; air stirring and mechanical stirring (recirculation of the bath by means of a pump). On the one hand, the air stirring is more vigorous than the mechanic stirring, so the matter transport to the anode surface is more efficient, but on the other hand the air bubbles may cause electrical disruption and therefore defects during the anodising process.

This experiment was also useful for evaluating the homogeneity of the anodic film thickness in complexes geometries. Two AA2024 samples were anodised (37 °C, 14 V, 5+20 min) in the TSA bath with different stirring mechanisms. Both samples had four 2 cm diameter PE tubes bonded to the surface as shown in fig. 47. The length of the tubes ranged from 2 to 10 cm, obtaining different relations between their diameter and their length. During the anodising process there no increase on the bath temperature was registered, ineffectual the stirring mechanism.

Figure 47. AA2024 specimen with four tubes of different length.

After anodising, the tubes were removed and the anodic film thickness was measured by means of eddy currents at 10 different locations of the Al surface at the bottom of the PE tube. These measures are shown in table 12.

The thicknesses obtained on the sample anodised under air stirring mechanism present similar mean thicknesses for all the **Ø** /L studied relations. However, the sample anodised under mechanic stirring show higher dispersion of the anodic film measures with higher standard deviation for all the **Ø** /L relations.

The stirring seems not to be very significant except in the case of the weaker mechanical stirring for the large **Ø** /L of the bonded tubes. Both air stirring and mechanical stirring achieve similar thicknesses after anodising in different geometries. In view of these results, all the anodising processes were undertaken under air stirring mechanism.

Table 12. Anodic film thicknesses measured by eddy currents on the AA2024 specimens anodised under different stirring mechanisms.

Stirring	Relation Ø/L	Mean thickness (µm)	Thicknesses (µm)									
Air	-	2.8±0.5	2.7	2.6	2.2	3.0	2.3	3.0	2.2	2.7	4.0	2.9
			3.7	4.0	3.1	2.7	2.7	2.8	2.7	2.6	2.1	2.5
	1:1	2.8±0.4	3.1	3.5	3.3	2.5	2.5	2.7	3.1	2.5	2.9	2.4
	1:2	2.9±0.5	2.2	3.2	3.1	3.5	3.9	2.7	2.7	2.7	2.5	2.9
	1:3	2.9±0.3	2.7	2.6	3.0	3.5	2.6	3.0	2.8	3.3	2.4	2.9
	1:5	2.8±0.6	3.5	3.2	3.7	3.1	2.6	2.0	1.7	2.5	2.7	2.4
Stirring	**Relation Ø/L**	**Mean thickness (µm)**	**Thicknesses (µm)**									
Mechanic	-	3.1±0.6	3.3	3.5	3.3	3.3	3.6	4.2	3.2	3.0	2.1	2.3
			3.4	2.7	2.2	3.5	3.3	3.7	3.0	2.4	3.0	2.4
	1:1	3.2±0.7	3.0	2.7	3.1	2.7	3.2	2.3	3.0	4.6	4.2	3.1
	1:2	3.4±0.6	3.2	3.0	4.0	3.4	3.0	3.2	3.3	4.8	3.1	3.0
	1:3	2.9±0.6	2.5	4.2	2.1	2.8	2.5	3.4	2.9	3.1	3.0	2.4
	1:5	2.8±0.7	3.6	2.0	2.8	3.9	3.0	2.7	2.6	2.0	2.0	3.1

5.1.3. Morphological characterisation of the anodic films

5.1.3.1. Scanning electron microscopy

The changes in both, the macrostructure and the microstructure of the surfaces of the alloys along the anodising process described in section 4.3., were observed by means of scanning electron microscopy (SEM). This morphological evaluation is a first and quick assessment of the parameter influence previous to the following in-detail evaluation of micromorphology by TEM, composition and electrochemical behaviour.

The following SEM pictures show the surface of the different aluminium alloy specimens after each step of the process, namely as received, degreasing, acid pickling and anodising.

AA2024

The SEM pictures of the AA2024 specimens after each step of the anodising treatment are shown in fig. 48.

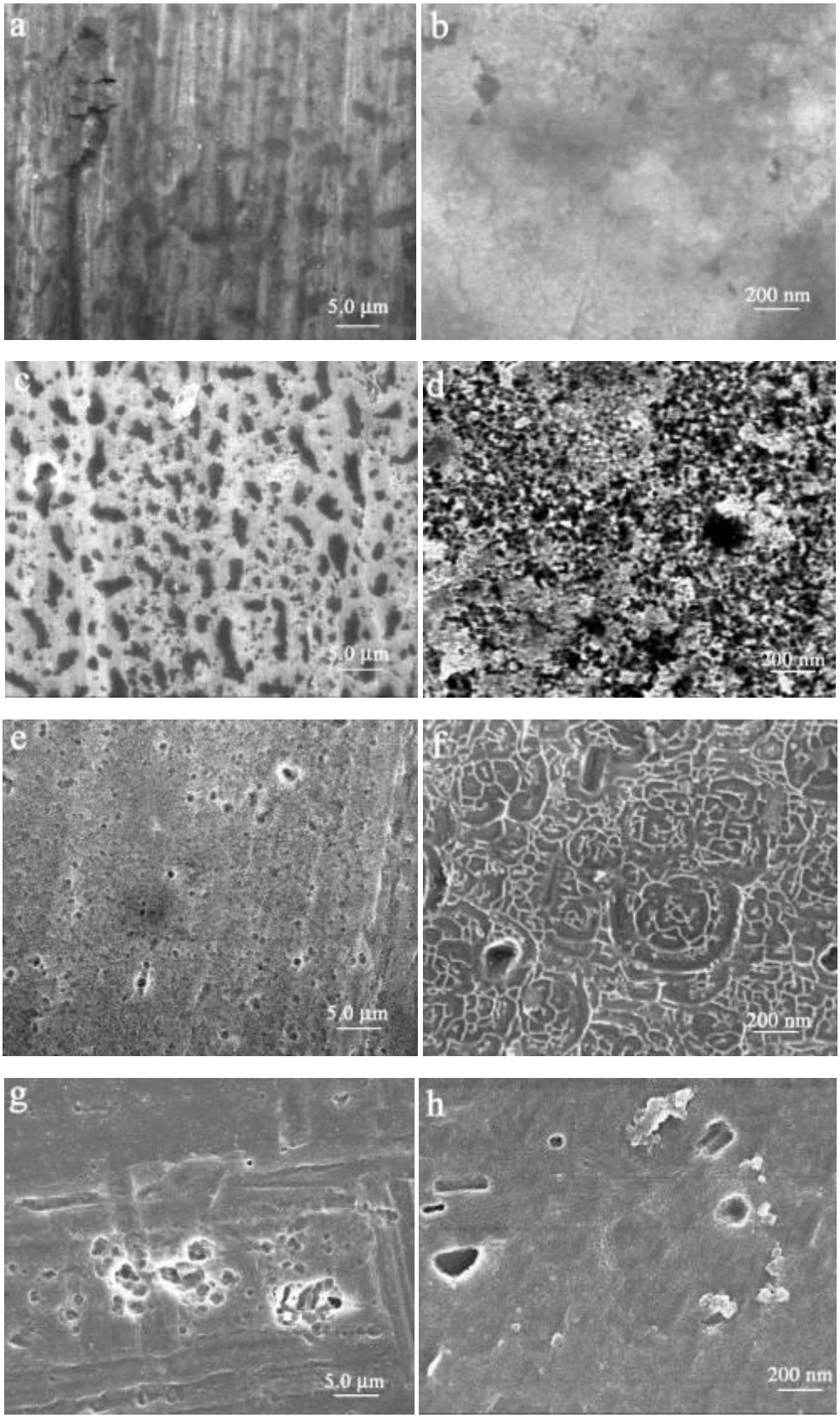

Figure 48. Morphological changes of the macrostructure and the microstructure on the surface of an AA2024 sample during the anodising process: (a,b) as received, (c,d) after degreasing, (e,f) after acid pickling, (g,h) anodized.

The as received AA2024 macro and micromorphology of the alloy surface (Fig. 48a and 48b, respectively) is masked by the presence of preservation oils. After degreasing, the real surface morphology is revealed; in the fig. 48c some second phase particles of the alloy and even some corrosion products are observed on the surface, the micromorphology in fig. 48d reveals a rough, disordered surface.

The acid pickling (Fig. 48e) removes the corrosion products and partially dissolves the second phase particles; i.e. fig. 49 shows a S-phase after the deoxidising process; Mg has dissolved into the electrolyte as Mg^{2+}, whereas the remaining Cu forms a very high surface area porous sponge structure, that will act as a cathode [103]. The micromorphology (fig. 48f) after this treatment presents a smoother, scalloped surface.

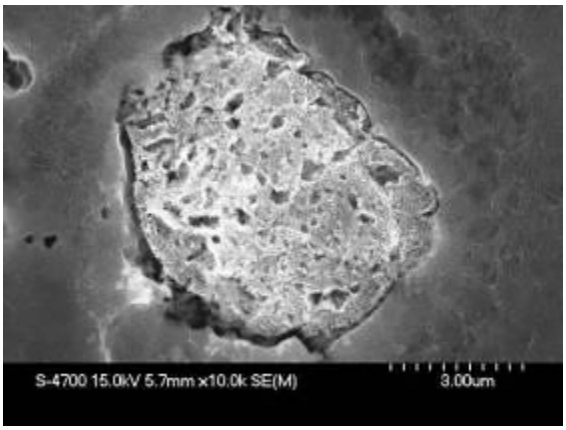

Figure 49. Scanning electron micrograph of an intermetallic particle on the surface of an AA2024 specimen after pickling.

The anodising process does not cause major changes on the macromorphology (fig. 48g), only a smothering of the surface is observed. As the growing of the anodic film is homogeneous, the voids generated during the acid pickling will remain on the surface covered also by the alumina film. In terms of microstructure (fig. 48h), the scalloped morphology is smoother and the nanoporosity of the film is revealed, although this porosity will be better evidenced by means of transmission electron microscopy.

Clad AA2024

The general morphology of the surface of the clad AA2024 along the anodising process is shown in fig. 50.

The pure aluminium layer on the as received surface (fig. 50a-b) is soft and therefore scratches on the surface easily appear. After the preservation oils removal (fig. 50c-d), a flat surface free of intermetallics is observed. The detailed morphology in fig. 50d shows that the scratches are relatively superficial. The acid pickling (fig. 50e) leads to a homogenous attack of the surface with preferential broadening of the existing voids and partial removal of the scratched surface, nevertheless, the micromorphology (fig. 50f) reveals a smoother, lumpy surface. After anodising (fig. 50g-h), the alumina film morphology resembles the pickled surface although the nanopore mouths at the film surface after anodising are not readily resolved.

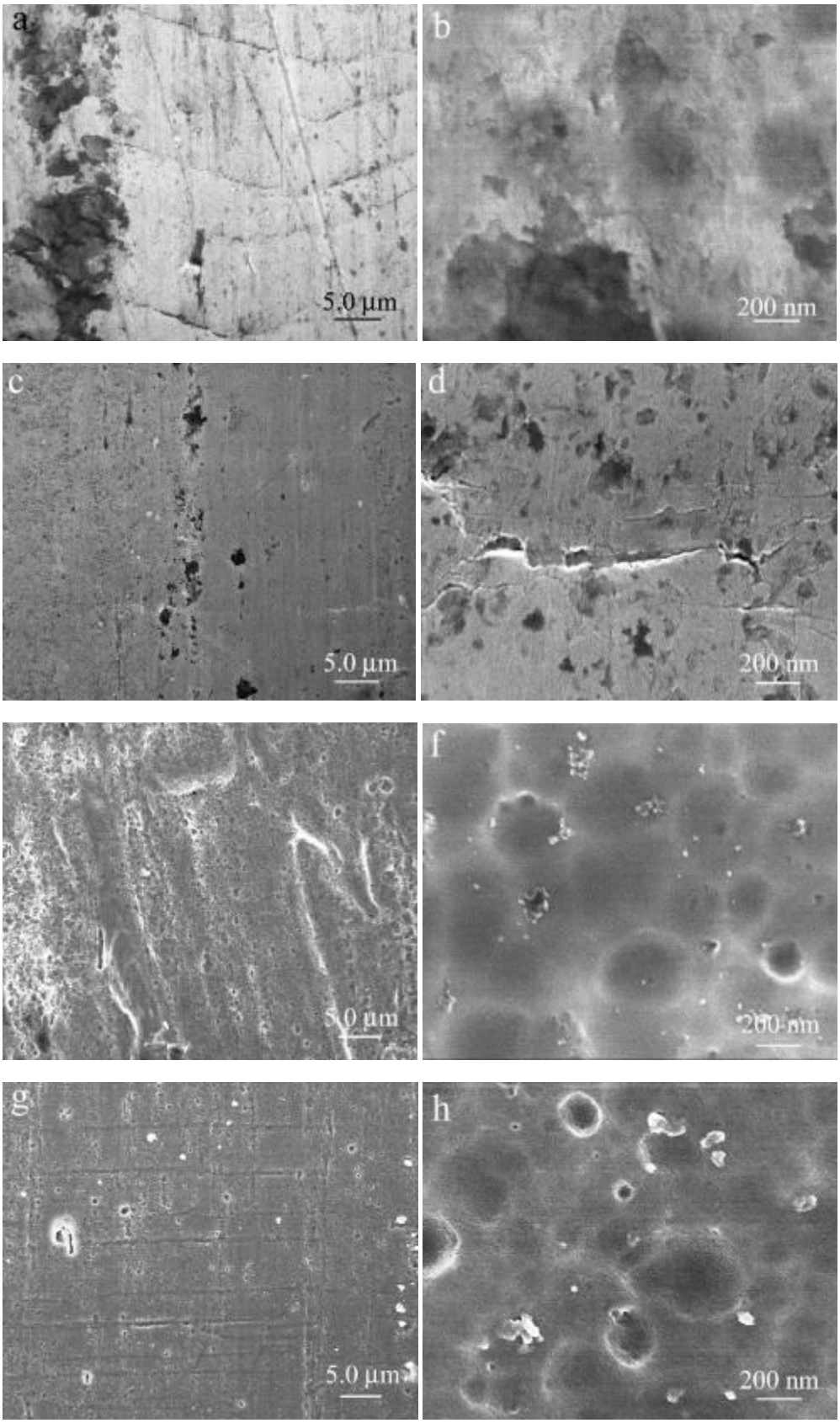

Figure 50. Morphological changes of the macrostructure and the microstructure on the surface of a clad AA2024 sample during the anodising process: (a,b) as received, (c,d) after degreasing, (e,f) after acid pickling, (g,h) anodized.

AA6061

The SEM pictures of the AA6061 specimens after each step of the anodising treatment are shown in fig. 51.

The as received AA6061 is shown in fig. 51a-b; the real morphology is covered by the preservation oils. After degreasing (fig. 51c), a stripped morphology with some voids is observed, whereas the fig. 51d reveals a rough surface and a high intermetallics phases density. The pickling process (fig.51e-f) dissolves most of the intermetallics and smoothes the surface. The morphology observed after anodising (fig. 51g-h) maintains the aspect of the pickled sample but the presence of alumina nanopores is evident.

AA7475

The general morphology of the surface of the AA7475 along the anodising process is shown in fig. 52.

The as received AA7475 (fig. 52a-b) shows some intermetallics particles, preservation oils and microcracks. Fig. 52c shows the morphology after degreasing; whereas micromorphology in Fig. 52d reveals extensive cracks and defects.

In this case, the acid pickling (fig. 52e) drastically affects the morphology; the μ-phase ($MgZn_2$) in the alloy presents a lower dissolution potential than the pitting potential of the alloy, [104]. This phase can be dissolved during the pickling process and that is the reason why some cracks appear in the grain boundaries. The micromorphology (fig.52f) reveals that the acid pickling eliminates the microcracks but the morphology obtained is porous and highly distorted, possibly due to the massive Mg removal during the acid pickling.

The anodic film is visualised in fig. 52g-h; as the Pilling-Bedworth ratio (ratio of the volume of the metal oxide formed to the consumed metal volume) of the Al_2O_3 is 1.28, the anodic film occupying more volume than the alloy partially repair these cracks. For the same reason, the pores observed in the micromorphology are partially closed. Again, the nanoporous structure of the anodic film is not readily resolved; nevertheless this will be better evidenced in the next section.

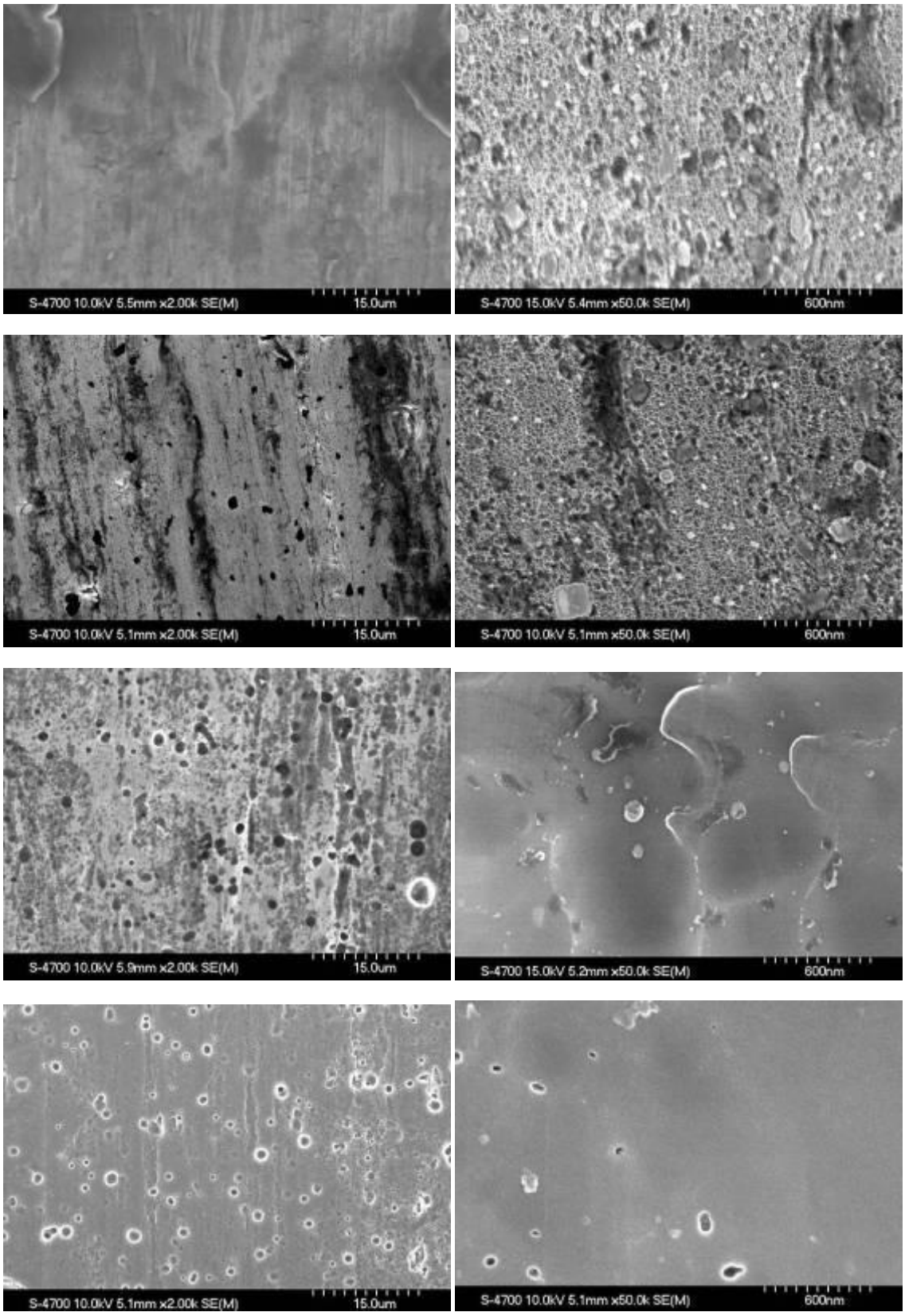

Figure 51. Morphological changes of the macrostructure and the microstructure on the surface of an AA6061 sample during the anodizing process: (a,b) as received, (c,d) after degreasing, (e,f) after acid pickling, (g,h) anodized.

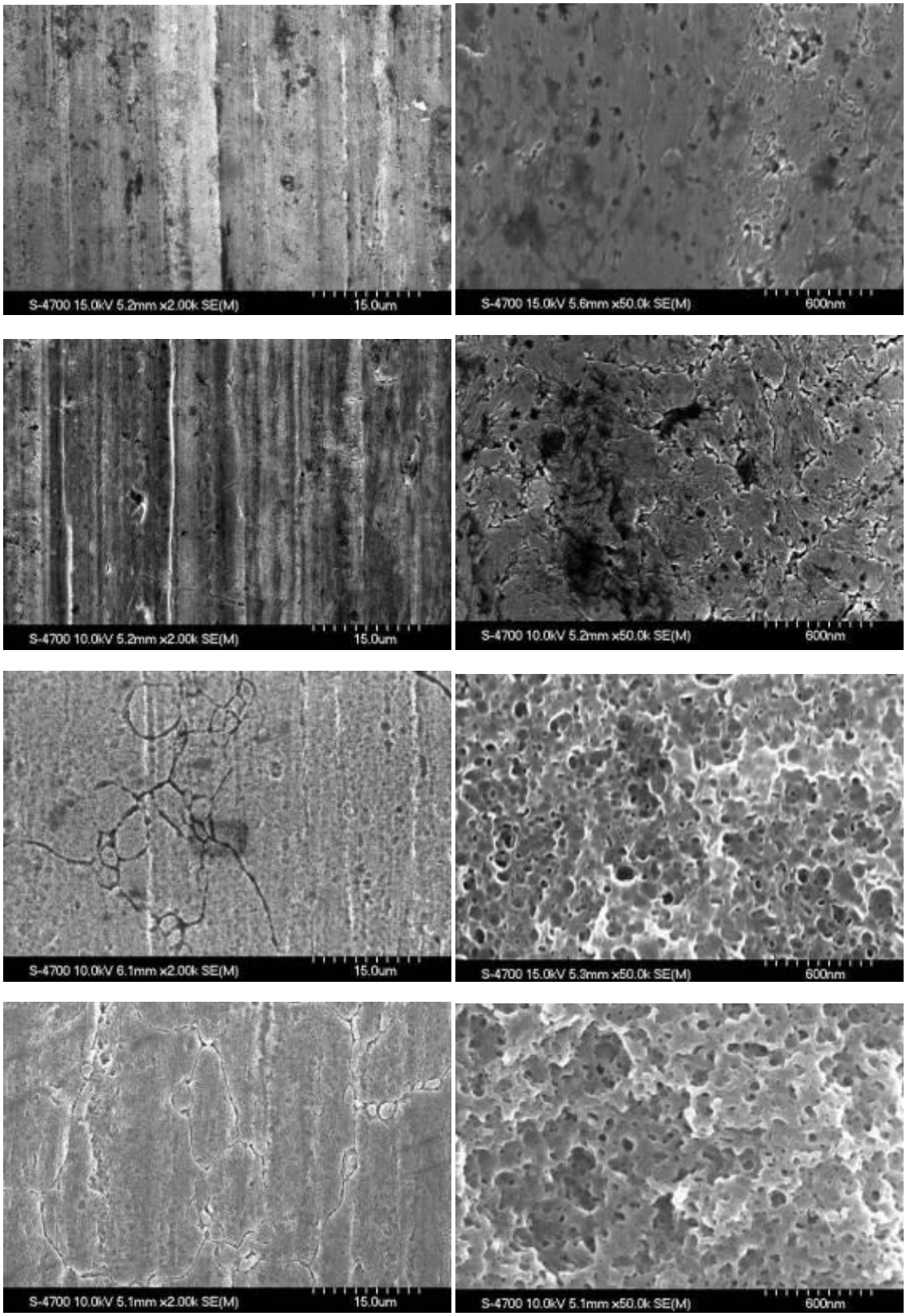

Figure 52. Morphological changes of the macrostructure and the microstructure on the surface of an AA7475 sample during the anodizing process: (a,b) as received, (c,d) after degreasing, (e,f) after acid pickling, (g,h) anodized.

5.1.3.2. Transmission electron microscopy

Transmission electron microscopy (TEM) images have been useful to reveal the fine microstructure of the barrier and porous layers grown on the different alloys and also to measure the thicknesses of the anodic film and the barrier layer.

AA2024

Fig. 53a shows an anodic film grown on AA2024. The measured thickness of 3.0 ± 0.1 µm is in good agreement with the value of 3.0 ± 0.5 µm measured by means of eddy currents. Two contrasting morphologies are evident across the film thickness, comprising an outer film layer of finer pore size and an inner layer of increased pore dimensions. The pore size is dependent on the anodising potential [105], thus the finer-featured outer layer is developed during the initial stage of increasing potential from the OCP to 14 V. The inner layer is generated at the constant potential of 14 V and reveals relatively regular film morphology of increased pore and cell dimensions.

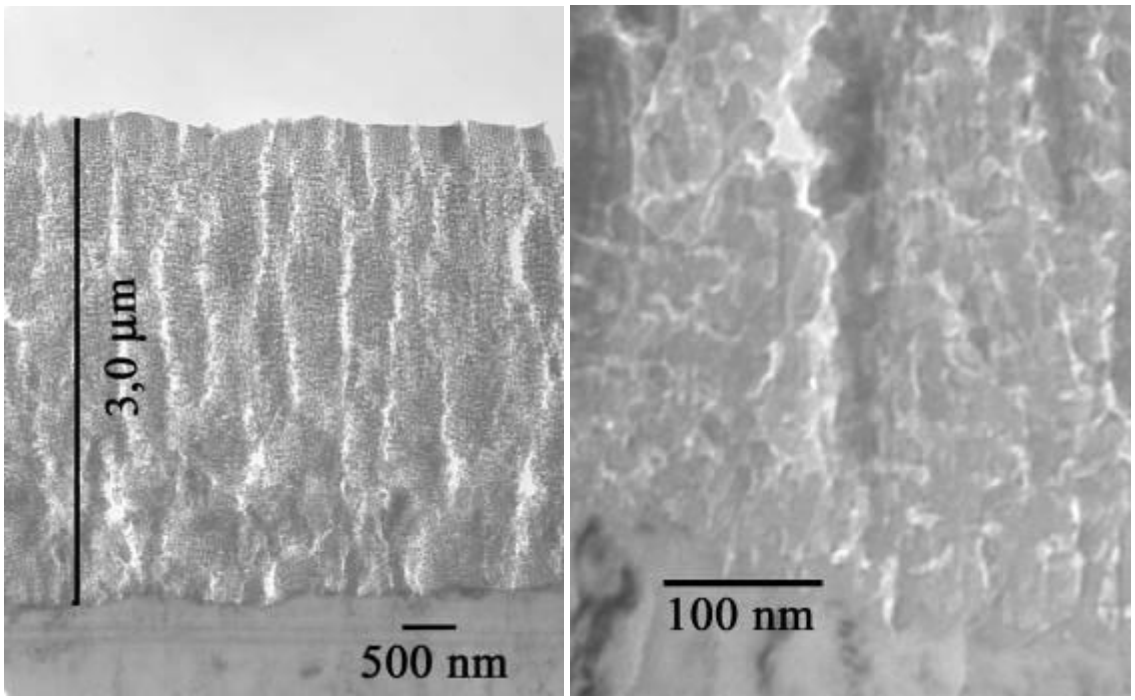

Figure 53. Transmission electron micrographs of ultramicrotomed sections of a TSA anodised AA2024 sample.

Fig. 54b shows a magnified image of the alloy/oxide interface. Here the anodic oxide morphology is observed. The anodic film is composed of a porous layer with lateral porosity, typical of a porous layer generated on copper containing alloys, and a barrier layer beneath the major pores. A thin region in the alloy immediately below the barrier layer displays a dark contrast that is attributed to the presence of a copper-enriched layer.

Based on different studies that will be following described, for many relatively dilute aluminium alloys, anodic film formation involves up to three key stages:

a) Preferential oxidation of those alloying elements less noble than aluminium,

b) Formation of a relatively pure alumina film, and

c) Oxidation of aluminium and all alloying elements at the alloy/film interface.

During the film growth of the anodic film on the AA2024, the major alloying elements (Mg, Cu and Zn) will be an important factor on the final morphology of the film. Moreover, although most of the S-phase (Al_2CuMg) of the AA2024 alloy has been removed from the surface during the acid pickling, some residuals intermetallics can remain and also they can arise to the substrate surface during the anodising process.

Mg will be preferentially oxidised during the initial potential ramp because its lower Gibbs free energy of oxide formation per equivalent ($\Delta G°/n$) will result in a faster MgO formation [104]. Nevertheless, Mg has lower single metal-oxygen bond strength than Al, resulting in a faster outward mobility. Finally, the Pilling-Bedworth ratio of the MgO is 0.81, this will lead to voids at the alloy film interface, as the volume occupied by the oxide is less than the originally occupied by the Mg in the solid solution. These voids generate a detached film, but the subsequent growth of relatively pure alumina with a Pilling-Bedworth ratio of 1.28 will fill these voids.

As stated before, after the formation of the detached film, a freshly pure alumina film will grow, but only for low potentials, when the difference in the Gibbs free energies of alumina and copper oxide formations are an important parameter. During the preferential oxidation of Al in the alloy/film interface, the Cu remaining in the solid solution, in the S-phase and in the θ-phase (Al_2Cu) will be accumulating beneath the film until reaching a minimal enrichment level. Once this enrichment is achieved, there will be simultaneous formation of Al_2O_3, MgO and CuO.

Curioni [32] demonstrated that the morphology of the alumina grown on AA2024 in sulphuric acid presented the same morphology than the alumina grown on pure aluminium when anodising at potentials up to 6 V. On the other hand anodising at 7 V and higher potentials will lead to the oxidation of the θ-phase (Al_2Cu).

Iglesias-Rubianes et al. [31] stated that the causes of the altered TSA film morphology on the copper-containing alloys are related to three factors:

-The enrichment of copper, which can affect the local composition of the film and possibly also the stress at the alloy/film interface and adhesion of the film to the alloy. This copper enriched layer permits the electrochemical potential near the alloy/film interface to rise sufficiently for oxidation of O^{2-} ions of the alumina to O_2 gas. The formation of oxygen bubbles at such impurities is suggested to be one cause of residual flaws in anodic alumina. [108]

-The presence of copper species and oxygen in the film, may affect the solubility of the film material in the anodizing electrolyte. The pore morphology may be less regular if pores formed by dissolution of film material change direction following interception of oxygen bubbles within the film. The gas present in oxygen-filled bubbles at high pressure, results in the rupture of the anodic film, with subsequent access of the anodizing electrolyte to the alloy/film interface. This provides a preferential path for current flow and consequent preferential anodic oxide growth. [109]

-The release of oxygen to the electrolyte; that causes rupture of the film.

Clad AA2024

The morphology of the anodic film grown on clad AA2024 is shown in fig. 54. The measured thickness of 3.1 ± 0.1 µm is in relatively good agreement with the value of 3.3 ± 0.5 µm measured by means of eddy currents. The fine-featured morphology developed during the initial potential stage is observed in the outer part of the film. Beneath this layer, an inner, regular film of increased pore and cell dimensions is shown.

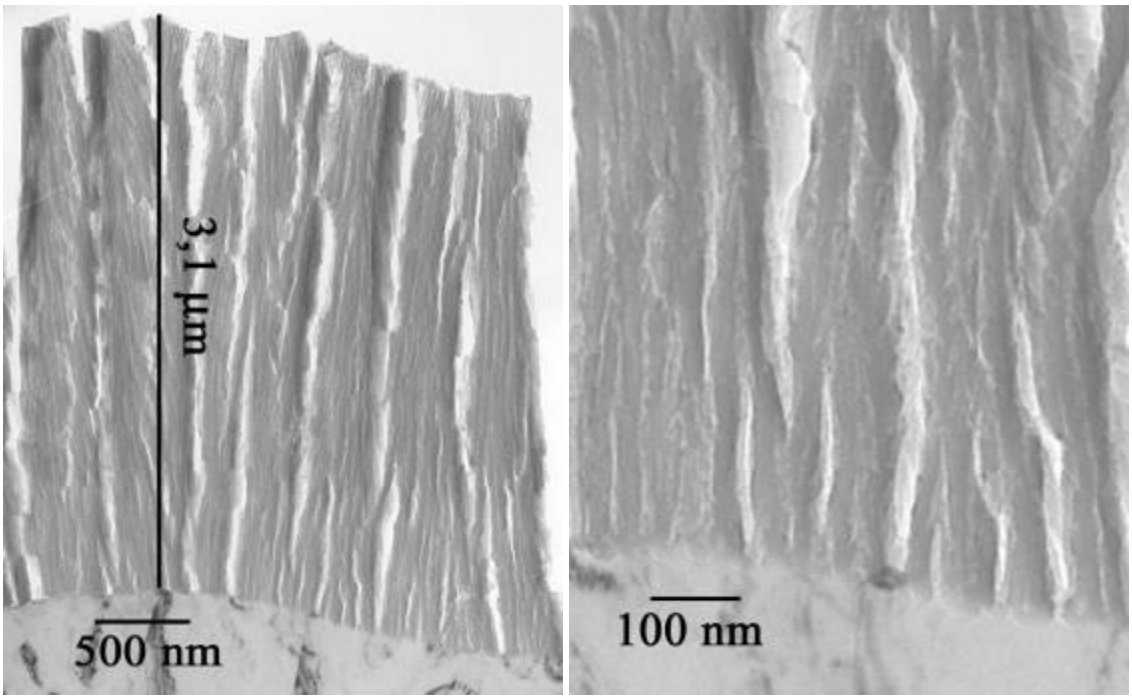

Figure 54. Transmission electron micrographs of ultramicrotomed sections of a TSA anodised clad AA2024 sample.

A highly organised film with straight pores is observed in the magnified image (fig. 54b). The barrier layer is well defined between the base of the pores and the alloy, and there is no evidence of any enriched layer beneath the barrier layer.

During the growth of the anodic film on clad AA2024, there is not oxygen formation due to the presence of second phase particles nobler than the aluminium and, therefore the lateral growth of the pores is not promoted.

AA6061

Fig. 55 shows the anodic film grown on AA6061. The measured thickness of 3.8 ± 0.1 µm is slightly lower than the value of 4.4 ± 0.8 µm measured by means of eddy currents. Besides, the finer-featured outer layer is not neatly observed. This two facts leads to think that the TEM section observed in the picture is bended or broken. Nevertheless, a regular porous film is observed.

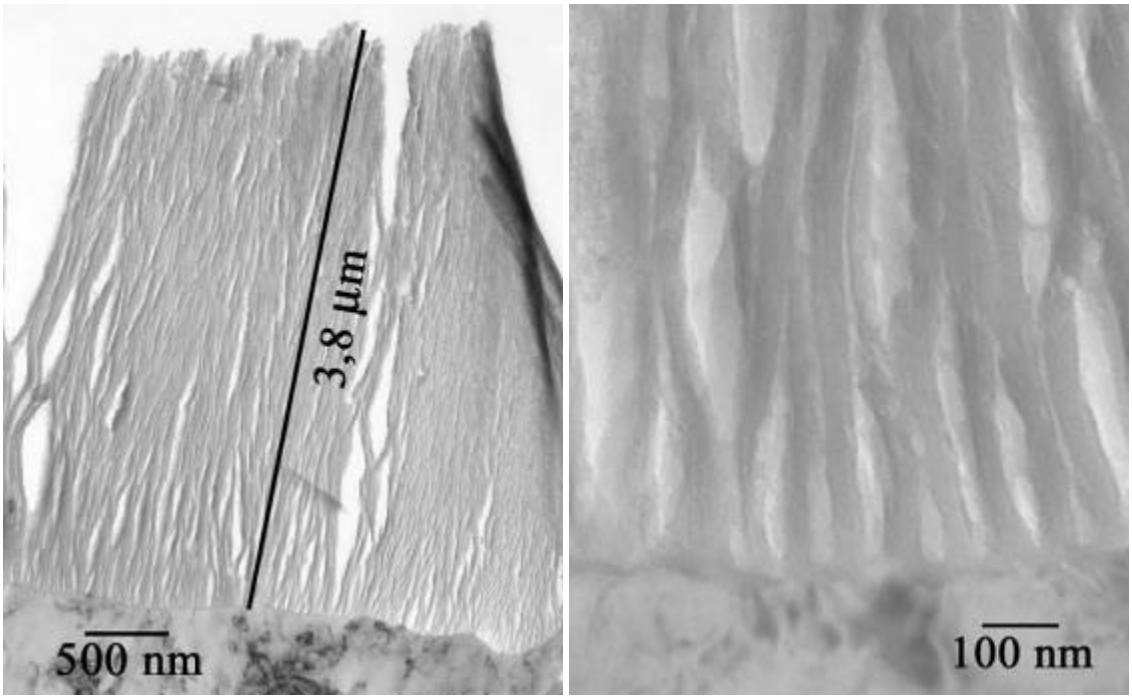

Figure 55. Transmission electron micrographs of ultramicrotomed sections of a TSA anodised AA6061 sample.

The magnified image (fig. 55b) shows an organised film with relatively straight pores. There is also a well defined barrier layer and no enriched layer beneath it. The regular structure of the anodic film, similar to that observed for the clad AA2024, is due to the absence of alloying elements nobler than aluminium. The major alloying element in this alloy is Mg, which is largely removed from the surface during the pickling process. Besides, the remaining Mg will be rapidly oxidised to Mg^{2+}, as previously described for the AA2024.

AA7475

The morphology of the anodic film grown on AA7475 is shown in fig. 56. The measured thickness of 3.9 ± 0.1 µm is in relatively good agreement with the value of 4.3 ± 0.7 µm measured by means of eddy currents. Furthermore, the presence of finer-featured pores due to the initial potential stage is revealed in the outer part of the film. The inner layer shows increased pore and cell dimensions.

The porous film shown in fig. 56b is disorganised and present lateral growth. The barrier layer is well defined beneath the major pores. The presence of a dark contrast in some parts beneath the barrier layer reveals the presence of an enriched layer, which can be composed of copper, zinc or both elements. The influence of the copper and the magnesium as alloying elements has been previously discussed. The role of Zn during the anodising process is similar to the described for copper; as the Zn is a nobler element than Al, there can exist an enrichment of Zn in the early stages of the anodising process, probably in form of Zn clusters, once a critical Zn enrichment has been achieved, Zn will be oxidised to Zn^{2+} ions, which migrate about 2.3 times faster than Al^{3+} [110].

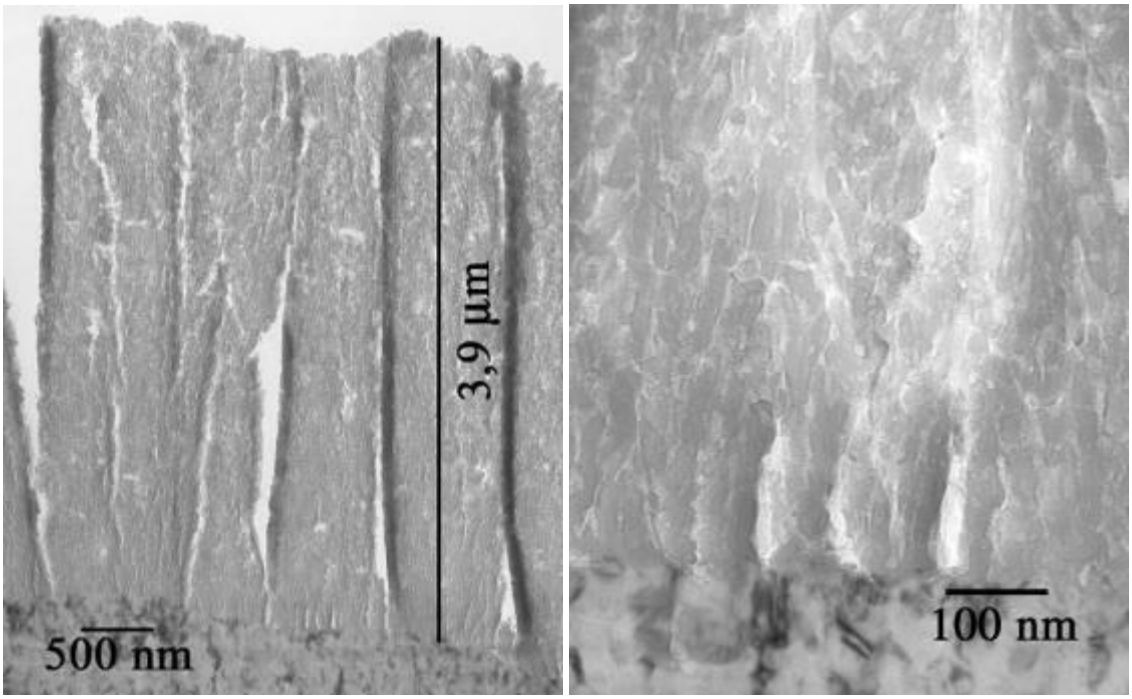

Figure 56. Transmission electron micrographs of ultramicrotomed sections of a TSA anodised AA7475 sample.

5.1.4. Chemical composition of the anodic films

Glow discharge optical emission spectroscopy (GDOES) depth profiles of anodised specimens of the four studied alloys are shown in fig. 57. For the sake of simplicity, only the major second phase elements of each alloy and the electrolyte elements have been plotted.

In general, the GDOES spectra of an anodised alloy can be divided in three different regions attending to the aluminium profile: (i) a constant aluminium yield attributed to the porous anodic film, (ii) a region of increasing aluminium yield due to the relatively rough alloy/film interface and (iii) a region of increased constant aluminium intensity associated with sputtering of the bulk alloy.

The presence and distribution of different elemental species in the anodic films are largely due to the mobilities of the respective ions in the anodic alumina films. The mobility of individual species depends largely on metal-oxygen bond energy as well as charge and ionic radius [111].

AA2024 specimen, (c) anodised AA6061 specimen and (d) anodised AA7475 specimen.

Oxygen signal is relatively constant in the porous anodic film. This signal decreases during the film/alloy interface until reaching background levels in the alloy region. Oxygen signal is mainly due to the oxygen in the alumina, and in a lesser extent can be also associated to sulphate and residuals tartaric species.

Sulphur signal present a relatively constant profile during the anodic film sputtering, with a maximum at the end of this region, then decreases in the interface region and finally the low signal in the alloy region.

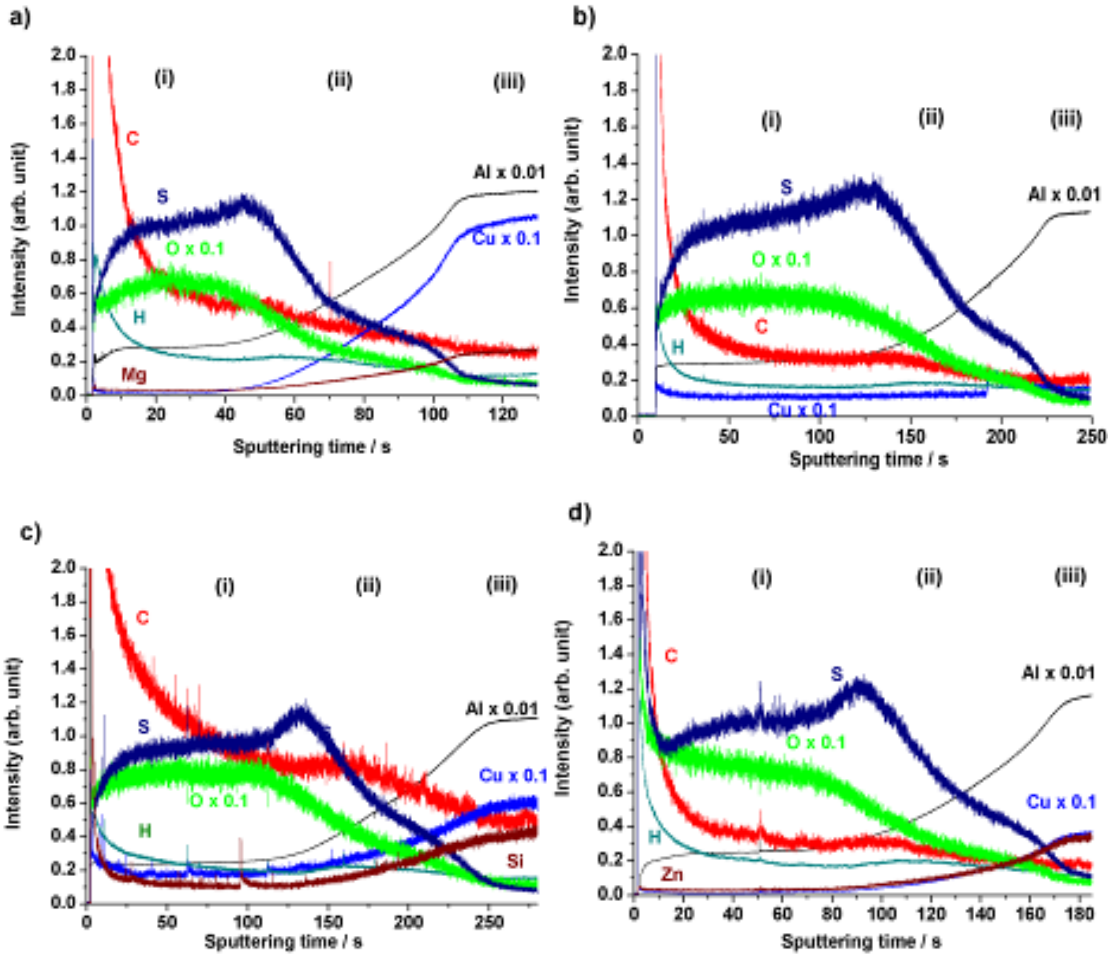

Figure 57. GDOES elemental depth profiles of an (a) anodised AA2024 specimen, (b) anodised clad

Carbon and Hydrogen signals present similar profiles than the sulphur. Sulphur is incorporated from the bath to the film in form of sulphate [112], the maximum in the sulphur signal at the beginning of the sputtering is attributed to the inwards migration of the sulphate anion. Carbon and hydrogen signals profiles are closely related, this fact leads to think that tartaric acid (or derived species) are incorporated in the anodic film. Besides, these two signals present a maximum approximately at the same sputtering time than the sulphur, indicating inwards but slower migration of the carbohydrate.

The alloying elements show a low signal in the anodic film region, an increase in the interface and an increased constant yield in the alloy region. The alloying elements generally present a faster mobility than the Al^{3+}, and the decrease of the alloying element signals to background signal in the anodic film confirms the hypothesis explained in the previous section.

5.1.5. Electrochemical behaviour of the alloys prior to anodising

The following electrochemical measures were taken on the degreased bare alloys used as substrates in this study to provide the baseline for further electrochemical characterisation of the anodic films.

5.1.5.1. Lineal polarisation

The polarisation curves of the different alloys (AA2024, clad AA2024, AA6061 and AA7475) recorded in 0.5 M NaCl are shown in the fig. 58. The four curves display similar cathodic and anodic branches. The limiting current densities of the cathodic branches are indicative of the reduction of dissolved oxygen. On the other hand, the value of the current density in the anodic branches rapidly increases with low increments of the applied potential. This indicates that the pitting potential is reached immediately after the corrosion potential in the high chloride containing test solution.

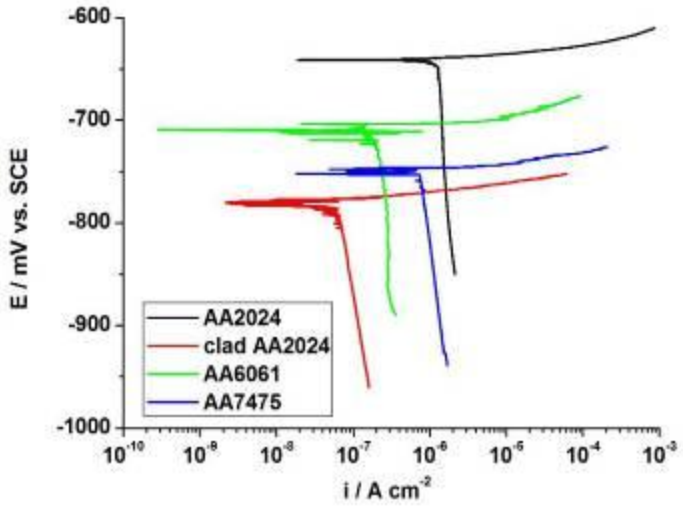

Figure 58. Polarisation curves of the degreased alloys measured after 1 h of immersion in a 0.5 M NaCl solution.

The parameters of the fitted polarization curves are shown in table 13. E_{corr} show the thermodynamic tendency of an alloy to be oxidised, that is to say corroded, and i_{corr} is a parameter proportional to the corrosion rate. Due to the limiting cathodic current behaviour, i_{corr} is calculated by extrapolation of this limiting cathodic current at the E_{corr} value.

Table 13. Corrosion parameters of the degreased alloys. icorr is calculated by extrapolation of the limiting cathodic current.

Alloy	E_{corr} (mV vs. SCE)	i_{corr} (nA cm^{-2})
AA2024	-641	1240
Clad AA2024	-780	64
AA6061	-708	175
AA7475	-751	723

E_{corr} of an aluminium alloy is highly influenced by the composition of the aluminium-rich solid solution, which constitutes the predominant volume fraction and area fraction of the alloy microstructure. Nevertheless, E_{corr} is not affected significantly by second-phase particles of microscopic size, but because these particles frequently have solution potentials differing from that of the solid-solution matrix in which they occur, localized galvanic cells may be formed between them and the matrix.

The effects of principal, alloying elements on solution potential of high-purity aluminium are shown in Fig. 59. For each element, the significant changes that occur do so within the range in which the element is completely in solid solution. Further addition of the same element, which forms a second phase, causes little additional change in solution potential.

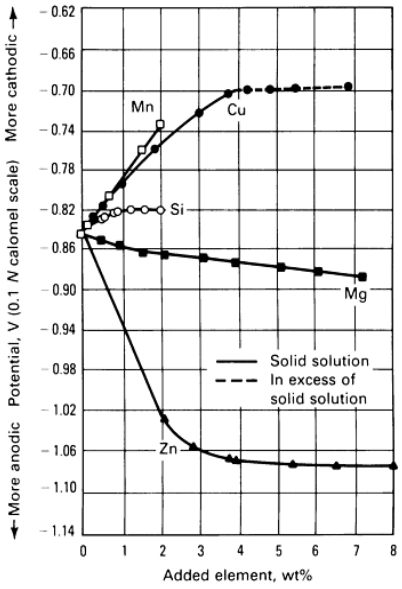

Figure 59. Effects of principal alloying elements on the electrolytic-solution potential of aluminium. Potentials are for solution-treated and quenched high-purity binary alloys in a solution of 53 g L^{-1} NaCl plus 3 g L^{-1} H_2O_2 at 25 °C [15]

The clad AA2024 can be considered as pure aluminium. The E_{corr} of this alloy is -780 mV vs. SCE. The effects of multiple elements in solid solution on solution potential are approximately additive. Conversely, the high copper content (4.5 wt. %) of the AA2024 makes the E_{corr} more cathodic (-641 mV vs. SCE) than the pure aluminium. The AA6061 contents Mg (1.4 wt. %) that displaces the E_{corr} to more anodic potentials and Si (0.65 wt. %) and Cu (0.18 wt. %) that displaces the E_{corr} to more cathodic potentials, the final E_{corr} of -708 mV is more cathodic than the pure aluminium. In the case of the AA7475, Zn (5.8 wt. %) and Mg (2.3 wt. %) make the E_{corr} more anodic and Cu (1.5 wt. %) has the contrary effect, the final E_{corr} is slightly more cathodic than the pure aluminium.

The relatively pure clad AA2024 i_{corr} is low (64 nA cm^{-2}). The presence of second-phase particles in the rest of the alloys will generate galvanic couples that increases i_{corr}; the diluted AA6061 i_{corr} is 175 nA cm^{-2}, whereas the copper has a noticeable influence on the i_{corr} of the AA7475 (723 nA cm^{-2}) and the AA2024 (1240 nA cm^{-2}).

5.1.5.2. Electrochemical impedance spectroscopy

The electrochemical impedance spectroscopy (EIS) measures of the bare, degreased alloys are shown in fig. 60.

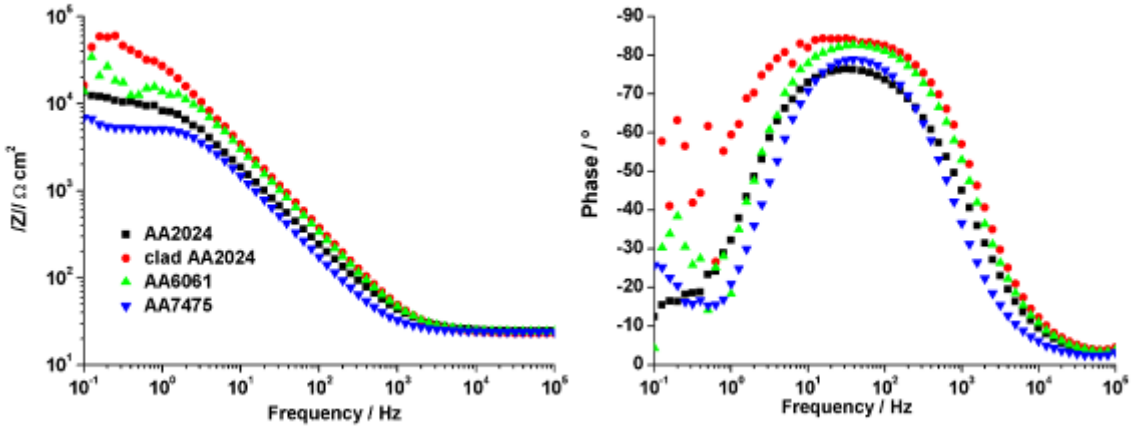

Figure 60. EIS spectra of the degreased alloys measured after 1 h of immersion in a 0.5 M NaCl solution.

The four alloys show a resistive behaviour in the low frequency range. The equivalent circuit selected for simulating these spectra consist of a double layer capacitor (C_b) and a charge transfer resistance (R_b) in the interface alloy/electrolyte, similar to the EC1 shown in section 4.3. The results of the fitting are shown in table 14.

Table 14. Results after fitting EIS data of the degreased alloys acquired in 0.5 M NaCl solution. The values in brackets indicate the dispersion factor of the constant phase element.

Alloy	C_b (µS cm^{-2})	R_b (kΩ cm^2)
AA2024	13.0 (0.89)	12.3
Clad AA2024	6.33 (0.94)	74.2
AA6061	7.12 (0.94)	22.2
AA7475	13.3 (0.94)	5.92

The typical capacitance values of the double layer estimated for bare metals are 20 to 60 µS cm^{-2} [88]. In the case of aluminium alloys, the lower C_b can be attributed to the thin oxide film formed immediately after air exposure, calculations of the thickness of this naturally film formed gives values of 0.7 to 1.4 nm.

R_b can be attributed to the different surface composition of the alloys and to the presence of second phase particles, therefore the purer alloys present higher R_b values. These results are consistent with the polarisation results in the previous section.

5.1.6. Anodising temperature effect on the corrosion resistance of the anodic films

In the industrial process, some variables of the system can not be so well controlled as in the laboratory. For example, in an industrial anodising tank containing thousand of litres the homogenization of the temperature can become a problem. Therefore, in order to determine the influence of the temperature on the behaviour of the anodic films against corrosion, samples of the variously alloys were anodised at three different temperatures: 32 °C, 37 °C and 42 °C.

5.1.6.1. Film thickness

The film thicknesses generated at different anodising temperatures on the different alloys were measured by means of eddy currents and are plotted in fig. 61.

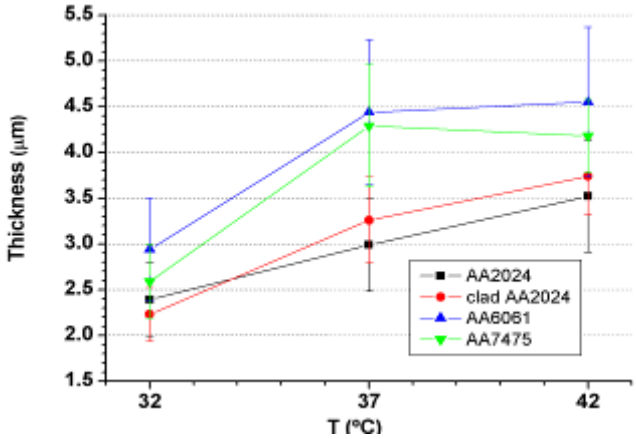

Figure 61. Film thickness of the anodic layers grown at different temperatures on the four alloys.

The thickness dependence of the films growth on AA2024 and clad AA2024 with the temperature are close to linearity in the range studied. In the case of the AA6061 and AA7475 alloys, there is a marked difference of the anodic film thickness anodised at 32 °C and 37 °C, but further increase of the temperature to 42 °C does not involve thicker anodic films.

The anodic film thickness is highly influenced by the anodising temperature. On the one hand, the kinetics of the reaction of the formation and dissolution of the film can be modified with temperature, so that the process seems to be more effective with increased temperatures. On the other hand the growth of the insulating anodic film will decrease the conductivity of the anode, so that, the effective electromotive force on the anode can be lowered with the thickening of the anodic film.

Apart from the anodic film thickness, morphological changes can occur in the pore diameter and the interpore distance, as those described by Sulka anodising highly pure electropolished aluminium at different temperatures [114]. Nevertheless, these features cannot be visualised by means of the electron-optical spectroscopies on the highly disorganised anodic films grown on real alloys. Therefore, EIS characterization was performed in anodic films growth at different temperature to reveal such possible effects. The following study is performed in not sealed samples after the anodising.

5.1.6.2. Electrochemical impedance spectroscopy

AA2024

Fig. 62 shows the evolution with immersion time in NaCl of the EIS spectra of the AA2024 samples anodised at different temperatures.

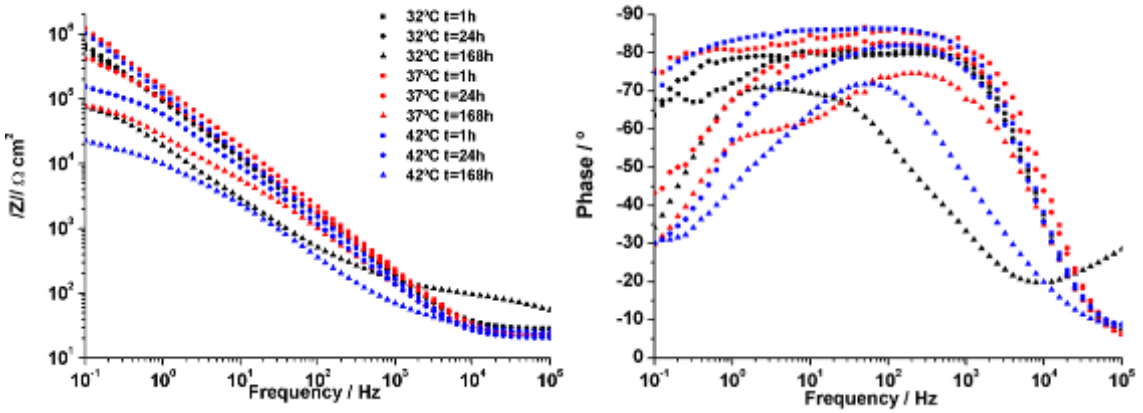

Figure 62. Bode plots of AA2024 specimens anodised at different temperatures after different immersion times in 0.5 M NaCl solution.

After 1 h of immersion all the samples anodised at different temperatures present a capacitive behaviour. A diminishment of the |Z| in the low frequency range is observed for the three samples after 24 h, being this fact more evident for the sample anodised at 42 °C. Further |Z| decrease in the low frequency range is manifested after 168 h of immersion, at that moment the sample anodised at 32 °C shows a Z increase in the high frequency range.

Table 15 displays the parameters obtained from the fitting of the EIS spectra to the EC1 described in the section 4.3.

Table 15. Results after fitting EIS data for the AA2024 specimens anodised at different temperatures after different immersion times in 0.5 M NaCl solution. The values in brackets indicate the dispersion factor of the constant phase element.

C_b (μS cm^{-2})	1 h	24 h	168 h	R_b (kΩ cm^2)	1 h	24 h	168 h
32 °C	1.05 (1.00)	2.01 (0.90)	11.1 (0.82)	**32 °C**	2409	710	120
37 °C	0.78 (1.00)	1.67 (0.91)	6.03 (0.82)	**37 °C**	3103	528	89.9
42 °C	1.11 (1.00)	2.79 (0.89)	18.2 (0.77)	**42 °C**	2624	159	24.9

The capacitance of the barrier layer, C_b is related to the thickness of the barrier layer, therefore increased values of C_b with immersion time can be related to the thinning or progressive damage of the barrier layer. The AA2024 sample anodised at 37 °C present the lowest value of the three samples after 1 h of immersion in 0.5 M NaCl solution, besides the increase of C_b, and the associated thinning of the barrier layer is slower for this sample. After 168 h, the samples anodised at 32 °C and 42 °C present C_b values in the range of the bare alloy (13.0 μS cm^{-2}), indicating that the barrier layer is largely degraded.

The resistance of the barrier layer, R_b is due to the charge transfer resistance of the barrier layer, the decrease of R_b with immersion time is attributed to the increase of local defects in the barrier layer.

R_b values after 1 h of immersion are in the same order of magnitude for the three samples. The R_b decrease after 24 h is evidencing an increase of local defects; this fact was corroborated when pits appeared on the surface of the three samples after 48-72 h of immersion. Corrosion

was generally extended after 168 h, the accumulation of corrosion products form an inhomogeneous layer that determines the low R_b.

Clad AA2024

The EIS spectra of the clad AA2024 specimens anodised at different temperatures and their evolution with immersion time in 0.5M NaCl solutions are shown in fig. 63.

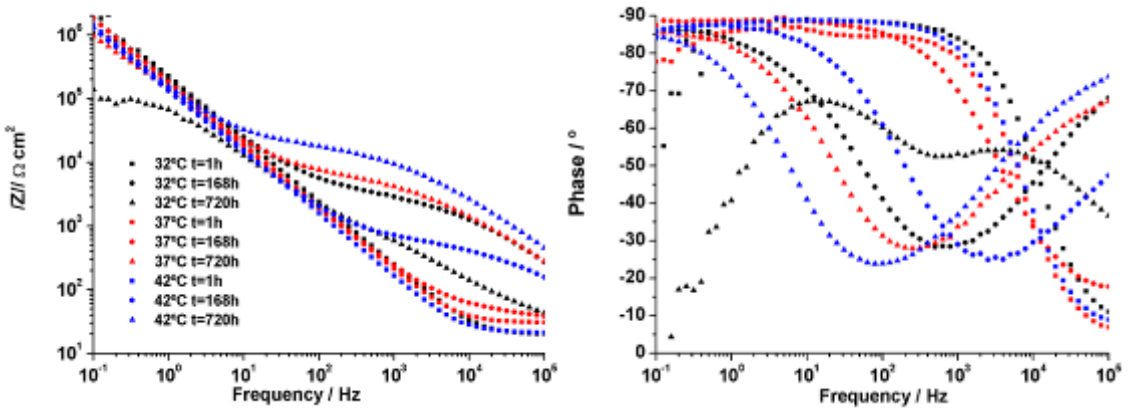

Figure 63. Bode plots of clad AA2024 specimens anodised at different temperatures after different immersion times in 0.5 M NaCl solution.

The anodised samples of the clad AA2024 showed a capacitive behaviour after 1 h of immersion for the three samples anodised at different temperatures. In contrast to the observed for the AA2024 alloy, the modulus of the impedance in the low frequency range does not diminish with immersion time, moreover, |Z| increases with immersion time in the high frequency range and a second time constant is evident for prolonged exposure to the 0.5 M NaCl solution. These phenomena are characteristic of a self-sealing process.

The fitting of these EIS spectra are displayed in table 16.

Table 16. Results after fitting EIS data for the clad AA2024 specimens anodised at different temperatures after different immersion times in 0.5 M NaCl solution. The values in brackets indicate the dispersion factor of the constant phase element.

C_b (µS cm^{-2})	1 h	168 h	720 h	R_b (kΩ cm^2)	1 h	168 h	720 h
32 °C	0.67 (1.00)	0.92 (0.91)	2.44 (0.82)	**32 °C**	>1000	710	115
37 °C	0.82 (1.00)	0.87 (0.99)	1.42 (0.88)	**37 °C**	>1000	>1000	>1000
42 °C	1.02 (1.00)	1.28 (0.95)	1.23 (0.88)	**42 °C**	>1000	>1000	>1000
C_p (µS cm^{-2})	1 h	168 h	720 h	R_p (Ω cm^2)	1 h	168 h	720 h
32 °C	-	0.30 (0.70)	1.28 (0.82)	**32 °C**	-	3803	437
37 °C	-	2.24e3 (0.21)	0.26 (0.71)	**37 °C**	-	236	19080
42 °C	-	0.26 (0.71)	0.26 (0.71)	**42 °C**	-	775	19080

C_b values after 1 h of immersion are lower for the sample anodised at 32 °C. There is a slight increase with immersion time that is more evident for the sample anodised at 32 °C.

The R_b values are in the same range after 1 h of immersion for the samples anodised at 37 °C and 42 °C. The R_b increases with immersion time as a consequence of the self-sealing process, in some cases to an extent that makes difficult its determination. Nevertheless, R_b after 1 h for the sample anodised at 32 °C is one order of magnitude lower than the other two samples, and this parameter decrease with longer exposure time.

The capacitance, C_p, and the resistance, R_p of the porous layer, are determined after 168 h and longer immersion time. As the plug of the pores is becoming more effective, C_p will decrease with immersion time and R_p will increase. These two facts are observed for the samples anodised at 37 °C and 42 °C.

The inverse evolution of the parameters for the sample at 32 °C after 720 h leads to think that two simultaneous processes, a corrosion process and a self-sealing process, are taking place, being the first one more important.

AA6061

Fig. 64 shows the evolution with immersion time in NaCl of the EIS spectra of the AA6061 samples anodised at different temperatures.

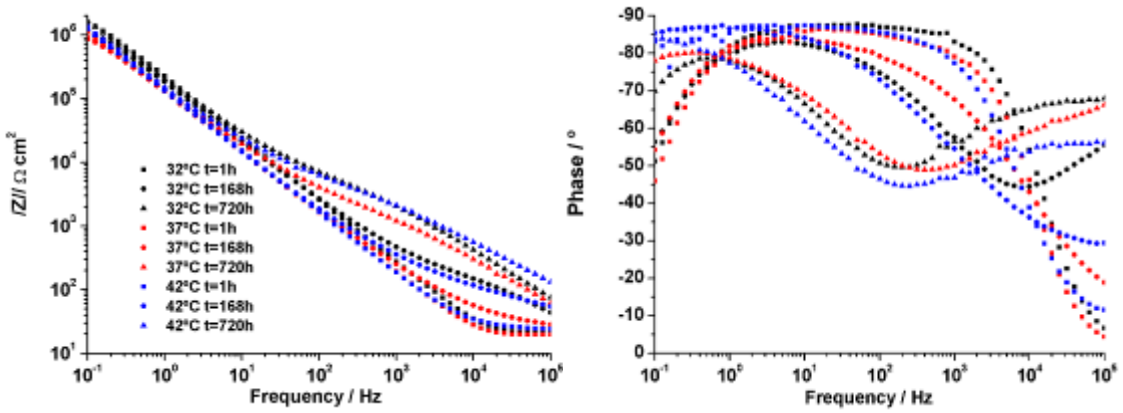

Figure 64. Bode plots of AA6061 specimens anodised at different temperatures after different immersion times in 0.5 M NaCl solution.

The EIS spectra after 1 h of immersion is similar for the samples anodised at the three different temperatures. The evolution of the EIS spectra is similar but slower to those performed by the clad AA2024 samples.

Table 17 summarises the fitting of the EIS spectra of the AA6061 samples anodised at different temperatures.

Table 17. Results after fitting EIS data for the AA6061 specimens anodised at different temperatures after different immersion times in 0.5 M NaCl solution. The values in brackets indicate the dispersion factor of the constant phase element.

C_b (μS cm^{-2})	1 h	168 h	720 h	R_b (kΩ cm^2)	1 h	168 h	720 h
32 °C	0.63 (1.00)	1.04 (0.91)	0.95 (0.87)	**32 °C**	2301	>1000	>1000
37 °C	0.99 (1.00)	1.35 (0.95)	1.46 (0.86)	**37 °C**	1135	>1000	>1000
42 °C	0.99 (1.00)	1.25 (0.98)	1.29 (0.86)	**42 °C**	5966	>1000	>1000
C_p (μS cm^{-2})	**1 h**	**168 h**	**720 h**	R_p (Ω cm^2)	**1 h**	**168 h**	**720 h**
32 °C	-	1.46 (0.76)	0.69 (0.76)	**32 °C**	-	219	5183
37 °C	-	140 (0.50)	1.40 (0.72)	**37 °C**	-	615	2268
42 °C	-	148 (0.38)	2.01 (0.62)	**42 °C**	-	4970	7318

After 1 h of immersion in the test solution, C_b is lower for the sample anodised at 32 °C, this can be attributed to a slower penetration of the solution through the finer pores generated at reduced temperature. In any case, this parameter increases slowly with immersion time for the three samples.

R_b is in the same range for the three samples after 1 h of immersion and increases with immersion time in the 0.5 M NaCl solution. The higher value and the quicker increase are for the sample anodised at 42 °C.

C_p is much lower for the sample anodised at 32 °C, this can be due to the generation of smaller pores during the anodising process at reduced temperature, therefore easier to self-seal.

R_p values grow for the three specimens as the self sealing process develops. Such values are higher for the sample anodised at 42 °C.

AA7475

The EIS spectra of the AA7475 specimens anodised at different temperatures and their evolution with immersion time in 0.5M NaCl solutions are shown in fig. 65.

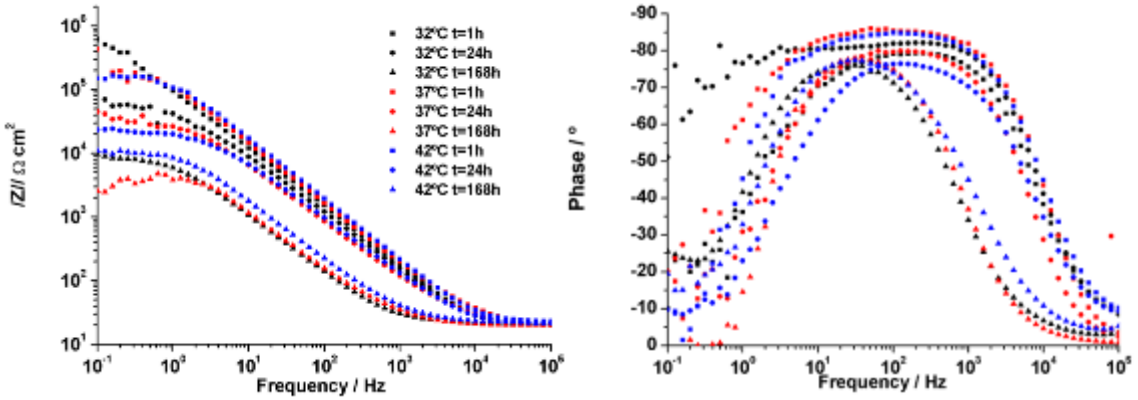

Figure 65. Bode plots of AA7475 specimens anodised at different temperatures after different immersion times in 0.5 M NaCl solution.

The samples anodised at different temperatures present low resistance compare to the other studied alloys; the modulus of the impedance rapidly decreases and the capacitive arch narrows with immersion time for the three specimens.

Table 18 shows the parameters obtained by fitting of the AA7475 EIS spectra.

Table 18. Results after fitting EIS data for the AA7475 specimens anodised at different temperatures after different immersion times in 0.5 M NaCl solution. The values in brackets indicate the dispersion factor of the constant phase element.

C_b ($\mu S\ cm^{-2}$)	1 h	24 h	168 h	R_b ($k\Omega\ cm^2$)	1 h	24 h	168 h
32 °C	1.17 (1.00)	2.79 (0.89)	23.4 (0.89)	**32 °C**	868	58.9	9.7
37 °C	1.09 (1.00)	2.97 (0.94)	14.7 (0.96)	**37 °C**	284	34.9	4.0
42 °C	0.81 (1.00)	3.63 (0.88)	13.5 (0.90)	**42 °C**	158	23.0	11.4

C_b rapidly increases with immersion time. The C_b values obtained after 168 h of immersion are higher than those obtained for the bare alloy (13.3 $\mu S\ cm^{-2}$). Therefore the barrier layer is completely degraded.

The resistance after 1 h of immersion is the lower of the studied alloys. Comparing the three samples, R_b is higher for the one anodised at 32 °C. Nevertheless, R_b rapidly decreases after 24 h of immersion. Pits were observed after 24-48 h of immersion and evolved to general corrosion. R_b values after 168 h are lower than those obtained for the bare AA7475 alloy (5.9 $k\Omega\ cm^2$).

In the AA7475, the cracks observed by means of SEM after the pickling process due to the preferential attack in the grain boundaries, could be a preferential site for the corrosion initiation since the anodising process covers the crack with alumina but the topology of the crack is maintained.

From the previous EIS measures, it can be concluded that the variation in ± 5 °C in the anodising temperature leads to a change in the thickness of the anodic film, the behaviour against corrosion studied by EIS showed that generally, the alloys anodised at 32 °C present lower corrosion resistance, whereas anodising at 42 °C does not majorly improve the corrosion resistance.

The highly organised films grown on clad AA2024 and AA6061 will perform a self sealing process, whereas the high copper content alloys present corrosion processes with immersion time.

5.1.7. Anodising time effect on the corrosion resistance of the anodic films

5.1.7.1. Film thickness

The film thicknesses of the anodic films generated at different anodising times on the four studied alloys were measured by means of eddy currents and are plotted in fig. 66.

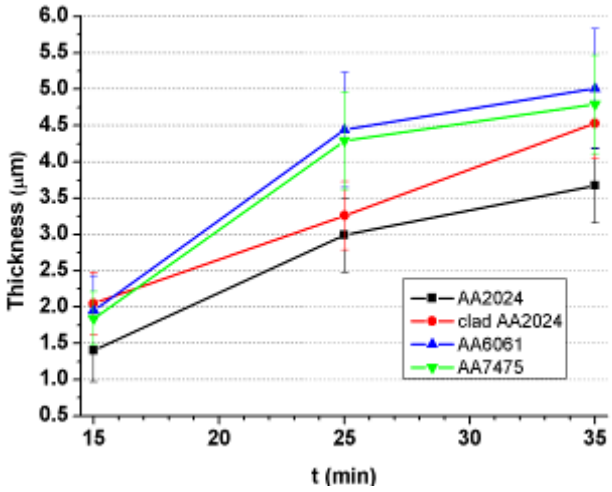

Figure 66. Film thickness of the anodic films grown at different times on the diverse alloys.

The anodic films generated after an anodising process of 15 min are below the desired thickness for use in the aerospace industry. The clad AA2024 present a growing dependence next to linearity in the studied range. The rest of the alloys show a relatively high film formation rate at short anodising times that decreases after prolonged anodising time.

The thickness of the films is not linearly dependant on the anodising time. The growth rate of the anodic film is faster at the early stages of the anodising process. As the anodic film is growing, the conductivity of the substrate is decreasing, so that, the effective driving force of the process is decreasing at the alloy/anodic film interface, where the new oxide material is formed. Once a critical film thickness has grown the balance between formation and solution of the anodic film is reached, therefore there will not be net growing of the anodic film [22].

5.1.7.2. Electrochemical impedance spectroscopy

AA2024

Fig. 67 shows the EIS spectra of the AA2024 samples anodised for different plateau times, acquired after different immersion times in 0.5 M NaCl solution.

The EIS spectra of the samples anodised for different times show similar behaviour after 1 h of immersion in 0.5 M NaCl solution. However, the degradation of the samples after 24 h of immersion is evidenced by the decrease of the modulus of the impedance and the phase dependence with the frequency in the low frequency range. Further |Z| decrease and

narrowing of the capacitive arch is observed after 168 h of immersion, especially in the sample anodised for the shorter time of 10 min.

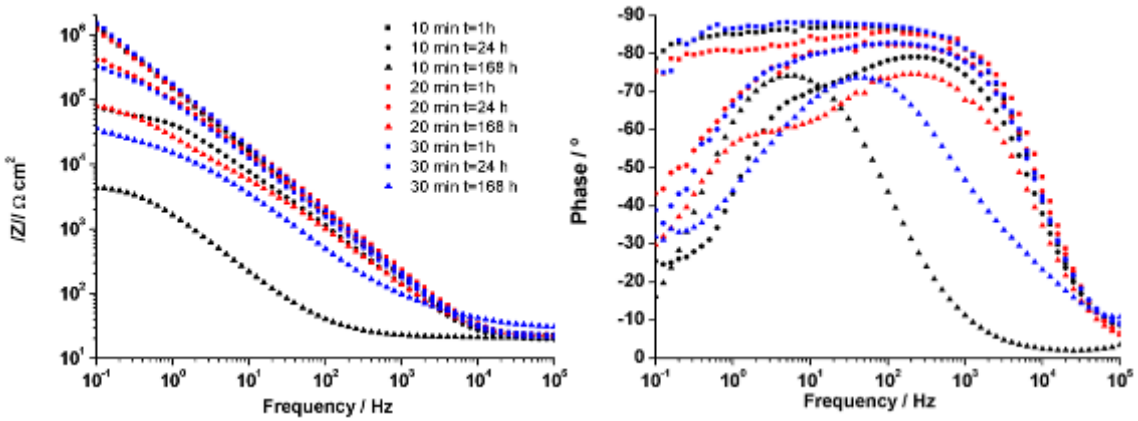

Figure 67. Bode plots of AA2024 specimens anodised for different plateau times after different immersion times in 0.5 M NaCl solution.

The fitted parameters for the previous EIS spectra are shown in table 19.

Table 19. Results after fitting EIS data for the AA2024 specimens anodised for different plateau times after different immersion times in 0.5 M NaCl solution. The values in brackets indicate the dispersion factor of the constant phase element.

C_b (μS cm^{-2})	10 min	20 min	30 min	R_b (kΩ cm^2)	10 min	20 min	30 min
1 h	0.94 (1.00)	0.78 (1.00)	0.84 (1.00)	**1 h**	5240	3103	1180
24 h	3.42 (0.88)	1.67 (0.91)	1.90 (0.91)	**24 h**	73.3	528	382
168 h	110 (0.89)	6.03 (0.82)	12.2 (0.79)	**168 h**	4.92	89.9	38.0

The capacitance of the barrier layer, C_b, is similar for the three samples after 1 h of immersion in 0.5 M NaCl, however, after 24 h of immersion, the degradation of the sample anodised for 10 min is noticeable, as C_b increased 4 times; whereas the samples anodised for 20 and 30 minutes only doubled C_b values. After 168 h, there is a high increase of C_b for the 10 min anodised sample. The best behaviour against corrosion is observed for the sample anodised for 20 min.

The resistance of the barrier layer was initially higher for the sample anodised for 10 min, although the three samples were in the same order of magnitude. After 24 h the R_b highly decreased for the sample anodised for the shorter time, being this decrease lower for the other two samples anodised for longer time. After 168 h of immersion in the test solution, the sample anodised for 10 min present R_b values close to the untreated alloy, whereas R_b values for the samples anodised for 20 and 30 minutes decreased in a lesser extent.

Clad AA2024

Figure 68 shows the EIS spectra of the clad AA2024 anodised for different plateau times.

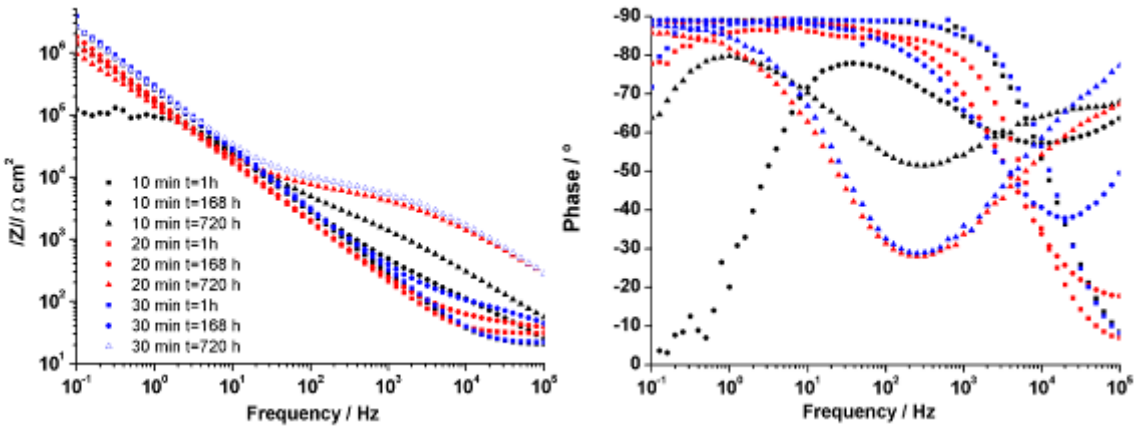

Figure 68. Bode plots of clad AA2024 specimens anodised for different plateau times after different immersion times in 0.5 M NaCl solution.

The self sealing process of the clad AA2024 samples anodised for different times during the immersion in the 0.5 M NaCl solution is noticeable after 168 h in the high frequency range. The modulus of the impedance for the sample anodised for 10 min decay in the low frequency range after 168 h and then increases.

The EIS spectra acquired after 1 h of immersion in the test solution were fitted with the EC3 described in section 4.3. for the anodised alloys, whereas the spectra recorded for longer immersion time were fitted with the equivalent circuit for anodised and sealed samples.

Table 20. Results after fitting EIS data for the clad AA2024 specimens anodised for different plateau times after different immersion times in 0.5 M NaCl solution. The values in brackets indicate the dispersion factor of the constant phase element.

C_b ($\mu S\ cm^{-2}$)	1 h	168 h	720 h	R_b ($k\Omega\ cm^2$)	1 h	168 h	720 h
10 min	0.57 (1.00)	0.84 (0.93)	1.06 (0.79)	**10 min**	76400	112	4750
20 min	0.82 (1.00)	0.87 (0.99)	1.42 (0.88)	**20 min**	22526	>1000	>1000
30 min	0.51 (1.00)	0.63 (0.97)	0.64 (0.94)	**30 min**	12800	>1000	>1000
C_p ($\mu S\ cm^{-2}$)	1 h	168 h	720 h	R_p ($\Omega\ cm^2$)	1 h	168 h	720 h
10 min	-	7.05 (0.68)	1.57(0.71)	**10 min**	-	258	3576
20 min	-	2.24e3(0.21)	0.26(0.71)	**20 min**	-	236	6536
30 min	-	4.76 (0.68)	0.1 (0.71)	**30 min**	-	133	8599

The capacitance of the barrier, C_b, showed modest change during the immersion in the test solution for the three samples, however, the resistance of the barrier layer, R_b, evidence different evolution.

The R_b decay of the clad AA2024 sample anodised for 10 min could be due to local disruption of the barrier layer after 168 h of immersion, however, the increase of R_b after 720 h could

indicate that the sample was self healed after longer exposure to the test solution. The samples anodised for 20 and 30 min present an increase in R_b due to the self-sealing process.

The capacitance of the porous layer, C_p, can only be determined after 168 h of immersion; at this point, the sealing process seems slower for the sample anodised for 20 min. As the self sealing process develops, C_p values decrease as observed after 720 h of immersion in the test solution.

The resistance of the electrolyte to penetrate in the pores of the porous layer, R_p, increases during the plugging of the pores for the three samples.

AA6061

Fig. 69 displays the EIS spectra of the AA6061 samples anodised for different plateau times.

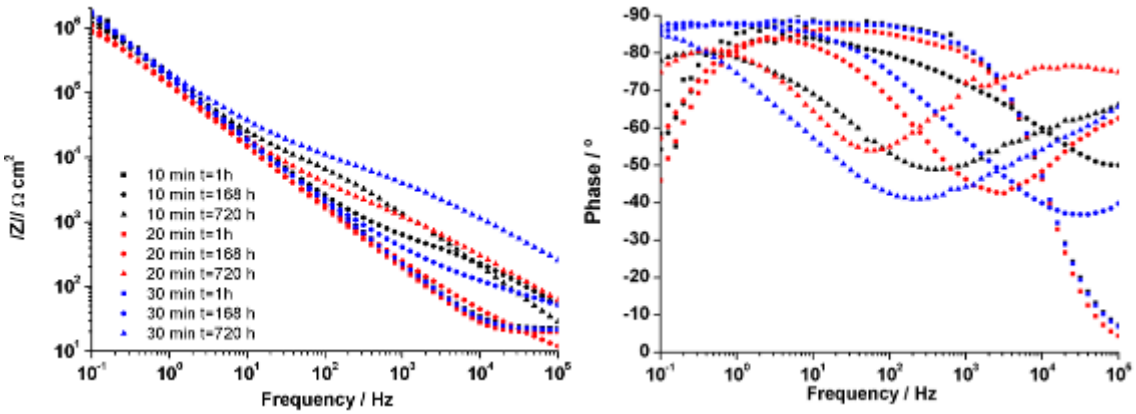

Figure 69. Bode plots of AA6061specimens anodised for different plateau times after different immersion times in 0.5 M NaCl solution.

The increase of the modulus of the impedance in the high frequency range with the exposure time to the test solution is obvious for the three samples. The EIS spectra after 1 h of immersion were fitted with the EC3 described in 4.3. for the anodised samples, whereas the rest of the data were fitted with the model proposed for anodised and sealed samples.

Table 21. Results after fitting EIS data for the AA6061 specimens anodised for different plateau times after different immersion times in 0.5 M NaCl solution. The values in brackets indicate the dispersion factor of the constant phase element.

C_b (μS cm^{-2})	1 h	168 h	720 h	R_b (kΩ cm^2)	1 h	168 h	720 h
10 min	0.73 (1.00)	1.09 (0.92)	1.08 (0.89)	**10 min**	2700	2776	31000
20 min	0.99 (1.00)	1.35 (0.95)	1.46 (0.86)	**20 min**	1135	1708	>1000
30 min	0.77 (1.00)	0.97 (0.98)	0.96 (0.86)	**30 min**	12800	>1000	>1000
C_p (μS cm^{-2})	**1 h**	**168 h**	**720 h**	R_p (Ω cm^2)	**1 h**	**168 h**	**720 h**
10 min	-	0.93 (0.76)	0.48 (0.87)	**10 min**	-	524	6152
20 min	-	140 (0.50)	1.40 (0.72)	**20 min**	-	615	2268
30 min	-	132 (0.38)	0.92 (0.63)	**30 min**	-	3500	12491

The evolution of the capacitance of the barrier layer, C_b, reveals little variation in the barrier layer during the test time for the three anodised AA6061 samples. However, the resistance of the barrier layer, R_b, increases with immersion time. The variation of these two parameters could indicate healing of the flawed areas in the barrier layer.

AA7475

The EIS spectra recorded in 0.5 M NaCl solution for the AA7475 specimens anodised for different times are shown in fig. 70.

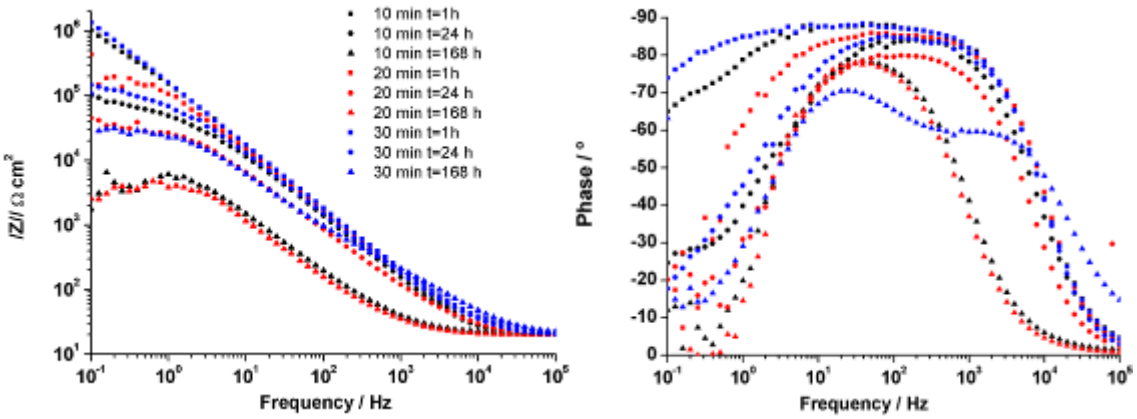

Figure 70. Bode plots of AA7475 specimens anodised for different plateau times after different immersion times in 0.5 M NaCl solution.

The decrease of the modulus of the impedance with immersion time in the high frequency range evidences corrosion processes. The EIS spectra were fitted with the equivalent circuit for anodised samples; the results are displayed in table 22.

Table 22. Results after fitting EIS data for the AA7475 specimens anodised for different plateau times after different immersion times in 0.5 M NaCl solution. The values in brackets indicate the dispersion factor of the constant phase element.

C_b ($\mu S\ cm^{-2}$)	10 min	20 min	30 min	R_b ($k\Omega\ cm^2$)	10 min	20 min	30 min
1 h	0.92 (1.00)	1.09 (1.00)	0.90 (1.00)	**1 h**	170	284	3950
24 h	1.88 (0.94)	2.97 (0.94)	1.47 (0.97)	**24 h**	8.1	34.9	122
168 h	12.5 (0.95)	14.7 (0.96)	8.11 (0.75)	**168 h**	0.53	4.0	7.1

The capacitance of the barrier layer, C_b, increases rapidly after 24 h for the three samples and decreases to values similar to those obtained for the bare alloy after 168 h for the samples anodised for 10 and 20 min.

The resistance of the barrier layer after 1 h of immersion is very low for the three samples compared to the rest of the alloys, besides, such R_b rapidly decrease after 24 h of immersion and reach values in the range of the bare alloy after 168 h.

The AA7475 alloy present low corrosion resistance in a chloride environment, ineffectual the anodising time.

From the previous observations, it can be concluded that anodising for short times (10 min) leads to anodic films with lower corrosion resistance than the specimens for longer time. In the case of anodising for 20 and 30 min, the corrosion resistance is acceptable and comparable for most of the alloys. However, from the industrial viewpoint, anodising for 20 min presents economical advantages compared to anodising for 30 min.

5.1.8. Effect of the permanence in the bath without current application after the anodising cycle

The effect of the permanence in the bath without current application after the anodising cycle is a very important parameter in the anodising industry, an excessive permanence of the anodised specimens in the bath or a defective rinsing operation can lead to degradation of the anodic film. Such degradation cannot usually be detected by quick quality test in the industry (visual inspection, conductivity of the film, measuring of the thickness by eddy currents...) and can arise once the complete coating system has been applied to the pieces (e.g. a painted part of the fuselage), causing big economical losses. In this section, the effect of the permanence in the bath without current application after the TSA anodising cycle will be evaluated for the AA2024, the AA6061 and the AA7475 alloys.

5.1.8.1. Anodic film thickness

The variation of the anodic oxide thickness with time of immersion in the anodising electrolyte without application of current is presented in fig. 71, showing a decrease of film thickness with immersion time for all alloys.

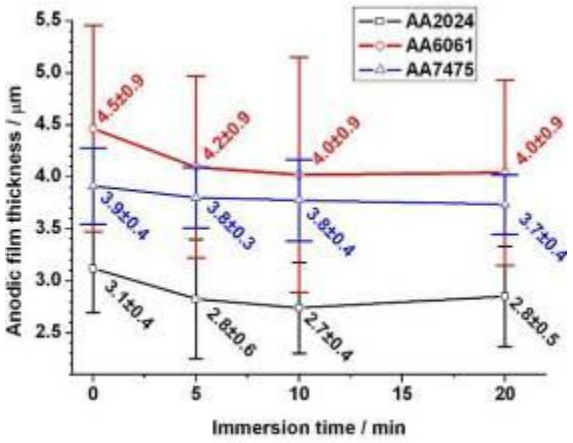

Figure 71. Variation of the anodic film thickness of the variously alloys with the immersion time in the TSA anodising bath measured by eddy currents.

In the case of the AA2024 specimens, the initial film thickness of 3.1 ± 0.4 µm decreased to 2.8 ± 0.6 µm after 5 min of immersion in the anodising electrolyte with little further change with increasing immersion time. The AA6061 specimens displayed an initial anodic film thickness of 4.5 ± 0.9 µm that decreased to 4.2 ± 0.9 µm after 5 min and to 4.0 ± 0.9 after 10 and 20 min. The AA7475 specimens gave an initial anodic film thickness of 3.9 ± 0.4 µm and no further degradation with time of immersion. Generally, the data reveal modest change in the total anodic film thickness with immersion time. However, precise measurements are difficult due to the variation of the initial porous anodic film thickness over the macroscopic surface of the aerospace alloys.

5.1.8.2. Morphological changes during the immersion in the anodising electrolyte after the anodising program

Scanning electron microscopy

The scanning electron micrographs in Fig. 72 display the surface morphology of the anodised specimens following immersion in the TSA bath for 0, 5, 10 and 20 min.

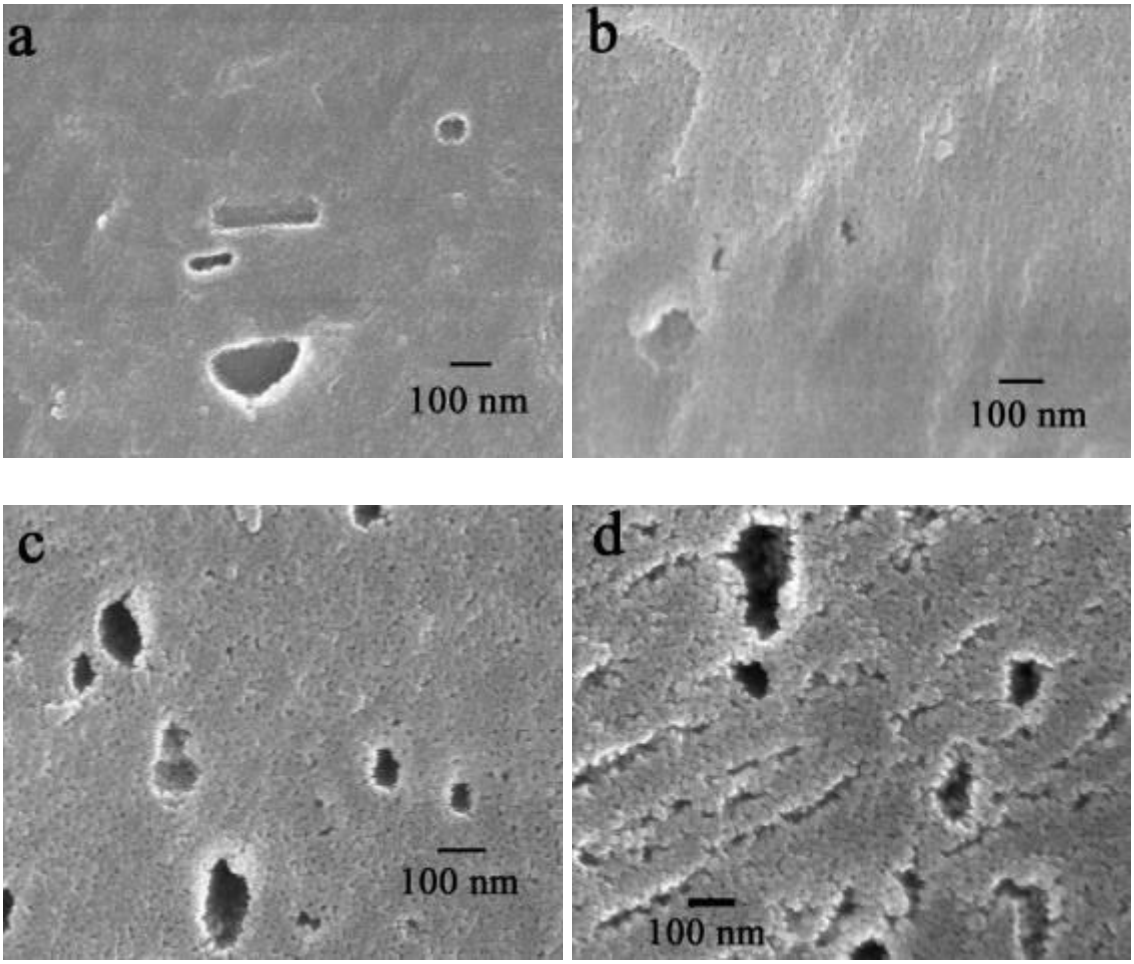

Figure 72. Scanning electron microscopy images of the surface of the anodic layers grown on AA2024 and withdrawn from the TSA anodising bath (a) immediately after (b) 5 min after, (c) 10 min after and (d) 20 min after the end of the anodising program.

On the specimen removed immediately from the TSA bath after anodising (fig. 72a) a relatively compact porous oxide morphology is evident over the macroscopic surface of the AA2024 alloy, with local regions of altered film morphology associated with the presence of second phase material. Evidence of pores widening is revealed after immersion for 5 minutes (fig. 72b); however after 10 minutes of immersion (fig. 72c) preferential dissolution of the oxide generated above second phase material is revealed. After immersion for 20 min, pore widening produces a sponge-like, open porous oxide morphology, displaying locations where dissolution has resulted in exposure of the alloy supporting relatively thin oxide films to the electrolyte (fig. 72d).

Transmission electron microscopy

The effect of immersion time in the anodising electrolyte on the morphology of the anodic films generated on the AA2024 alloy is shown in the ultramicrotomed sections of Fig.73.

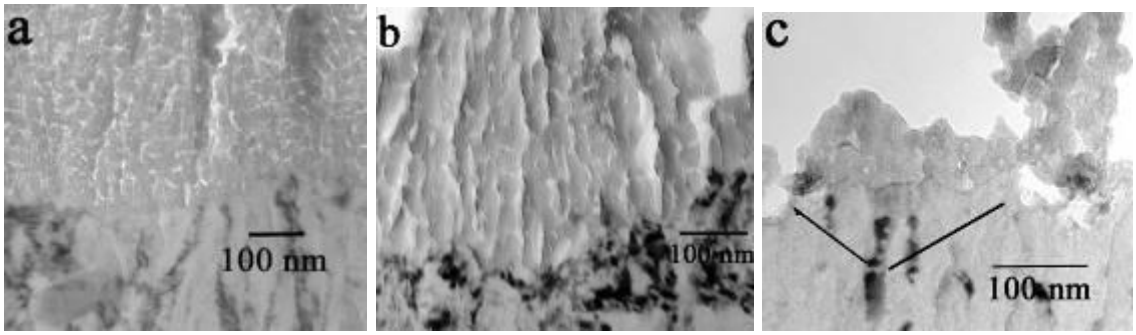

Figure 73. Transmission electron microscopy images of the alloy/film interface of the anodic layers grown on AA2024 and withdrawn from the TSA anodising bath (a) immediately after (b) 5 min after and (c) 20 min after the end of the anodising program.

Fig.73a displays the porous anodic oxide film on the AA2024 after immediate removal from the anodising electrolyte. In comparison, after immersion for 5 min in the TSA bath without application of current (Fig. 73b), the widening of the base of the pores indicates that chemical dissolution of the pore walls and the barrier layer has occurred. The barrier layer is no longer distinguishable after immersion for 20 min in the anodising electrolyte (Fig. 73c). This anodic film is more fragile than the previous with the porous skeleton collapsing after sufficient undermining by chemical dissolution and it is generally disrupted during mechanical sectioning with the diamond knife for ultramicrotomy.

The electronoptical techniques clearly indicated degradation of the porous layer through the immersion of the AA2024 specimens in the anodising bath.

5.1.8.3. Influence of the immersion time on the corrosion protection behaviour.

Electrochemical impedance spectroscopy

The effect of immersion time in the anodising electrolyte was examined by EIS, which was undertaken in 0.5 M Na_2SO_4 or 0.5 M NaCl electrolyte, in order to probe the specific contributions to the overall behaviour from generalized chemical dissolution of the porous

anodic film and barrier layer, and from local defects. Using this approach, it is possible to separate the contributions to the EIS spectrum due to the barrier layer (independent on the electrolyte employed for impedance spectroscopy) and the defects where corrosion initiates (dependent on the electrolyte employed for impedance spectroscopy).

EIS spectra of TSA anodised (unsealed) specimens recorded in 0.5 M Na_2SO_4 solution, are displayed in Fig.74.

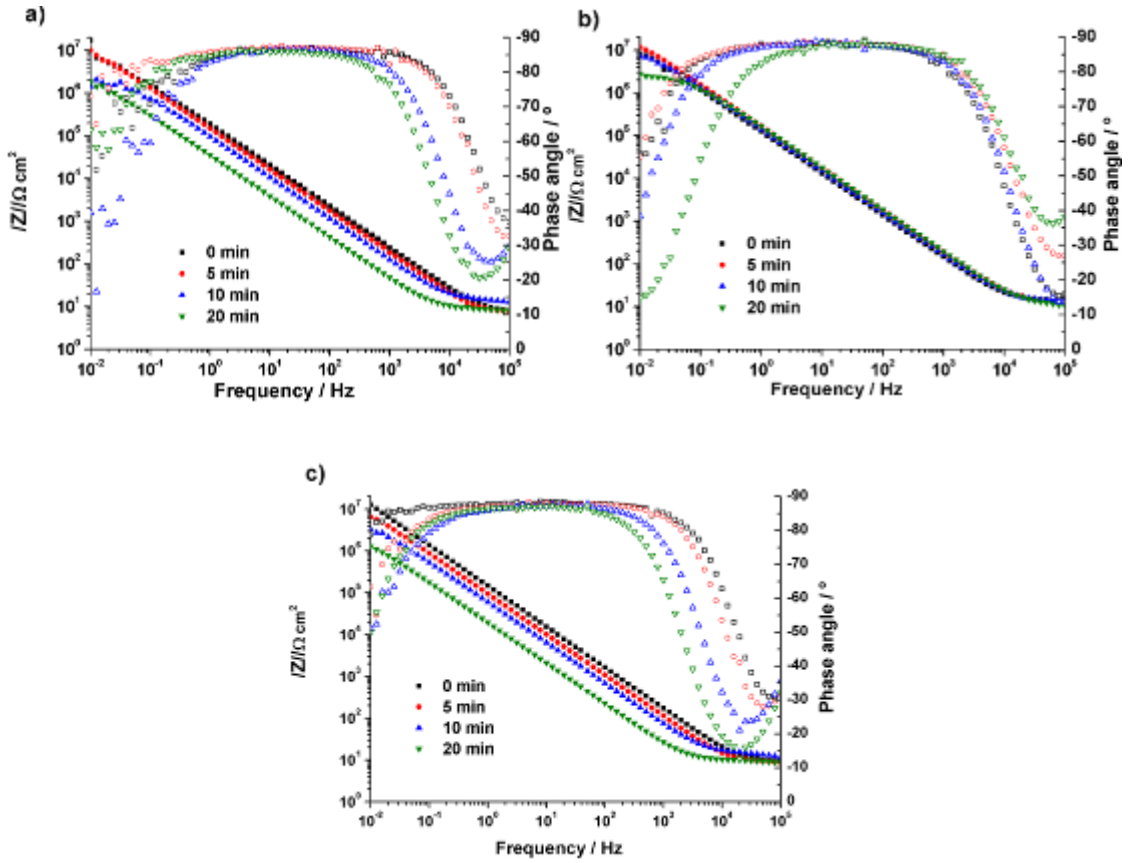

Figure 74. EIS spectra recorded in 0.5 M Na_2SO_4 solution of (a) AA2024 (b) AA6061 and (c) AA7475 anodised samples withdrew from the TSA anodising bath after different times.

The effect of time of immersion in the anodising electrolyte prior to rinsing of the anodised alloys is evidenced by the decrease of the impedance modulus ($|Z|$) and a narrowing of the phase angle plot, particularly for the AA2024 and AA7475 alloys.

The nearly neutral 0.5 M Na_2SO_4 test solution is not chemically reactive to the anodised substrate; therefore, no significant corrosion is expected to occur during the 1 h immersion period prior to EIS measurement. This is qualitatively confirmed by scrutiny of the low frequency region of the $|Z|$ response, where no plateau region is observed.

EIS spectra of the TSA anodised AA2024, AA6061 and AA7475 specimens recorded in 0.5 M NaCl solution, where localized corrosion is expected to initiate at defects on the filmed alloy surface, are shown in Fig.75. Corrosion is evident from the low frequency region of the impedance spectra which, unlike the spectra recorded in Na_2SO_4 solution, reveal a well-defined plateau for specimens that had been immersed for more than 5 min in the anodising electrolyte.

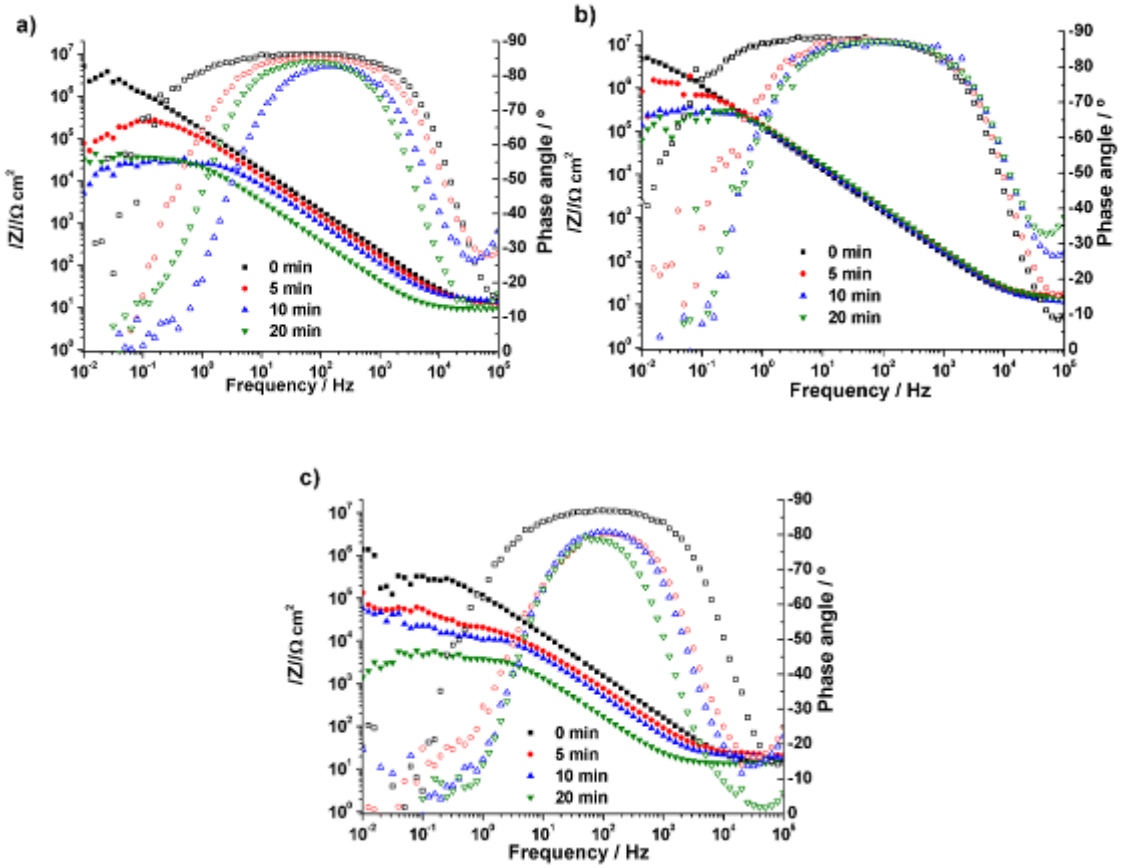

Figure 75. EIS spectra recorded in 0.5 M NaCl solution of (a) AA2024 (b) AA6061 and (c) AA7475 anodised samples withdrew from the TSA anodising bath after different times.

EIS spectra of TSA anodised AA2024 alloy recorded in NaCl are presented in Fig.75a. The specimen removed from the TSA electrolyte immediately after anodising shows a largely capacitive behaviour. The specimens immersed in the anodising electrolyte for 5, 10 and 20 min show a reduction in $|Z|$, and a narrowing of the phase angle plot, indicating a progressive degradation of the anodic film. Fig.75b shows EIS spectra of the TSA anodised AA6061 specimens. Degradation of these specimens with immersion time in the anodising electrolyte is less rapid than for the AA2024 alloy since, after 5 min immersion in the anodising electrolyte, only a slight decrease of $|Z|$ and a narrowing in the phase angle plot are evident. EIS spectra after 10 and 20 min in the anodising electrolyte show further reductions of $|Z|$. Fig.75c shows EIS spectra of the TSA anodised AA7475 alloy specimens, indicating reduced corrosion resistance. The impedance modulus for the specimen removed immediately from the anodising electrolyte revealed a low frequency plateau and a relatively narrow phase angle plot, indicating corrosion activity.

Following the fitting procedure described in section 4.3., a value of C_b, independent on the test electrolyte, and values of C_d and R_d, dependent on the test electrolyte and representative of the corrosion behaviour due to local defects in the anodic oxide, can be obtained.

The barrier layer thicknesses, calculated from the fitting for all anodised specimens, are presented in Fig.76.

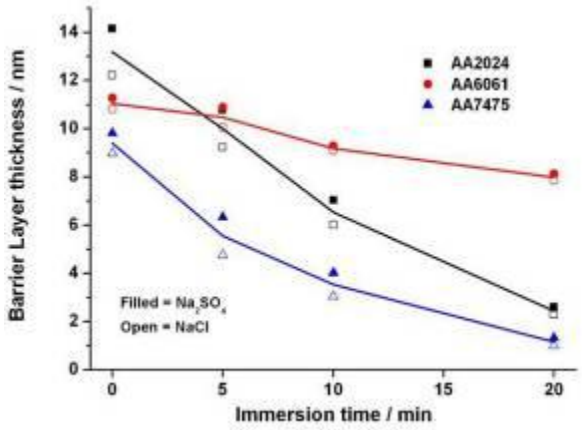

Figure 76. Calculated barrier layer thicknesses from the C_b values obtained from the fitting of the anodised specimens in the two test electrolytes. The lines are the mean value of the barrier layer thicknesses obtained in the two test electrolytes.

Generally, the thickness of the barrier layer decreased with immersion time in the electrolyte after termination of anodising. Thinning of the barrier layer for the AA6061 alloy was only 2 nm after immersion for 20 min, while the thickness of the barrier layer was reduced by approximately 10 nm after immersion for 20 min in the case of the AA2024 and AA7075 alloys.

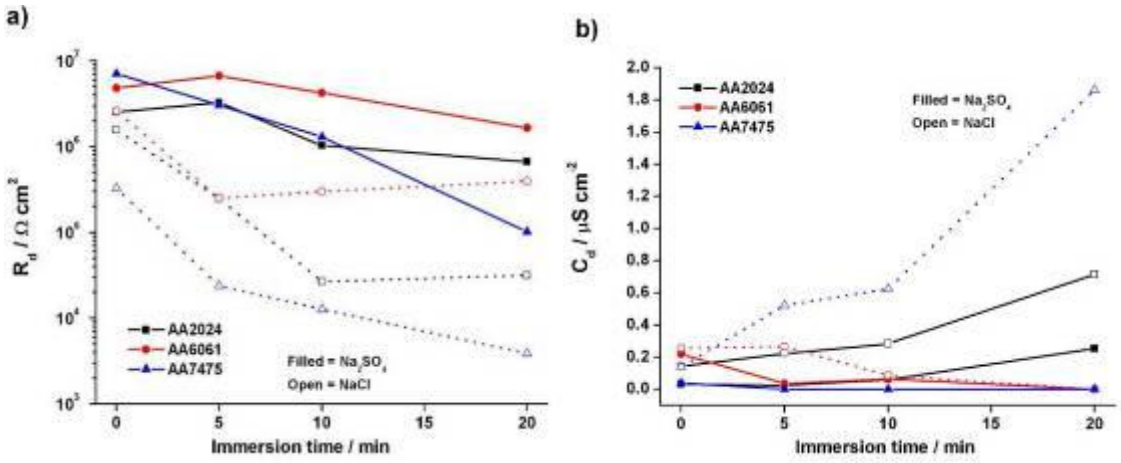

Figure 77. Values of (a) R_d and (b) C_d obtained from the fitting of the anodised specimens in the two test electrolytes.

Concerning R_d, obtained for the specimens in NaCl (Fig. 77a), it decreased more markedly for the AA7075 alloy, followed by the AA2024 and AA6061 alloys. Correspondingly, the capacitance associated with the presence of defects in the anodic oxide (Fig. 77b) increased rapidly with immersion time for the AA7075 and AA2024 alloys, while it remained relatively low for AA6061 alloy. R_d and C_d, determined in the sodium sulphate solution, were significantly higher and lower respectively compared with the values obtained in the NaCl solution, as expected due to the absence of significant corrosion.

From the previous, it is generally concluded that the degradation of the anodic oxide film associated with prolonged immersion after the termination of anodising was more severe for the AA2024 and AA7075 alloys compared with the AA6061 alloy.

The TEM showed different morphologies and also different barrier layer thicknesses for the three alloys studied; the relatively high copper and zinc contents of the AA2024 andAA7475 are responsible for the altered film morphologies, and such morphologies may be more susceptible to dissolution during immersion in the anodising electrolyte. Further, TEM and SEM showed qualitative degradation of the barrier layer and the widening of the pore mouths of at the surface of the anodised AA2024 alloy with immersion time in the anodizing electrolyte. EIS analysis in two different electrolytes, namely 0.5 M Na2SO4 and 0.5M NaCl, allowed evaluation of the extent of the damage during the immersion in the anodising electrolyte, providing a tool for estimating the final anticorrosion performance. A significant thinning of the barrier layer and development of local defects in the oxide was observed after immersion of the AA2024 and AA7475 alloys in the anodising electrolyte. Conversely, degradation of the porous anodic oxide for the AA6061 alloy was more limited than for the previous alloys.

5.2. Postreatments

This chapter is divided in two parts, the first one deals with the classical sealing postreatments utilised in the aircraft industry; namely sealing in boiling deionised water (Hot water sealing or HWS) and sealing in a boiling dichromate salt solution (Dichromate sealing or DS). Here, the sealability of the new TSA anodic films by these common sealing processes is studied by means of morphological and chemical characterisation of the sealed films along with corrosion resistance tests.

The second part is the study on the use of alternative cold postreatments based on chemical conversion coatings instead of the hot aqueous sealing. It is assessed the possibility that the chemicals of the solutions employed for producing chemical conversion coating on aluminium could be incorporated and react into the pores of the TSA anodic film. This hypothesis was evaluated by the comparison of Cr (VI) and Cr (III) commercial conversion coatings.

5.2.1. Sealing

5.2.1.1. Morphological characterisation

Fig. 78 shows the morphology of the anodised specimens after the sealing process undertaken for 40 min in a boiling deionised water bath.

The macrostructure of the HWS-TSA anodised samples is not heavily modified by the sealing process compared to the anodised surfaces for all the alloys studied in chapter 5.1. For example, voids (fig. 78 a,e)and scratches (fig. 78c,e) are still evident and the cracks appeared during the pickling process can be still observed on the HWS-TSA anodised AA7475 (fig. 78g). However, the magnified images (fig. 78 b,d,f,h) show important changes on the surface of the specimens, showing the flake-like structure of the sealed samples [114]. These structures are due to the growth of a pseudobohemite film on the surface by hydration of the anodic film that plugs the mouth of the surface nanopores. The flake-like structure seems independent of the anodic film beneath it because the four displayed micromorphologies are very similar.

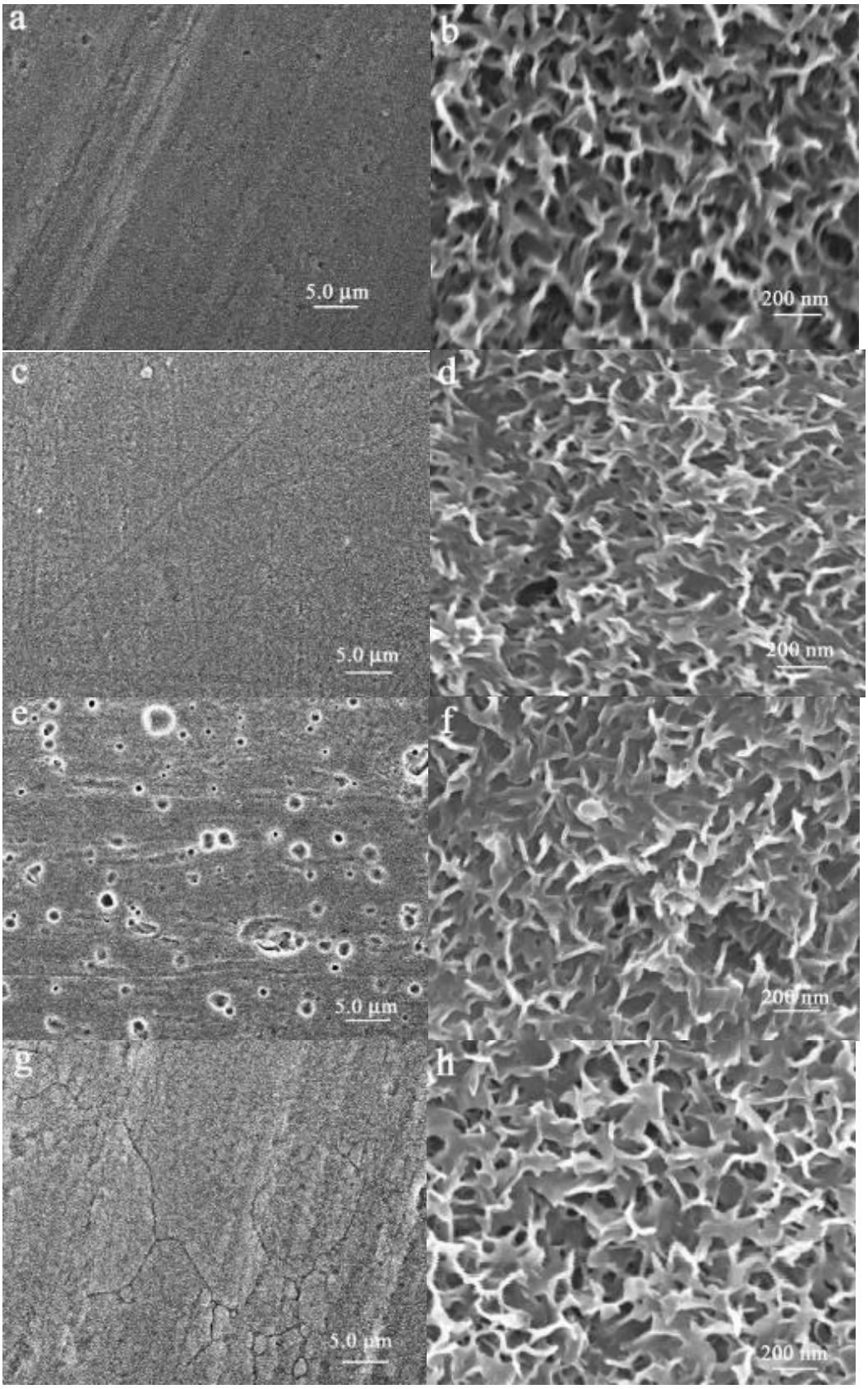

Figure 78. Morphology of the macrostructure (a,c,e,g) and the microstructure (b,d,f,h) on the surface of anodised specimens after the 40 min HWS process: (a,b) AA2024 (c,d) clad AA2024 (e,f) AA6061, (g,h) AA7475.

The morphology of the anodised specimens subsequently sealed in boiling dichromate solution for 20 min are shown in fig. 79.

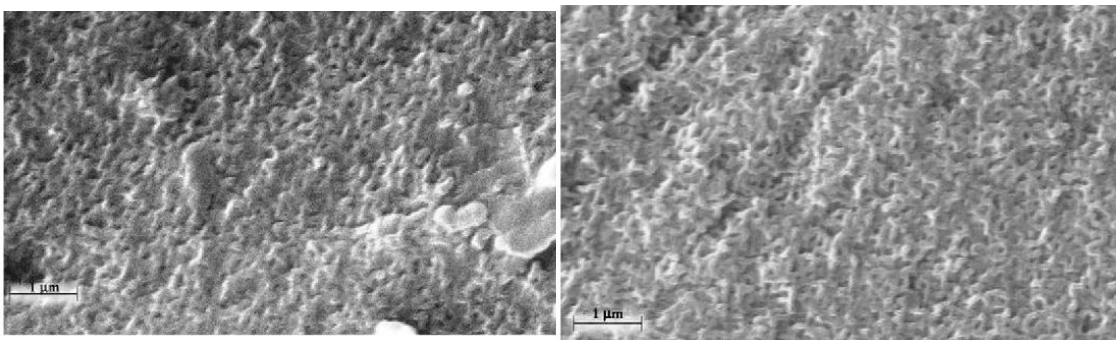

Figure 79. Morphology of the structure of the surface of anodised specimens after the 20 min DS process: (a) AA2024 and (b) clad AA204.

Observations of the surface of the DS specimens reveals flake-like morphology similar to that observed for the HWS specimens.

5.2.1.2. Chemical composition

Glow discharge optical emission spectroscopy depth profiles of the AA2024 specimens anodised and sealed in boiling water (HWS) or sealed in boiling water containing 30 mM potassium dichromate (DS) are shown in fig. 80.

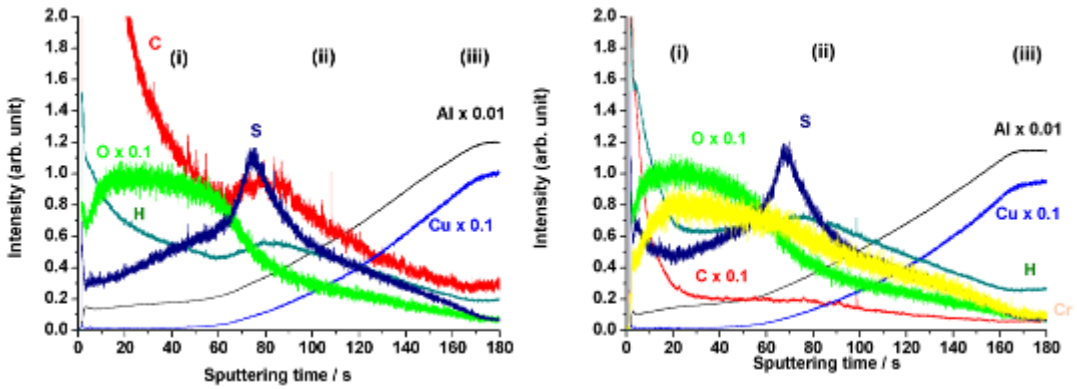

Figure 80. GDOES elemental depth profiles of an (a) anodised + HWS AA2024 specimen, (b) anodised + DS AA2024 specimen.

The depth profiles of the elements in the HWS (fig.80a) and the DS (fig.80b) samples show similar shapes; the depth profile of these sealed samples slightly change compared to the anodised samples described in section 5.1.

The aluminium profile displays three differenced regions; the first one (i) is a plateau attributed to the anodic film that appears for short sputtering times. Following this plateau, there is a slope (ii) caused by the roughness of the sample and finally another plateau (iii) of increased intensity indicates the sputtering has reached the alloy. The copper signal is closely related to the aluminium signal in the three regions.

The oxygen signal is relatively constant in the first plateau and then decreases to background levels. The signal is qualitatively more intense for the anodised and sealed samples than for the anodised samples due to the hydration of the porous layer.

The hydrogen signal is also qualitatively more intense in the case of the sealed specimens due to the hydration of the pores. This signal is also closely related to the carbon signal; this relation is due to the presence of carbohydrates in the anodic film.

Comparing with the composition shown in 5.1 for not sealed films the main difference is the lower signal of sulphur in the outermost part of the films. The decreased signal of the sealed specimens in the early sputtering times suggests a qualitative decrease of the sulphur content in the anodic film. This fact was previously reported by means of EDX [112] and is attributed to the desorption of sulphate species that were adsorbed on the surface of the pore walls during the anodising process.

Between the HWS and DS results it is evident the presence of chromium in the TSA anodic film hot sealed in the presence of dichromate. The chromium signal in the AA2024 DS sample presents similar depth profile than the oxygen signal and the plateau in the region (i) indicates a relatively uniform distribution of dichromate along the anodic film.

5.2.1.3. Influence of anodising temperature on the corrosion resistance after sealing

AA2024

Fig. 81 shows the EIS spectra of the AA2024 samples anodised at different temperatures and subsequently immersed in boiling water for 40 min (fig.81a,b) or immersed in 30 mM $K_2Cr_2O_7$ boiling solution for 20 min (fig.81c,d).

All the sealed-TSA anodised AA2024 samples show two clearly differenced time constants after 1 h of immersion. The one appearing in the low frequency range is attributable to the barrier layer and the one in the high frequency range reflects the properties of the porous layer. Evolution of the EIS spectra after 720 h immersion show a decrease in the modulus of the impedance in the high frequency range in the case of the HWS-sealed samples; whereas the DS-anodised samples show stable spectra along the experiment.

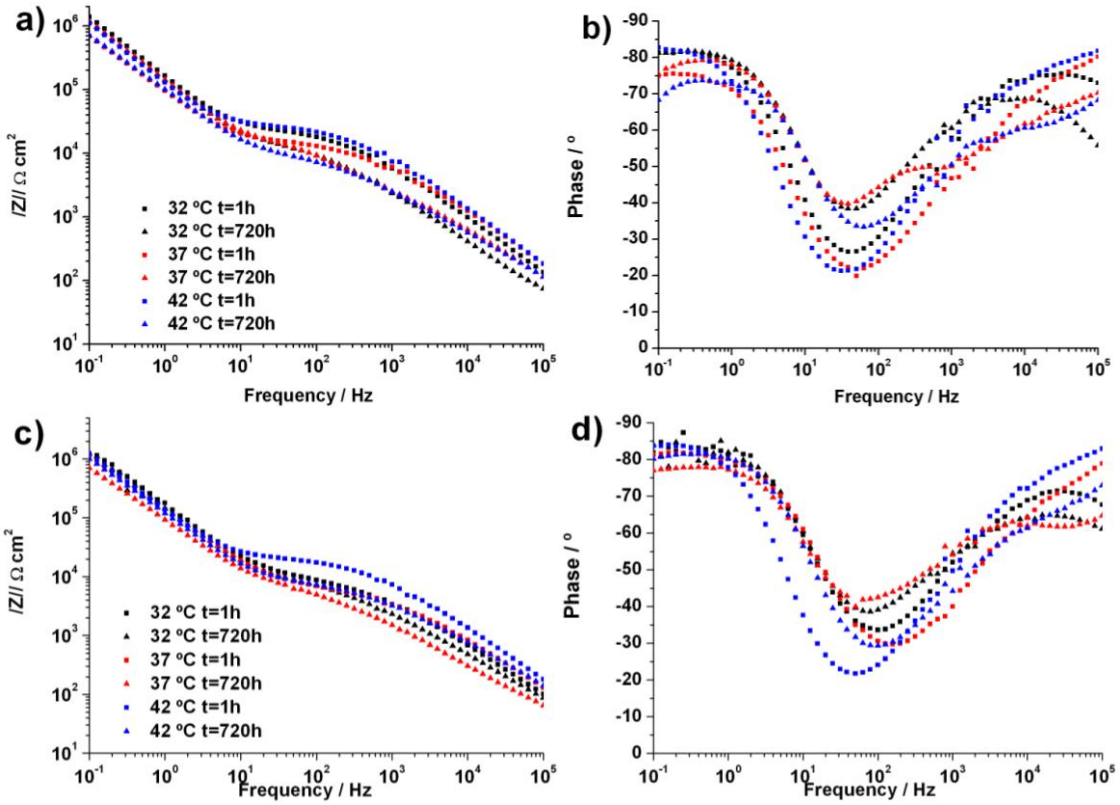

Figure 81. Bode plots after different immersion times in 0.5 M NaCl solution of AA2024 specimens anodised at different temperatures and subsequently (a,b) HWS or (c,d) DS.

The EC3 utilised for fitting the EIS data for all the sealed samples is described in section 4.3. Table 23 shows the results after the fitting of the EIS spectra in fig. 81.

Table 23. Results after fitting EIS data after different immersion times in 0.5 M NaCl solution for the AA2024 specimens anodised at different temperatures and subsequently HWS or DS. The values in brackets indicate the dispersion factor of the constant phase element.

Sealing	C_b (μS cm^{-2})	1 h	168 h	720 h	R_b (kΩ cm^2)	1 h	168 h	720 h
HWS	**32 °C**	1.11 (0.93)	1.23 (0.92)	1.31 (0.93)	**32 °C**	>1000	>1000	>1000
	37 °C	1.10 (0.93)	1.32 (0.91)	1.55 (0.93)	**37 °C**	>1000	>1000	>1000
	42 °C	1.43 (0.93)	1.59 (0.90)	2.15 (0.86)	**42 °C**	>1000	>1000	>1000
DS	**32 °C**	1.05 (0.94)	1.14 (0.94)	1.21 (0.95)	**32 °C**	>1000	>1000	>1000
	37 °C	1.09 (0.95)	1.17 (0.94)	1.18 (0.94)	**37 °C**	>1000	>1000	>1000
	42 °C	1.30 (0.94)	1.50 (0.92)	1.54 (0.92)	**42 °C**	>1000	>1000	>1000
Sealing	**C_p (nS cm^{-2})**	**1 h**	**168 h**	**720 h**	**R_p (kΩ cm^2)**	**1 h**	**168 h**	**720 h**
HWS	**32 °C**	91.0 (0.85)	211 (0.80)	432 (0.79)	**32 °C**	20.4	13.9	11.7
	37 °C	60.8 (0.84)	300 (0.75)	962 (0.70)	**37 °C**	31.9	17.2	14.0
	42 °C	69.7 (0.84)	352 (0.75)	687 (0.71)	**42 °C**	24.9	10.8	7.8
DS	**32 °C**	254 (0.79)	691 (0.72)	572 (0.75)	**32 °C**	9.2	25.3	18.8
	37 °C	51.8 (0.86)	260 (0.77)	249 (0.75)	**37 °C**	3.6	8.6	2.8
	42 °C	70.5 (0.84)	331 (0.77)	513 (0.75)	**42 °C**	8.1	10.0	7.4

The capacitance of the barrier layer, C_b, after 1 h of immersion seems to be independent from the anodising temperature for all the samples. The increase of C_b for the HWS-TSA anodised specimens after prolonged exposure to the test solution suggests a slow degradation of the barrier layer. In the case of DS-TSA anodised samples, C_b value is similar for the three samples and increases slightly with immersion time. However; this increment and therefore the degradation of the barrier layer seems to be lower for the DS-anodised samples than for the HWS-anodised samples.

The resistance of the barrier layer, R_b, cannot be accurately calculated in the studied frequency range because the phase spectra show a capacitive behaviour for all the samples at 0.1 Hz. In any case, R_b values are over 10^6 Ω cm^2 for al the samples after 720 h of immersion.

The capacitance of the porous layer, C_p, can depend on the anodic film thickness and on the sealing quality. This parameter is higher for the sample anodised at 32 °C and HWS because the anodic film generated at 32 °C is thinner. However this fact is not observed between the sample anodised at 37 °C and the thicker anodic films growth at 42 °C, as C_p values are similar. These results suggest that for a given anodic film thickness, C_p is thus mainly dependant on the sealing quality. On the other hand, the increase of C_p with immersion time denotes degradation of the outer anodic film for the three specimens. C_p of the DS-anodised samples shows the same trend previously observed for the HWS-anodised samples; that is to say C_p is higher for the thinner anodic film obtained at 32 °C and lower but relatively similar for the two other specimens. However, the increase of C_p is lower for the three DS-anodised samples after 720 h of immersion time compared to the HWS-anodised samples.

The resistance of the electrolyte to penetrate inside the pores can be a good estimation of the plugging process inside the pores after the sealing. That is to say, worse sealed pores would show a lowering of the pore resistance, R_p, with the immersion time in the test solution. The initial R_p values are higher for the sample anodised at 37 °C and HWS; nevertheless, this parameter decreases for the three HWS-anodised samples with immersion time, suggesting further penetration of the test solution in the pores. On the other hand, R_p is initially lower for the DS-anodised samples than for the HWS-anodised samples. That could be an indication that plugging of the pores is less effective during the shorter DS process because the immersion time was shorter (20 min instead of 40 min for HWS). However R_p decreased after 168 h but increased after 720 h of immersion showing a progressive resistance increment.

In general, the HWS and the DS processes seem to be of the same quality for the AA2024 anodised at 37 and 42 °C and slightly less effective for the samples anodised at 32 °C. However, the lower increase of C_b and C_p jointly with the variation of R_p for the DS samples denotes the inhibitory effects of the dichromate species absorbed in the pores during the sealing process.

In order to compare with a salt corrosion test and to essay a representative number of samples, six samples of all the conditions were prepared anodising three samples of each condition in two different anodising cycles and in different days. The salt spray test results are summarised in table 24.

Table 24. Salt spray test results for AA2024 samples anodised at different temperatures and sealed in different baths.

Anodising T (°C)	Sealing	96 h		336 h	
		Pits dm^{-2}	% pass	Pits dm^{-2}	% pass
32	HWS	1.0	100	8.6	0
	DS	0	100	1.1	100
37	HWS	0.4	100	5.7	0
	DS	0	100	0.6	100
42	HWS	1.0	100	5.4	17
	DS	0	100	0.8	100

All the sealed samples passed the test after 96 h; however the HWS samples presented some pits whereas no pits were visually observed for any of the DS samples. After 336 h, only the DS samples passed the test. Concerning the HWS samples, it seems to be confirmed the slightly worse behaviour of the anodising samples at the lower temperature with an increased number of pits.

Clad AA2024

The EIS results of clad AA2024 specimens anodised at different temperatures and subsequently sealed in HWS bath for 40 min or in a DS bath for 20 min are shown in fig. 82.

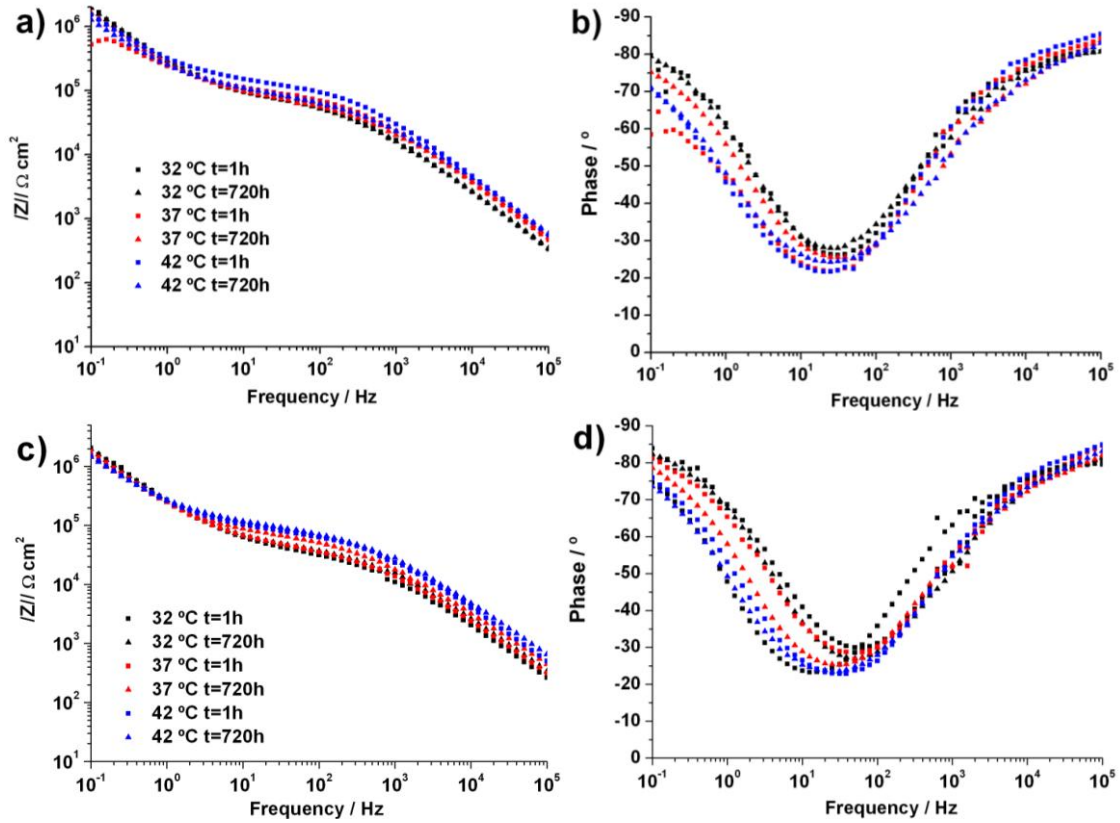

Figure 82. Bode plots after different immersion times in 0.5 M NaCl solution of clad AA2024 specimens anodised at different temperatures and subsequently (a,b) HWS or (c,d) DS.

Two time constants are observed for all the sealed specimens. In general, the modulus of the impedance decays with immersion time for all the HWS-anodised specimens, especially in the high frequency range. On the contrary, the EIS spectra for the DS-anodised specimens present moderate changes in both, the modulus of the impedance and the phase, after 720 h of testing.

The parameters obtained from fitting of the EIS spectra with the equivalent circuit for sealed samples are shown in table 25.

Table 25. Results after fitting EIS data after different immersion times in 0.5 M NaCl solution for the clad AA2024 specimens anodised at different temperatures and subsequently HWS or DS. The values in brackets indicate the dispersion factor of the constant phase element.

Sealing	C_b ($\mu S\ cm^{-2}$)	1 h	168 h	720 h	R_b ($k\Omega\ cm^2$)	1 h	168 h	720 h
HWS	**32 °C**	0.77 (0.83)	0.79 (0.82)	0.80 (0.83)	**32 °C**	>1000	>1000	>1000
	37 °C	0.77 (0.76)	0.98 (0.76)	0.96 (0.78)	**37 °C**	>1000	>1000	>1000
	42 °C	0.97 (0.74)	1.07 (0.74)	1.19 (0.73)	**42 °C**	>1000	>1000	>1000
DS	**32 °C**	0.77 (0.85)	0.95 (0.87)	0.80 (0.85)	**32 °C**	>1000	>1000	>1000
	37 °C	0.89 (0.82)	1.03 (0.83)	0.99 (0.81)	**37 °C**	>1000	>1000	>1000
	42 °C	1.03 (0.78)	1.14 (0.78)	1.06 (0.75)	**42 °C**	>1000	>1000	>1000
Sealing	**C_p ($nS\ cm^{-2}$)**	**1 h**	**168 h**	**720 h**	**R_p ($k\Omega\ cm^2$)**	**1 h**	**168 h**	**720 h**
HWS	**32 °C**	34.5 (0.85)	51.6 (0.82)	44.7 (0.83)	**32 °C**	66.5	69.2	68.8
	37 °C	17.6 (0.87)	39.5 (0.81)	34.2 (0.82)	**37 °C**	137	63.9	66.3
	42 °C	15.3 (0.87)	34.7 (0.82)	31.1 (0.82)	**42 °C**	113	79.2	75.5
DS	**32 °C**	49.2 (0.84)	95.2 (0.79)	40.2 (0.84)	**32 °C**	34.8	21.2	40.8
	37 °C	43.2 (0.84)	72.4 (0.79)	42.9 (0.81)	**37 °C**	39.4	31.5	63.3
	42 °C	21.3 (0.86)	45.3 (0.80)	26.1 (0.82)	**42 °C**	72.9	41.1	84.8

The capacitance of the barrier layer, C_b, is similar for the three HWS-TSA anodised samples and increases slowly with immersion time. The initial C_b values and their evolution for the DS-TSA anodised samples are very similar to those obtained for the HWS-TSA anodised clad AA2024 samples. There is a slight increase in the C_b values after 168 h of immersion, however, these values decreased to almost the initial values after 720 h.

The R_b cannot be calculated precisely and only an estimation of its lower value can be done, R_b was above 1000 $k\Omega\ cm^2$ during the test for all the samples.

The capacitance of the porous layer, C_p is, as previously observed for the unclad alloy, higher for the thinner film grown at 32 °C than for the samples anodised at higher temperature after 1 h of immersion. C_p increases after 168 h of immersion for all the samples but then slightly decrease after 720 h in the case of the HWS-anodised samples. The capacitance of the porous layer, C_p, showed higher values for the three DS-anodised samples compared to the HWS-anodised samples after 1 h of immersion, probably because the shorter sealing process does not plug the pores so efficiently. C_p presented increased values after 168 h exposure to the 0.5 M NaCl solution for the three DS- anodised samples and a recovery of the initial values after 720 h of immersion.

In the case of the HWS-anodised samples, the resistance of the porous layer to the penetration of the electrolyte is lower for the sample anodised at 32 °C after 1 h of immersion. However, the values of R_p after 168 h are similar for the three specimens, and their values maintained after 720 h.

The variation of these parameters indicates a good behaviour of the HWS-TSA anodised clad AA2024 samples; although the initial quality of the film obtained at 32 °C is lower. The regular structure of the anodic films jointly with the absence of second phase particles suggest that self healing of possible defects or damaged areas of the films during the corrosion test is taking place during the immersion in NaCl solution.

The resistance of the solution to penetrate in the pores of the film is lower for the DS-anodised samples than for the HWS-anodised samples after 1 h of immersion; that is to say, R_p values decrease after 168 h of immersion. However, the increase of R_p jointly with the decrease of C_p after 720 h of immersion leads to think that the sealing process continues during the test.

Therefore, the action of the dichromate trapped in the pores of the film is evident for long exposure times, avoiding the degradation of the film and allowing the self-healing of the specimens. In the case of the clad AA2024 alloy, the longer sealing time results in better behaviour against corrosion for short test times, whereas the influence of the incorporation of corrosion inhibitors is appreciable for long test times.

Salt spray test results for the clad AA2024 samples anodised at various temperatures and subsequently HWS or DS are summarised in table 26.

Table 26. Salt spray test results for clad AA2024 samples anodised at different temperatures and sealed in different baths.

Anodising T (°C)	Sealing	96 h		336 h	
		Pits dm^{-2}	% pass	Pits dm^{-2}	% pass
32	HWS	0.6	100	3.1	17
	DS	0	100	0.4	100
37	HWS	0.9	100	1.9	83
	DS	0	100	0.1	100
42	HWS	0.8	100	0.9	100
	DS	0	100	0.6	100

The salt spray test results reveal better performance of the DS-anodised samples for the two test times, passing the requirement after 336 h for all the anodising temperatures. On the other hand, HWS-anodised samples achieved good results in the case of the samples anodised at 37 and 42 °C after 336 h exposure but not if was as anodised at 32 °C. The number of pits after 336 h seems to have a relation with the anodising temperature.

AA6061

The EIS spectra after different immersion time in a 0.5 M NaCl solution of the AA6061 samples anodised at various temperatures and HWS for 40 min or DS for 20 min are shown in fig. 83.

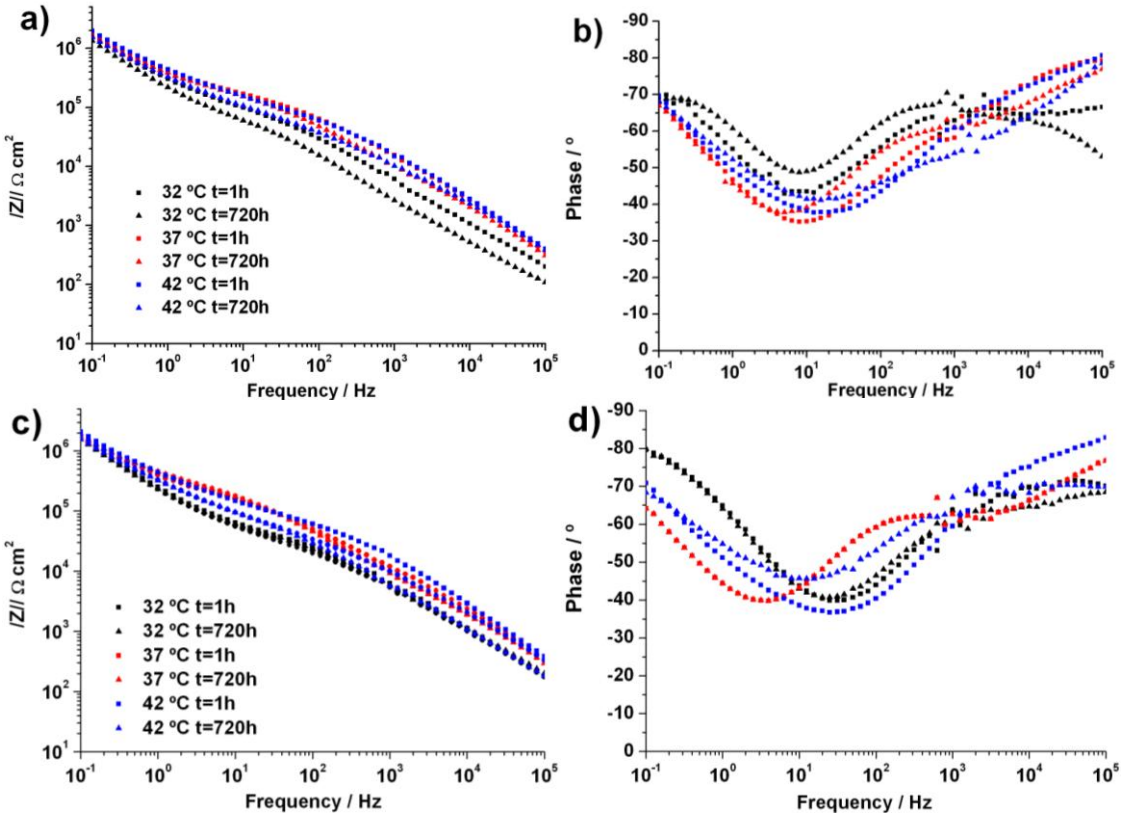

Figure 83. Bode plots after different immersion times in 0.5 M NaCl solution of AA6061 specimens anodised at different temperatures and subsequently (a,b) HWS or (c,d) DS.

In general, the two signatures corresponding to the barrier and the porous layer properties are not so well discriminated as in the rest of the studied alloys. Observation of the HWS-anodised EIS spectra show particularly low values of impedance for the sample anodised at 32 °C after 1 h in the high frequency range and marked decrease of the modulus of the impedance after 720 h. On the contrary, the samples anodised at higher temperatures present higher modulus of the impedance after 1 h of immersion and modest changes after 720 h. In the case of the DS-anodised samples, little change is observed after prolonged exposure time to the 0.5 M NaCl solution. The fitted parameters are shown in table 27.

There is a common behaviour for the two postreatments in the variation of C_b values during immersion of the samples in the corrosive solution. C_b is slightly higher for the samples anodised at 32 °C and sealed after 1 h of immersion. Nevertheless, the increase in C_b values for all the HWS-anodised and DS-anodised samples are not remarkable after 168 h and 720 h of immersion.

On the other hand, the resistance of the barrier layer is always maintained over 1 MΩ cm^2 for the three specimens up to 720 h of immersion in the 0.5 M NaCl solution.

Table 27. Results after fitting EIS data after different immersion times in 0.5 M NaCl solution for the AA6061 specimens anodised at different temperatures and subsequently HWS or DS. The values in brackets indicate the dispersion factor of the constant phase element.

Sealing	C_b ($\mu S\ cm^{-2}$)	1 h	168 h	720 h	R_b ($k\Omega\ cm^2$)	1 h	168 h	720 h
HWS	**32 °C**	0.91 (0.80)	1.00 (0.79)	1.16 (0.82)	**32 °C**	>1000	>1000	>1000
	37 °C	0.78 (0.72)	0.82 (0.76)	0.84 (0.76)	**37 °C**	>1000	>1000	>1000
	42 °C	0.71 (0.72)	0.82 (0.76)	0.92 (0.69)	**42 °C**	>1000	>1000	>1000
DS	**32 °C**	0.89 (0.82)	0.93 (0.84)	0.97 (0.84)	**32 °C**	>1000	>1000	>1000
	37 °C	0.76 (0.71)	0.84 (0.74)	0.85 (0.75)	**37 °C**	>1000	>1000	>1000
	42 °C	0.67 (0.70)	0.81 (0.73)	0.89 (0.73)	**42 °C**	>1000	>1000	>1000
Sealing	**C_p ($nS\ cm^{-2}$)**	**1 h**	**168 h**	**720 h**	**R_p ($k\Omega\ cm^2$)**	**1 h**	**168 h**	**720 h**
HWS	**32 °C**	353 (0.73)	568 (0.70)	735 (0.74)	**32 °C**	96.9	84.6	57.4
	37 °C	82.1 (0.78)	176 (0.73)	216 (0.72)	**37 °C**	125	162	185
	42 °C	69.7 (0.80)	300 (0.69)	248 (0.70)	**42 °C**	84.1	63.4	55.2
DS	**32 °C**	192 (0.78)	319 (0.74)	322 (0.73)	**32 °C**	37.3	32.5	44.3
	37 °C	62.1 (0.80)	153 (0.74)	227 (0.73)	**37 °C**	125	138	219
	42 °C	38.4 (0.85)	187 (0.74)	250 (0.78)	**42 °C**	69.1	43.3	55.7

In the case of the HWS-TSA anodised AA6061 specimens, the C_p value obtained after 1 h of immersion is higher than for the samples anodised at higher temperature and subsequently HWS. Besides, the increase of C_p is markedly higher for the sample anodised at low temperature. The behaviour of the DS-TSA anodised samples are similar to that observed for the HWS-TSA anodised samples. However, a comparative study of the C_p values reveals that the values of the DS-TSA anodised specimens are lower than those for the HWS-TSA anodised samples even after 1 h of immersion. This contrasting feature can be due to a relatively worst sealing process in the case of the AA6061 alloy compared to the rest of the alloys. Therefore the effect of the dichromate is readily observed even after very short immersion time, especially in the case of the samples anodised at 32 °C.

R_p values are slightly higher for the HWS-TSA anodised specimens, indicating increased resistance to the penetration of the test solution through the pores after 1 h of immersion. However a decrease of this resistance during the test is observed for the samples anodised at 32 and 42 °C and HWS. These changes are similar but subtler in the case of the corresponding DS-anodised samples. Eventually, the R_p values for the samples anodised at 37 °C and sealed increase during the experiment.

Therefore, general observation of the parameters obtained after the different sealing processes of the anodised AA6061 specimens reveals little differences between HWS or DS after 720 h of test.

The results of the salt spray test are shown in table 28. The salt spray test show that after 96 h of exposure to the corrosive environment, all the DS- anodised samples passes the test, however, the HWS-anodised samples present a higher pit density. The samples anodised at 37 and 42 °C and HWS success in the test, whereas the samples anodised at 32 °C and HWS present 4.6 pits dm^{-2} and fail the test.

Table 28. Salt spray test results for AA6061 samples anodised at different temperatures and sealed in different baths.

Anodising T (°C)	Sealing	96 h		336 h	
		Pits dm^{-2}	% pass	Pits dm^{-2}	% pass
32	HWS	4.6	16	8.0	0
	DS	0	100	2.7	0
37	HWS	1.2	100	1.8	67
	DS	0	100	1.2	100
42	HWS	1.0	100	1.4	83
	DS	0	100	0.9	83

The visual inspection of the samples after 336 h of exposure reveals that no sample anodised at 32 °C pass the test ineffectual the sealing process. ⅔ of the samples anodised at 37 °C and HWS pass the test, meanwhile the whole of the DS-anodised samples passes the test with lower pit density. In the case of the samples anodised at 42 °C and sealed, most of the specimens pass the test, being lower the pit density for the samples sealed in boiling potassium dichromate solution. Again, for the different postreatments the pit density is dependant on the thickness of the anodic film.

AA7475

The EIS spectra of the AA7475 samples anodised at various temperatures and sealed in boiling water for 40 min or in boiling dichromate solution for 20 min are shown in fig. 84.

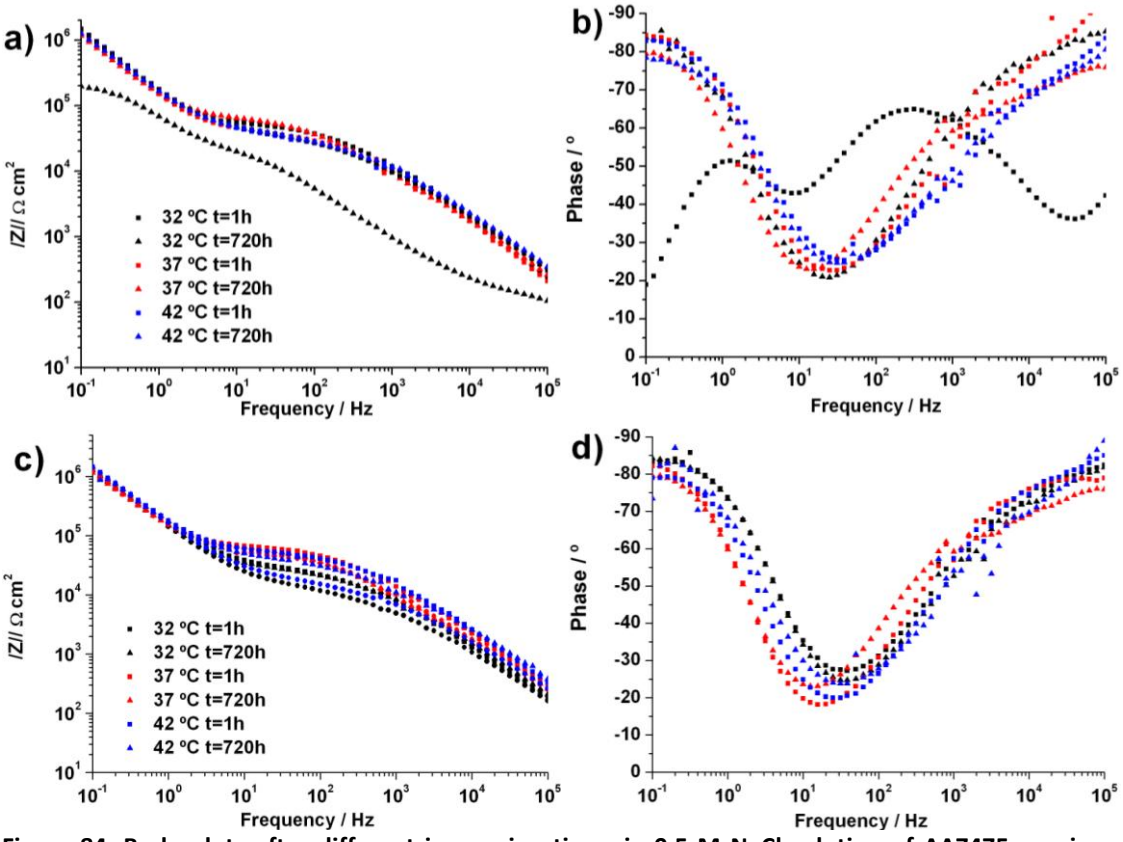

Figure 84. Bode plots after different immersion times in 0.5 M NaCl solution of AA7475 specimens anodised at different temperatures and subsequently (a,b) HWS or (c,d) DS.

The Bode plots reveal similar impedance spectra for the HWS-anodised and DS-anodised samples after 1 h of immersion in the test solution. The EIS spectra for the samples anodised at 37 and 42 °C and subsequently HWS reveal modest changes after 720 h of immersion. However, the sample anodised at the lowest temperature presents a marked decrease of the impedance in all the frequency range. In the case of the DS-anodised AA7474 specimens, the unique effect observed during the immersion in the test solution is a decrease in the modulus of the impedance after 720 h immersion for all the samples. Table 29 shows quantitative information about the features described above.

Table 29. Results after fitting EIS data after different immersion times in 0.5 M NaCl solution for the AA7475 specimens anodised at different temperatures and subsequently HWS or DS. The values in brackets indicate the dispersion factor of the constant phase element.

Sealing	C_b ($\mu S\ cm^{-2}$)	1 h	168 h	720 h	R_b ($k\Omega\ cm^2$)	1 h	168 h	720 h
HWS	**32 °C**	1.18 (0.93)	1.19 (0.90)	3.68 (0.71)	**32 °C**	>1000	>1000	283
	37 °C	1.22 (0.94)	1.35 (0.91)	1.55 (0.94)	**37 °C**	>1000	>1000	>1000
	42 °C	1.09 (0.90)	1.10 (0.90)	1.25 (0.87)	**42 °C**	>1000	>1000	>1000
DS	**32 °C**	1.15 (0.91)	1.25 (0.92)	1.26 (0.92)	**32 °C**	>1000	>1000	>1000
	37 °C	1.29 (0.93)	1.42 (0.90)	1.37 (0.92)	**37 °C**	>1000	>1000	>1000
	42 °C	1.11 (0.90)	1.13 (0.91)	1.15 (0.90)	**42 °C**	>1000	>1000	>1000
Sealing	**C_p ($nS\ cm^{-2}$)**	**1 h**	**168 h**	**720 h**	**R_p ($k\Omega\ cm^2$)**	**1 h**	**168 h**	**720 h**
HWS	**32 °C**	41.6 (0.86)	85.8 (0.82)	684 (0.99)	**32 °C**	46.8	37.7	7.09
	37 °C	55.5 (0.84)	139 (0.79)	421 (0.70)	**37 °C**	36.0	21.6	40.6
	42 °C	83.9 (0.78)	109 (0.77)	88.4 (0.77)	**42 °C**	31.9	35.3	34.4
DS	**32 °C**	79.7 (0.83)	170 (0.78)	88.2 (0.81)	**32 °C**	26.6	12.8	25.5
	37 °C	42.1 (0.84)	75.5 (0.81)	112 (0.78)	**37 °C**	60.8	48.9	61.2
	42 °C	32.9 (0.85)	154 (0.76)	75.3 (0.78)	**42 °C**	48.4	16.9	38.4

The values of the capacitance of the barrier layer, C_b, after 1 h of immersion are roughly similar for all the AA7475 samples anodised at different temperatures and sealed. Besides, there is a slow increase during the exposure to the 0.5 M NaCl solution. Only the sample anodised at 32 °C and HWS reveals a significant increment of the C_b after 720 h of immersion.

The high R_b values indicate that the barrier layer is very stable for most of the samples, whereas the samples anodised at 32 °C and HWS present a value markedly lower.

In the case of the HWS-anodised AA7475 specimens, C_p is lower for the sample anodised at 32 °C after 1 h of immersion, and increases with the anodising temperature. However, this parameter randomly varies with the immersion time. The sample anodised at 32 and 37 °C and HWS doubles its C_p value after 168 h and continues growing after 720 h. The sample anodised at 42 °C and HWS maintains relatively constant values during the immersion in the test solution. The resistance of the electrolyte to penetrate through the pores decreases for the sample anodised at 32 °C and HWS during the experiment, whereas in the case of the sample anodised at 37 °C and HWS decreases after 168 h of immersion and then increases after 720 h. The sample anodised at 42 °C and HWS maintains constant R_p values.

The capacitance of the porous layer, C_p, for the DS-anodised samples shows increased values with lower anodising temperature after 1 h of immersion; this tendency was also observed for the previous alloys and was attributed to a thinner anodic film. C_p values increase after 168 h of immersion and decrease after 720 h for the samples anodised at 32 and 42 °C and DS, whereas slightly increases for the sample anodised at 37 °C and DS during the experiment. In any case, the C_p values for the three DS-anodised samples are lower than the corresponding HWS-anodised samples after 720 h of immersion due to the marked influence of the dichromate.

The influence of the dichromate salt is also noticeable following the evolution of the resistance of the electrolyte to penetrate through the pores of the film (R_p), the values of this parameter decreased after 168 h of immersion for the three DS-anodised samples and increased to their initial values after 720 h of immersion in the test solution.

This unexpected behaviour can be due to the probability of finding defective areas on the anodic structure. This feature can not be underestimated for the AA7475 due to the apparent grain boundary attack appeared during the acid pickling treatment and previously observed by SEM, which feature is maintained after the anodising and the sealing process.

The neutral salt spray tests results for the AA7475 samples anodised at various temperatures and sealed in boiling water or in boiling dichromate solution are shown in table 30.

Table 30. Salt spray test results for AA7475 samples anodised at different temperatures and sealed in different baths.

Anodising T (°C)	Sealing	96 h		336 h	
		Pits dm^{-2}	% pass	Pits dm^{-2}	% pass
32	HWS	6.7	16	6.9	0
	DS	0	100	2.8	33
37	HWS	1.4	83	5.3	0
	DS	0	100	0.1	100
42	HWS	1.9	67	2.6	50
	DS	0	100	2.0	67

The salt spray test results after 96 h for the HWS-anodised samples present a high pit density, especially for the samples anodised at 32 °C and HWS, which fail the test. A higher success percentage is obtained for the samples anodised at higher temperatures and HWS. In the other hand, all the samples DS-anodised passed the 96 h test.

After 336 h, the samples HWS-anodised present a high pit density, although there is a relation between the increased anodising temperatures and the lower pit density, to the extent that one half of the samples anodised passed the test. The samples DS-anodised passed the test when the anodic film was grown at 37 or 42 °C.

From the salt spray test results of the four studied alloys, some points can be concluded. In general, two effects are observed; on the one hand, the thicker alumina film obtained anodising at higher temperature makes more difficult the penetration of the corrosive fog medium to the base of the pores. Therefore a lower pit density is obtained for the different test time for the samples anodised at higher temperature and sealed. On the other hand, the dichromate adsorbed on the pore walls of the anodic films during the DS process clearly slows down the pitting corrosion.

5.2.1.4. Influence of anodising time on the corrosion resistance after sealing in boiling water.

Fig. 85 shows the EIS spectra of the AA2024, clad AA2024, AA6061 and AA7475 samples anodised for different plateau times and sealed in boiling water for 40 min after the anodising program.

The samples anodised for 10 min and HWS show lower modulus of the impedance after 1 h of immersion in the test solution than the samples anodised for longer time and HWS. Besides, the decrease of $|Z|$ in the high frequency range after 720 h of immersion is more remarkable for the sample anodised for 10 min. Table 31 summarises the results after fitting the EIS spectra to the equivalent circuit described for sealed samples. Conversely, the sample anodised for 10 min and HWS evidence different shape and low $|Z|$, this spectrum was fitted with the EC described for anodised samples.

In general, the capacitance of the barrier layer, C_b, presents similar values after 1 h of immersion in the 0.5 M NaCl solution for the three samples anodised for different times and HWS for each alloy. These values increased during the experiment, being this fact more marked after 720 h of immersion always for the sample anodised for 10 min and HWS. This observation reveals worst behaviour against corrosion for the samples anodised for the shorter time. Another remarkable feature, comparing every single anodising time for all the alloys, is that after 168 h and 720 h of immersion, the high copper content alloys (AA2024 and AA7475) present higher C_b values than the low copper content alloys. This evidences extended corrosion in the low ordered, copper-containing anodic films.

The resistance of the barrier layer, R_b, remains over 1 MΩ cm^2 during the test time for most of the samples. However, the evolution of the barrier layer parameters evidence slight degradation of the barrier layer. The only exception is the AA7475 sample anodised for 10 min and HWS, which present a low R_b value after 720 h of immersion. Such R_b value denotes heavy degradation of the barrier layer.

Comparing the C_p values after 1 h of immersion of the AA2024 samples anodised for different times and HWS, the higher value is obtained for the sample anodised for 10 min, a minimum value for the sample anodised for 20 min and increased value for the sample anodised for 30 min. Interestingly, C_p values increases with the immersion time in the 0.5 M NaCl solution except for the sample anodised for 30 min. In this case, the evolution of C_p up to 168 h is similar to that observed for the rest of the samples. However, after 720 h of immersion, C_p value maintained relatively constant.

The sample anodised for 20 min present the higher R_p value, in any case, R_p halves for the three samples after 720 h of immersion, indicating similar evolution of the penetration process of the test solution through the sealed pores.

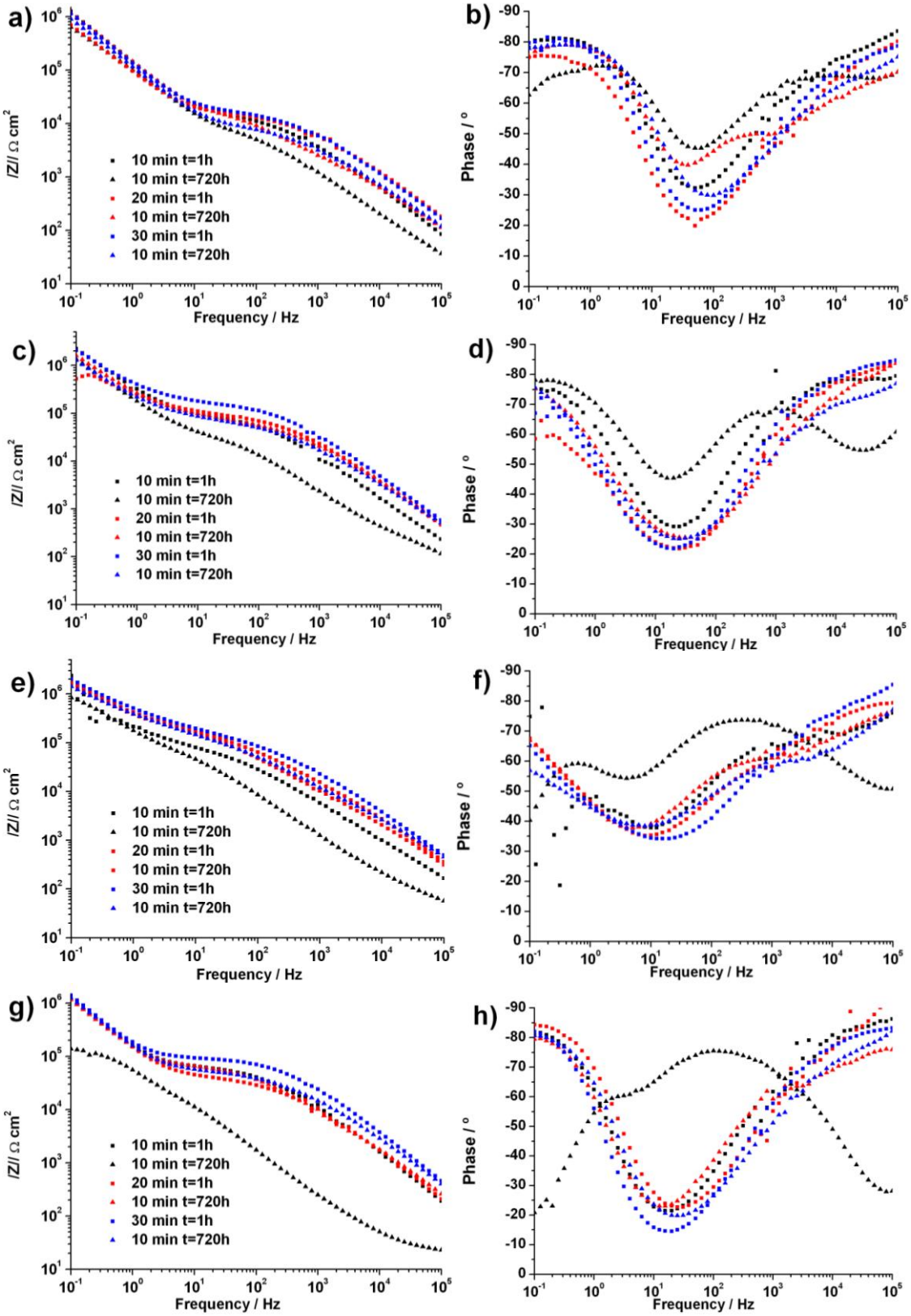

Figure 85. Bode plots after different immersion times in 0.5 M NaCl solution of (a,b) AA2024, (c,d) clad AA2024, (e,f) AA6061 and (g,h) AA7475 specimens anodised for different plateau times and subsequently sealed in boiling water (HWS).

Table 31. Results after fitting EIS data after different immersion times in 0.5 M NaCl solution for the AA2024, clad AA2024, AA6061 and AA7475 specimens anodised different plateau times and subsequently sealed (HWS). The values in brackets indicate the dispersion factor of the constant phase element.

Alloy	C_b ($\mu S\ cm^{-2}$)	1 h	168 h	720 h	R_b ($k\Omega\ cm^2$)	1 h	168 h	720 h
AA2024	10 min	1.29 (0.92)	1.42 (0.90)	2.08 (0.87)	10 min	>1000	>1000	>1000
	20 min	1.10 (0.93)	1.32 (0.91)	1.55 (0.93)	20 min	>1000	>1000	>1000
	30 min	1.36 (0.92)	1.59 (0.89)	1.68 (0.90)	30 min	>1000	>1000	>1000
Clad AA2024	10 min	0.71 (0.84)	1.02 (0.86)	1.13 (0.88)	10 min	>1000	>1000	>1000
	20 min	0.77 (0.76)	0.98 (0.76)	0.96 (0.78)	20 min	>1000	>1000	>1000
	30 min	0.56 (0.80)	0.61 (0.79)	0.62 (0.79)	30 min	>1000	>1000	>1000
AA6061	10 min	1.18 (0.78)	1.42 (0.71)	1.39 (0.74)	10 min	>1000	>1000	>1000
	20 min	0.77 (0.72)	0.82 (0.76)	0.84 (0.76)	20 min	>1000	>1000	>1000
	30 min	0.66 (0.68)	0.95 (0.77)	0.94 (0.67)	30 min	>1000	>1000	>1000
AA7475	10 min	1.24 (0.92)	2.60 (0.77)	3.16 (0.81)	10 min	>1000	>1000	173
	20 min	1.22 (0.94)	1.35 (0.91)	1.55 (0.94)	20 min	>1000	>1000	>1000
	30 min	1.14 (0.94)	1.17 (0.92)	1.26 (0.91)	30 min	>1000	>1000	>1000
Alloy	**C_p ($nS\ cm^{-2}$)**	**1 h**	**168 h**	**720 h**	**R_p ($k\Omega\ cm^2$)**	**1 h**	**168 h**	**720 h**
AA2024	10 min	179 (0.83)	326 (0.70)	1168 (0.77)	10 min	12.4	9.6	5.5
	20 min	60.8 (0.84)	300 (0.75)	962 (0.70)	20 min	31.9	17.2	14.0
	30 min	118 (0.81)	388 (0.74)	314 (0.76)	30 min	15.3	8.3	7.7
Clad AA2024	10 min	35.7 (0.88)	97.3 (0.82)	412 (0.81)	10 min	70.4	27.1	28.1
	20 min	17.6 (0.87)	176 (0.73)	34.2 (0.82)	20 min	137	63.9	66.4
	30 min	10.3 (0.89)	16.9 (0.86)	17.5 (0.85)	30 min	137	126	129
AA6061	10 min	264 (0.77)	498 (0.93)	413 (0.97)	10 min	62.8	17.7	11.7
	20 min	82.1 (0.78)	139 (0.79)	216 (0.72)	20 min	125	162	185
	30 min	34.5 (0.84)	95.8 (0.77)	205 (0.71)	30 min	115	97.0	109
AA7475	10 min	43.0 (0.87)	305 (0.91)	161 (0.97)	10 min	55.4	26.8	-
	20 min	55.5 (0.84)	139 (0.79)	421 (0.70)	20 min	36.0	21.6	40.6
	30 min	21.0 (0.86)	48.1 (0.81)	54.7 (0.80)	30 min	86.0	62.7	47.8

Salt spray test results

The results of the salt spray test for the four alloys anodised for different times and subsequently sealed in boiling water for 40 min are shown in table 32.

After 96 h of exposure to the corrosive environment, all the samples of the different alloys anodised for 10 min present more than 2 pits dm^{-2}, therefore all of them fail the test. On the other hand, the samples anodised for 20 and 30 min generally pass the test; although the thicker anodic films obtained in the samples anodised at 30 min do not result in lower pit density.

Table 32. Salt spray test results for various alloys samples anodised for different times and HWS.

Alloy	Anodising time (min)	96 h		336 h	
		Pits dm^{-2}	% pass	Pits dm^{-2}	% pass
AA2024	**10**	5.1	0	-	-
	20	0.4	100	5.7	0
	30	1.4	83	4.9	0
Clad AA2024	**10**	3.6	33	6.0	0
	20	0.9	100	1.9	83
	30	0.9	100	1.6	83
AA6061	**10**	7.8	0	-	-
	20	1.2	100	1.8	67
	30	3.7	33	4.3	0
AA7475	**10**	7.8	0	-	-
	20	1.4	83	5.3	0
	30	1.3	100	3.8	0

Visual inspection of the samples after 336 h of exposure reveals increased pit density for all the samples, to the extent that the high copper content alloys (AA2024 and AA7475) fail the test. Only the samples anodised for 20 and 30 min of the purest clad AA2024 alloy pass the test. The former alloys present lower pit density for the thicker films obtained after anodising for 30 min. Exceptionally, the AA6061 samples anodised for the longest time present worse corrosion resistance than the samples anodised for 20 min.

5.2.1.5. Effect of the immersion time in the anodising bath on the sealability of the anodised samples

The aim of this experiment is checking the sealability of the flawed anodic films. Specimens of AA2024, AA6061 and AA7475 were anodised (37 °C, 20 min) and immediately water rinsed after the anodising cycle or kept into the TSA bath after anodising for 5, 10 or 20 min. After withdrawal from the TSA bath, all the specimens were water rinsed and sealed in boiling water for 40 min.

Fig.86a shows EIS spectra of TSA anodised and HWS AA2024 alloy specimens. A decrease of $|Z|$ in both signatures, the barrier layer (low frequencies) and the hydrated porous layer (high frequencies), can be observed with increasing immersion time in the anodising electrolyte. After immersion in the anodising electrolyte for 20 min, only one time constant was revealed, and the impedance modulus was reduced by 2-3 orders of magnitude at all frequencies, suggesting that the porous anodic oxide was largely removed. EIS spectra for anodised and sealed AA6061 TSA specimens are shown in Fig.86b. The barrier layer and porous layer signatures are well discriminated as for the AA2024 alloy; however increased immersion time in the anodising electrolyte did not result in major variation of the EIS spectra, unlike that for the AA2024. The EIS spectra for the TSA anodised and sealed AA7475 specimens are shown in Fig.86c. As for the AA2024 alloy, a reduction of the impedance modulus at all frequencies with time of immersion is evident, suggesting degradation of the anodic film.

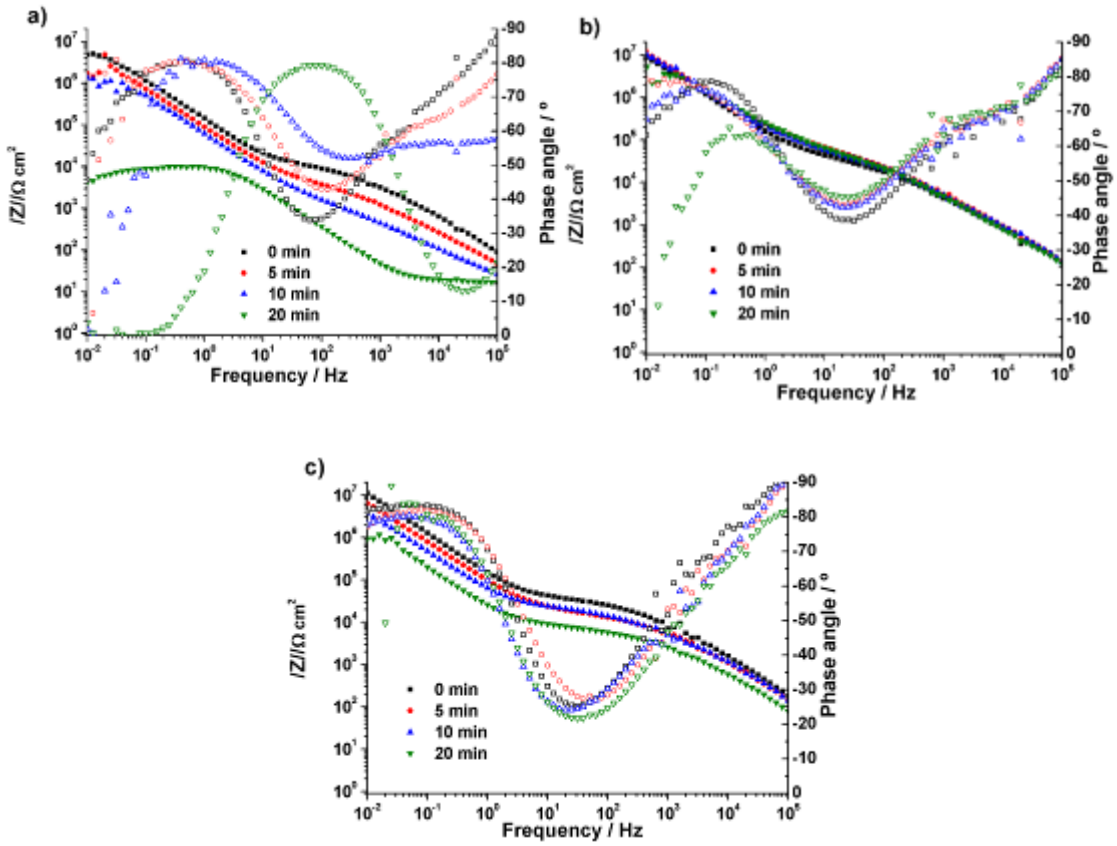

Figure 86. EIS spectra recorded in 0.5 M NaCl solution of (a) AA2024 (b) AA6061 and (c) AA7475 anodised samples withdrew from the TSA anodising bath after different times and subsequently rinsed and sealed.

Table 33 shows the fitted parameters of the EIS spectra in fig. n with the equivalent circuit proposed for sealed samples.

Table 33. Fitting results for the EIS data acquired in 0.5 M NaCl solution on different anodised specimens withdrew from the TSA anodising bath after different times and subsequently rinsed and sealed.

Anodised and HWS alloy	Remaining time (min)	R_b (MΩ cm^2)	C_b (μS cm^{-2})	R_p (kΩ cm^2)	C_p (nS cm^{-2})
AA2024	0	10.3	1.15 (0.91)	11.1	207 (0.82)
	5	2.61	1.31 (0.95)	5.06	838 (0.76)
	10	1.09	1.53 (0.96)	1.38	1480 (0.80)
	20	7.6e-3	6.37 (0.94)	-	-
AA6061	0	ND	0.65 (0.84)	59.8	216 (0.79)
	5	ND	0.74 (0.83)	60.6	193 (0.78)
	10	ND	0.81 (0.84)	54.7	234 (0.77)
	20	ND	0.98 (0.90)	41.6	276 (0.77)
AA7475	0	ND	1.15 (0.93)	32.8	64.2 (0.84)
	5	ND	1.80 (0.90)	15.9	120 (0.82)
	10	ND	3.02 (0.89)	19.6	168 (0.79)
	20	ND	8.03 (0.87)	7.20	331 (0.78)

Salt spray test

This test was carried out in triplicate of all the variously TSA anodised and sealed alloys. Table 34 summarizes the results after exposure to the salt spray for 96 h.

Table 34. Salt spray test results for various anodised aluminium alloys samples kept in the anodising bath after the end of the anodising cycle and subsequently HWS.

Anodised and sealed alloy	Time before withdrawal from the anodising bath (min)	Visual aspect	Pit density (Pits dm^{-2})
AA2024	0	Good	0.9
	5	Good	4.2
	10	Large corroded areas	-
	20	General corrosion	-
AA6061	0	Good	0
	5	Good	0
	10	Good	0
	20	Good	0
AA7475	0	Good	1.4
	5	Localised corrosion	3.5
	10	Localised corrosion	8
	20	Localised corrosion	8.2

The appearance of the TSA anodised and sealed AA2024 specimens after the test is shown in Fig. 87.

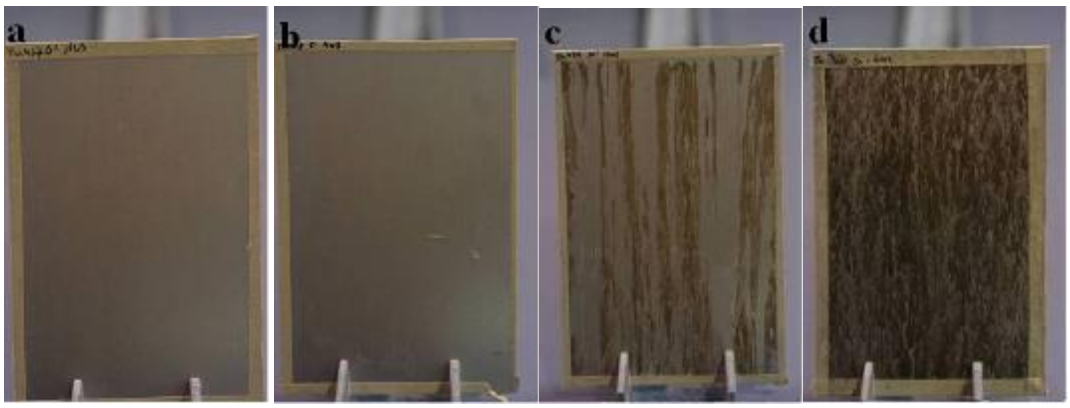

Figure 87. AA2024 specimens anodised and withdrew from the TSA anodising bath (a) immediately after, (b) 5 min after, (c) 10 min after and (d) 20 min after the end of the anodising program and sealed after 96 h exposure to salt spray test.

AA2024 specimens removed from the bath immediately or after only 5 minutes of immersion in the anodising electrolyte show a good general appearance, with 0.9 and 4.2 pits dm^{-2}, respectively. However, after a remaining time of 10 min, large corroded areas are observed on the specimen. Moreover, general corrosion is observed for the specimen removed after immersion for 20 min.

The TSA anodised and sealed AA6061 alloy reveals a good general appearance, with no pits or flawed areas observed visually after different immersion times in the anodising electrolyte.

The AA7075 alloy specimens that had been anodised, immediately rinsed and sealed revealed a relatively low pit density (1.4 pit dm^{-2}). However, after immersion for 5 min, the pit density increased to 3.5 pit dm^{-2}, and some flawed areas were visually observed. The specimens immersed for 10 and 20 min displayed pit densities of 8 and 8.2 pit dm^{-2} respectively, and large flawed areas were observed.

The SST results agree qualitatively with the findings from EIS. However, from a practical viewpoint, SST presents several disadvantages compared with the electrochemical method. Since SST is based on visual inspection, days or even weeks may be necessary to separate specimens qualitatively, whereas, for EIS measurements, the time is reduced significantly, i.e. 1 h or less may be sufficient if a single frequency is used as representative of sealing quality.

5.3. Chemical conversion coatings

5.3.1.1. Morphology

Fig. 88 shows the morphology of the AA2024 specimens anodised and subsequently postreated by immersion for 1 min in Alodine or in a commercial Cr (III) product.

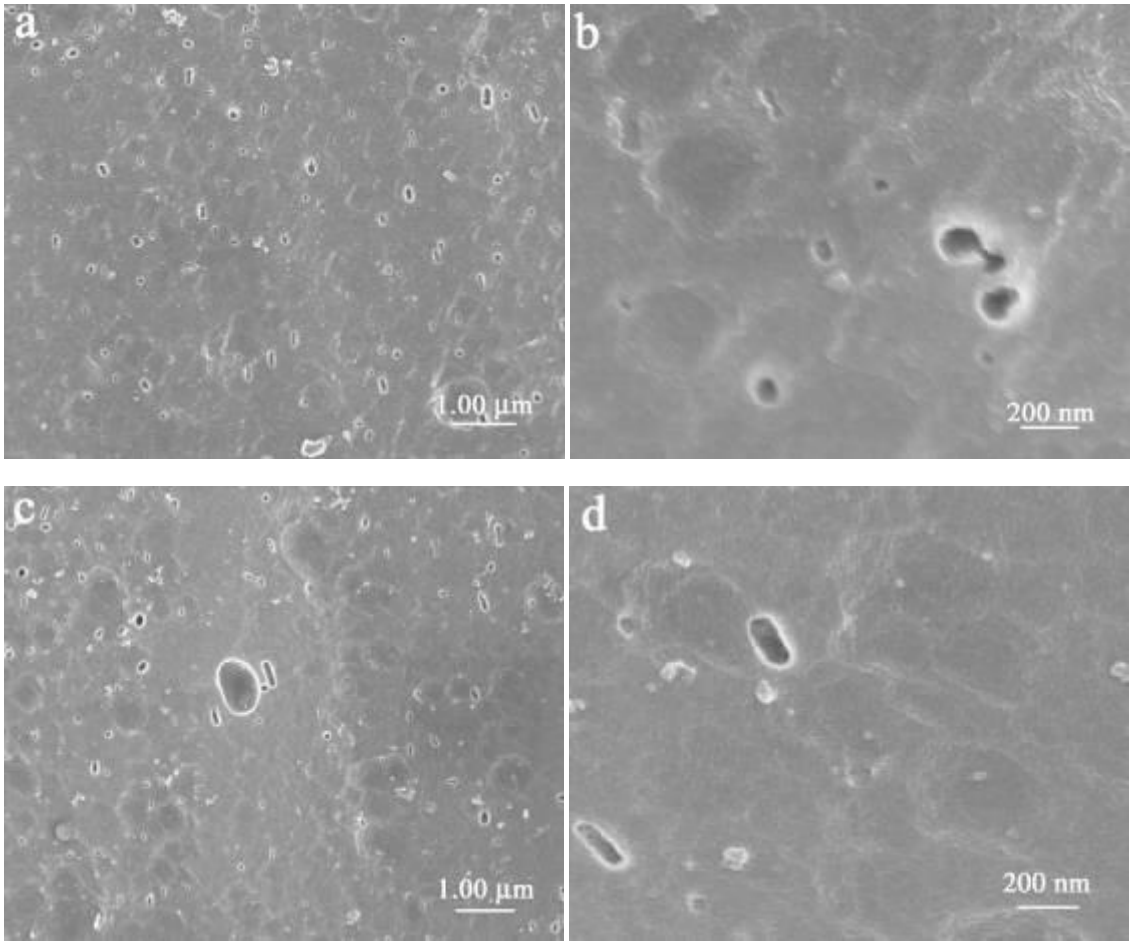

Figure 88. Morphology of the AA2024 specimens TSA anodised and postreated: (a,b) Alodine 1200, (c,d) Commercial Cr (III) compound.

The macro and micromorphology observed in the figure evidence that these two postreatments do not produce changes on the surface of the anodic films, as the scalloped morphology remains and micropores can still be distinguished.

5.3.1.2. Chemical composition

The qualitative chemical composition obtained by GDOES of the AA2024 samples anodised and subsequently postreated in Alodine or in commercial Cr (III) compound is shown in fig. 89.

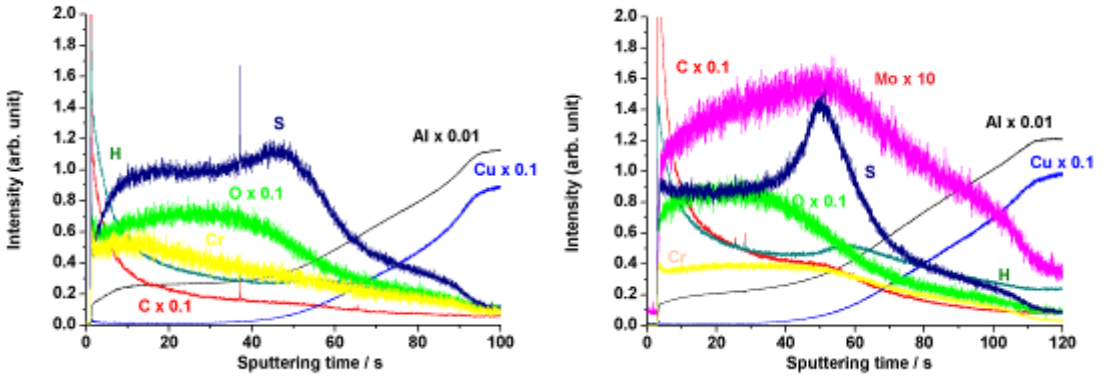

Figure 89. GDOES elemental depth profiles of the AA2024 specimens TSA anodised and postreated by immersion for 1 min in (a) Alodine, (b) Commercial Cr (III) compound.

The depth profiles of the elements of the alloy (Al and Cu) and most of the elements incorporated from the bath (O, C and H) for both samples resemble the depth profile of the anodised samples without postreatment.

In the case of the sample postreated in Alodine (fig. 89a), the sulphur maintains the depth profile observed for the anodised sample, on the contrary that the sulphur release observed after HWS or DS (Section 4.3.1). On the other hand, chromium has been incorporated to the anodic film; the depth profile of this element during the sputtering of the anodic film region present an initial plateau that decrease after about 15 s. This fact indicates the chromium species are present in the outer region of the anodic film and seems that do not penetrate to the base of the pores as can be compared with the deeper incorporation in the DS specimens.

The sample postreated by immersion in Commercial Cr (III) compound (fig. 89b) present a modified sulphur profile with a peak of increased intensity at the final sputtering of the anodic film. This is attributable to inwards migration of the sulphates adsorbed on the porous film during the postreatment. Apart from this feature, two new elements, chromium and molybdate appear in the GDOES spectra. The flat profile of the chromium in the anodic film region leads to think that it is uniformly distributed across the anodic film, whereas the molybdate present an ascending profile in the anodic film region that indicates accumulation of molybdenum species in the inner parts of the film. As it was explained in the 4.3., the commercial Cr (III) compound is a proprietary solution for production of chromate free chemical conversion coatings and this GDOES show that beside the Cr III ions it contains some molybdenum specie as corrosion inhibitor.

5.3.1.3. Electrochemical impedance spectroscopy

AA2024

Fig. 90 shows the EIS spectra acquired after different immersion times in a 0.5 M NaCl solution. Fig. 90a,b shows the EIS spectra of the AA2024 specimens anodised at various temperatures and subsequently immersed in Alodine for 1 min. Fig. 90c,d shows the EIS spectra of the AA2024 samples anodised at 37 °C for 20 min and immersed in the commercial Cr (III) compound for 1 min.

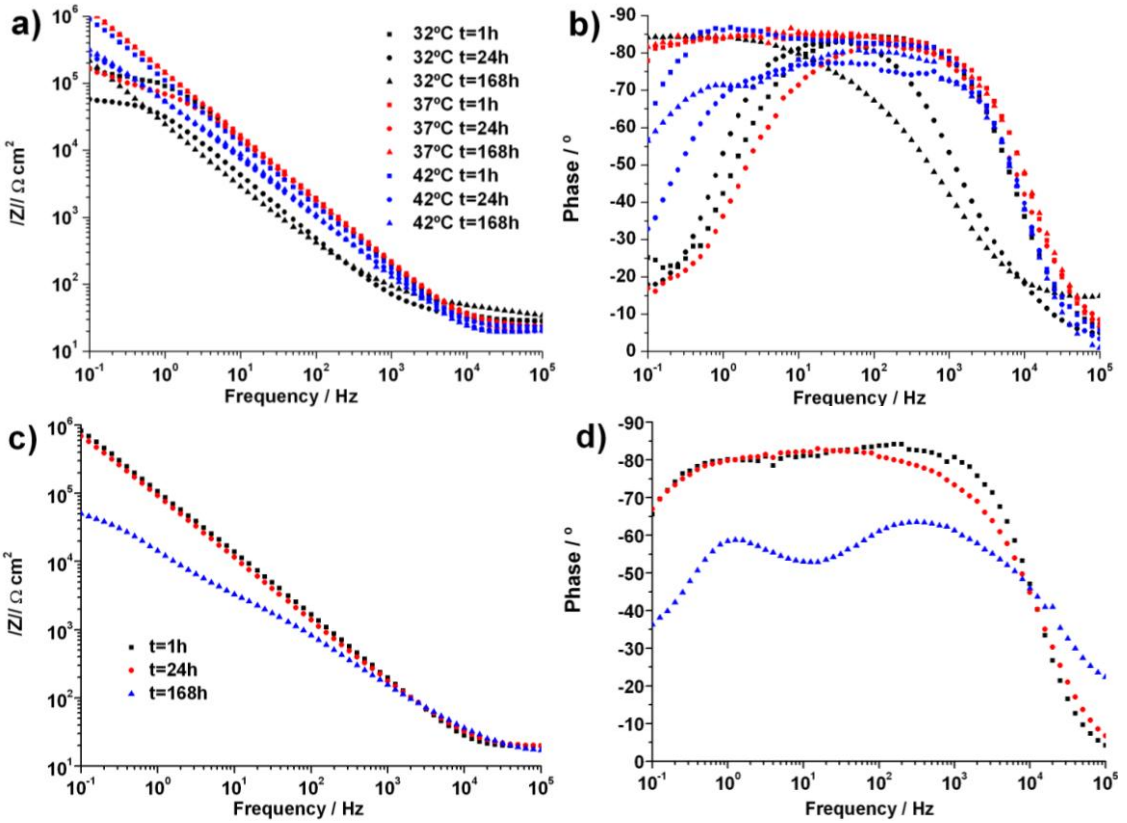

Figure 90. Bode plots after different immersion times in 0.5 M NaCl solution of AA2024 specimens (a,b) anodised at different temperatures and subsequently postreated with Alodine or (c,d) anodised at 37 °C and subsequently postreated with the commercial Cr(III) compound.

The EIS spectra after 1 h of immersion in the 0.5 M NaCl solution for the AA2024 samples anodised at different temperatures and postreated in Alodine are similar, the modulus of the impedance decreases for the three samples after 168 h exposure to the test solution, being this fact more accused for the sample anodised at the lowest temperature. However, after 720 h of exposure, an increase in $|Z|$ in the high frequency range is observed for the three Alodine-anodised AA2024 specimens. The EIS spectra were fitted with the EC1 described in section 4.3. for anodised samples, these results are shown in table 35.

In the case of the AA2024 specimen anodised at 37 °C and postreated in the cold Cr (III) bath, the EIS spectra after 1 h and 24 h of immersion in the test solution are very similar. However, the modulus of the impedance in the low frequency range significantly decreases after 168 h of immersion in the low frequency range. The EIS spectra were fitted with the EC1 described in section 4.3. for anodised samples and the results are shown in table 35. Eventually, the EIS spectra after 168 h of immersion show two time constants, as there is not a satisfactory explanation for such behaviour, the low frequency spectra (10^{1} down to 10^{-1} Hz) was fitted to the EC2 described in section 4.3 for anodised samples.

According to both SEM observations and EIS spectra, these cold postreatments do not seal the pores as previously observed for the two conventional sealing processes (HWS and DS).

Table 35. Results after fitting EIS data for the AA2024 specimens anodised at different temperatures and subsequently postreated with Alodine after different immersion times in 0.5 M NaCl solution.

Post Treatment	C_b ($\mu S\ cm^{-2}$)	1 h	24 h	168 h	R_b ($k\Omega\ cm^2$)	1 h	24 h	168 h
Cr (VI)	**32 °C**	1.23(0.95)	4.92(0.93)	8.47(0.87)	**32 °C**	135	59.7	>1000
	37 °C	1.21(0.94)	1.55(0.92)	1.24(0.94)	**37 °C**	>1000	109	>1000
	42 °C	1.58(0.94)	3.40(0.88)	3.51(0.87)	**42 °C**	>1000	317	676
Cr (III)	**37 °C**	1.66(0.92)	2.03(0.91)	18.9(0.69)	**37 °C**	>1000	>1000	115

In the case of the AA2024 specimens anodised at different temperatures and postreated in the cold Cr (VI) bath, the capacitance of the barrier layer is relatively similar for the three samples after 1 h of immersion in the test solution. C_b increase for the three samples after 24 h of immersion, but this increment only continues after 168 h for the thinner anodic film obtained at 32 °C. The samples anodised at 37 and 42 °C and Alodine postreated maintain constant C_b values after 168 h of immersion. The resistance of the barrier layer, R_b decrease after 24 h but increases after 168 h, this fact can be due to the action of the Cr (VI) in the film acting as a corrosion inhibitor and healing the flawed areas.

The AA2024 sample anodised at 37 °C and postreated in the cold Cr (III) bath presents values similar to that observed for the Cr (VI) postreated samples after 1 h of immersion in the 0.5 M NaCl solution. After 24 h the smaller C_b and higher R_b indicate better behaviour against corrosion, however this protective system is heavily degraded after 168 h of immersion. Therefore, the Cr (III) conversion coatings are clearly less effective after extended exposure time than the Cr (VI) conversion coatings.

Comparing the results shown in this table with those previously obtained for the AA2024 specimens anodised at different temperatures without postreatment (section 5.1), some differences are observed. C_b is initially lower for the postreated samples. This can be due to a slight attack of the anodic film by the additives contained in the cold postreatment bath (such as F^-) to promote the formation of the Cr/Al hydroxide of the chemical conversion coatings. Moreover, the results obtained after 168 h of immersion, reveals the effective inhibition of the Cr (VI) for all the anodising temperatures, whereas Cr (III) coatings does not demonstrate any beneficial effect after 168 h of immersion.

Salt spray test was undertaken on 6 specimens for each condition, the results of the test are summarised in table 36.

Table 36. Salt spray test results.

Anodising T (°C)	Postreatment	96 h		336 h	
		Pits dm^{-2}	% pass	Pits dm^{-2}	% pass
32	Alodine	-	-	3.7	50
37	Alodine	-	-	2.4	67
	Cr (III)	0.9	100	>20	0
42	Alodine	-	-	1.7	83

From the salt spray testing, it is clear that cold postreatments are less effective against pitting corrosion than the homologous sealing process (DS for Alodine and HWS for Cr (III)). However the relation between layer thickness and pit density is manifested in the samples anodised at

different temperature and postreated in the Cr (VI) bath. This test corroborates the Cr (III) postreatment is not as effective as the Cr(VI) postreatment, as previously observed by EIS.

Clad AA2024

The EIS study of the cold postreatments on the clad AA2024 alloy is shown in fig. 91. The EIS spectra of the clad AA2024 specimens anodised at various temperatures and postreated in Alodine are shown in fig. 91a,b. Whereas, EIS spectra after immersion for various times in a 0.5 M NaCl solution of a clad AA2024 sample anodised at 37 °C for 20 min and immersed in the commercial Cr (III) compound for 1 min is shown in fig. 91c,d.

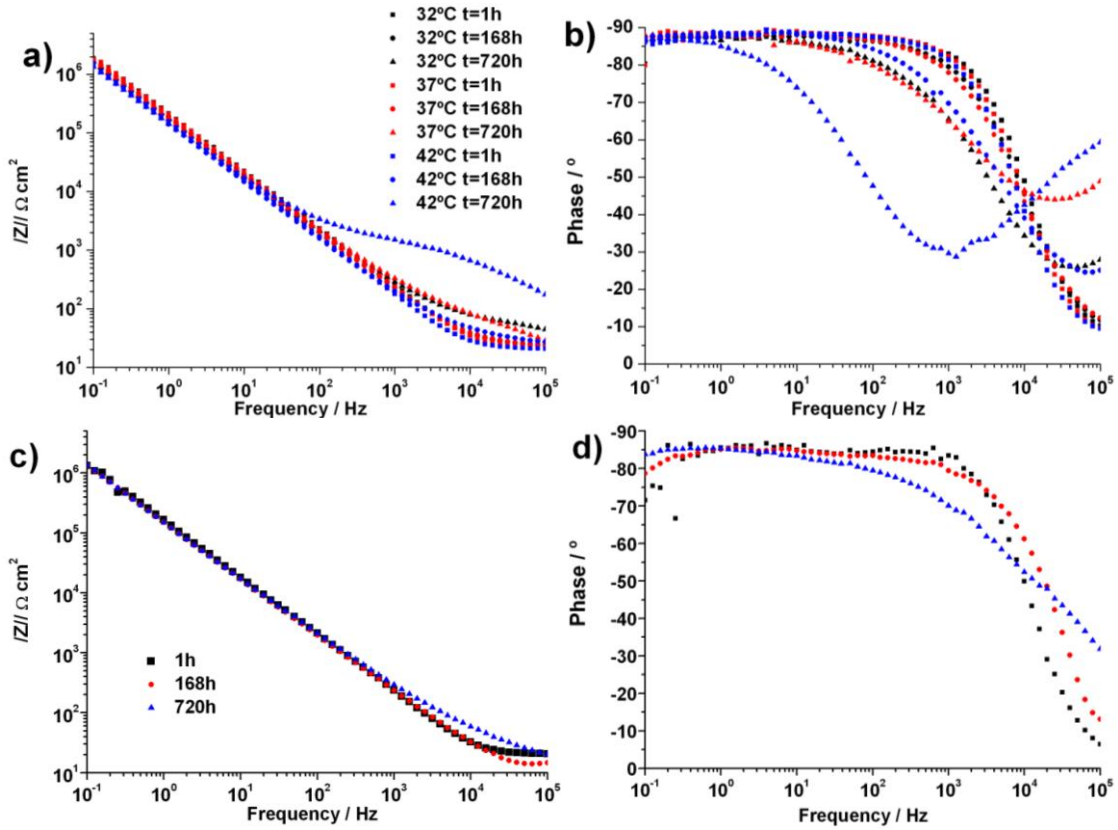

Figure 91. Bode plots after different immersion times in 0.5 M NaCl solution of clad AA2024 specimens (a,b) anodised at different temperatures and subsequently postreated with Alodine or (c,d) anodised at 37 °C and subsequently postreated with the commercial Cr(III) compound.

The EIS spectra after 1 h of immersion in the test solution of the clad AA2024 samples anodised at different temperatures and cold postreated in the cold Cr (VI) or Cr (III) baths present the same shape. After 168 h of immersion the spectra remains similar in the low frequency range and increases in the high frequency range. Further increase in the high frequency range is observed after 720 h immersion, especially for the sample anodised at 42 °C and cold postreated in Alodine. The EIS spectra acquired after 1 h and 168 h of immersion in the 0.5 M NaCl solution were fitted with the equivalent circuit proposed for anodised samples, whereas the spectra recorded after 720 h of immersion were fitted with the equivalent circuit described for sealed samples. Table 37 summarises these fittings.

Table 37. Results after fitting EIS data for the clad AA2024 specimens anodised at different temperatures and subsequently postreated with Alodine after different immersion times in 0.5 M NaCl solution.

Post treatment	C_b (μS cm^{-2})	1 h	168 h	720 h	R_b (kΩ cm^2)	1 h	168 h	720 h
Cr (VI)	**32 °C**	0.78(0.98)	0.89(0.97)	0.98(0.97)	**32 °C**	>1000	>1000	>1000
	37 °C	0.80(0.98)	0.93(0.97)	0.93(0.96)	**37 °C**	>1000	>1000	>1000
	42 °C	1.07(0.98)	0.93(0.96)	1.23(0.92)	**42 °C**	>1000	>1000	>1000
Cr (III)	**37 °C**	1.07(0.95)	1.20(0.94)	1.17(0.95)	**37 °C**	>1000	>1000	>1000
Post treatment	C_p (μS cm^{-2})	**1 h**	**168 h**	**720 h**	R_p (Ω cm^2)	**1 h**	**168 h**	**720 h**
Cr (VI)	**32 °C**	-	-	1e3 (0.23)	**32 °C**	-	-	2910
	37 °C	-	-	48.6(0.49)	**37 °C**	-	-	251
	42 °C	-	-	0.75(0.67)	**42 °C**	-	-	1953
Cr (III)	**37 °C**	-	-	154(0.47)	**37 °C**	-	-	84.3

Both postreatments maintain relatively constant values of C_b and high R_p values; this indicates good resistance of the barrier layer to the corrosive environment. Besides, a second constant of time, characteristic of a self-sealing process is observed for all the samples. Such self-sealing process is more effective in the clad AA2024 sample anodised at 42 °C and postreated in the cold Cr (VI) solution. The direct comparison between two clad AA2024 samples anodised at 37 °C and postreated in the cold Cr (VI) or the Cr (III) solutions after 1 h of immersion reveals lower, but comparable performance of the Cr (III) postreated sample.

Comparing the parameters in this table with those obtained for the clad AA2024 samples anodised at different temperature without further postreatments (section 5.1) two different features can be observed: On the one hand C_b values increased in a lesser extent for the cold postreated samples after 720 h of immersion, indicating effective protection of the corrosion inhibitors contained in both postreatment baths. On the other hand, the slower appearance of a second constant time, jointly with the slower increase of the R_p values for the postreated samples indicate slower self sealing process retarded thus by the thin chemical conversion layer on the anodic film structure.

Salt spray test was undertaken on the clad AA2024 anodised at different temperature and postreated in the cold Cr (VI) bath. The results are in the following table.

Table 38. Salt spray test results.

Postreatment	Anodising T (°C)	336 h	
		Pits dm^{-2}	% pass
Alodine	**32**	2.8	33
	37	2.2	87
	42	1.2	100

The salt spray test is sensitive to the layer thickness of the film, the thickest layers obtained anodising at higher temperature present thus lower pit density after 336 h of exposure to the corrosive environment.

AA6061

The study of the cold postreatment on the anodised AA6061 samples is shown in fig. 92. Fig. 92a,b shows the EIS spectra of the AA6061 specimens anodised at various temperatures and subsequently immersed in Alodine for 1 min. Fig. 92c,d shows the EIS spectra after immersion for various times in a 0.5 M NaCl solution of the AA6061 samples anodised at 37 °C for 20 min and immersed in the commercial Cr (III) compound for 1 min.

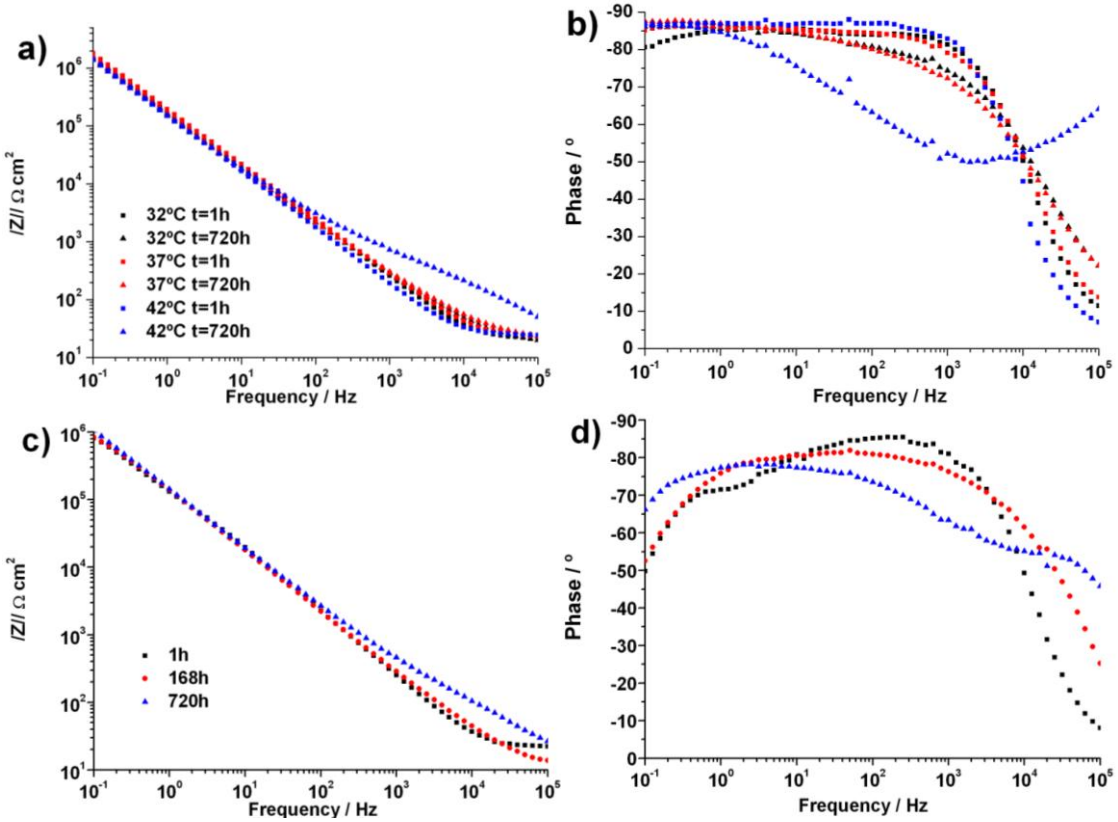

Figure 92. Bode plots after different immersion times in 0.5 M NaCl solution of AA6061 specimens (a,b) anodised at different temperatures and subsequently postreated with Alodine or (c,d) anodised at 37 °C and subsequently postreated with the commercial Cr(III) compound.

The variation of the AA6061 samples anodised at different temperatures and postreated in cold postreatment baths is similar to that previously observed for the clad AA2024 alloy. The parameters obtained by fitting to the equivalent circuit described for the anodised or anodised and sealed samples are shown in table 39.

The anodised AA6061 samples postreated in the Cr (VI) or in the Cr (III) bath present similar behaviour: C_b increases after 168 h of immersion and decrease after 720 h of exposure to the test solution. R_b values are always over 1 M Ω cm^2.

Table 39. Results after fitting EIS data for the AA6061 specimens anodised at different temperatures and subsequently postreated with Alodine after different immersion times in 0.5 M NaCl solution.

Post treatment	C_b (μS cm^{-2})	1 h	168 h	720 h	R_b (kΩ cm^2)	1 h	168 h	720 h
Cr (VI)	**32 °C**	0.98(0.95)	1.07(0.94)	1.06(0.96)	**32 °C**	>1000	>1000	>1000
	37 °C	0.90(0.94)	1.07(0.93)	0.99(0.97)	**37 °C**	>1000	>1000	>1000
	42 °C	1.10(0.96)	1.69(0.92)	1.19(0.91)	**42 °C**	>1000	>1000	>1000
Cr (III)	**37 °C**	1.55(0.89)	1.59(0.87)	1.46(0.88)	**37 °C**	>1000	>1000	>1000
Post treatment	C_p (μS cm^{-2})	**1 h**	**168 h**	**720 h**	R_p (Ω cm^2)	**1 h**	**168 h**	**720 h**
Cr (VI)	**32 °C**	-	-	62.1(0.60)	**32 °C**	-	-	2105
	37 °C	-	-	45.5(0.60)	**37 °C**	-	-	2230
	42 °C	-	-	3.90(0.65)	**42 °C**	-	-	1185
Cr (III)	**37 °C**	-	-	105(0.45)	**37 °C**	-	-	193

The appearance of a second time constant allows evaluating the self-sealing process of the samples. Such sealing process is similar for all the Alodine postreated-anodised AA6061 specimens but slightly slower for the Cr (III) postreated specimen.

The comparison of these values with the anodised AA6061 specimens (table n in section 4.1) reveals increased corrosion resistance and slower self-sealing process of the Alodine postreated samples. However, the Cr (III) postreatment is ineffectual since the evolution of C_b values during the experiment is very similar to that observed for the anodised specimens without sealing or postreatment. Besides the self-sealing process in the case of the Cr (III) postreated sample is slower.

Table 40 summarises the results of the salt spray test undertaken on the AA6061 specimens anodised and postreated in Alodine.

Table 40. Salt spray test results.

Postreatment	Anodising T (°C)	336 h	
		Pits dm^{-2}	% pass
Alodine	**32**	3.2	33
	37	2.0	67
	42	2.2	83

The results are similar to those observed for the previous alloys, the sample anodised at lower temperature mostly fail the test; whereas the increase of the anodising temperature, and therefore the film thickness, increases the probability of succeed in the test.

AA7475

Fig. 93 shows the EIS spectra after immersion for various times in a 0.5 M NaCl solution of the AA7475 samples anodised and postreated in a cold solution. The EIS spectra of the AA7475 specimens anodised at various temperatures and postreated in Alodine are shown in fig. 93a,b. Whereas Fig. 93c,d shows the EIS spectra of the AA7475 sample anodised at 37 °C for 20 min and immersed in the commercial Cr (III) compound for 1 min.

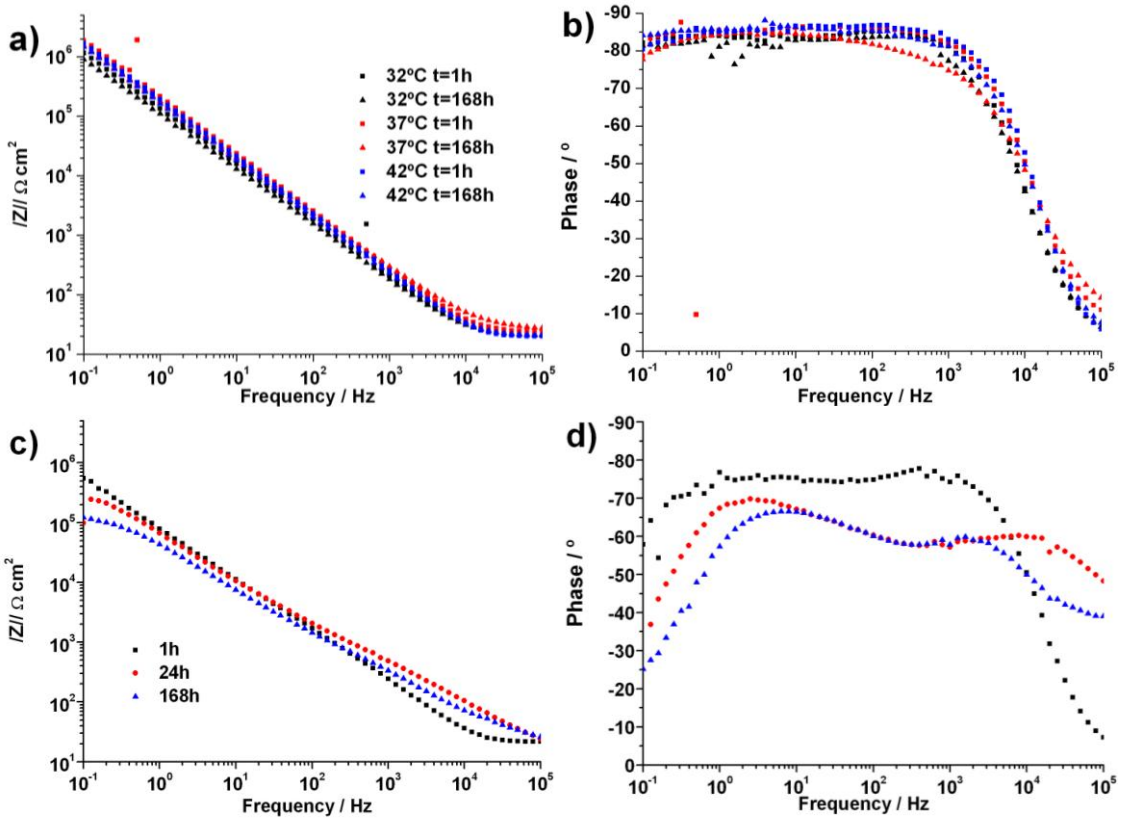

Figure 93. Bode plots after different immersion times in 0.5 M NaCl solution of AA7475 specimens (a,b) anodised at different temperatures and subsequently postreated with Alodine or (c,d) anodised at 37 °C and subsequently postreated with the commercial Cr(III) compound.

The EIS spectra of the AA7475 specimens anodised at different temperatures and postreated in Alodine show a constant modulus of the impedance after 168 h of immersion in the test solution. Conversely, whereas the sample anodised at 37 °C and subsequently postreated in the Cr (III) bath shows a decrease of the impedance in the low frequency range, and an increment in the high frequency range.

All the Alodine postreated spectra were fitted with the equivalent circuit described for anodised samples (EC1). In the case of the Cr (III) postreated EIS specimens, only the spectra acquired after 1 h of immersion was fully fitted with this model, whereas the EIS spectra of extended corrosion time were fitted with the same model but only in the frequency range of 10^{-1} to 10^{1} Hz.

Table 41. Results after fitting EIS data for the AA7475 specimens anodised at different temperatures and subsequently postreated with Alodine after different immersion times in 0.5 M NaCl solution.

Post treatment	C_b (μS cm^{-2})	1 h	24 h	168 h	R_b (kΩ cm^2)	1 h	24 h	168 h
	32 °C	0.94(1.00)	1.59(0.93)	1.67(0.93)	**32 °C**	>1000	>1000	>1000
Cr (VI)	**37 °C**	0.61(1.00)	1.61(0.91)	1.00(0.93)	**37 °C**	>1000	>1000	>1000
	42 °C	0.71(1.00)	1.00(0.96)	1.06(0.95)	**42 °C**	>1000	>1000	>1000
Cr (III)	**37 °C**	2.49(0.86)	4.38(0.78)	4.37(0.78)	**37 °C**	>1000	508	294

The C_b for the three Alodine postreated specimens are comparable after 1 h of immersion in the test solution, this parameter increases for the three samples after 24 h but C_b maintains or even decrease after 168 h of immersion. This fact, jointly with the high values of R_p denotes protection of the anodic film by the Cr (VI) species on the sample incorporated to the anodic layer.

The inhibitory properties of the Cr(III) conversion coating are also visible, but in a lesser extent than in the Cr (VI) postreated samples. In the first case the main inhibiting specie could be some molybdate meanwhile in the latter the specie is Cr (VI).

The comparison of these results with those obtained for the AA7475 specimens anodised at different temperature without further postreatment (section 5.1.) evidence improved behaviour against corrosion for the postreated samples. This fact is especially visible for the Cr (VI) postreated specimens. Such marked inhibitory effect could be attributed to accumulation of corrosion inhibitors in the structural flaws caused by the attack of the grain boundaries of the alloy during the pickling process.

The salt spray test results for the Alodine postreated-anodised AA7475 specimens are shown in table 42.

Table 42. Salt spray test results.

Postreatment	Anodising T (°C)	336 h	
		Pits dm^{-2}	% pass
Alodine	**32**	3.3	33
	37	1.3	50
	42	2.2	50

According to the eddy current measures in the section 5.1., there is not difference between the thicknesses of the anodic film growth at 37 and 42 °C for this alloy. Such feature is observed in the salt spray test, where the AA7475 samples anodised at 37 and 42 °C present similar results.

5.4. Primers and paints

It is of paramount importance to test the compatibility between the TSA bath and the paint systems**.** As indicated in the introduction, most of the aluminium alloys parts in the aircraft industry are usually painted (90-95%). One of the key objectives of a anodising process is to secure and excellent adhesion with the paint. This chapter is divided in two parts; the first one deals with the behaviour against corrosion of the coating system composed of an anodic film generated in the TSA bath and a Cr-loaded solvent based primer currently used in the aircraft industry. The aim of this first part is evaluating how can affect the anodic films generated in the TSA bath on both, the adherence of the primer and the corrosion resistance of the coating system.

The second part introduces some new chromium containing and chromium free water based coating systems that are tested in combination with TSA films.

5.4.1. Cr-loaded primer

The primer utilised in the aircraft finishing is an epoxy primer solvent based containing strontium dichromate; for the sake of simplicity, it will be named Cr-loaded primer. The primer was applied with a conventional air spray gun.

5.4.1.1. Primer thickness

The thickness of the system (comprising the anodic film and the organic coating) was measured by eddy currents, these data are shown in fig. 94.

All the samples present acceptable coating system thickness (between 15 and 35 µm) for the aerospace industry application.

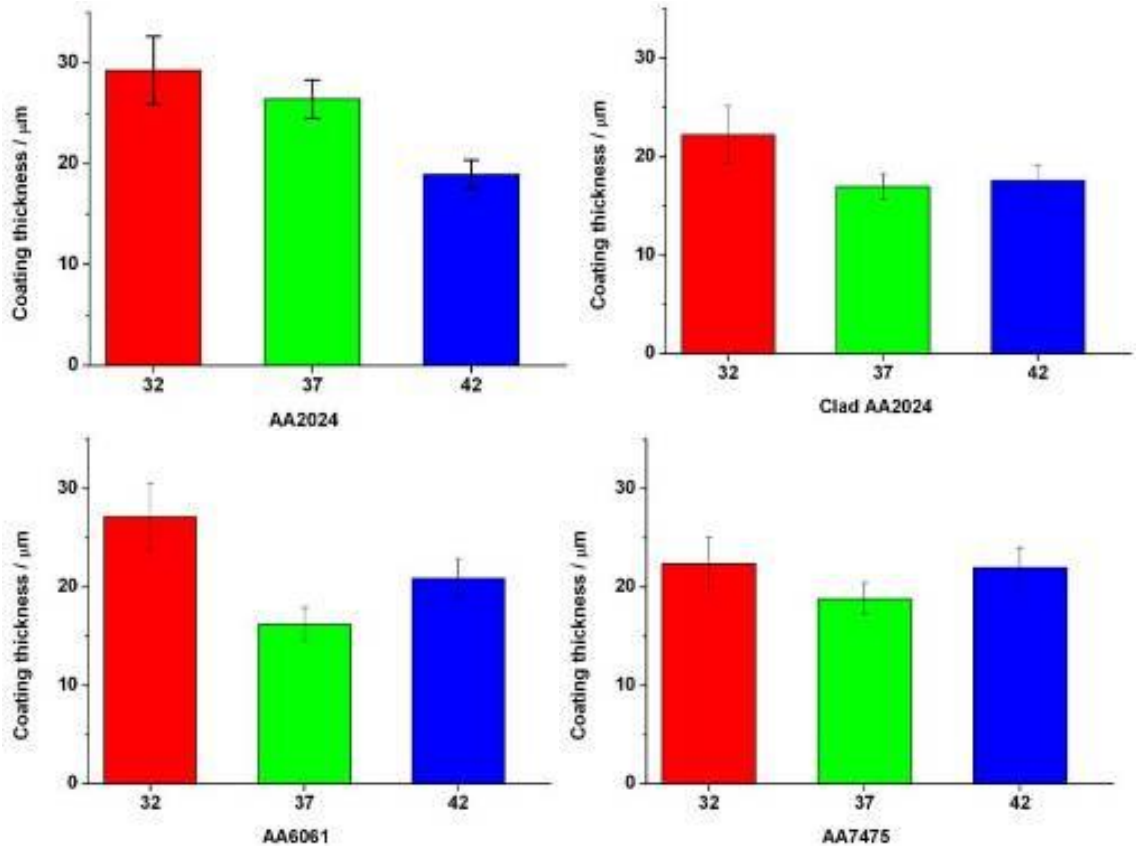

Figure 94. Coating thickness (anodic film + primer) of the specimens anodised at different temperaturas and primed with a Cr-loaded solvent-based organic primer: (a) AA2024 (b) clad AA2024 (c) AA6061 (d) AA7475.

5.4.1.2. Primer adherence

The adherence of the primer to the anodic film was evaluated according to ISO 2409 in dry conditions and wet conditions (after 14 days immersion in distilled water). The test was undertaken on AA2024, clad AA2024, AA6061 and AA7475 specimens TSA anodised at various temperatures and subsequently primed with the Cr-loaded primer.

The results obtained are classified in a six-step classification (0 to 5) attending to the visual appearance of surface of cross-cut area from which flaking has occurred. The result is considered to be 0 when the edges of the cuts are completely smooth and none of the squares of the lattice is detached. The result of the test is classified as 1 when there is detachment of small flakes of the coating at the intersections of the cuts and a cross-cut area not greater than 5 % is affected. The desirable results for the aircraft industry are classification 0 for dry cross cut test and 1 for wet cross cut test. Fig. 95. shows detailed image of the lattice after the test.

The result of the wet cross cut test for the sample in the fig. n is 0, it is clear that none of the squares of the lattice have been dethatched after the test. In general, the results obtained for all the triplicate tested samples in dry and wet condition was 0. Therefore, the adherence between the TSA anodic film and the Cr-loaded primer is excellent.

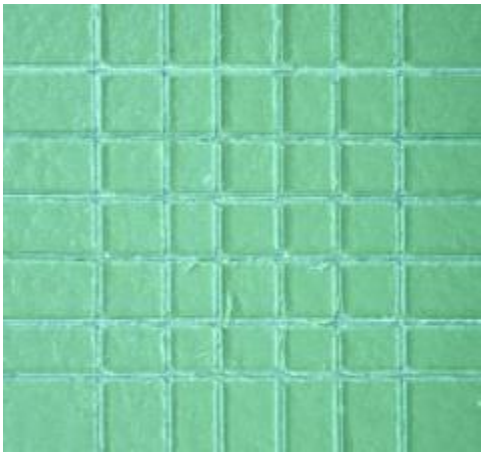

Figure 95. Detail of the surface of a clad AA2024 specimen anodised at 37 °C and primed with the Cr-loaded primer after wet cross cut test (result 0).

5.4.1.3. Study of the corrosion resistance of the coating system on different alloys by electrochemical impedance spectroscopy

In agreement with Murray [115], usually organic coating degradation proceeds through a number of stages. In a first approximation, these stages can be easily followed and differenced just observing the shape of the EIS spectra:

- Perfect coating. Starting from an ideal coating in the initial exposure to an electrolyte, the Bode plot shows a straight line of slope -1 with high impedance at low frequency and a phase angle of -90°.
- Water absorption. The coating absorbs water and therefore the impedance decrease but maintains a linear relationship with frequency. The slope does not change and the phase angle remains at -90°.
- Development of pore resistance. Once the electrolyte penetrating the coating creates a path to the underlying surface, the pore resistance decrease, this is evidenced in the EIS spectra by the appearance of a frequency independent plateau at the low frequency range, the phase angle is no longer constant with frequency and the value is 90° only at high frequencies. At this stage, there is not significant corrosion of the underlying surface.
- Initiation of corrosion of the substrate. As the electrolyte penetrates the coating and the underlying substrate contact with the electrolyte is increased, corrosion is initiated. The impedance in the low frequency range decreases in the Bode plot and a second constant of time appears. However, visual evidences do not usually accompany this corrosion process.
- Major coating damage. Finally, during the general corrosion o the substrate, the modulus of the impedance continues decreasing in the low frequency range. At this point, evidences of corrosion (e.g. delamination) are visually observed.

The EIS spectra of different aluminium alloys specimens (AA2024, clad AA2024, AA6061 and AA7475) anodised at various temperatures for 20 min in a TSA bath and primed are shown in fig. 96.

The EIS plots show some general trends for all the alloys. After 1 h of immersion time, the modulus of the impedance at 0.1 Hz show values comprised between 10^8 and 10^9 Ω cm^2 for all the tested conditions, this is indicative of a good coating system [89]. According to the former classification of the corrosion stage of an organic coating, direct observation of the EIS spectra after 1 h of immersion time reveals that two different phenomena can be taking place. On the one hand, there is a linear relationship between the impedance and the frequency in the studied frequency window; this indicates that the organic coating is absorbing water from the electrolyte. On the other hand, the phase angle at high frequencies presents values next to 90°. Although there is not a clear frequency independent plateau in the modulus of the impedance, the phase angle below 10 Hz diminish; such behaviour can indicate an early stage of the degradation of the organic coating.

In the case of longer immersion time in the 0.5M NaCl solution, a progressive decrease of the modulus of the impedance was observed, although only EIS spectra after 1440 h exposure has been plotted for the sake of simplicity. These EIS spectra show a $|Z|$ drop in all the measured frequency range, but especially in the low frequency range characteristic of the aluminium oxide/electrolyte interface beneath the organic coating. Besides, these changes are more marked in the samples anodised at 32 °C for most of the alloys.

The EIS spectra were fitted with the EC4 described in section 4.3. corresponding to a metal coated with an organic coating. The resistance of the pores of the coating and the resistance of the interface could not be determined accurately because of the overlapping of the two time constants. However, the calculated capacitances of the anodic film/electrolyte interface (C_{dl}) and the organic coating (C_c) give valuable information about the degradation of both the substrate and the organic coating.

The C_{dl} values calculated after different immersion times in the test solution for the AA2024, clad AA2024, AA6061 and AA7475 anodised in a TSA bath at various temperatures and Cr-loaded primed are shown in table 43.

The capacitance of the anodic film/electrolyte interface (C_{dl}) is due to the electrolyte penetrating through the organic coating that has reached the surface of the anodic film. During the experiment, C_{dl} is in the range of the nS, these values are lower than those observed for the anodised samples without organic coating directly exposed to the same test electrolyte (section 4.1.), where the interface between the based of the pores of the anodic film and the electrolyte (C_b) was in the range of µS.

In table 43, a progressive increase of C_{dl} is observed during the test for all the samples. This growth is random and is mainly due to the probability of the electrolyte to penetrate through the pores of the organic coating. However, after 1440 h of immersion the AA2024, AA6061 and AA7475 samples anodised at 32 °C and Cr-loaded primed present C_{dl} values about 1 order of magnitude higher than the corresponding samples anodised at higher temperatures. This could indicate an increased corrosion activity in these samples, probably due to the thinner anodic films obtained at relatively low temperatures. In any case, the behaviour of the coating system is excellent for all the studied samples.

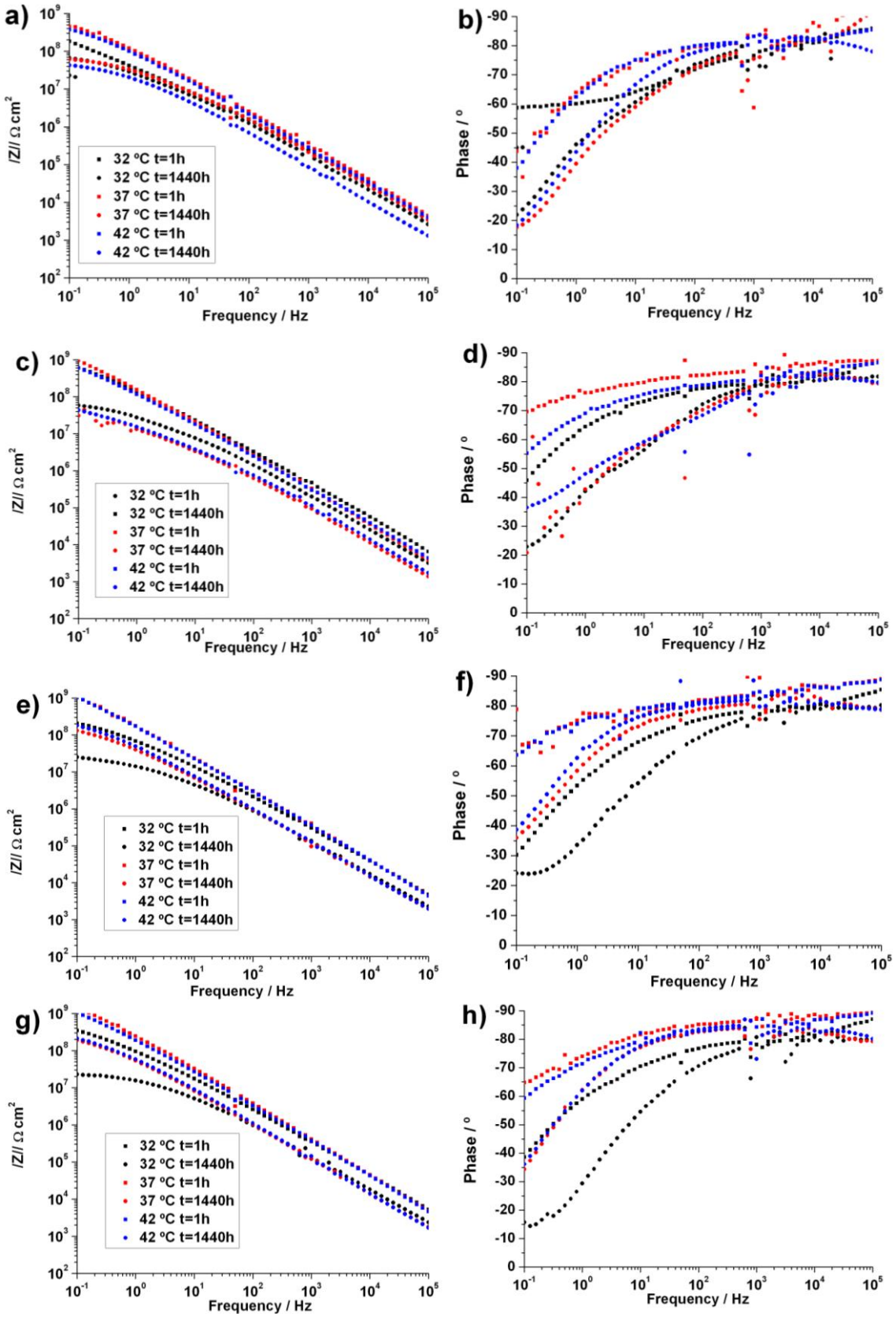

Figure 96. Bode plots after different immersion times in 0.5 M NaCl solution of (a,b) AA2024, (c,d) clad AA2024, (e,f) AA6061 and (g,h) AA7475 specimens anodised at different temperatures and subsequently primed with a chromium-containing primer.

Table 43. C_{dl} values obtained by fitting EIS data after different immersion times in 0.5 M NaCl solution of the aluminium alloys specimens anodised at diverse temperatures and subsequently primed with a chromium-containing primer.

Alloy	Anodising temperature	C_{dl} (nS cm^{-2}) after different immersion times in 0.5 M NaCl				
		1 h	168 h	720 h	1440 h	2160 h
AA2024	32 °C	0.82 (0.80)	5.84 (0.43)	11.0 (0.35)	7.69 (0.60)	-
	37 °C	0.44 (0.75)	5.15 (0.43)	7.82 (0.48)	5.94 (0.61)	-
	42 °C	1.49 (0.51)	-	9.87 (0.46)	10.9 (0.42)	12.2 (0.50)
Clad AA2024	32 °C	1.32 (0.69)	2.46 (0.59)	5.76 (0.51)	10.2 (0.47)	14.5 (0.37)
	37 °C	0.96 (0.72)	101 (0.42)	42.5 (0.37)	27.0 (0.45)	26.3 (0.46)
	42 °C	1.46 (0.68)	-	20.6 (0.47)	19.6 (0.53)	23.1 (0.49)
AA6061	32 °C	2.91 (0.57)	12.2 (0.40)	15.5 (0.39)	28.7 (0.30)	28.4 (0.21)
	37 °C	0.49 (0.57)	10.0 (0.24)	7.23 (0.43)	5.71 (0.36)	-
	42 °C	0.89 (0.73)	6.08 (0.20)	12.1 (0.30)	4.89 (0.28)	-
AA7475	32 °C	2.08 (0.62)	10.1 (0.26)	9.46 (0.45)	14.7 (0.38)	22.0 (0.32)
	37 °C	0.51 (0.78)	3.14 (0.53)	4.43 (0.48)	3.58 (0.51)	-
	42 °C	0.59 (0.37)	4.25 (0.26)	-	4.30 (0.40)	-

Table 44 shows the C_c values obtained after different immersion times in the test solution for AA2024, clad AA2024, AA6061 and AA7475 anodised at different temperatures and Cr-loaded primed.

Table 44. C_c values obtained by fitting EIS data after different immersion times in 0.5 M NaCl solution of the aluminium alloys specimens anodised at diverse temperatures and subsequently primed with a chromium-containing primer.

Alloy	Anodising temperature	C_c (nS cm^{-2}) after different immersion times in 0.5 M NaCl solution				
		1 h	168 h	720 h	1440 h	2160 h
AA2024	32 °C	0.31 (0.99)	1.03 (0.97)	1.40 (0.91)	2.44 (0.89)	-
	37 °C	0.24 (0.99)	1.52 (0.92)	1.49 (0.93)	0.73 (0.97)	-
	42 °C	1.13 (0.92)	-	3.18 (0.92)	3.39 (0.93)	3.59 (0.93)
Clad AA2024	32 °C	0.42 (0.96)	0.80 (0.93)	0.96 (0.94)	1.40 (0.92)	2.29 (0.90)
	37 °C	0.50 (0.98)	2.63 (0.91)	3.13 (0.92)	3.08 (0.93)	3.18 (0.93)
	42 °C	0.61 (0.96)	-	2.39 (0.92)	2.03 (0.94)	2.29 (0.93)
AA6061	32 °C	0.98 (0.92)	1.59 (0.91)	2.11 (0.91)	3.50 (0.88)	5.37 (0.86)
	37 °C	0.84 (0.94)	2.23 (0.89)	2.43 (0.91)	3.04 (0.91)	-
	42 °C	0.44 (0.99)	2.28 (0.88)	2.96 (0.90)	2.85 (0.91)	-
AA7475	32 °C	0.66 (0.94)	1.44 (0.91)	1.82 (0.91)	2.92 (0.89)	4.50 (0.87)
	37 °C	0.64 (0.95)	1.84 (0.91)	2.15 (0.93)	2.42 (0.93)	-
	42 °C	0.83 (0.93)	2.05 (0.94)	-	2.12 (0.94)	-

The capacitance of the coating (C_c) after 1 h of immersion for all the studied samples is that of a typical undamaged coating with good barrier properties, about 1 nS cm^{-2} [89]. C_c values grow up progressively for all the samples with immersion time. The similarities of the C_c values lead to think that during the test, the behaviour of the organic coating is independent of the underlying anodic film.

Considering that the main phenomena occurring during the test is the water absorption of the organic coating, the evolution of the water absorbed by the Cr-loaded primer on the different specimens can be calculated by means of the Brasher-Kingsbury model.

If the organic coating is considered as a parallel plate capacitor, the its capacitance is related with the relative dielectric constant

$$C = \varepsilon\varepsilon_0 A / d$$

Considering ε_0 (dielectric constant of free space, $8.854e^{-14}$ F cm^{-1}), A (surface area of the coating) and d (the coating thickness) as constant values and taking into account that the relative dielectric constant for polymers is 3-8 [116] and for pure water at 25 °C is 78.9, an increase in the capacitance must be due to the water uptake.

According to a formula proposed by Hartshorn, Megson & Rushton [117] for a coating composed of three phases – solid, water and air – the mixed dielectric constant of the coating would be given by:

$$\varepsilon_x = \varepsilon_s^{\phi s}\, \varepsilon_w^{\phi w}\, \varepsilon_a^{\phi a} \quad (1)$$

where ϕ represents the volume fraction of each of the components, and the subscripts s, w and a correspond to the solid phase, the water and the air, respectively.

By taking the dielectric constant of air as $\varepsilon_a \approx 1$ and taking into consideration that for low water content $\phi_s = 1 - \phi_w - \phi_a \approx 1$, re-arrangement of equation (1) gives the Brasher and Kingsbury equation [118]:

$$\phi_s = \log (C_t/C_0)/\log (\varepsilon_w) \quad (2)$$

where C_t and C_0 are the values of capacitance at an instant t and for the "dry" coating, respectively.

The Brasher-Kingsbury equation (2) assumes that the increase of the coating capacitance is only due to the ingress of water, that there is no swelling of the film and that the distribution of water in the film is uniform and with a low volume fraction.

In general, the % water uptake was calculated taking the capacitance of the coating, C_c, after 1 h of immersion in the test solution as C_0 for each single sample. C_t was the C_c after longer exposure times.

Fig. 97 shows the evolution of the water uptake for the Cr-loaded primer on variously anodised alloys during the immersion in a 0.5 M NaCl solution.

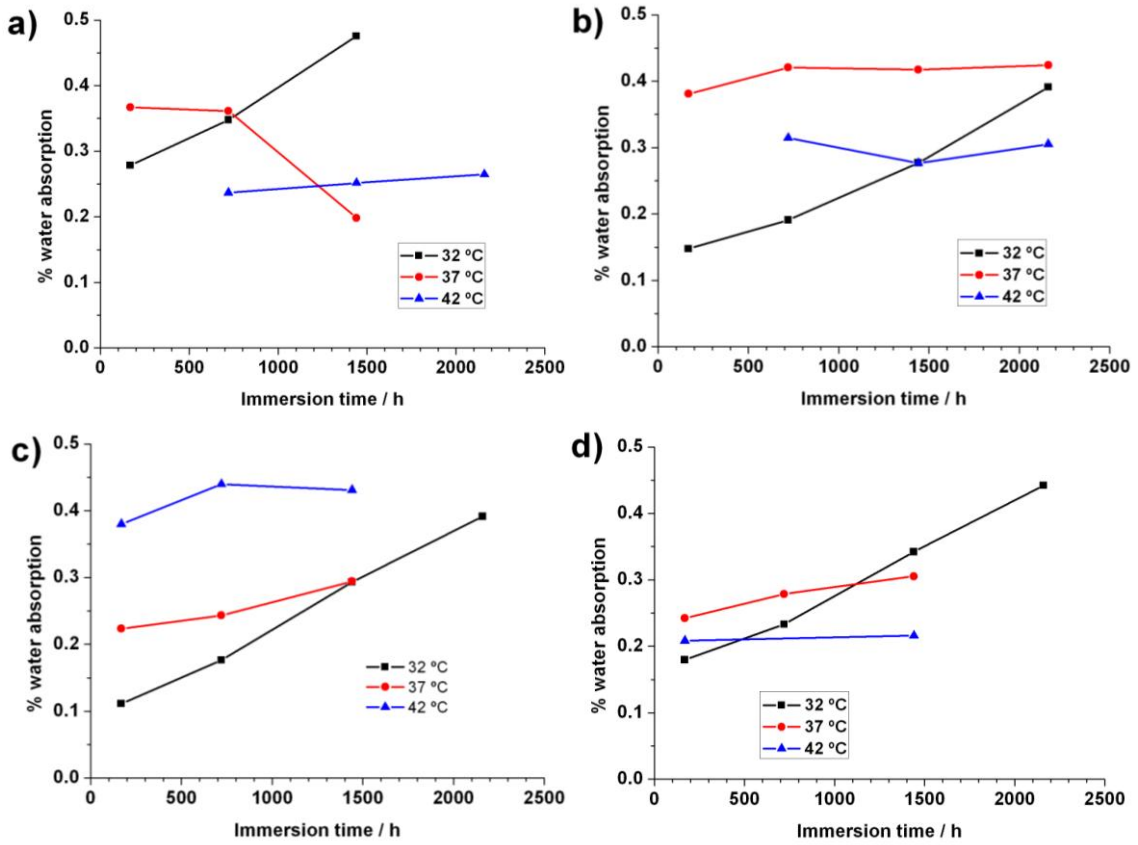

Figure 97. % of water absorbed by the primer applied on (a) AA2024, (b) clad AA2024, (c) AA6061 and (d) AA7475 specimens anodised at variously temperatures. The % absorbed water at different immersion times is related to the EIS measurement after 1 h of immersion for each alloy.

In general, the water absorption during the test time is low; in some cases the water absorption achieves values about 0.4 % after 168 h of immersion and maintain relatively constant during the test time. Other samples show lower water uptake after 168 h but progressive water absorption with immersion time. In any case, the values obtained are always below 0.5 %.

Visual inspection of the samples after the end of the test revealed no signs of blistering or detachment of the primer, only loss of colour due to the leaching of chromates was evident (fig. 98).

Figure 98. Visual aspect of a primed specimens after 2180 h of immersion in 0.5 M NaCl solution.

The protective system composed of an aluminium alloy, an anodic film generated in a TSA bath and a Cr-loaded primer performed both good adhesive properties between the anodic film and the primer and excellent corrosion resistance properties. Therefore, it can be concluded that the TSA anodic films are suitable for supporting the primers currently utilised in the aircraft industry. This is a very important feature for the substitution of the chromic acid baths.

5.4.2. Water-based primers and paints

The needs of reducing the toxicity of the primers and paints by both the elimination of volatile organic compounds (VOC) and dichromate from the paint formulation are becoming essential to fulfil new regulations and some manufacturers commercialise this kind of primers. However, the introduction of such primers in the aerospace industry is challenging due to the demanding requirements associated with aircraft safety and reliability.

Therefore, some new water-based primers were tested on different treated AA2024 specimens with a double aim; firstly, testing the compatibility of different treatments and the water-based primers and secondly, testing the corrosion resistance of the water-based primers themselves.

Two different water-based primers were evaluated: a Cr-containing water-based primer and a non Cr-containing water-based primer but with corrosion inhibitors. The formulation of these primers becomes significantly more complex than the organic solvent based primers. Most of the components of a primer including water dispersible/emulsifiable binders, film forming resins, pH buffers, anti-foaming agents, surfactants and fungicides have to be considered simply due to the presence of water [119].

Besides, in the case of the Cr-free primer, new corrosion inhibitors, such as oxides, hydroxides phosphates and borates of calcium, magnesium and zinc [120] as well as an ion exchange silica of low toxicity [121] has been tested with promising results.

The water-based primers were applied on AA2024 specimens. Such specimens were prepared following different surface treatments prior to the primer application, namely acid pickling, acid pickling plus Cr (VI) CCC (Alodine 1200) and acid pickling plus TSA anodising. Both primers were also tested after the application of a topcoat.

The topcoat is expected to work as a barrier that impedes the penetration of organic fluids, but it will not provide corrosion resistance to the coating system.

The following table summarises the tested coating systems. For the sake of simplicity, the abbreviations defined in table 45 will be used in the following discussion.

Table 45. Summary of the different treated AA2024 specimens and nomenclature.

Pretreatment/Painting	Cr-containing water-based primer (C)	Non Cr-containing water-based primer (N)	Cr-containing water-based primer + topcoat (CT)	Non Cr-containing water-based primer + topcoat (NT)
Pickling (1)	1C	1N	1CT	1NT
Pickling + Alodine (2)	2C	2N	2CT	2NT
Pickling + TSA anodising (3)	3C	3N	3CT	3NT

5.4.2.1. Thickness of the coating system

The thickness of the coating systems was measured by eddy currents on 10 locations of a set of three samples anodised and coated with the different coating systems. The results are shown in fig. 99.

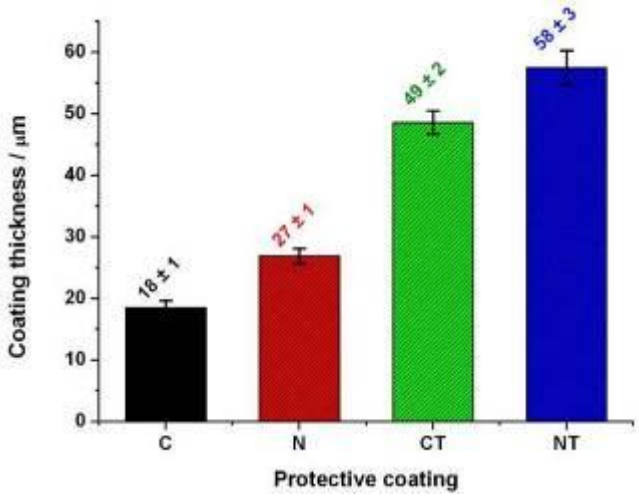

Figure 99. Coating thickness of the AA2024 specimens anodised and coated with different coating systems.

The thicknesses of the protective systems were in accordance with those defined by the manufacturer. It is important to remind that the coating application has to be minimal to avoid weight gain in the airplane and usually is kept between 15 and 35 µm. The thickness of the Cr-containing water-based primer is comparable to that applied on the Cr-loaded primer (see section 4.3.1.1.). The non Cr-containing water-based primer was applied in a slightly thicker coating, resulting approximately 10 µm thicker in both N and NT samples. The topcoat was applied simultaneously in both C and N primed samples and therefore the thickness is presumable the same and about 30 µm according figure 99.

5.4.2.2. Study of the corrosion resistance of the different coating systems on AA2024 by electrochemical impedance spectroscopy.

The evaluation of the behaviour against corrosion of the coating systems described in table 45 was studied by EIS. The EIS plots of these samples after different immersion times in a 0.5 M NaCl solution are shown in fig. 100.

It is important to emphasize that the different pretreatments before primer application result in notable physical differences among the studied samples. In the case of the pickled and coated samples (named as 1), the interface is a metal/electrolyte interface, the Alodine and coated samples (2) interface is a metal oxide /electrolyte interface, with the Al somehow passivated by the formation of a mixed Cr-Al hydroxide by the action of the Alodine. The anodised and coated sample interface is a pure metal oxide/electrolyte interface (3). That interface between the underlying surface and the electrolyte penetrating through the primer will be directly observable by means of the double layer, C_{dl}, value according the equivalent circuit electrochemical corrosion theory.

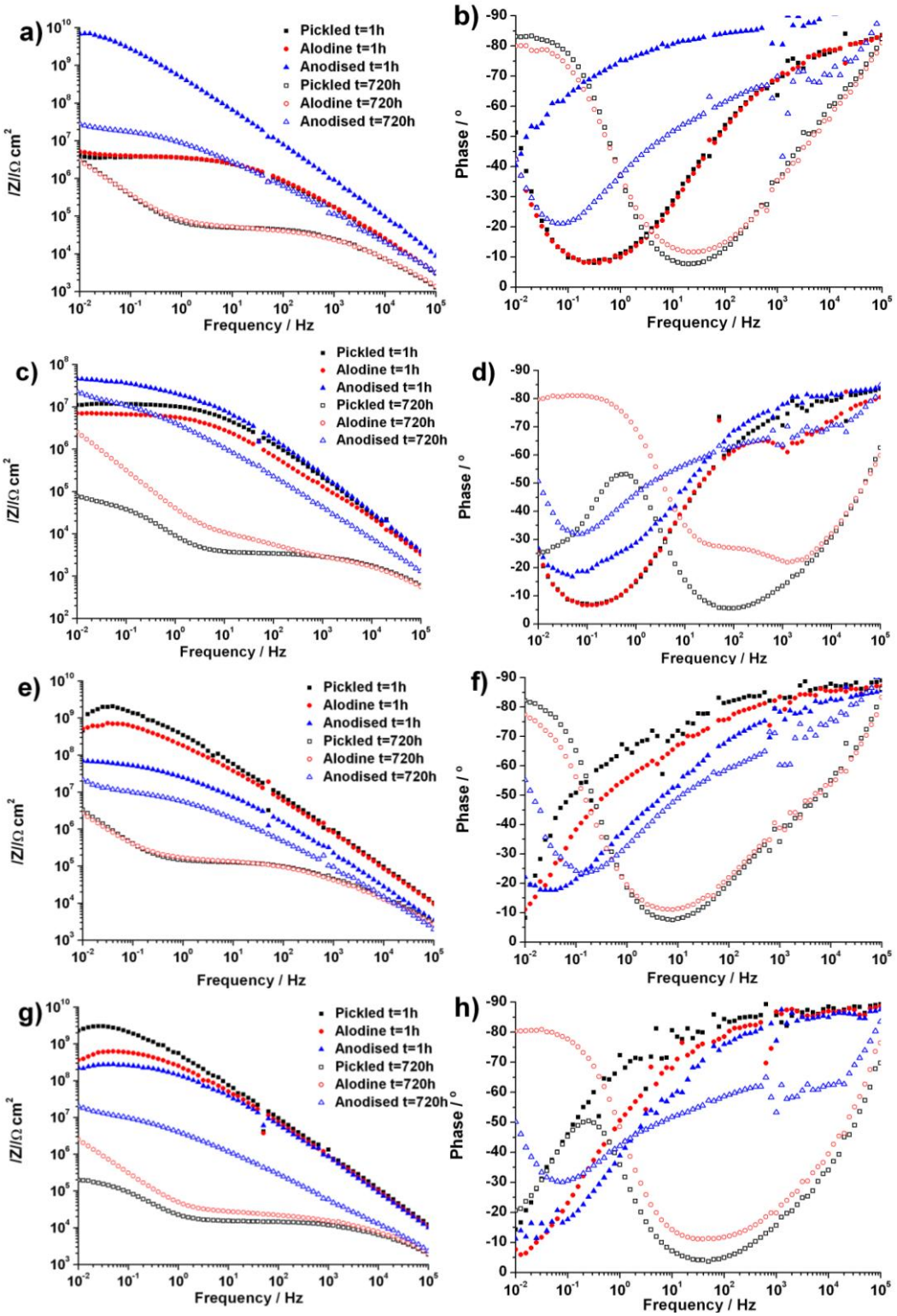

Figure 100. Bode plots after different immersion times in 0.5 M NaCl solution of AA2024 specimens pickled, pickled + Alodine or anodised and (a,b) primed with a chromium-containing water-based primer, (c,d) primed with a non chromium-containing water-based primer (e,f) primed with a chromium-containing water-based primer + topcoat finish (g,h) primed with a non chromium-containing water-based primer + topcoat finish.

Observation of the EIS spectra in fig. 100ab reveals that the 3C sample present high $|Z|_{0.1\ Hz}$ (over 10^9 Ω cm^2) after 1 h of immersion and a phase angle frequency independent at high frequencies. According to the diagnosis criteria described in the beginning of this chapter, after 1 h of immersion the coating has absorbed water and the pore resistance is diminishing. The $|Z|$ decrease after 720 h of immersion indicates further water uptake and decrease of the pore resistance.

In the case of the 1C and 2C samples, there is a plateau frequency-independent (about 5 $x10^6$ Ω cm^2) in the low frequency range indicates corrosion initiation of the substrate even after only 1 h of immersion. Besides, after 720 h exposure to the corrosive solution, a second constant of time is observed for the two samples, this is characteristic of extended underlying corrosion processes.

The EIS spectra of the specimens primed with the non-chromium containing primer (fig. 100cd) reveals that the sample 3N present lower $|Z|_{0.1\ Hz}$ after 1 h of immersion (about $5x10^7$ Ω cm^2) than the sample 3C. However, the results after 720 h of immersion for these two samples in the low frequency range are very similar. The samples that were not anodised before priming (samples 1N and 2N) show the same shape that the observed for the samples 1C and 2C after 1 h of immersion. However, further decrease of the EIS spectra after 720 h for the sample 2N, and especially for the sample 1N is observed. Therefore the substrate underlying the primer in the 1N sample has experienced extended corrosion compared to the 2N sample.

The topcoat clearly slows down the penetration of the solution after 1 h of immersion. This is evident by simple visual observation of the EIS spectra of the 1CT and 2CT samples (fig. 100ef) compared to the samples without topcoat (samples 1C and 2C in the fig. 100cd). The similar phenomenon was observed for the 1NT and 2NT samples after 1 h of exposure to the test solution (fig. 100gh). After 720 h of immersion the $|Z|$ of these four samples (1CT, 2CT, 1NT and 2NT) severely fall and show two constants of time, at this point the behaviour of each sample is that observed for the respective primed sample without topcoat.

In the case of the anodised samples, the topcoat shows modest changes in the EIS spectra. In fact, 3C shows higher $|Z|$ than 3CT after 1 h of exposure; however the evolution of the EIS spectra after 720 h leads to similar shapes and $|Z|$ values. The 3NT samples perform similar behaviour than the 3N samples for short and long immersion times.

Quantitative analysis of the evolution of the EIS spectra previously discussed is shown in table 46.

The clear differences in the C_{dl} values observed after 1 h of exposure to the test solution between the 3C sample and the 1C and 2C samples evidence the dissimilarities of the metal/electrolyte and metal oxide/electrolyte interfaces. Considering that the water uptake of the coating after 1 h is comparable for all the samples (values of C_c after 1 h in table 47) the corrosion processes are quicker in the metal/electrolyte than in the metal oxide interfaces. This is confirmed by the remarkable increase of C_{dl} values for 1C (4.4 µS cm^{-2}) and 2C (3.5 µS cm^{-2}) samples after 168 h of exposure to the test solution. On the contrary, the anodised sample 3C (C_{dl} = 0.027 µS cm^{-2}) present values two orders of magnitude lower that are relatively constant during the test.

Table 46. C_{dl} values obtained by fitting EIS data after different immersion times in 0.5 M NaCl solution of various AA2024 specimens protected with different coating systems.

Sample	C_{dl} (nS cm^{-2}) after different immersion times in 0.5 M NaCl					
	1 h	168 h	336 h	720 h	1440 h	2140 h
1C	18.1(0.59)	4348(0.94)	4288(0.94)	4288(0.94)	4126(0.94)	4011(0.92)
2C	43.2(0.34)	3501(0.84)	3607(0.86)	3886(0.88)	3861(0.88)	4068(0.90)
3C	0.31(0.54)	26.8(0.34)	35.8(0.40)	28.4(0.45)	30.5(0.43)	31.8 (0.43)
1N	14.6(0.71)	18402(0.88)	29473(0.94)	30710(0.94)	32673(0.94)	41823(0.92)
2N	14.2(0.65)	3994 (0.91)	4061 (0.91)	3969 (0.90)	4609(0.89)	4028 (0.88)
3N	17.0(0.45)	83.2 (0.56)	89.2 (0.55)	56.3 (0.52)	66.3(0.50)	-
1CT	0.69(0.55)	4180(0.93)	4176(0.93)	4026(0.93)	3901(0.93)	3713(0.91)
2CT	1.25(0.66)	3689(0.83)	4025(0.85)	4063(0.85)	4387(0.86)	4359(0.86)
3CT	12.3(0.47)	32.9 (0.55)	51.0 (0.39)	51.3 (0.44)	30.2(0.55)	-
1NT	0.45(0.24)	4451(0.91)	9950(0.84)	15009(0.89)	20407(0.78)	25952(0.76)
2NT	2.00(0.13)	4589(0.90)	4707(0.91)	4788 (0.90)	4832(0.90)	4715(0.59)
3NT	3.79(0.30)	43.7(0.62)	78.2(0.52)	64.7(0.55)	55.8(0.58)	-

C_{dl} for the 1C sample remained relatively constant during the rest of the experiment. However, in the case of the 2C sample, C_{dl} is lower than for the 1C sample but progressively increases until reaching similar values than the 1C sample. This dissimilarity can be due to the action of the chromate of the passive film formed by the Alodine process. The low effect of the Alodine conversion coating leads to think that the inhibitory effect is mainly due to the Cr contained in the water-based primer. This fact was observed by Twite [122] in similar systems composed of aluminium, a chromium conversion coating and a Cr-loaded solvent based primer.

The evolution of the C_{dl} for the AA2024 samples primed with the N primer is different. After 1 h of immersion the three samples (1N, 2N and 3N) present similar values, although the resistance to water uptake is lower than that exhibited by the C primer (capacitance of the coating in table n+1 is higher for the N samples), the thicker coating of the N primer (27 ± 1 µm compared to 18 ± 1 µm) can rather delay the solution from reaching the substrate/electrolyte interface comparing with the thinner C primer specimens.

The sample 1N only contains the inhibitors of the N primer. Such inhibitors present a fairly poor resistance to corrosion or perhaps are quickly consumed, as C_{dl} increases 3 orders of magnitude only in 168 h of immersion. Besides C_{dl} continues growing during the test, and blistering of the coating due to accumulation of voluminous corrosion products could be visually observed. (fig. 101). The 2N sample present C_{dl} values similar to those observed for the 2C sample after 168 h and longer immersion times. In this case the inhibitory effect of chromate of the chromate conversion coating is comparable to that observed by the pigments contained in the C primer of the samples 1C and 2C. The increase with immersion time of C_{dl} for the 3N sample is higher, but comparable to that observed for the 3C sample.

Therefore, the C_{dl} analysis evidences that for this water-based primers, the effect of the pretreatment before priming of the sample is, by far, much more important than the inhibitory pigments of the primers.

Table 47 shows the calculated values of the capacitance of the water-based primers and topcoat.

Table 47. C_c values obtained by fitting EIS data after different immersion times in 0.5 M NaCl solution of various AA2024 specimens protected with different coating systems.

Sample	C_c (nS cm^{-2}) after different immersion times in 0.5 M NaCl					
	1 h	168 h	336 h	720 h	1440 h	2140 h
1C	0.47(1.00)	35.7(0.73)	38.7(0.73)	37.1(0.74)	34.7(0.75)	33.7(0.76)
2C	2.87(0.87)	54.8(0.83)	61.6(0.69)	54.7(0.71)	48.5(0.72)	50.8(0.73)
3C	0.23(0.98)	5.87(0.79)	5.61(0.81)	6.21(0.81)	5.82(0.82)	5.29(0.83)
1N	2.79(0.85)	404(0.61)	366(0.62)	201(0.67)	186(0.70)	121(0.73)
2N	1.30(0.93)	857(0.57)	841(0.58)	782(0.59)	609(0.58)	496(0.61)
3N	1.45(0.90)	22.3(0.78)	16.2(0.80)	15.0(0.81)	12.3(0.83)	-
1CT	0.21(0.98)	39.3(0.66)	49.6(0.64)	49.8(0.65)	52.0(0.66)	47.0(0.67)
2CT	0.31(0.95)	51.3(0.64)	69.9(0.62)	72.3(0.63)	80.6(0.63)	66.2(0.64)
3CT	0.95(0.95)	1.10(0.96)	4.97(0.85)	5.92(0.83)	3.18(0.90)	-
1NT	0.25(0.95)	29.7(0.69)	50.4(0.66)	65.3(0.68)	44.4(0.70)	41.6(0.70)
2NT	0.40(0.92)	63.0(0.64)	141(0.59)	115(0.62)	109(0.63)	98.4(0.64)
3NT	0.32(0.94)	1.22(0.91)	11.2(0.77)	7.26(0.80)	7.39(0.78)	0.32(0.94)

The capacitance of the coating is dependant on the coating material and thickness, a good coating present initial C_c values between 0.1-1 nS cm^{-2} [89]. The C_c values are relatively similar after 1 h of exposure for the samples with a common primer.

The properties of the coating are expected to be independent of the underlying substrate for short immersion times, however, after 168 h of immersion, there exist a difference of one order of magnitude between the anodised substrates and the not anodised substrates. These results suggest that the degradation of the coating is advancing in two ways: on the one hand the penetration of water, salts and oxygen from the solution through the coating is a common phenomena for all the samples. On the other hand, the corrosion products formed in the interface substrate/electrolyte can create stresses that involve coating deformation or detachment. This second feature was especially observed for the 1N and 1NT samples, which presented the higher C_{dl} values (fig. 101).

As a result, the water uptake for the non-anodised specimens could not be calculated by the Braser-Kingsbury equation. The water uptake of the anodised and primed samples will be discussed in the next section.

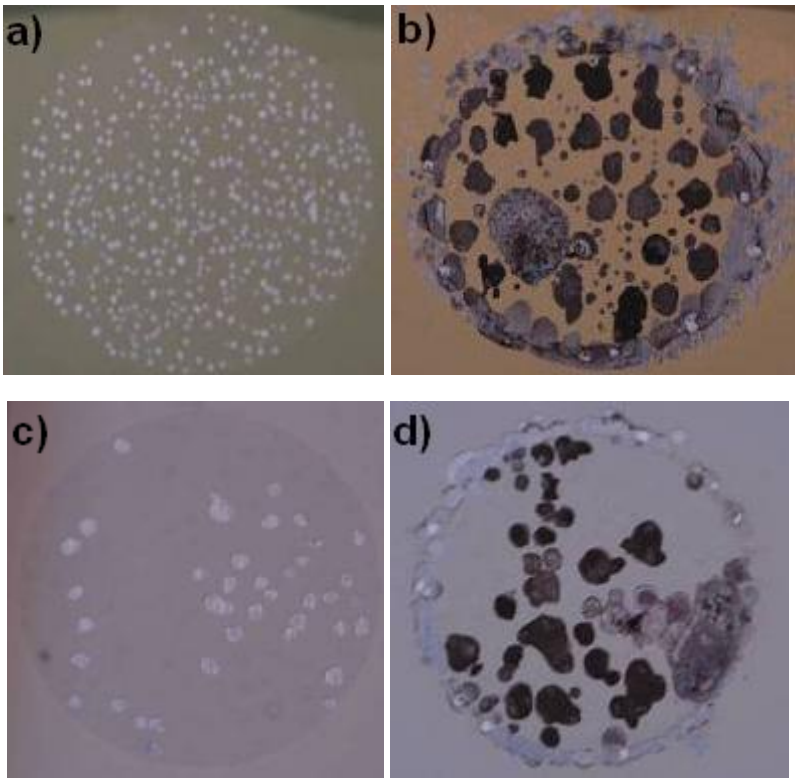

Figure 101. Visual aspect of the (a) 1C (b) 1N (c) 1CT and (d) 1CN specimens after 2140 h of immersion in the 0.5 M NaCl solution.

5.4.2.3. Study of the effect of the test solution temperature on the corrosion resistance of the anodised and coated AA2024 specimens by electrochemical impedance spectroscopy

From previous section, it is clear that the best of the studied surface treatments (pickling, chemical conversion coating or TSA) combined with the water-based primer is the generation of a TSA anodic film. The following step was to evaluate the behaviour against corrosion of such samples at different test temperatures.

The evolution of the EIS spectra with immersion time in a 0.5 M solution at different times for the AA2024 anodised in TSA and finished with different coating systems are shown in fig. 102.

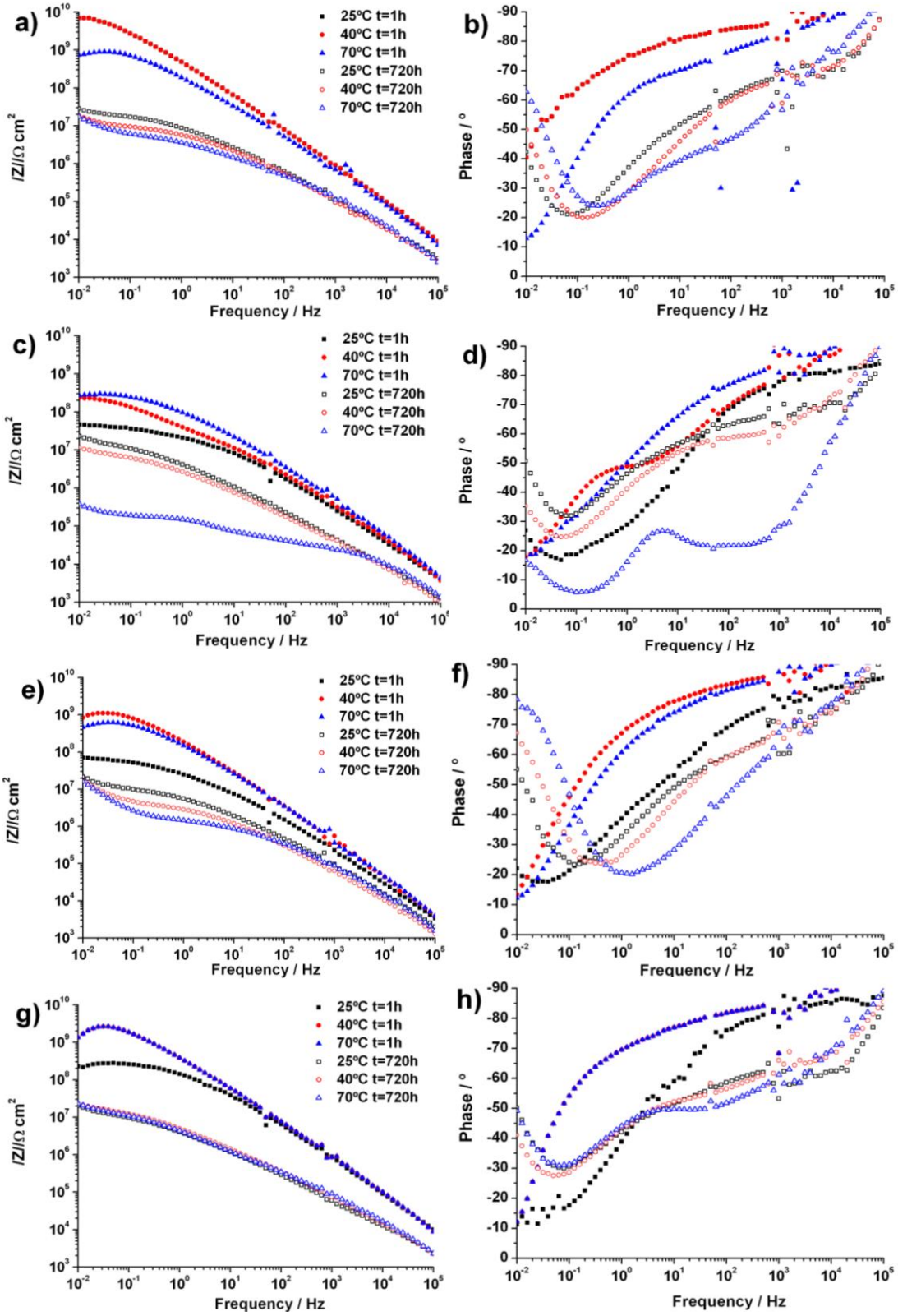

Figure 102. Bode plots after different immersion times in 0.5 M NaCl solution at various temperatures of AA2024 specimens anodised and (a,b) primed with a chromium-containing water-based primer, (c,d) primed with a non chromium-containing water-based primer (e,f) primed with a chromium-containing water-based primer + topcoat finish (g,h) primed with a non chromium-containing water-based primer + topcoat finish.

In all cases the EIS spectra is recorded after waiting (approximately 1 h) to the specimen and cell to reach the room temperature after the variable time of immersion at the fixed high temperature.

After 1 h of immersion for the different samples, the EIS spectra for each coating system are similar in the high frequency range, indicating similar behaviour of the coating. On the contrary, they differ in the low frequency range. This characteristic is attributable to the probability of the electrolyte to pass through the amorphous, porous primer, which is not necessarily equal after 1 h of immersion.

After 720 h of immersion in the test solution, the impedance decreased for all the samples. This drop of the Z was more marked with increased test temperatures. In the case of the C primed, CT primed or NT samples, only small differences in the high frequency region were observed. However, in the case of the N samples, the effect of the temperature was especially noticeable for the sample tested at 70 °C.

The quantification of these features was possible by fitting of the EIS spectra with the EC4. The calculations of the C_{dl} values are shown in table 48.

Table 48. C_{dl} values obtained by fitting EIS data after different immersion times in 0.5 M NaCl solution at different temperatures of various AA2024 specimens anodised and protected with different coating systems.

Finishing	Test solution temperature	C_{dl} (nS cm^{-2}) after different immersion time in 0.5 M NaCl			
		1 h	168 h	336 h	720 h
Cr-containing primer	RT	0.31 (0.54)	26.8 (0.34)	35.8 (0.40)	28.4 (0.45)
	40 °C	0.31 (0.54)	65.5 (0.34)	52. 3 (0.41)	45.3 (0.43)
	70 °C	0.93 (0.71)	183 (0.23)	37.9 (0.29)	91.0 (0.42)
Non Cr-containing primer	RT	17.0 (0.45)	83.2 (0.56)	89.2 (0.55)	56.3 (0.52)
	40 °C	7.32 (0.61)	83.7 (0.58)	89.7 (0.56)	92.4 (0.57)
	70 °C	9.13 (0.50)	141 (0.59)	145 (0.68)	1305 (0.60)
Cr primer + topcoat	RT	12.3 (0.47)	32.9 (0.55)	51.0 (0.39)	51.3 (0.44)
	40 °C	1.00 (0.64)	137 (0.33)	128 (0.32)	126 (0.27)
	70 °C	1.36 (0.57)	733 (0.85)	715 (0.84)	667 (0.83)
Non Cr primer + topcoat	RT	3.79 (0.30)	43.7 (0.62)	78.2 (0.52)	64.7 (0.55)
	40 °C	3.79 (0.30)	44.5 (0.58)	54.5 (0.58)	56.6 (0.58)
	70 °C	3.79 (0.30)	73.4 (0.49)	60.0 (0.51)	76.8 (0.51)

The initial capacitance of the interface anodic film/electrolyte (C_{dl}) presents some variation after 1 h of immersion. However, after 168 h the effect of temperature is observable for all the studied coatings; C_{dl} values are higher for the increased test temperatures. This tendency continues during the rest of the experiment. After 720 h, The C primer shows better behaviour than the N primer for all the studied temperatures.

On the other hand, the degradation of the coating can be qualitatively estimated by fitting of the C_c from the EIS spectra. The results are shown in table 49.

Table 49. C_c values obtained by fitting EIS data after different immersion times in 0.5 M NaCl solution at different temperatures of various AA2024 specimens anodised and protected with different coating systems.

Finishing	Test solution temperature	C_c (nS cm^{-2}) after different immersion time in 0.5 M NaCl			
		1 h	168 h	336 h	720 h
Cr-containing primer	RT	0.23 (0.98)	5.87 (0.79)	5.61 (0.81)	6.21 (0.81)
	40 °C	0.23 (0.98)	5.29 (0.83)	4.79 (0.84)	5.05 (0.84)
	70 °C	0.40 (0.94)	4.71 (0.81)	3.39 (0.83)	0.99 (0.95)
Non Cr-containing primer	RT	1.45 (0.90)	22.3 (0.78)	16.2 (0.80)	15.0 (0.81)
	40 °C	0.66 (0.96)	4.03 (0.96)	2.89 (0.95)	8.03 (0.88)
	70 °C	0.37 (1.00)	7.58 (0.83)	6.24 (0.86)	23.1 (0.75)
Cr primer + topcoat	RT	0.95 (0.95)	1.10 (0.96)	4.97 (0.85)	5.92 (0.83)
	40 °C	0.37 (0.99)	16.5 (0.79)	12.6 (0.82)	12.3 (0.82)
	70 °C	0.44 (0.98)	8.11 (0.81)	10.9 (0.80)	16.0 (0.77)
Non Cr primer + topcoat	RT	0.32 (0.94)	1.22 (0.91)	11.2 (0.77)	7.26 (0.80)
	40 °C	0.32 (0.94)	0.60 (0.99)	0.83 (0.97)	1.29 (0.95)
	70 °C	0.32 (0.94)	0.97 (0.96)	0.89 (0.97)	5.16 (0.84)

The coating capacitances are relatively similar for all the samples after 1 h of immersion. The increase of Cc is small after 720 h of immersion for all the studied samples and they vary randomly; there is not thus a clear effect of the temperature on the degradation of the coating. Therefore, these organic coatings perform good behaviour under extreme test conditions. The water uptake of the primers can be calculated by the Braser-Kingsbury modelling (see 5.3.1). Such water absorption during the experiment is shown in fig. 103.

The water uptake of the various coatings seems to be little influenced by the test temperature. The variation of the water uptake is random during the test and ranges between 0.3% and 1.0% after 720 h. However, to some extend the water-based primers seem to be more prone to the water absorption than the Cr-loaded solvent based primer discussed in section 5.3.1.

On the contrary, the corrosion of the substrate is influenced by the temperature; higher test temperature has resulted in higher capacitance of the interface anodic film/electrolyte. This fact is especially marked for the N coatings at 70 °C. However, the extended corrosion of the substrate with temperature cannot be attributed to a quicker water uptake of the coating, which is relatively independent of the test temperature. A reasonable explanation can be the favoured kinetics of corrosion of the anodic film with increased temperatures.

To sum up, the water-based primers applied on TSA films seems to be a promising alternative for the Cr-loaded solvent based primer in terms of resistance to corrosion. But the future of the water-based coatings is subjected to the finding of an inhibitor pigment comparable to strontium dichromate, especially in long-term functions.

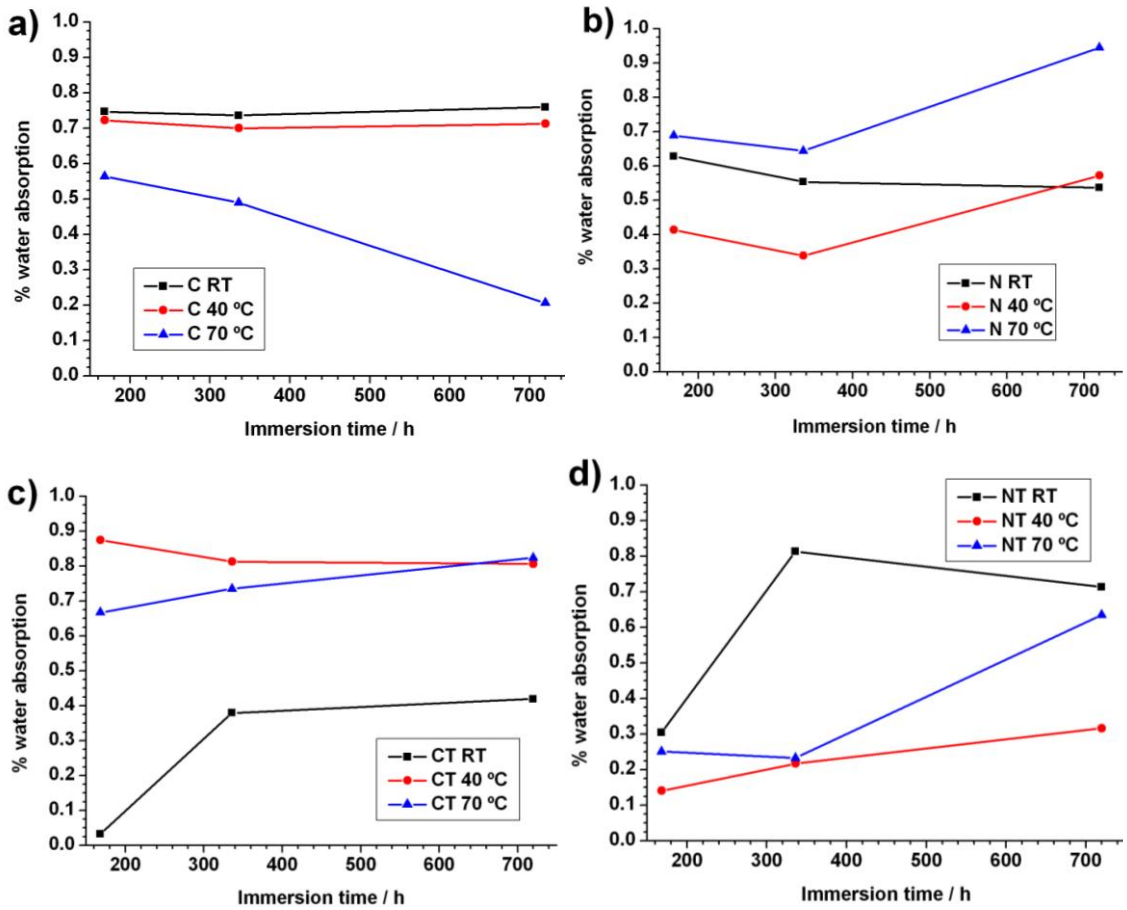

Figure 103. % of water absorbed during the immersion in 0.5 M NaCl solution at different temperatures by the AA2024 specimens anodised and (a) C primed, (b) N primed, (c) CT painted and (d) NT painted. The % absorbed water at different immersion times is related to the EIS measurement after 1 h of immersion for each sample.

5.5. Effect of a molybdate salt addition to TSA bath

There exist a number of chemicals that can act as a cathodic, an anodic or a mixed inhibitor when are present on the surface of an electrode or in the environment. These chemicals are usually incorporated in small amounts.

The objective of this chapter is to assess the possibility of adding an inhibitor salt to the TSA bath with the aim of incorporating such salt or derived species to the anodic film and therefore to improve the resistance against corrosion of the anodic films. From a list of environmentally compliant salts including vanadates, permanganates, cerium salts, etc. The selected reagent was sodium molybdate because it is relatively inexpensive (the determining factor in any industry) than other compounds.

The first step consisted then on the optimisation of the concentration of the molybdate salt in the TSA bath; for this, some samples were laboratory-scale anodised in TSA baths containing different amounts of the molybdenum salt, with the rest of anodising parameters fixed (see chapter 4.1.). The conductivity of the different baths and the thickness of the anodic films generated on them were measured. Besides, the protective effect of the films was evaluated by means of potentiostatic polarisation.

The upscale of the process was possible once the optimised Na_2MoO_4 concentration had been established. In the industrial-scale MoTSA bath, the influence of the stirring rate of the bath on the anodic films was evaluated by means of electrochemical impedance spectroscopy.

After that, the research was focused on the chemical species present in the new MoTSA bath, especially attending to the oxidation state of the molybdate-derived species by means of cyclic polarisation.

Following the previous, a comparative study between the anodic films generated in TSA and MoTSA was undertaken. This investigation included morphological characterisation (SEM and TEM); chemical characterisation (GDOES, RBS, XPS); electrochemical characterisation (EIS and potentiostatic polarisation) and corrosion test (salt spray test).

5.5.1. Optimisation of the anodising conditions

5.5.1.1. Optimisation of the concentration of the sodium molybdate in the TSA bath

A preliminary laboratory-scale study tested different additions (0-0.5 M) of Na_2MoO_4 to a TSA bath (0.53 M $C_4H_6O_6$, 0.46 M H_2SO_4).

Fig. 104 shows the thickness of the anodic films generated on AA2024 samples in the presence of different Na_2MoO_4 concentrations. The thickness obtained for the TSA process in the absence of Na_2MoO_4 is 3.5 ± 0.4 µm. A decrease of the thickness with increased Na_2MoO_4 concentration can be observed, obtaining 2.6 ± 0.6 µm in the presence of 0.25 M Na_2MoO_4. Anodic film thicknesses generated in TSA with higher Na_2MoO_4 concentrations (0.5 M) were below 2.0 µm, therefore below the desired thickness for the use in the aerospace industry.

The variation of the ionic conductivity with the Na_2MoO_4 concentration is also plotted in Fig. 104 (in red). Molybdate ions present higher volume than the other species present in the bath. Therefore, the ionic conductivity decreases with increased Na_2MoO_4 concentration, being

lower the effective current employed in the process, thus thinner anodic layers are obtained for the same anodising conditions.

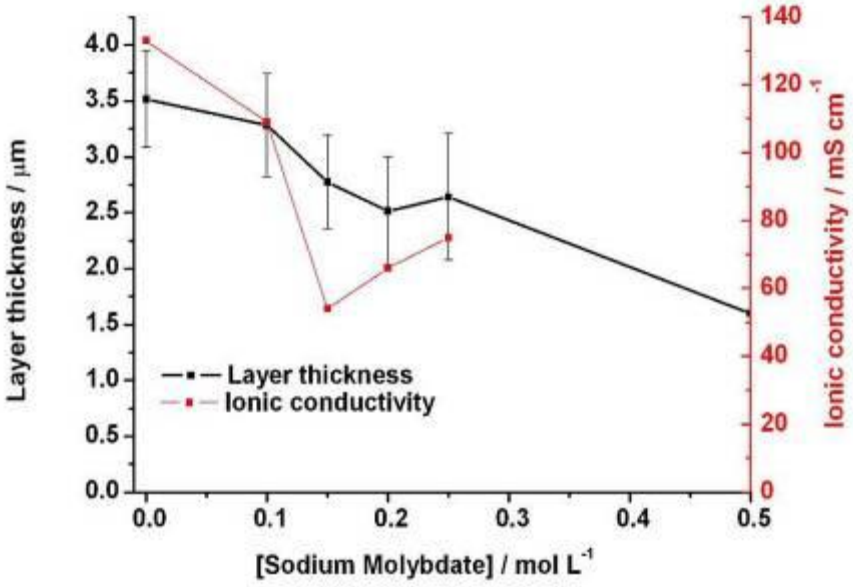

Figure 104. Variation of layer thickness (black) and ionic conductivity (red) of the bath with the addition of sodium molybdate.

This laboratory scale study showed that the anodic films grown on AA2024 in a TSA bath adding up to 0.25 M Na_2MoO_4 present acceptable thicknesses for the aerospace industry.

Clad AA2024 samples were anodised under the same anodising conditions (37 °C, 14 V, 5+20 min) in TSA solutions containing different amounts of Na_2MoO_4. Polarisation curves (fig. 105) were recorded after 1 h of immersion in a 0.5M NaCl solution in order to determine the influence of the addition of the inhibitor salt to the bath on the performance of the anodic films against corrosion.

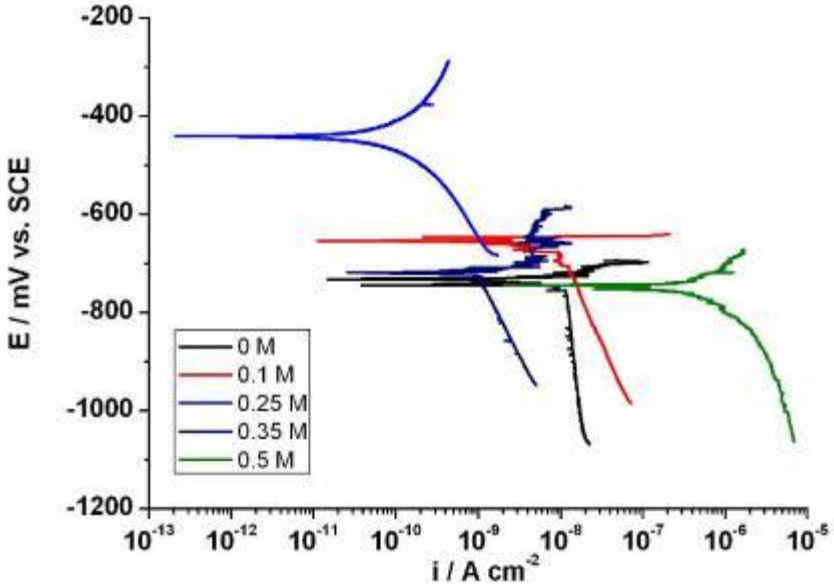

Figure 105. Polarisation curves recorded in 0.5 M NaCl after 1 h of immersion of clad AA2024 specimens anodised in a TSA bath containing different concentrations of Na_2MoO_4.

Fig. 105 shows that small additions up to 0.35 M of Na_2MoO_4 to the TSA bath result in a decrease of the i_{corr} and a displacement of the E_{corr} to less negative potentials for the clad AA2024 samples. Nevertheless, the clad AA2024 samples anodized in presence of 0.5 M Na_2MoO_4 present a higher i_{corr} and more negative E_{corr} than the sample anodised in the absence of inhibitor salt. Table 50 summarizes the corrosion parameters calculated for the samples.

Table 50. Corrosion parameters for TSA and MoTSA clad AA2024 specimens.

[Na_2MoO_4] (M)	E_{corr} (mV vs SCE)	i_{corr} (nA cm^{-2})	Relation $i_{corr\ (TSA)}$ / $i_{corr\ (MoTSA)}$
0	-733	12.6	1
0.10	-646	10.6	1.2
0.25	-441	0.32	40
0.35	-714	0.86	15
0.50	-744	226	0.06

The relation $i_{corr\ (TSA)}$ / $i_{corr\ (MoTSA)}$ gives an idea of the protective effect of the addition of the inhibitor salt. Anodising in the presence of 0.1 M Na_2MoO_4 has little effect on the behaviour against corrosion. The inhibitory effect of the molybdenum salt is extensively observed with increased concentrations; the additions of 0.25 M and 0.35 M result in a corrosion rate 40 and 15 times slower, respectively. Nevertheless, anodising clad AA2024 samples in a TSA bath containing 0.5 M Na_2MoO_4 results in an increase of the i_{corr} and therefore worst anticorrosive properties than the samples anodised in the TSA bath without inhibitor salt. It has to take into account that increasing Na_2MoO_4 decreases anodic layer thickness. Therefore the good result found with a concentration of 0.25 M in the bath is achieved with a thinner anodic layer. This concentration can be taken as an optimum between better performance and lower current efficiency of the bath.

From now on the TSA bath containing the optimised sodium molybdate concentration will be named MoTSA bath.

5.5.1.2. Influence of the stirring rate on the anodic layer thickness and corrosion resistance.

Three AA2024 samples were anodised in a 160 L MoTSA bath with different stirring rates. The layer thicknesses of these samples measured by eddy currents are displayed in fig. 106.

The thicknesses of the AA2024 samples anodised in the absence of stirring or gentle stirring are slightly higher than the anodic film generated stirring vigorously the anodising bath.

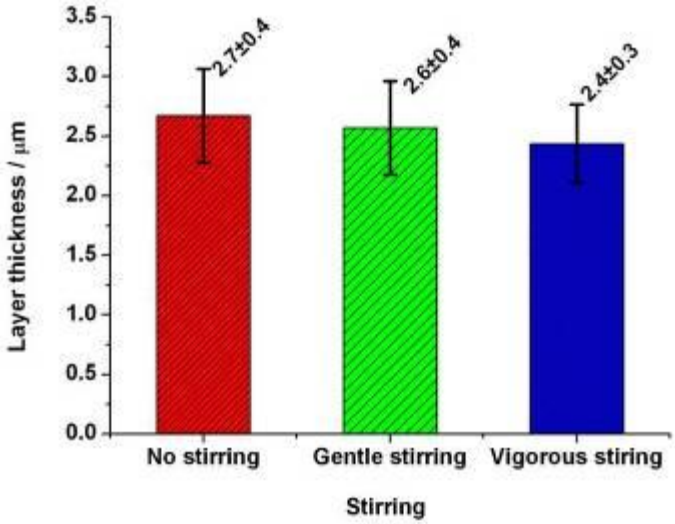

Figure 106. Influence of the stirring rate on the anodic layer thickness.

The influence of stirring on the corrosion behaviour was evaluated by means of electrochemical impedance spectroscopy (EIS), the experimental data are shown in fig. 107.

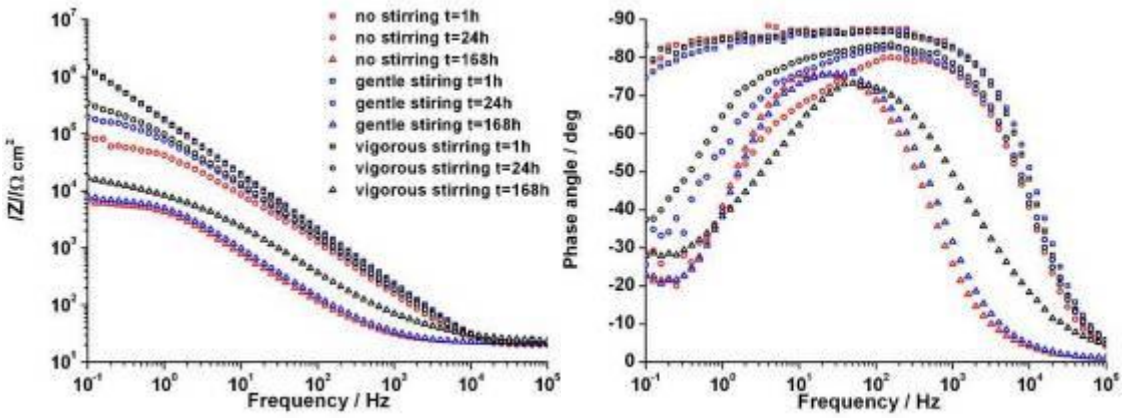

Figure 107. EIS spectra of MoTSA anodised AA2024 specimens without stirring (red), gently stirred (blue) and vigorously stirred (black).

The behaviour after 1 h of immersion in 0.5 M NaCl is similar for the three specimens. After 24 h of immersion, impedance modulus, $|Z|$, decreased in the low frequency range for the three samples. Moreover, the phase angle turned from capacitive to resistive behaviour for the low frequency range and the capacitive arch narrowed. These facts were more accused for the specimen anodised without stirring. EIS spectra after 168 h showed further degradation of the specimens, being the sample anodised with vigorous stirring the one with best behaviour against corrosion.

The differences in the electrochemical behaviour of the samples anodised under various stirring conditions after 168 h immersion in 0.5 M NaCl seem small, nevertheless these differences can be visually observed in the macrographs in fig. 108.

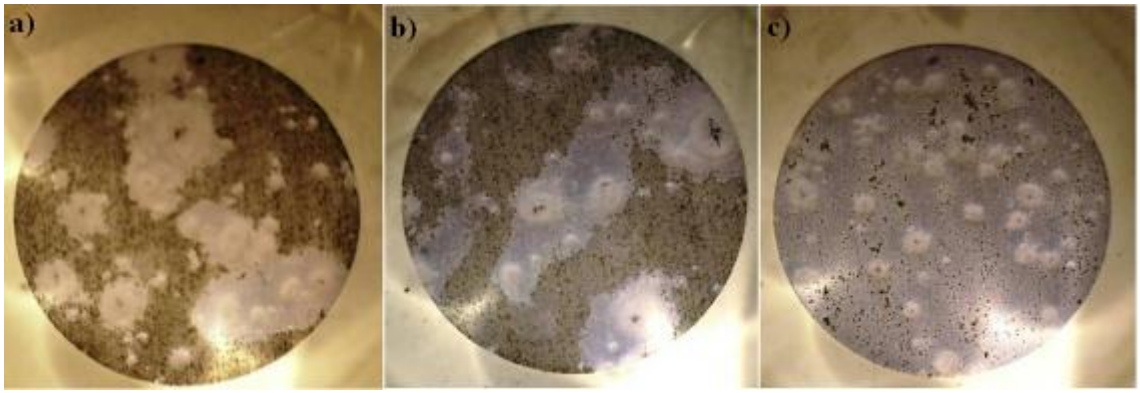

Figure 108. Macrographs of MoTSA anodised AA2024specimens (a) without stirring (b) gently stirred and (c) vigorously stirred after 168 h immersion in a 0.5 M NaCl solution.

The samples without stirring or gently stirred during the anodising process present a surface mostly covered with corrosion products. During the immersion in 0.5 M NaCl solution, initial pitting was observed after 72 h, these pits, probably copper particles, are surrounded by white aluminium hydroxide areas. Nevertheless, general corrosion expanded with longer exposure time to the test solution. The sample anodised under vigorous stirring present a number of pits, but general corrosion did not appear after 168 h of immersion.

The stirring rate is thus an important parameter for the MoTSA bath; an initial hypothesis to explain these effects is that the molybdate ions in acid media form high volume polymers that present low mobility in the bath. The chemistry of the molybdate will be discussed in the next section.

5.5.2. Chemistry of the molybdate in the MoTSA bath.

Initially, the MoTSA bath is colourless, as the TSA bath is. After the first anodising cycle, the bath colour turns to red, and it slowly goes to navy blue with subsequent anodising cycles. These changes in the bath can be attributed to three different phenomena:

- The formation of molybdate polymers in acid media.
- The Mo (VI) reduction on the cathodes during the anodising program.
- The formation of complexes between molybdate and tartaric acid.

The colourless tetrahedral molybdate anion $[MoO_4]^{2-}$ present a multiple protonation equilibriums [123]. The tetrahedral oxyanion is stable and inert under basic conditions but is readily protoned upon acidification. The first protonation, with log K_1 = 3.47, generates $[HMoO_4]^-$. The second, occurring with log K_2 = 4.74 (≈log K_1 due to an accompanying increase in coordination number) yields $MoO_3(OH_2)_3$, $MoO_2(OH)_2(OH_2)_2$, or $Mo(OH)_6$.

Besides, condensation leading to polyoxomolybdates occurs. The predominant species are the heptamolybdates, $[H_xMo_7O_{24}]^{(6-x)-}$ (x= 1–3) and the octamolybdates, $[Mo_8O_{26}]^{4-}$ and $[HMo_8O_{26}]^{3-}$ The equilibrium species present in acidic solutions (pH < 2) has not been reliably identified in the literature. Although salts of $[Mo_{36}O_{110}(H_2O)_{16}]^{8-}$ have been isolated from such solutions, it is expected to have a mixture of polyoxomolybdates in the MoTSA bath. In any case, these polyanions derived from the $[MoO_4]^{2-}$ have an important size.

Polymeric ion formation could be symbolised with the reaction 1:

$$n\ MoO_4^{2-} + 2n\ H^+ \rightarrow H_{2n}(Mo_nO_{4n})\ (1)$$

This molecule can dehydrate to give the different polyanions previously cited. For simplicity, during this study, to symbolise the polymeric forms, the formula H_2MoO_4 will be used (n=1). Moreover, according to Eq. (1), polyanion formation consumes protons. Consequently, the addition of molybdate species in acid solutions increases the pH and decreases the ionic conductivity due to the consummation of species with a high mobility.

The reduction of acid solutions containing molybdate species has been reported [124,125]. The Mo compounds generated during the reduction present the formula H_xMoO_3.

In acid solutions containing 0.5 M MoO_4^{2-} the reduction of the Mo (VI) was reported, observing a change in the solution colour from colourless to navy blue.

$$H_2MoO_4 + e^- + H^+ \rightarrow HMoO_3 + H_2\ (2)$$

In acid solutions containing 0.1 M MoO_4^{2-} during reduction of the colourless H_2MoO_4 a green compound appears, corresponding to H_2MoO_3 formation. H_2MoO_3 could be the result of H_2MoO_4 reduction (Eq. 3, or $HMoO_3$ reduction (Eq. 4):

$$H_2MoO_4 + 2e^- + H^+ \rightarrow H_2MoO_3 + H_2O\ (3)$$

$$HMoO_3 + e^- + H^+ \rightarrow H_2MoO_3\ (4)$$

However, H_2MoO_3 species is unstable and it oxidises in a red compound (i.e., $H_{1.5}MoO_3$ species):

$$2H_2MoO_3 \rightarrow 2H_{1.5}MoO_3 + e^- + H^+\ (5)$$

$H_{1.5}MoO_3$ species is also unstable and it oxidises with time to give polyanions H_2MoO_4:

$$2H_{1.5}MoO_3 + 2H_2O \rightarrow 2H_2MoO_4 + 3e^- + 3H^+\ (6)$$

Besides, Cavaleiro et al. demonstrated by NMR different molybdate-tartaric complexes can exist in solution [126].

To sum up, multiple kinds of complexes, polyanions and derived molybdate species with different oxidation state can coexist in the anodising bath. However, in any case the Mo polyanions and Mo-tartaric acid complexes are heavy molecules with a reduced mobility.

The influence of the ageing of the MoTSA bath is under research. No significant changes have been observed in terms of corrosion resistance after anodising 4 m^2 of different aluminium alloys in a 160 L bath.

5.5.3. Electrochemical behaviour of molybdate species in TSA solution.

The behaviour of the molybdate species in TSA solution was electrochemically evaluated by means of cyclic voltammetry. Fig. 109 shows voltammogramms recorded on gold electrode from OCP to -600 mV vs. SCE, at a scan rate of 10 mV s^{-1} and 25 °C.

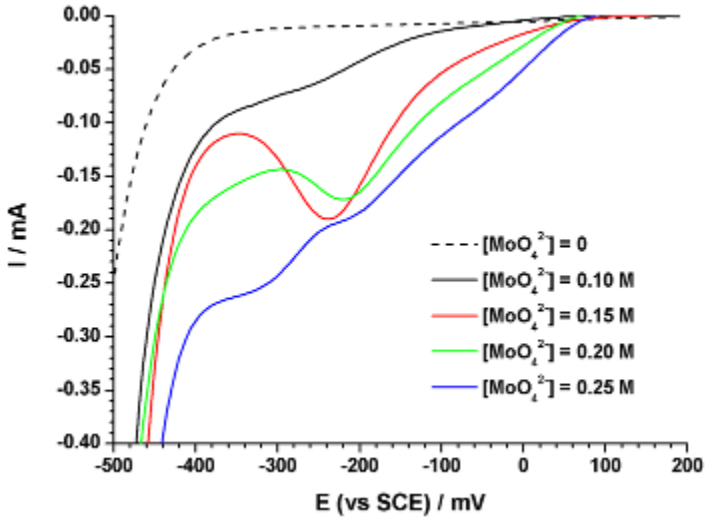

Figure 109. Voltammogramms on gold electrode in a TSA solution with 0 M, 0.10 M, 0.15 M, 0.20 M and 0.25 M sodium molybdate. Scan rate=10 mV·s^{-1}.

Voltammogramm registered in a TSA solution (dotted line) shows an inactive region between OCP and -350 mV vs. SCE, this means that no red/ox reactions due to the tartaric or the sulphuric acid are taking place in that region. The increase of the current below -350 mV vs. SCE is due to the evolution of hydrogen.

So that, the increase of current appearing in the region between OCP and -350 mV vs. SCE for the MoTSA solutions can be attributed to red/ox reactions of molybdate species in solution.

Voltammogramms registered in MoTSA solution shows a peak at -250 mV vs SCE for the four MoTSA solutions, this signal is attributed to the reduction of Mo (VI) species to Mo (V) species.

In the case of the TSA solution containing 0.25 M molybdate, a second peak appears at -310 mV vs. SCE, probably Mo (V) species are reduced to Mo (IV) species. This reduction might happen in a lesser extend for the rest of molybdate solutions, but the second peak is not readily seen.

Although the cathodic current increase seems to be related to the molybdate concentration, this is not a reliable method for an accurate determination of molybdate is solution, since the ageing of the bath involves red/ox reductions that change the initial oxidation state of the Mo species.

Fig. 110 shows cyclic voltammogramms recorded on a gold electrode with an initial scan from OCP to -600 mV vs. SCE, followed by a scan from -600 mv vs.SCE to 1800 mV vs SCE and a final reversed scan from 1800 mV vs. SCE to OCP. All scans were recorded at a 10 mV s^{-1} scan rate.

The increase of the current above 1600 mV vs. SCE is due to the oxygen evolution. TSA voltammogramm (dotted line) shows only small signals for the oxidation of gold in the forward scan (950 mV vs. SCE) and a peak of the reduction of the gold oxide in the reverse scan (900 mV vs. SCE).

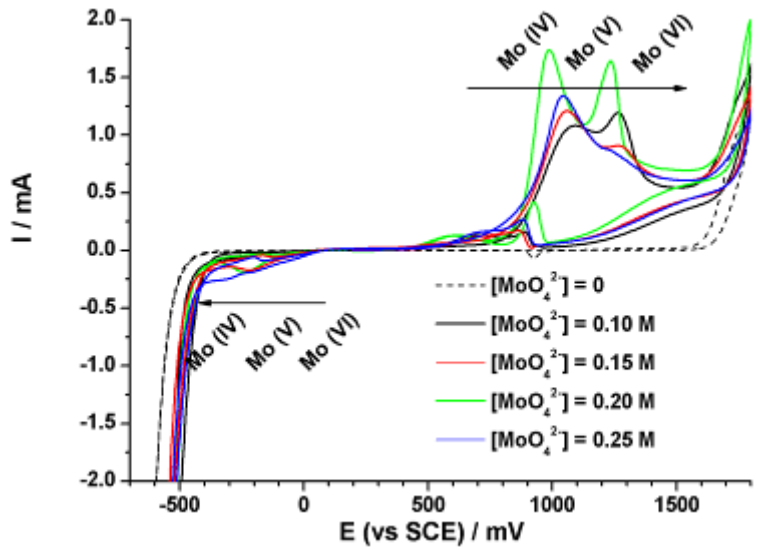

Figure 110. Cyclic voltammogramms on gold electrode in TSA solution with 0 M, 0.10 M, 0.15 M, 0.20 and 0.25 M sodium molybdate. Scan rate=10 mV·s^{-1}.

In the case of the MoTSA baths, initial scan shows the same results than described above. Forward scan reveals two oxidation peaks, the first one at 980 mV vs. SCE correspond to the oxidation of Mo (IV) species in solution to Mo (V), the second one at 1300 mV vs. SCE correspond to the oxidation of Mo (V) species to Mo (VI). The reversed scans show anodic currents in the 950-900 mV vs. SCE region, indicating that these red/ox processes are very irreversible. The reversed scan below 0 mV vs. SCE shows the reduction of Mo species as described above.

From this study, it can be concluded that, during the anodising process, red/ox reactions involving Mo (VI), Mo (V) and Mo (IV) species are occurring at the same time in the bath. The elevated driving force of the process at 14 V could result in the following reactions:

Cathode: Mo (VI) → Mo (V) Anode: Mo (V) → Mo (VI)

Mo (V) → Mo (IV) Mo (IV) → Mo (V)

5.5.4. Morphological characterisation of the anodic films grown in a MoTSA bath.

5.5.4.1. Anodic layers thickness

Fig. 111 shows the thicknesses of the anodic layers generated in a TSA and a MoTSA bath under the same anodising conditions for different aluminium alloys. In general, thinner anodic films are obtained in the MoTSA bath.

The ionic conductivity in a TSA bath is 120-140 mS cm^2, whereas the MoTSA bath presents lower conductivity (75-85 mS cm^2). This diminishment in conductivity causes a decrease in the driving force of the process thus in the thickness of the anodic layers.

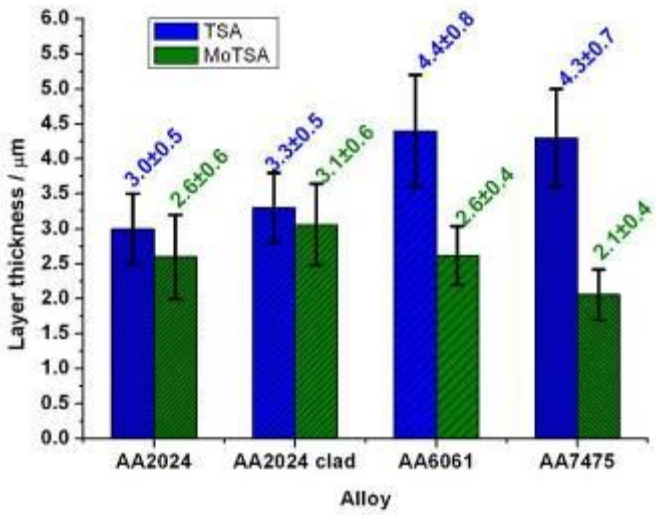

Figure 111. Anodic layer thicknesses generated in TSA and MoTSA baths for different aluminium alloys under the same anodising conditions, measured by eddy currents.

5.5.4.2. Morphological characterization by means of scanning electron microscopy

Fig. 112 shows SEM images of the surfaces of the TSA and MoTSA anodised AA2024 specimens.

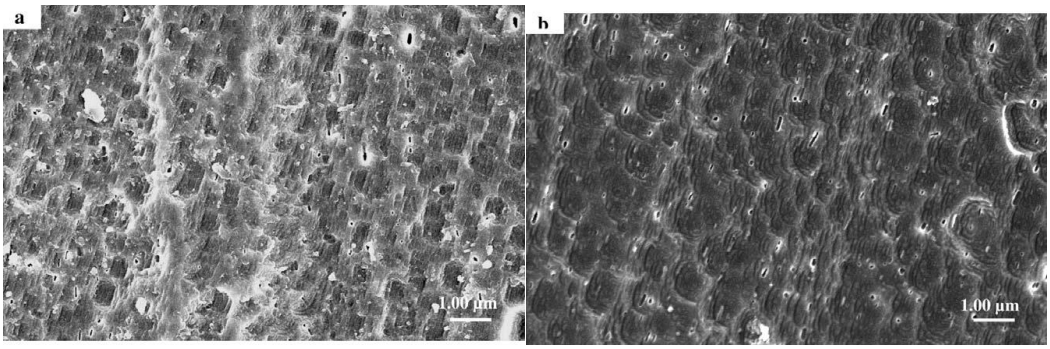

Figure 112. Scanning electron micrographs of the surfaces of (a) the TSA anodised AA2024 specimen and (b) a MoTSA anodised AA2024 specimen.

At the magnification displayed, the pore mouths at the film surface after TSA anodising are not readily resolved. Generally, the surface reveals features characteristic of the initially etched alloy, where a scalloped appearance is developed. Fine cavities at the surface, associated with loss of second phase material, are also revealed. Broadly similar features are evident after MoTSA anodising, indicating that the surface of the anodic film is little influenced by the addition of Na_2MoO_4 to the anodising bath.

5.5.4.3. Morphological characterization by means of transmission electron microscopy

Two anodised specimens in the TSA and MoTSA baths are displayed in Fig. 113.

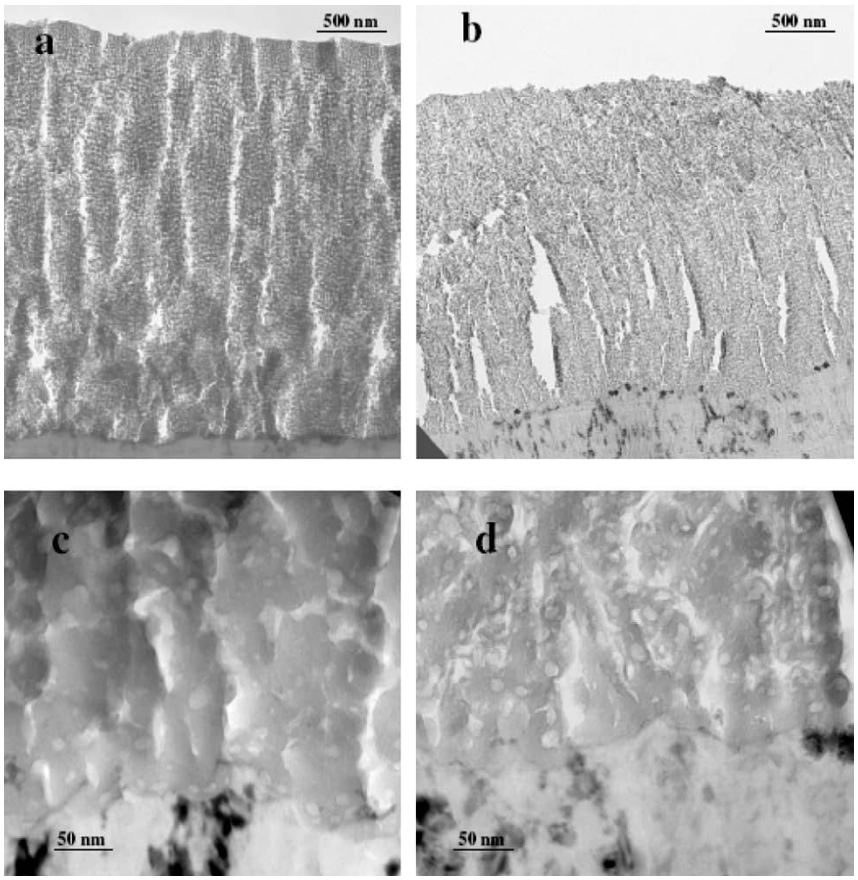

Figure 113. Transmission electron micrographs of ultramicrotomed sections of (a and c) TSA and (b and d) MoTSA anodised AA2024 specimens: (a and b) general views of the porous anodic film attached to the alloy substrate; (c and d) regions showing the alloy/anodic film interface.

Direct measurement of the anodic film thicknesses from Figs. 2a and b give values 2.8 ± 0.1 µm for TSA and 2.4 ± 0.1 µm for MoTSA, in relatively good agreement with the eddy current measurements. In both cases, two contrasting film morphologies are evident across the film thickness, comprising an outer film layer of fine pore size and an inner layer of increased pore dimensions. It is well known that the pore size is dependent on the anodising potential [93]. Thus, the finer-featured outer layer is developed during the initial stage of increasing potential from the OCP to 14 V, and the inner layer is generated at the constant potential of 14 V and reveals relatively regular film morphology of increased pore and cell dimensions. Curioni et al. [32] have reported different film morphologies for AA2024 specimens anodised at different constant potentials in sulphuric acid; additionally, anodic films generated at potentials below 6 V display a film morphology that is closely similar to that revealed on high purity aluminium. In the magnified images of Figs. 113c and d, the alloy-oxide interface region is evident. Here the anodic oxide morphology, composed of a porous layer with lateral porosity, typical of a porous film generated on copper-containing alloys, and a barrier layer beneath the major pores, is observed. A thin region in the alloy immediately below the barrier layer displays a dark contrast that is attributed to the presence of a copper-enriched layer. Such copper enrichment has been reported previously [111, 127,128]; its presence is considered to be responsible for

the generation of flaws in anodic films. Iglesias-Rubianes et al. [31] also suggested that oxidation of the copper-enriched regions is associated with the generation of a porous film morphology with significant lateral porosity, due to a cyclic phenomena involving oxygen generation [108,129] that causes a local disruption of the barrier layer film material and film rupture, and subsequent repair through local film growth.

5.5.5. Chemical characterization

5.5.5.1. Glow discharge optical emission spectroscopy

Fig. 114 shows the GDOES spectra of AA2024 samples anodised in TSA and MoTSA baths.

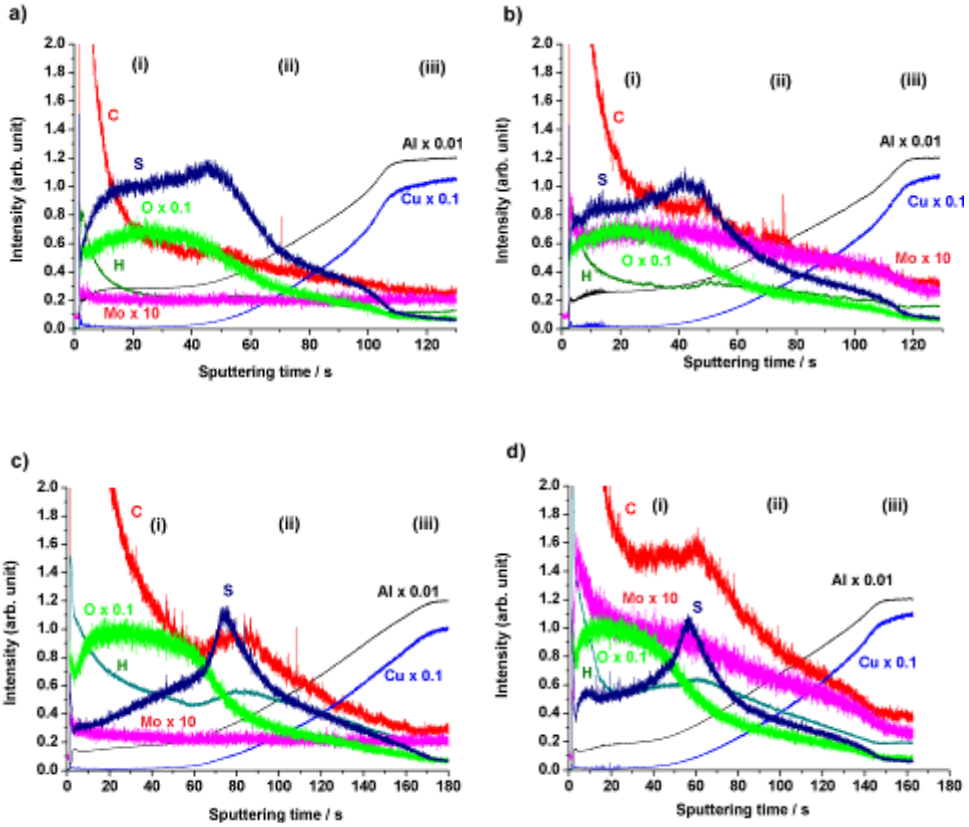

Figure 114. GDOES elemental depth profiles of AA2024 samples (a) TSA anodised (b) MoTSA anodised (c) TSA anodised and HWS (d) MoTSA anodised and HWS.

Fig. 114a and b correspond to two AA2024 samples anodised in TSA and MoTSA bath, respectively. The elements of the alloy (Al and Cu) and the common elements in the bath (C, H, O and S) present very similar depth profiles. The Mo in the fig. 114a is the background signal in the element. In the fig. 114b there is a small Mo signal that is magnified 10 times; here, a plateau for short sputtering times that correspond to the anodic film is observed. Then there is a decrease in the anodic film/alloy interface and finally the Mo signal reaches an intensity value close to the background signal observed in the previous sample.

According to the studies of Thompson et al. [130], molybdate species are converted to Mo^{6+} ions due to the high field during anodising; therefore these ions should not be present in the

anodic film because they present an outward mobility. Conversely, the results shown here demonstrate there are small amounts of Mo in the film. This fact could be due to residual molybdate and derived species adsorbed in the pores during the anodising process but not being part of the structure of the anodic film.

GDOES depth profiles in fig. 114c and 114d respectively show two AA2024 samples anodised in TSA and MoTSA bath and subsequently sealed in boiling water. The direct comparison of this two depth profiles show roughly similar distribution of the elements except for the Mo. The changes in the molybdenum profile between the anodised specimens and the anodised and sealed specimens are similar to those observed for the sulphur profile. The changes in the sulphur profile were previously discussed in section 5.1; they were majorly due to desorption of the sulphur species on the surface of the pores of the anodic film. In the case of the molybdenum, the desorption process can be slower due to the low mobility of the species.

The GDOES depth profile analysis shows that the molybdenum is incorporated to the anodic film in a low quantity in the sample anodised in the MoTSA bath. The differences observed between the MoTSA unsealed and sealed samples lead to think that the molybdate species are not incorporated to the anodic structure, but they are absorbed on the surface of the pores. Moreover, the rest of the elements do not modify their distribution across the anodic film compared to a TSA anodised sample.

5.5.5.2. Rutherford backscattering spectroscopy

Rutherford backscattering spectroscopy (RBS) was employed as a complementary technique for the GDOES depth profile analysis. This technique provides quantitative depth composition profiles of the anodic films.

Fig. 115a and b shows the experimental and simulated RBS spectra of two AA2024 samples anodised in TSA and MoTSA bath, respectively.

The continuous line in the spectra is the simulated data using the SIMNRA software code, with the resultant film compositions recorded in table 51.

The signals from elements with high mass (high Z) appear at high energies; in the sample anodised in TSA (Fig. 115a), the copper signal appeared at higher energy (1530 keV). Copper is the heaviest element in the specimen and, therefore, the signal for atoms near the surface of the specimen appear free of background. The calculated atomic concentration in this region is 0.01%, increasing to 0.14% in the layer representing most of the film thickness (table 51). The insert in Fig. 115a shows no signal from molybdenum which, if present, should appear at channel 625. The anodic film/alloy interface can be located from the increase in the yield around channel 125 due to the increase of the copper concentration in the alloy compared with the anodic film. In the oxide, both the aluminium and copper contents are lower than in the alloy. The increase of the aluminium edge in the alloy is not revealed because the helium ion emerging from such a depth after collision with an aluminium atom has insufficient energy to escape from the specimen, or it has such a low energy that it can not be detected by the surface barrier particle detector. The calculated anodic oxide thicknesses are about 1.5×10^{19} atom cm^{-2} and 9×10^{18} for specimens anodised in the absence and in the presence of molybdate, respectively.

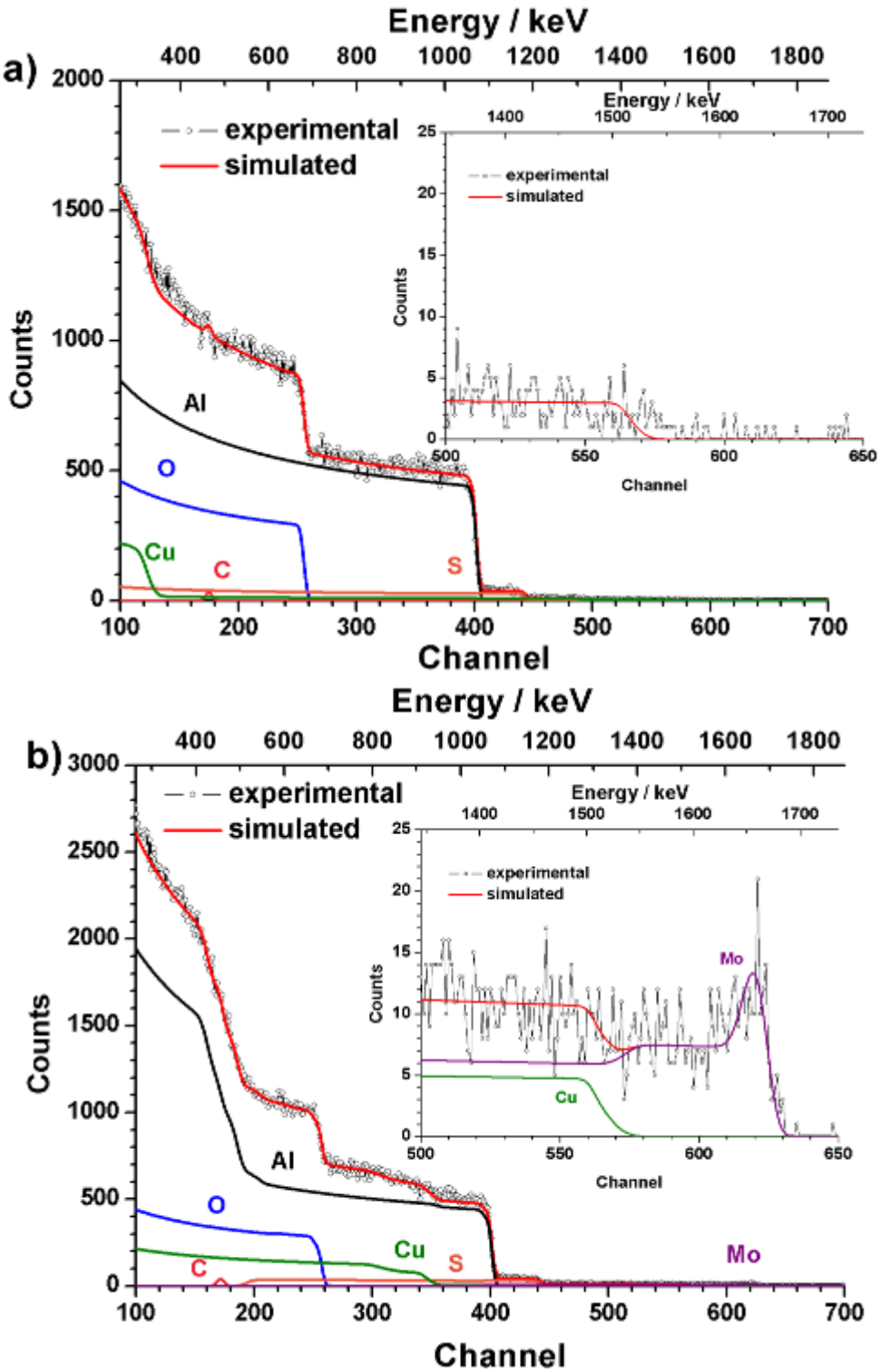

Figure 115. RBS spectra of (a) an AA2024 TSA anodised specimen and (b) an AA2024 MoTSA anodised specimen.

Table 51. Atomic composition of a TSA anodic film as obtained from RBS

Layer	Areal atomic density ($1 \cdot 10^{15}$ atoms·cm^{-2})	Concentration (%)				
		C	O	Al	S	Cu

1	200	19.99	47.40	31.0	1.6	0.01
2	2700	0	62.45	36.0	1.5	0.05
3	12200	0	62.43	36.0	1.4	0.14
4	Alloy	0	0	98.1	0	1.9

The effect of adding molybdate to TSA on the anodic film is clearly seen from the shape of the spectrum of Fig. 115b. Since the anodic film is thinner, the aluminium edge at the alloy/anodic oxide interface is observed around channel 170, and the copper edge at the interface is located at about channel 320. In the insert of Fig. 115b, the signal for molybdenum, the heaviest element in the specimen, appears around channel 625. The amount of molybdenum can be determined since the signal is free of background. Table 52 shows that molybdenum is present at low concentration, i.e. 0.15% in the outer layer and decreasing in the inner film regions to 0.05%. It is not detected at depths below 7.7 x 10^{18} atom cm^{-2} because the molybdenum signal overlaps with the signals from other elements.

Table 52. Atomic composition of a MoTSA anodic film as obtained from RBS

Layer	Areal atomic density ($1 \cdot 10^{15}$ atoms·cm^{-2})	Concentration (%)					
		C	O	Al	S	Cu	Mo
1	200	19.0	48.0	31.37	1.5	0.02	0.15
2	100	19.0	49.0	30.28	1.6	0.02	0.10
3	1500	0	61.9	36.19	1.7	0.08	0.06
4	5600	0	61.0	37.70	1.6	0.08	0.05
5	300	0	58.4	39.83	1.6	0.10	0.05
6	400	0	56.4	40.90	1.6	1.1	0
7	500	0	36.4	60.80	1.6	1.2	0
8	400	0	18.4	78.50	1.6	1.5	0
9	Alloy	0	0	98.10	0	1.9	0

RBS results confirm that molybdenum species are present in the anodic films generated in MoTSA but in low concentrations all across the film.

5.5.5.3. X-ray photoelectron spectroscopy

The X-ray photoelectron spectroscopy technique allows analysing the surface of the AA2024 MoTSA anodised specimen. Fig. 116 shows the binding energy region characteristic of the internal electron levels of the Mo 3d.

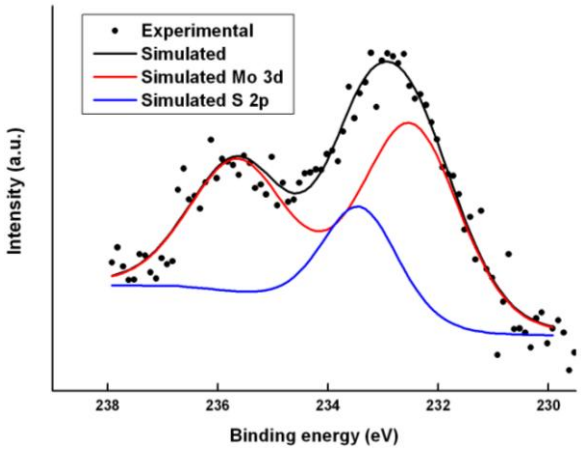

Figure 116. Magnified XPS spectrum of the Mo (3d) peak.

In the figure, it can be observed the presence of a doublet in the region of the Mo (3d), attributed to Mo (VI) oxide supported on alumina [131], at 232.5 eV. The region of the S (2p) overlaps with the region of the Mo (3d), the presence of S is detected (233.4 eV) in the sample.

From this result, it is clear that the molybdenum species adsorbed in the pores of the anodic film are uniquely Mo (VI) species.

5.5.6. Electrochemical behaviour

5.5.6.1. Linear polarisation

Polarisation curves of two AA2024 samples anodised in TSA and MoTSA were recorded in a 0.5 M NaCl solution. Different areas of the samples were measured after 1 h and 168 h immersion in the test solution; the curves are shown in fig. 117.

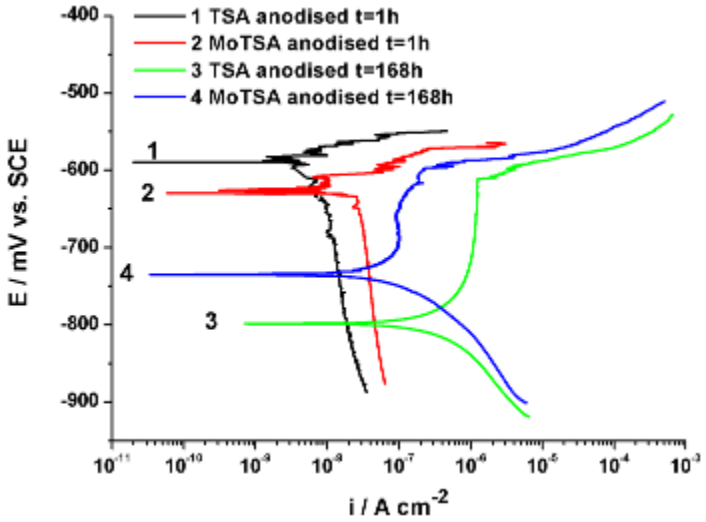

Figure 117. Polarisation curves of (a) TSA anodised AA2024 specimen and (b) MoTSA anodised AA2024 specimen after different immersion times in 0.5 M NaCl solution.

The polarisation curves for the samples anodised in TSA and MoTSA after 1 h immersion in the test solution display a similar shape: limiting cathodic current and pitting potential (E_{pit}) immediately after the corrosion potential (E_{corr}). The evolution after 168 h is also similar: a decrease of the E_{corr} and increased i_{corr} being these facts less marked in the case of the MoTSA sample. The corrosion parameters calculated by Tafel fit are shown in Table 53:

Table 53. Corrosion parameters for TSA and MoTSA AA2024 specimens.

Specimen	t (h)	i_{corr} ($nA \cdot cm^{-2}$)	E_{corr} (mV vs. SCE)	E_{pit} (mV vs. SCE)
TSA anodised	**1**	8	-594	-562
AA2024	**168**	1590	-798	-611
MoTSA anodised	**1**	24	-627	-601
AA2024	**168**	132	-735	-598

The similarities between the corrosion parameters for the TSA and MoTSA anodised samples after 1 h of immersion lead to think that the molybdate incorporated in the anodic film has not modified the film itself. In any case, the beneficial effect of the molybdenum after 168 h of immersion is clear since the E_{corr} diminish in a lesser extent for the MoTSA anodised specimen and interestingly, its i_{corr} is about 10 times lower than the calculated for the TSA anodised specimen. From these results it seems that Molybdenum species though do not modify the film it provides some protective effects against degradation in NaCl.

5.5.6.2. Electrochemical impedance spectroscopy of the anodised samples

AA2024

The EIS spectra recorded for two AA2024 specimens anodised in TSA or in MoTSA after immersion for different times in a 0.5 M NaCl solution are shown in fig. 118.

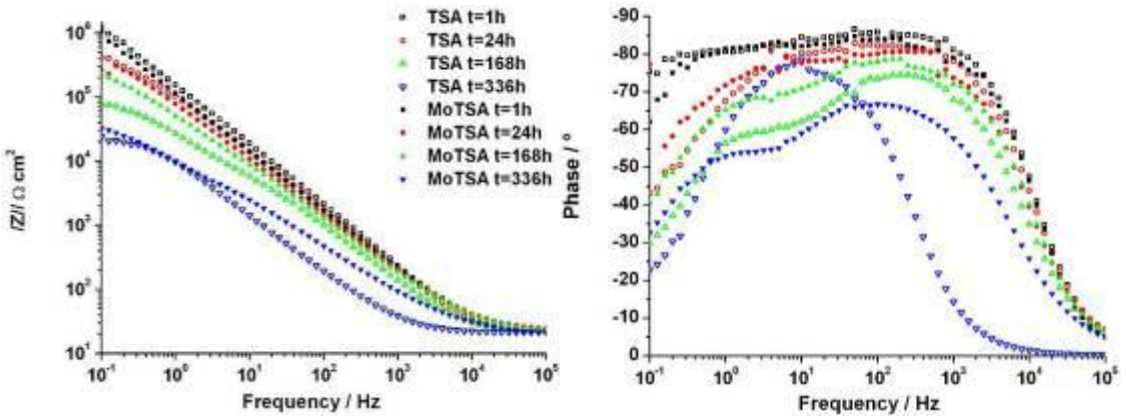

Figure 118. Bode plots of AA2024 specimens anodised in TSA bath (open) or MoTSA (filled) bath after different immersion times in 0.5 M NaCl solution.

The evolution of the EIS spectra for both specimens is the expected diminishment of the impedance modulus and the capacitance arch narrowing. Nevertheless, these two facts are slower for the sample anodised in the MoTSA bath. The spectra were fitted with the EC2

described in section 4.3. This model takes into account the flawless and the flawed areas that change during the immersion time. The fitted data are shown in table 54

Table 54. Results after fitting EIS data for the AA2024 specimens anodised in TSA and MoTSA baths after different immersion times in 0.5 M NaCl solution. The values in brackets indicate the dispersion factor of the constant phase element.

Parameter	Bath	Immersion time (h)			
		1	24	168	336
C_b (µS cm^{-2})	TSA	0.60	0.63	0.78	21.2
	MoTSA	0.65	0.63	0.60	1.04
C_d (µS cm^{-2})	TSA	0.67 (0.78)	1.52 (0.73)	8.74 (0.65)	-
	MoTSA	0.95 (0.82)	2.49 (0.75)	3.87 (0.73)	25.5 (0.64)
R_{b+d} (kΩ cm^2)	TSA	26502	718	144	10.7
	MoTSA	3219	3635	444	66

C_b values are related to the thickness of the barrier layer; MoTSA anodised specimen after immersion for 1 h displays higher C_b values compared with the specimen anodised in the absence of molybdate species.

The calculated barrier layer thicknesses were 14.7 and 13.6 nm for TSA and MoTSA anodised AA2024 specimens, respectively, in agreement with the expected values. A reduced barrier layer thickness was revealed in the specimen anodised in the presence of molybdate, as a consequence of the increase of the resistance of the MoTSA electrolyte; here, for the fixed 14 V potential applied across the anodising cell, the increased electrolyte resistance associated with molybdate addition results in a decreased potential available at the specimen surface and, consequently, in the generation of a porous anodic oxide with a barrier layer of reduced thickness.

Interestingly, for the specimen anodised in the presence of molybdate, the value of C_b is relatively constant up to 168 h of immersion in 0.5 M NaCl and slightly higher after 336 h immersion. Conversely, the C_b values of the sample anodised in the absence of molybdate increased with immersion time, and especially after 336 h of immersion. This fact can be related to the thinning of the barrier layer during immersion time, which is more accused for the sample anodised in the absence of molybdate.

On the other hand, the increase of C_d with immersion time denotes an increase in the number of defects. The value of C_d was higher in the case of the specimen anodised in the presence of molybdate, suggesting an increased number of defects initially present on the surface. This is in agreement with the polarisation results, where the cathodic current, associated with oxygen reduction at the cathodic sites available on the alloy surface, was approximately double for the specimen anodised in the presence of molybdate. Conversely, C_d was higher after 168 h and 336 h of immersion for the sample anodised in TSA.

The initial R_{b+d} value is 1 order of magnitude higher for the TSA anodised sample, but after 24 h this value strongly decreased meanwhile, for the MoTSA sample remains constant. After immersion for 168 h, R_{b+d} decreased for both specimens and, after 336 h, R_{b+d} for the TSA anodised sample was near the value measured on the bare alloy. This suggests that the majority of the alloy surface is exposed directly to the electrolyte, as in the case of the uncoated specimen. Accordingly, on the Bode plots, the time constant associated with the presence of the anodic oxide film is not revealed.

Fig. 119 shows optical micrographs of the surfaces of the TSA and MoTSA anodised AA2024 specimens after immersion in 0.5 M NaCl for 168 h.

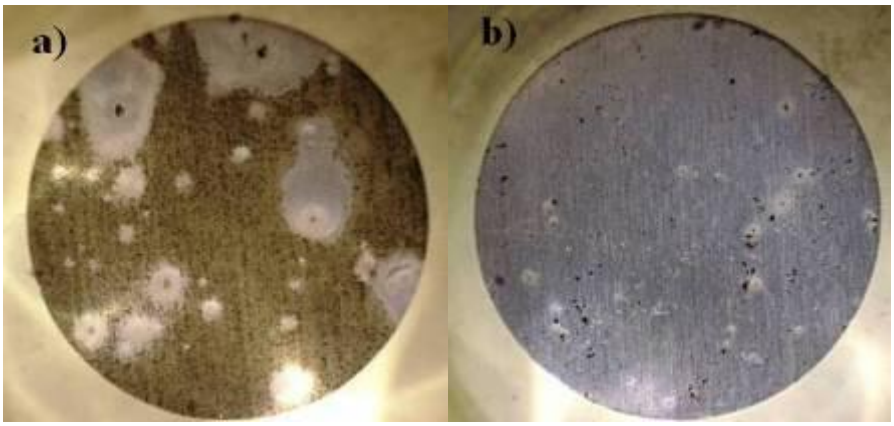

Figure 119. Macroscopic images of (a) TSA anodised AA2024 specimen and (b) MoTSA anodised AA2024 specimen after 168 h immersion in 0.5 M NaCl solution.

In agreement with the previous analysis, the TSA anodised specimen displays a dark surface which is indicative of accumulation of copper on surface due to preferential attack of the alloy matrix. On this specimen, a relatively low number of pits is evident, surrounded by areas of uncorroded alloy. In this case, two kinds of corrosion are evident: a relatively uniform attack of the general surface, resulting in the generation of a high number of copper-rich locations (black areas), and localized attack (pitting). In areas close to the pitting, the alloy may be protected from corrosion due to the effect of cathodic protection induced by the pitting, while in the areas far from the pit a more generalized corrosion occurs. The presence of black copper-rich regions suggests that the anodic oxide film is largely absent from the alloy surface after 168 h of immersion. Conversely the MoTSA anodised AA2024 specimen reveals a generally clean surface with about 60 pits evident. This is in agreement with the EIS and potentiodynamic polarisation results, suggesting that after 168 h of immersion the anodic oxide film is still covering most of the alloy surface.

Clad AA2024

Fig. 120 corresponds to the EIS spectra of the clad AA2024 specimens anodised in the presence or the absence of the inhibitor salt.

The clad AA2024 specimens anodised in different baths present similar behaviour after 1 h immersion and their evolution in the test electrolyte is closely related. The initial EIS spectra that present one constant of time are modified with immersion time by increase of the modulus of the impedance in the high frequency range.

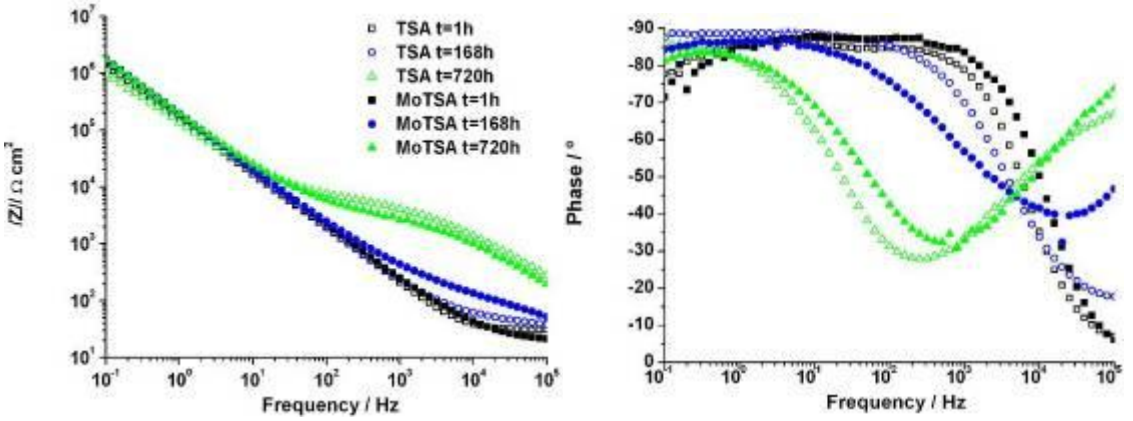

Figure 120. Bode plots of clad AA2024 specimens anodised in TSA bath (open) or MoTSA (filled) bath after different immersion times in 0.5 M NaCl solution.

The calculated parameters are shown in table 55 some of the EIS measurements are not shown in the fig. 120 for the sake of simplicity. The measures after 1 h were fitted with the EC1 for anodised samples described in section 4.3.; in these two fittings, C_d was not included because their values were very low. The subsequent measures were fitted with the EC3 described for sealed samples.

Table 55. Results after fitting EIS data for the clad AA2024 specimens anodised in TSA and MoTSA baths after different immersion times in 0.5 M NaCl solution. The values in brackets indicate the dispersion factor of the constant phase element.

Parameter	Bath	Immersion time (h)			
		1	168	336	720
C_b (µS cm^{-2})	TSA	0.82 (1.00)	0.88 (0.99)	0.94 (0.98)	1.42 (0.88)
	MoTSA	0.76 (1.00)	0.91 (0.95)	0.94 (0.93)	0.98 (0.89)
C_p (µS cm^{-2})	TSA	-	2239 (0.21)	93.4(0.46)	0.26 (0.71)
	MoTSA	-	456 (0.45)	2.10(0.61)	0.29 (0.73)
R_b (kΩ cm^2)	TSA	52345	142500	>100000	>100000
	MoTSA	6102	109782	>100000	>100000
R_p (Ω cm^2)	TSA	-	235	889	6536
	MoTSA	-	555	1086	3811

The capacitance of the barrier layer, C_b, after 1 h immersion and its increased values with immersion time is roughly similar for the two samples. These changes could be due to the combination of two phenomena: on the one hand the partial dissolution of the barrier layer due to the attack of the chlorine ions increases C_b values; on the other hand, the formation of new aluminium oxide in the pores makes the barrier layer and the pore walls thicker, and therefore will decrease C_b.

C_p can only be calculated for 168 h immersion and longer. This parameter decreases with immersion time for both samples as the self sealing process is getting more effective.

R_b values increases with immersion time to the extent that it is not possible to determine them accurately after 336 h and longer immersion times.

The increase of R_p is due to the plugging of the pores that prevent the electrolyte from reaching the barrier layer.

As a conclusion, it seems clear that molybdate does not interfere in the self sealing process of the clad AA2024.

The improvement in the corrosion resistance of the clad AA2024 when anodising in the MoTSA bath is not evident in the EIS spectra for short immersion time, however this beneficial effect was previously observed in the polarization measurements.

AA6061

The EIS spectra recorded in 0.5M NaCl for two anodised samples in TSA and MoTSA are shown in the fig. 121:

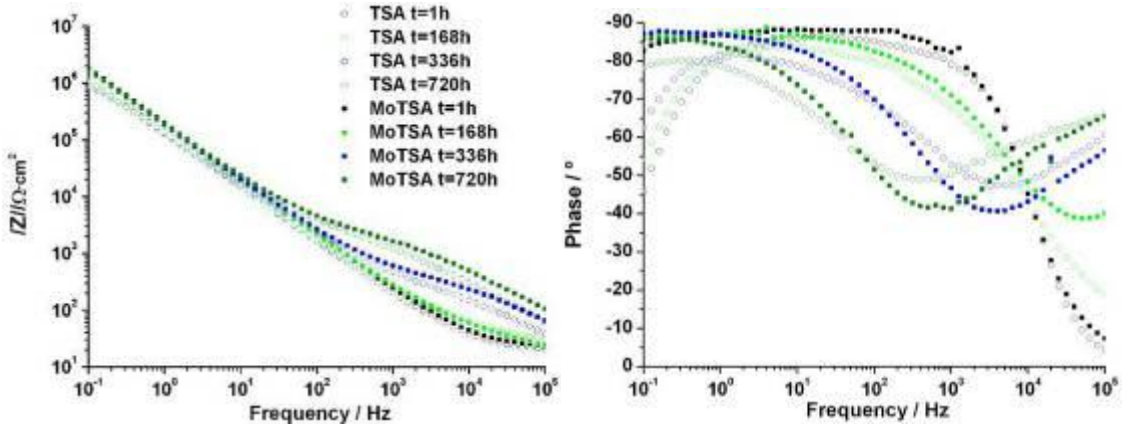

Figure 121. Bode plots of AA6061 specimens anodised in TSA bath (open) or MoTSA (filled) bath after different immersion times in 0.5 M NaCl solution.

The anodised samples show similar behaviour than the observed previously for the clad AA2024 specimens; although the self-sealing process seems slower for this alloy.

The parameters of the fitted EIS spectra are shown in table 56. The EC1 described in 4.3. was used for fitting the EIS spectra after 1 h immersion. The EC3 used for sealed samples was selected for fitting of the EIS spectra after 168 h immersion.

Table 56. Results after fitting EIS data for the AA6061 specimens anodised in TSA and MoTSA baths after different immersion times in 0.5 M NaCl solution. The values in brackets indicate the dispersion factor of the constant phase element.

Parameter	Bath	Immersion time (h)			
		1	168	336	720
C_b (µS cm^{-2})	TSA	0.99 (1.00)	1.35 (0.99)	0.94 (0.98)	1.46 (0.88)
	MoTSA	0.72 (1.00)	0.93 (0.95)	0.94 (0.93)	1.45 (0.89)
C_p (µS cm^{-2})	TSA	-	140 (0.50)	93.4(0.46)	1.40 (0.72)
	MoTSA	-	379 (0.36)	2.10(0.61)	2.29 (0.72)
R_b (kΩ cm^2)	TSA	1338	1706	>1000	>1000
	MoTSA	11172	14759	>1000	>1000
R_p (Ω cm^2)	TSA	-	615	889	2268
	MoTSA	-	399	1086	2739

The samples anodised in TSA and MoTSA show a similar evolution of all the parameters. C_b is initially lower for the MoTSA sample, it is increased after 168 h immersion and then slightly decreases for the TSA anodised sample or maintains its value in the case of the MoTSA anodised sample after 336 h. Both specimens reach the same value after 720 h. The variation of C_b is dependant on the balance between the degradation of the barrier layer and the formation of new hydrated alumina in the pores. This balance is displaced to the degradation of the anodic layer although it is very slow for both samples.

The capacitance of the porous layer, C_p, decreases equally for both samples as the self-sealing process gets more effective.

Rb values are initially higher for the MoTSA anodised samples, but they grow for both samples to values not quantifiable in the selected frequency range.

The resistance of the electrolyte to penetrate the pores, R_p, is only quantifiable after 168 h of immersion; this value grows with immersion time because the mouth of the pores is narrowing.

AA7475

Fig. 122 shows the EIS spectra of the samples anodised in the absence and the presence of molybdate salt in the bath measured after different immersion time in the test electrolyte.

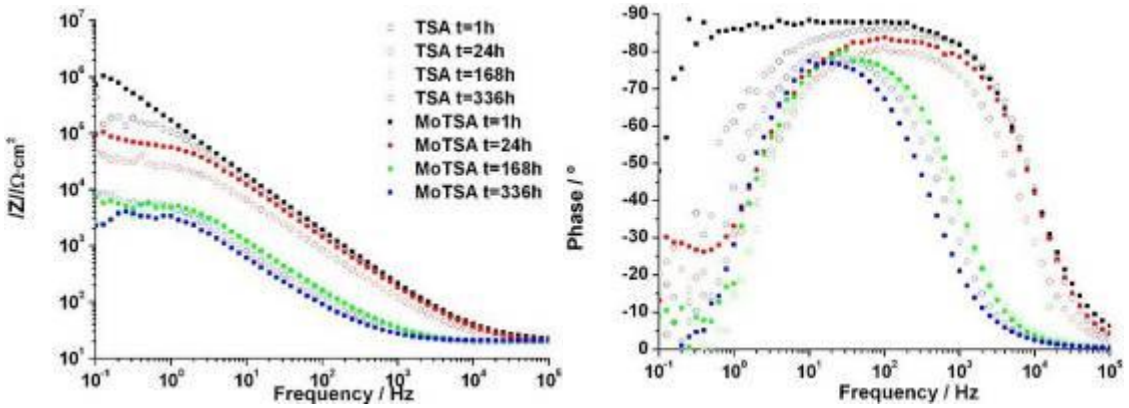

Figure 122. . Bode plots of AA7475 specimens anodised in TSA bath (open) or MoTSA (filled) bath after different immersion times in 0.5 M NaCl solution.

The modulus of the impedance rapidly decreases after 24 h of immersion in the 0.5 M NaCl solution for both specimens. Extended degradation of the anodic films is observed after 168 h o f immersion.

Table 57 shows the fitted values of the EC1 shown in section 4.3.

The initial capacitance of the barrier layer, C_b, is similar for both samples; after 24 h of immersion, C_b increases for both samples. This fact jointly with the rapid decrease of the resistance of the anodic film R_{b+d}, indicate degradation of the barrier layer. This phenomenon continues after 168 h, and is especially severe for the TSA anodised sample.

Table 57. Results after fitting EIS data for the AA7475 specimens anodised in TSA and MoTSA baths after different immersion times in 0.5 M NaCl solution. The values in brackets indicate the dispersion factor of the constant phase element.

Parameter	Bath	Immersion time (h)		
		1	24	168
C_b (μS cm^{-2})	TSA	0.86	1.47	14.1
	MoTSA	0.87	0.98	4.89
C_d (μS cm^{-2})	TSA	0.73(0.83)	4.83 (0.61)	-
	MoTSA	-	4.71 (0.39)	11.0 (0.91)
R_{b+d} (kΩ cm^2)	TSA	26502	718	144
	MoTSA	3219	3635	444

C_d present a very low value for the MoTSA sample, therefore its contribution was not taken into account. The capacitance of the detached areas of the anodic film increases with immersion time; signifying the film is easily attacked by the chlorine in the test solution.

The samples anodised in the MoTSA bath present a slower degradation of the barrier layer for the early immersion time; nevertheless both samples are heavily damaged after 168 h of immersion.

5.5.6.3. Electrochemical Impedance spectroscopy of the anodised and sealed samples

The EIS spectra of the anodised and sealed samples were all fitted with the EC3 described in section 4.3. for sealed samples.

AA2024

The comparison between the EIS spectra of the samples anodised in the TSA and the MoTSA bath and subsequently sealed are shown in fig. 123:

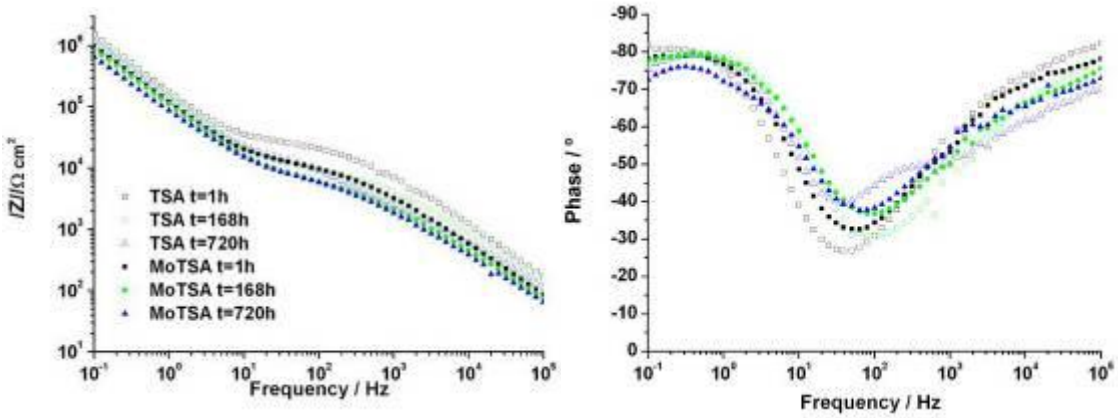

Figure 123. Bode plots of AA2024 specimens anodised in TSA bath (open) or MoTSA (filled) bath and subsequently sealed after different immersion times in 0.5 M NaCl solution.

The presence of two constants of time evidences the sealing of the specimens. The sample TSA anodised present higher modulus of the impedance in the high frequency range than the MoTSA sample after 1 h of immersion; this signify the plugging of the pores is more effective in the first sample. The evolution of the EIS spectra is similar for both samples; a decrease of Z in the high frequency range with immersion time. These changes are better evidenced by evaluation of the fitted parameters shown in table 58.

Table 58. Results after fitting EIS data for the AA2024 specimens anodised in TSA and MoTSA baths and subsequently sealed in boiling water after different immersion times in 0.5 M NaCl solution.

Parameter	Bath	Immersion time (h)			
		1	168	336	720
C_b (µS cm^{-2})	TSA	1.10 (0.93)	1.32 (0.91)	1.50 (0.86)	1.55 (0.93)
	MoTSA	1.65 (0.89)	1.77 (0.88)	1.75 (0.88)	2.37 (0.85)
C_p (nS cm^{-2})	TSA	60.8 (0.84)	300 (0.75)	260 (0.79)	1801 (0.70)
	MoTSA	176 (0.82)	332 (0.80)	360 (0.79)	725 (0.75)
R_b (kΩ cm^2)	TSA	>100000	>100000	>100000	>100000
	MoTSA	>100000	>100000	>100000	>100000
R_p (kΩ cm^2)	TSA	31.9	17.2	6.8	10.8
	MoTSA	9.8	5.4	5.8	6.1

The capacitance of the barrier layer, C_b, slowly increases with immersion time for both samples; indicating a degradation of the barrier layer.

The capacitance of the porous layer, C_b, is lower for the TSA sample, but this parameter evolves in a lesser extent in the case of the MoTSA sample. Therefore, possibly the widening mouth of the pores by attack of the chloride is slower in the case of the MoTSA sample.

The capacitive behaviour is clear at 0.1 Hz in the phase plot, so that the resistive behaviour is not observed and the barrier layer resistance values, R_b, cannot be accurately determined in the registered frequency range.

The resistance of the porous layer, R_p, in the case of the TSA specimen decreases up to ⅓ of its initial value after 720 h; whereas the MoTSA sample shows R_p decreases after 168 h but then maintain relatively constant values after 720 h of immersion; these values are about ⅔ of the initial value. Here, the protective action of the molybdate species adsorbed on the anodic film is evidenced.

Clad AA2024

The comparison between the EIS spectra of the clad AA2024 samples anodised in the TSA and the MoTSA bath and subsequently sealed are shown in fig. 124:

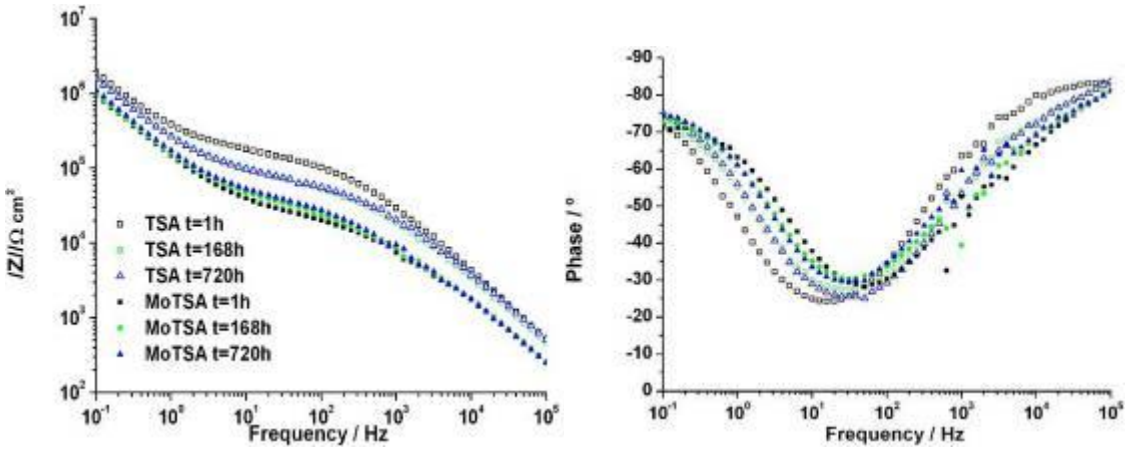

Fig. 124. Bode plots of clad AA2024 specimens anodised in TSA bath (open) or MoTSA (filled) bath and subsequently sealed after different immersion times in 0.5 M NaCl solution.

As observed for the unclad AA2024, attending to the modulus of the impedance, the quality of sealing of the sample anodised in TSA seems better than the one anodised in the presence of molybdate salts. The results of the fitting are shown in table 59.

Table 59. Results after fitting EIS data for the clad AA2024 specimens anodised in TSA and MoTSA baths and subsequently sealed in boiling water after different immersion times in 0.5 M NaCl solution.

Parameter	Bath	Immersion time (h)			
		1	168	336	720
C_b (µS cm^{-2})	TSA	0.77 (0.76)	0.98 (0.76)	1.10 (0.76)	0.96 (0.78)
	MoTSA	1.60 (0.79)	1.53 (0.78)	1.48 (0.79)	1.39 (0.81)
C_p (nS cm^{-2})	TSA	17.6 (0.87)	39.5 (0.81)	41.1 (0.81)	34.2 (0.82)
	MoTSA	126 (0.77)	137 (0.76)	129 (0.77)	120 (0.78)
R_b (kΩ cm^2)	TSA	>100000	>100000	>100000	>100000
	MoTSA	>100000	>100000	>100000	>100000
R_p (kΩ cm^2)	TSA	137	63.9	52.2	66.3
	MoTSA	21.5	28.7	30.5	35.1

The capacitances of both components of the anodic film; the barrier layer (C_b) and the porous layer (C_p) are smaller for the sample anodised in TSA; but the trend of these values with the immersion time indicates slight degradation of the anodic film. However; the initial C_b and C_p values for the sample anodised in the MoTSA bath are higher than the TSA sample diminish with immersion time; this could indicate the sealing of the sample is still occurring during the immersion in the test solution.

R_b cannot be determined but maintains high values after 720 h test for both samples.

The resistance of the porous layer halved after 168 h of immersion and maintained constant for longer immersion times. The behaviour of the MoTSA sample is different because R_p grows with immersion time. These observations enhance the previous hypothesis: although the sealing quality is lower, the sample anodised in the MoTSA bath present a self-sealing process during immersion in corrosive chlorine solution; whereas the better sealed TSA anodised sample slightly degrades under the same test conditions.

AA6061

Figure 125 shows the EIS spectra of the samples anodised in the TSA and the MoTSA baths and subsequently sealed in boiling water.

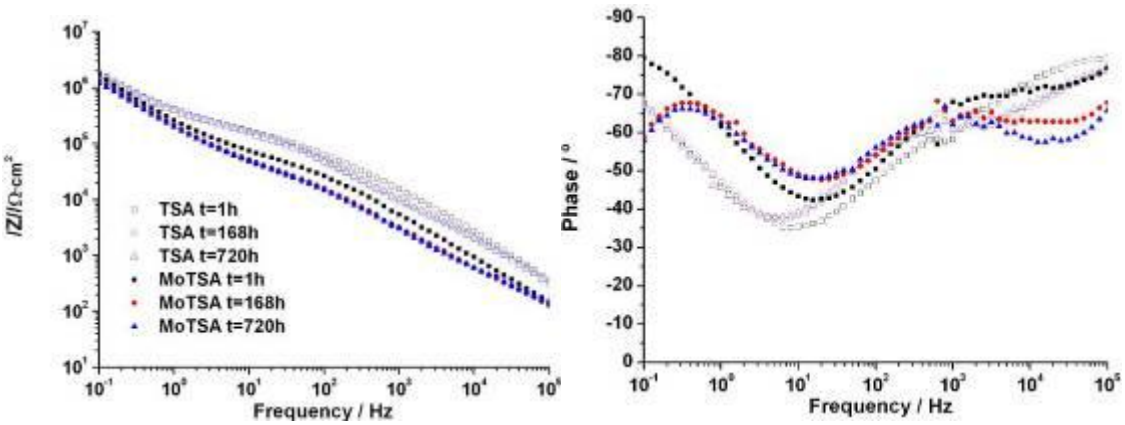

Fig. 125. Bode plots of AA6061 specimens anodised in TSA bath (open) or MoTSA (filled) bath and subsequently sealed after different immersion times in 0.5 M NaCl solution.

Here the difference in the sealing quality is observed again; the impedance modulus decreases for both samples with immersion time. The fitted parameters are shown in table 60.

Table 60. Results after fitting EIS data for the AA6061 specimens anodised in TSA and MoTSA baths and subsequently sealed in boiling water after different immersion times in 0.5 M NaCl solution.

Parameter	Bath	Immersion time (h)			
		1	168	336	720
C_b (μS cm^{-2})	TSA	0.78 (0.72)	0.82 (0.76)	0.84 (0.76)	0.88 (0.75)
	MoTSA	0.89 (0.82)	1.14 (0.78)	1.18 (0.79)	1.27 (0.78)
C_p (nS cm^{-2})	TSA	82.1 (0.78)	176 (0.73)	215 (0.72)	299 (0.70)
	MoTSA	222 (0.78)	752 (0.72)	914 (0.70)	1113 (0.68)
R_b (kΩ cm^2)	TSA	>1000	>1000	>1000	>1000
	MoTSA	>1000	>1000	>1000	>1000
R_p (kΩ cm^2)	TSA	125	162	184	215
	MoTSA	52.0	28.3	28.4	34.3

The increase of C_b with immersion time is slow for both samples. Besides, R_b maintained over 1 MΩ cm^2 for both specimens. This indicates slow degradation of the barrier layer during the test.

The capacitance of the porous layer, C_p, is initially higher for the MoTSA sample and is rapidly increased with immersion time. The resistance of the electrolyte in the porous layer increased continuously for the TSA specimen during the test, however, R_p decreased after 168 h and then maintained relatively constant. These facts indicate the sealing of the anodic film is more effective for the TSA sample than for the MoTSA sample. Besides the evolution of C_p and R_p parameters lead to think that the sealing quality is more determining in the corrosion resistance than the molybdates adsorbed in the anodic film.

AA7475

The EIS spectra of the AA7475 samples anodised in the presence and the absence of molybdate salt and subsequently sealed are shown in fig. 125.

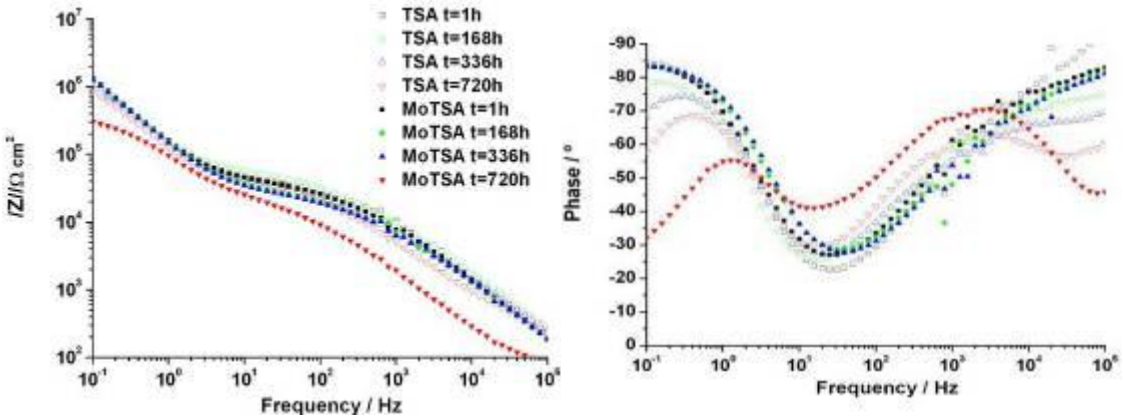

Figure 126. Bode plots of AA7475 specimens anodised in TSA bath (open) or MoTSA (filled) bath and subsequently sealed after different immersion times in 0.5 M NaCl solution.

In the figure, the EIS spectra for the anodised samples in different electrolytes present similar shape after 1 h of immersion and their evolution is analogous except for the 720 h immersion. The fitted parameters are shown in table 61.

Table 61. Results after fitting EIS data for the AA7475 specimens anodised in TSA and MoTSA baths and subsequently sealed in boiling water after different immersion times in 0.5 M NaCl solution.

Parameter	Bath	Immersion time (h)			
		1	168	336	720
C_b (µS cm^{-2})	TSA	1.22 (0.94)	1.35 (0.91)	1.43 (0.89)	1.55 (0.94)
	MoTSA	1.19 (0.91)	1.24 (0.90)	1.26 (0.91)	2.88 (0.71)
C_p (nS cm^{-2})	TSA	55.5 (0.84)	139 (0.79)	223 (0.73)	421 (0.70)
	MoTSA	83.7 (0.82)	107 (0.81)	116 (0.80)	773 (0.80)
R_b (kΩ cm^2)	TSA	>1000	>1000	>1000	>1000
	MoTSA	>1000	>1000	>1000	587
R_p (kΩ cm^2)	TSA	46.8	37.7	36.0	21.8
	MoTSA	34.4	24.6	23.5	11.4

The capacitance of the barrier layer is initially similar for both specimens; however, the evolution of this parameter after 720 h of immersion evidences extended corrosion processes for the specimen HWS-MoTSA anodised. R_b maintains high values expect for the MoTSA specimen after 720 h of immersion.

C_p increases progressively for the HWS-TSA anodised specimen. However, in the case of the MoTSA specimen, such parameter slightly evolves up to 336 h, whereas after 720 h of immersion markedly increased.

R_p decreases for both samples during the experiment; however, such decrease is more accused in the case of the HWS-MoTSA anodised specimen after 720 h.

The sealed MoTSA sample present slightly better corrosion resistance after short immersion times; 336 h, but the performance of this sample heavily decreases after 720 h, such behaviour could be due to local defects.

5.5.7. Salt spray test

The neutral salt spray test was carried out in order to corroborate the beneficial effects of the adsorption of molybdate species on the anodic films grown on different alloys. Table 62 summarises the results of this test; all the samples are anodised and sealed in boiling water (HWS).

Table 62. Salt spray test results

Alloy	Anodising bath	Nº specimens	96 h		336 h	
			Pits dm^{-2}	% pass	Pits dm^{-2}	% pass
AA2024	TSA	6	0.4	100	5.7	0
	MoTSA	4	0.4	100	1.1	100
Clad AA2024	TSA	6	0.9	100	1.1	100
	MoTSA	3	0.2	100	0.4	100
AA7475	TSA	6	1.4	83	5.3	0
	MoTSA	3	1.1	100	6.0	0

The AA2024 specimens showed similar behaviour after 96 h of exposure to the corrosive environment ineffectual the anodising bath; however, the totality of the samples anodised in the MoTSA bath presented a lower pit density and succeeded in passing the test after 336 h of exposure.

The whole clad AA2024 specimens successfully passed the test, although the samples anodised in the MoTSA bath presented lower pit density after 96 h and 336 h of exposure.

In the case of the AA7475 specimens, the results after 96 h of exposure show lower pit density in the case of the MoTSA specimens and conversely to the TSA specimens, all the MoTSA samples passed the test. Nevertheless all the AA7475 samples failed the test after 336 h of exposure.

These results are in qualitative agreement with those obtained by electrochemical techniques; the samples anodised in the MoTSA bath presented enhanced resistance against corrosion for the AA2024 specimens, and for short immersion time for the AA7475 specimens. Meanwhile there was no difference in the results obtained for the clad AA2024.

5.5.8. Paint adherence of TSA and MoTSA

AA2024 specimens anodised in the MoTSA bath (37 °C, 14 V, 5 min+20 min) were primed with the Cr-loaded solvent-based organic primer previously described in section 5.3.1. The results of the dry and wet cross-cut test on the MoTSA anodic film were similar to that obtained for the AA2024 specimens anodised in the TSA bath. Therefore, it is concluded that the addition of molybdate species to the anodising bath does not influence the paint adherence between the primer and the anodic film.

5.6. Accelerated corrosion tests

This chapter presents the study of the influence of both, the concentration of Cl^- and the temperature testing conditions on the resistance against corrosion of AA2024 specimens TSA anodised and HWS sealed. Such study has a double aim: on the one hand the investigation of the stability of the protective system under extremer temperature conditions, on the other hand, the study of the viability of accelerated corrosion tests.

5.6.1. Influence of the NaCl concentration on the behaviour against corrosion of AA2024 specimens at different test temperatures

AA2024 specimens TSA anodised (37 °C, 5+20 min, 14 V) and sealed in boiling water (HWS) for 40 min were exposed to various concentrations of a NaCl solutions (0.05, 0.125, 0.25 or 0.5 M NaCl) at RT, 35 or 45 °C. Electrochemical impedance was measured after 1, 24, 48, 72, 96 and 168 h of immersion for all the specimens. Such EIS measures were always undertaken at RT, letting the specimens to low down their temperature to RT for at least 1 h before each measurement.

The EIS spectra were fitted with the electrochemical circuit for anodised and sealed specimens (EC3), described in section 4.4.3.3. From such fitting, values of the capacitance of the barrier layer, C_b, the capacitance of the porous layer, C_p, and the resistance of the electrolyte in the pores, R_p, were obtained. In all the cases, the values of the resistance of the barrier layer were always above 1 MΩ cm^2 and could not be thus accurately determined in the studied frequency window (10^5 to 10^{-2} Hz).

The values of C_b for all the AA2024 specimens TSA anodised and HWS are shown in fig. 127.

General observation of the evolution of the capacitance shows little variation of C_b during the immersion in the different concentrated NaCl electrolytes. For a given test temperature, initial values ranging between 1.00 and 1.10 µS cm^2 tend to increase during the immersion time for all the specimens immersed in the NaCl electrolyte at different concentrations. However, such C_b values never pass over 1.50 µS cm^2. Besides, there is not a clear relation between the increase of the test temperature and the increase of C_b.

Therefore, the degradation of the barrier layer is not markedly influenced by the NaCl concentration or the test temperature.

Fig. 128 shows the evolution of the capacitance of the porous layer during the immersion of the specimens in various concentrated NaCl solutions at different temperatures.

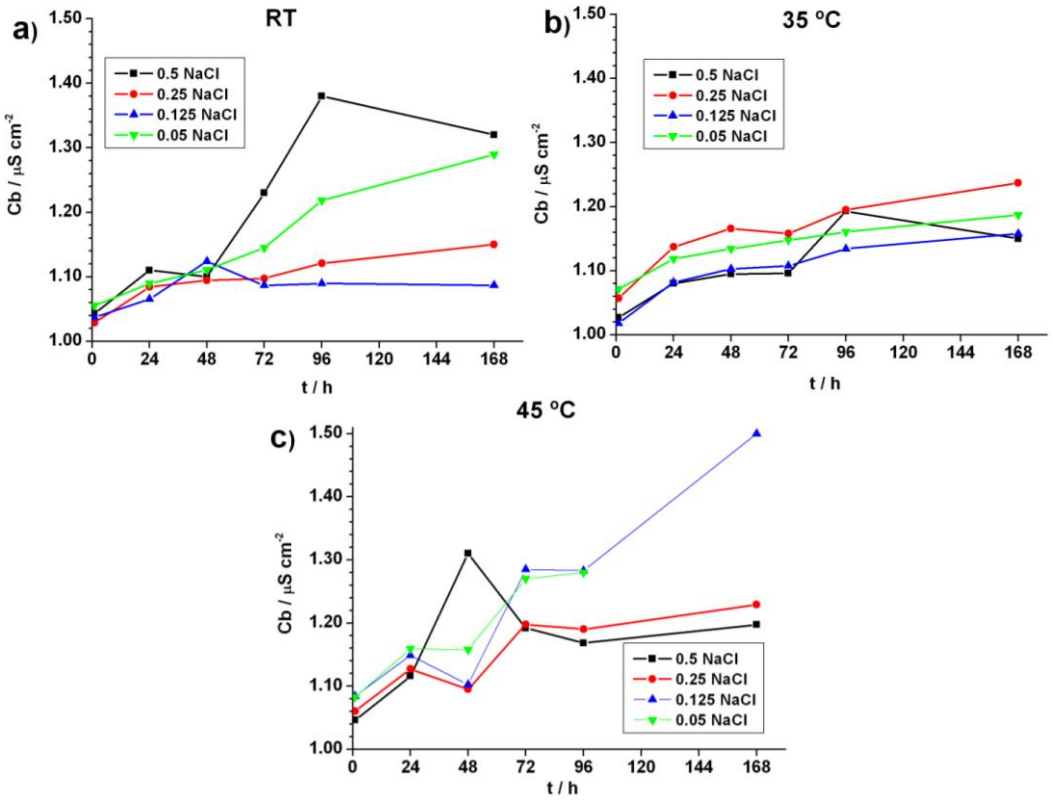

Figure 127. Evolution of the capacitance of the barrier layer of AA2024 specimens anodised and sealed (HWS) exposed at various NaCl concentrations at (a) RT, (b) 35 °C and (c) 45 °C.

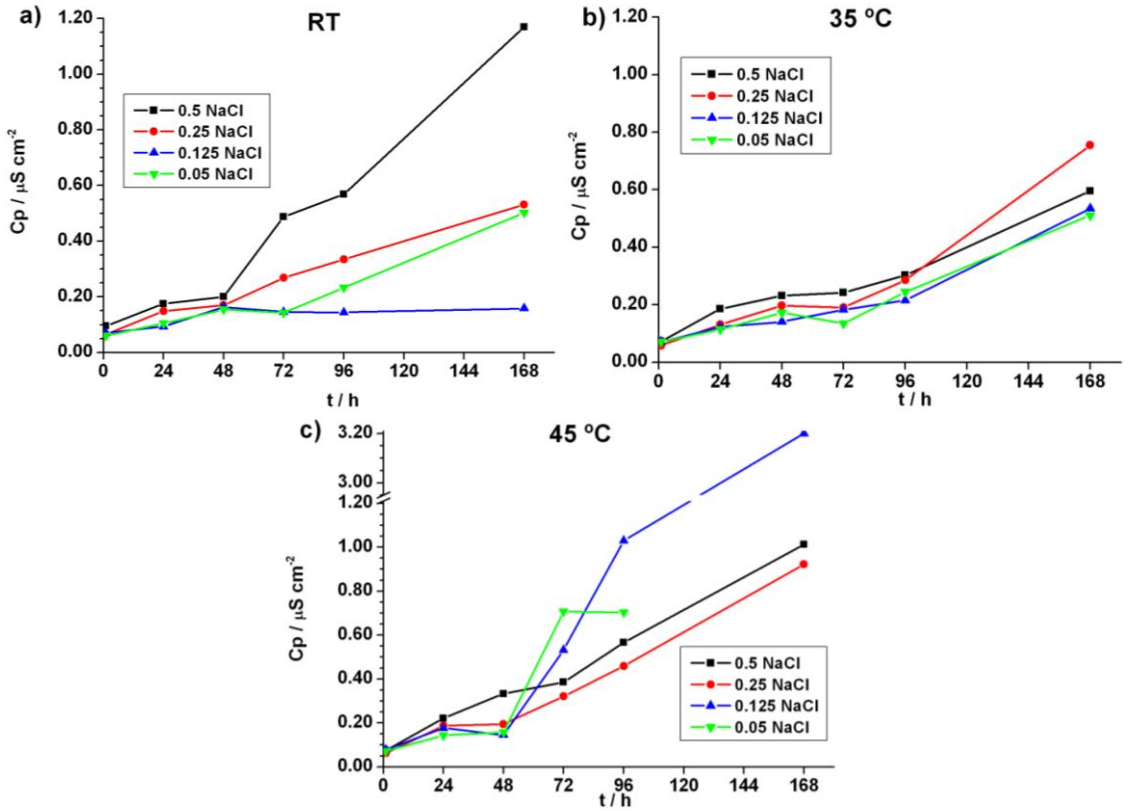

Figure 128. Evolution of the capacitance of the porous layer of AA2024 specimens anodised and sealed (HWS) exposed at various NaCl concentrations at (a) RT, (b) 35 °C and (c) 45 °C.

Comparison between the evolution of the capacitance of the porous layer evidences that C_p is not dependant on the temperature of the test solution. Conversely, the values of C_p, especially after 96 and 168 h of immersion, are higher for the relatively concentrated NaCl solutions (0.5 M and 0.25 M) than for the diluted NaCl solutions (0.125 M and 0.05 M) in all the studied temperature range. That is to say, degradation of the porous layer is dependant on the concentration of the aggressive ions in the test solution, although it is independent on the test temperature up to 45 °C.

Fig. 129 shows the evolution of the resistance of the electrolyte to penetrate through the pores.

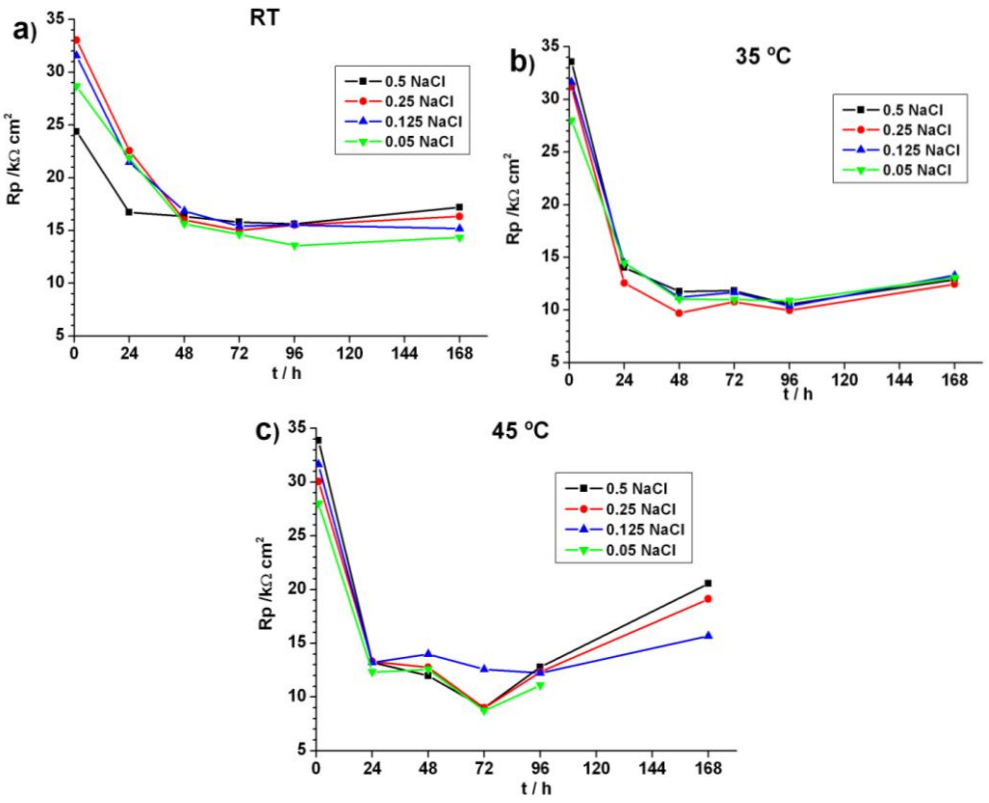

Figure 129. Evolution of the resistance of the porous layer of AA2024 specimens anodised and sealed (HWS) exposed at various NaCl concentrations at (a) RT, (b) 35 °C and (c) 45 °C.

The resistance of the test solution to penetrate through the pores decreases for all the specimens during the first 48 h of exposure to the test solution for the three temperatures. After that time, R_p remains relatively constant for all the specimens tested at RT and for the most diluted specimens at 35 and 45 °C. This evidences that the electrolyte completely penetrated though the pore and reached the base of the pores. However, in the case of the AA2024 specimens immersed in 0.5 M NaCl solution at 35 and 45 °C, R_p presents a minimal value after 72 h of immersion and then tends to increase. Such behaviour can be due to extended corrosion phenomena in the most concentrated solutions. But that behaviour is only clearly evidenced in the capacitance parameter previously discussed, therefore the increase of the R_p values after 72 h can corresponds to an early stage of the corrosion of the sealed anodic films.

To sum up, little influence of the NaCl concentration has been observed in the studied range of temperatures. Such feature evidences a good behaviour of the TSA anodised and hot water

sealed specimens in the presence of diluted Cl^- aqueous solutions but also in the presence of test solutions comparable to sea water concentration. Besides, the corrosive activity of the NaCl solution is not markedly increased with temperatures up to 45 °C. On the other hand, moderate increase of the test temperature does produce an accelerating effect in the immersion test.

5.6.2. Influence of the test temperature on the behaviour against corrosion of AA2024

AA2024 specimens TSA anodised and HWS were immersed in 0.5 M NaCl solution at various temperatures. From the viewpoint of the interior of the in-service conditions of an aircraft, these temperatures were normal (RT, 35 and 45°C) and abnormal increased temperatures (60 and 70 °C).

EIS measures were undertaken after 1, 24, 48, 72, 96 and 168 h of immersion for all the specimens. Such measures were always taken at RT, letting the system to cold down for about 1 h before the measurement.

The EIS spectra were fitted with the equivalent circuit proposed for sealed samples (EC3); the values obtained from such fittings are plotted in fig. 130.

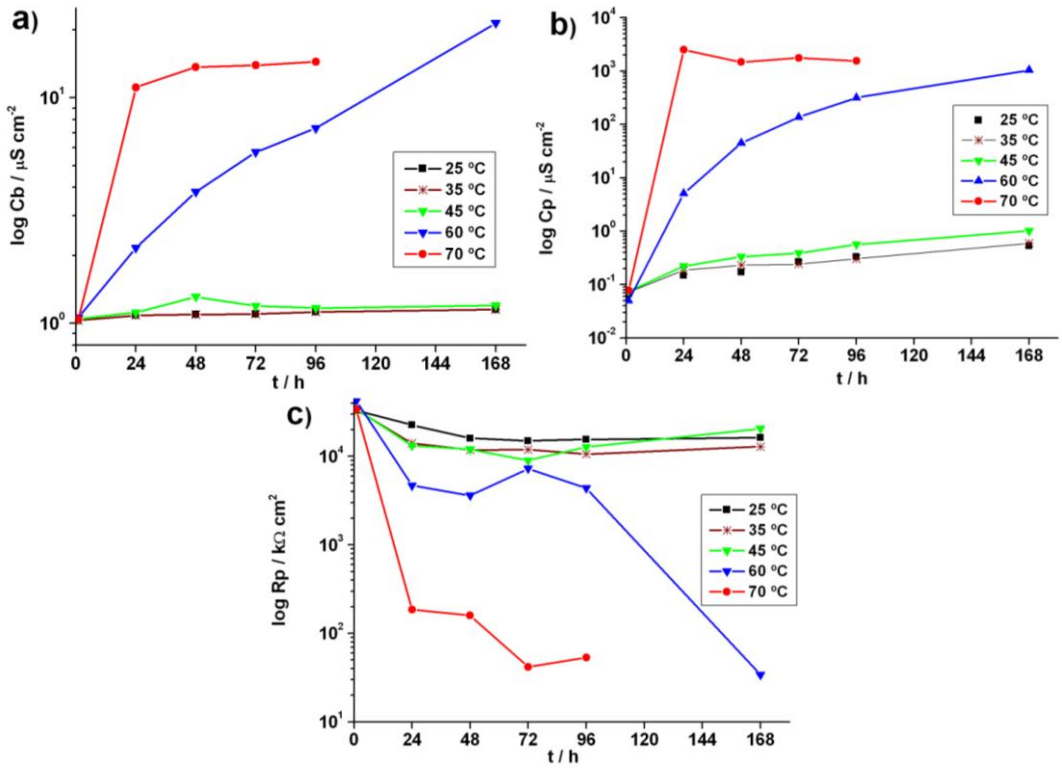

Figure 130. Evolution of the EIS parameters of the AA2024 specimens TSA anodised and HWS after different immersion times in 0.5 M NaCl solution at various temperatures (a) C_b (b) C_p and (c) R_p.

The values of the EIS parameters found for RT, 35 and 45 °C in the fig n are those previously shown in section 5.5.1. The logarithmic scale makes them to appear closer. Besides, marked differences between the samples tested up to 45 °C and the samples tested at 60 °C and 70 °C are evident after 24 h of immersion. The samples tested at 60 °C showed local corrosion phenomena after only 24 h of immersion, and this local corrosion further extended during the test. Furthermore, the samples tested at 70 °C evidenced general corrosion phenomena after 24 h of immersion, consequently, the test for these samples was stopped after 96 h.

Contrasting to the relatively constant C_b values for the specimens tested up to 45 °C, the capacitance of the barrier layer progressively increased for the AA2024 TSA anodised and HWS specimen tested at 60 °C. In the case of the specimen tested at 70 °C, C_b greatly increased after 24 h of immersion and remained constant for the rest of the experiment, evidencing probably a total degradation of the barrier layer.

The same features observed for the C_b are also noticeable for the evolution of the capacitance of the barrier layer. Attending to the evolution of the resistance of the electrolyte to penetrate through the pores, R_p decreases progressively for the specimen tested at 60 °C and abruptly after only 24 h of immersion in the 0.5 M NaCl solution at 70 °C.

Therefore, the anodised and HWS samples corrosion resistance is little influenced by the temperature up to 45 °C degrees. However, the corrosion rate of the barrier and the porous layer is increased for 60 and especially at 70 °C. The kinetics of the corrosion mechanism of the samples is thus boosted at 60 °C and 70 °C, this leads to think that accelerated corrosion test at high temperatures lasting some hours could simulate the slow degradation of the films at room temperature. However, more study is needed to check the degradation mechanism at RT and elevated temperature is the same. In any case, from the point of view of application of TSA in commercial aircrafts, the HWS-TSA has shown the resistance within the normal operating temperatures.

6. Conclusions

6. Conclusions

The most remarkable conclusions of this work are the following:

1. The reliability and robustness of the tartaric acid/sulphuric acid bath was demonstrated, since during 3 years of working, the anodic films obtained in the same TSA bath performed good constant behaviour against corrosion and consistent results for all the properties measured.

2. The thickness of the anodic films generated in the TSA bath for all the alloys was dependant on the anodising parameters. For all alloys, an increase of the anodising temperature or time leads to thicker anodic films.

3. The morphology of the anodic films is dependant on the alloy substrate, in general, higher copper containing alloys present distorted porous film, whereas low copper containing alloys present organised films as observed by scanning electron microscopy and transmission electron microscopy.

4. The alumina films was contaminated with sulphate and tartaric (or derived tartaric) species from the electrolyte and alloying elements from the alloy, as demonstrated by GDOES.

5. The corrosion resistance of the anodic films was dependant on both, the alloy and the anodising conditions. Generally, the samples anodised at lower temperatures or times performed lower corrosion resistance. Besides, the behaviour against corrosion was strongly influenced by the presence or absence of copper in the alloy: anodic films on high copper content alloys tend to degradation whereas those on low copper content alloy show self-sealing processes even in the aggressive chloride test solution.

6. The time of immersion in the electrolyte after termination of anodising does not affect significantly the total anodic film thickness. However, degradation of the barrier layer and generation of local defects occur during the immersion period in the chemically reactive anodising electrolyte. This effect is more accused for the higher copper containing alloys.

7. The conventional hot sealing postreatments were compatible with the TSA anodising process. Such hot sealing processes were influenced by the previous anodising conditions but broadly enhanced the resistance against corrosion for the four aerospace alloys. In general, the Cr-free hot water sealing process performs better for short immersion time in a 0.5 M NaCl electrolyte, whereas for longer exposure time, the hot dichromate sealing turned out to be better protection.

8. Cold postreatments did not markedly modify the anodic films, but corrosion inhibitors seem to incorporate (probably adsorbed) in the pore wall of the anodic films. In the case of a chromate conversion coating, the protection was effective since decreased degradation of the anodic films was observed by EIS. Conversely, the Cr (III) conversion coatings were not effective for inhibiting the corrosion processes.

9. TSA anodic films were compatible with the conventional solvent-based Cr-loaded paints, showing excellent corrosion resistance and paint adhesion even for the samples anodised at relatively low temperature.

10. The kind of surface treatment prior to paint with water-based coatings was found to be a key parameter, the corrosion resistance was lower for the pickling samples and the Cr (VI) conversion coatings, whereas TSA anodised specimens perform better against corrosion.

11. The testing temperature was found to be an important parameter in the case of water-based coating systems; corrosion was accelerated with an increase of test temperature, especially over 60 °C.

12. Anodising in the MoTSA electrolyte generated a porous anodic film with Mo^{6+} species presented across the anodic film thickness. The addition of a molybdenum salt did not significantly change the anodic layer film morphology as observed by SEM and TEM.

13. However, Molybdenum salt addition to TSA bath enhanced the behaviour of anodised copper containing alloys against corrosion. Moreover, the MoTSA process did not inhibited the self sealing process observed for the low copper containing alloys.

14. The paint adherence of the MoTSA anodic films is comparable to that observed for the TSA anodic films.

6. Conclusiones

Las conclusiones más relevantes de este trabajo se indican a continuación:

1. Se ha demostrado la fiabilidad y la robustez del baño de ácido tartárico/ácido sulfúrico, ya que, durante tres años de trabajo, las capas anódicas obtenidas en el mismo baño de TSA mostraron un constante y buen comportamiento frente a la corrosión y resultados consistentes para todas las propiedades medidas.

2. El espesor de las capas anódicas generadas en baño de TSA para todas las aleaciones es dependiente de los parámetros de anodizado. Para todas las aleaciones, un incremento de la temperatura de anodizado o tiempo da como resultado capas anódicas más gruesas.

3. La morfología de las capas anódicas depende de la aleación utilizada como sustrato, en general, las aleaciones con mayor contenido de cobre presentan películas porosas distorsionadas, mientras que las aleaciones con bajo contenido en cobre presentan películas organizadas como se observó mediante microscopía electrónica de barrido y microscopía de transmisión electrónica.

4. Las capas de alúmina están contaminadas con especies de sulfato y ácido tartárico (o derivadas del ácido tartárico) del electrolito y con elementos aleantes de la aleación, como se demostró mediante GDOES.

5. La resistencia a la corrosión de las capas anódicas depende de la aleación y de las condiciones de anodizado. Generalmente, las muestras anodizadas a menores temperaturas o tiempos mostraron una resistencia a la corrosión menor. Además, el comportamiento frente a la corrosión está fuertemente influenciado por la presencia o la ausencia de cobre en la aleación: las películas anódicas sobre las aleaciones con alto contenido en cobre tienden a degradarse, mientras que aquellas sobre las aleaciones con bajo contenido en cobre muestran un proceso de auto-sellado incluso en la agresiva disolución test de cloruros.

6. El tiempo de inmersión en el electrolito después de la finalización del anodizado no afecta significativamente al espesor total de la capa anódica. Sin embargo, la degradación de la capa barrera y la generación de defectos locales ocurren durante el periodo de inmersión en el electrolito, que es químicamente reactivo. Este efecto es más acusado en las aleaciones de alto contenido en cobre.

7. Los postratamientos convencionales de sellado en caliente son compatibles con el proceso de anodizado en TSA. Tal proceso de sellado en caliente está influenciado por las condiciones de anodizado previas, pero, a grandes rasgos, aumentaron la resistencia frente a la corrosión para las cuatro aleaciones aeroespaciales. En general, el proceso de sellado en agua caliente libre de cromatos funciona mejor para tiempos de inmersión cortos en un electrolito de NaCl 0.5 M, mientras que para tiempos de exposición más largos, el sellado en dicromato caliente resulto ser una mejor protección.

8. Los postratamientos en frío no modificaron notablemente las películas anódicas, pero los inhibidores de corrosión parecen incorporarse (probablemente adsorbidos) en las paredes de los poros de las películas anódicas. En el caso de una película de conversión

química de cromato, la protección es efectiva, puesto que disminuyó la degradación de las películas anódicas. Por el contrario, las películas de conversión química de Cr (III) no inhiben los procesos de corrosión efectivamente.

9. Las películas anódicas de TSA son compatibles con las pinturas convencionales de base disolvente con cromatos, mostrando una excelente resistencia a la corrosión y adherencia de pintura incluso para las muestra anodizadas a temperatura relativamente baja.

10. El tipo de tratamiento antes de la imprimación base agua es un parámetro decisivo, la resistencia a la corrosión es menor para las muestras decapadas y para las películas de conversión química, mientras que las muestras anodizadas en TSA muestran un mejor comportamiento frente a la corrosión.

11. La temperatura de test es un parámetro importante en el caso de las pinturas base agua; la corrosión se acelera con el incremento de temperatura, especialmente por encima de 60 °C.

12. El anodizado en un electrolito de MoTSA genera capas anódicas porosas con especies de Mo^{6+} presentes a lo largo de la capa anódica. La adición de una sal de molibdeno al baño de TSA no cambia la morfología de la capa de manera significativa como se observó mediante SEM y TEM.

13. Sin embargo, la adición de una sal de molibdeno al baño de TSA aumentó la resistencia frente a la corrosión de las aleaciones de alto contenido en cobre anodizadas. Además, el proceso en MoTSA no inhibe el proceso de autosellado para las aleaciones con bajo contenido en cobre.

14. La adherencia de pintura de las capas anódicas de MoTSA es comparable a la observada en las capas de TSA

7. References

7. References

1. EPA Federal Register, National Emission Standards for Hazardous Air Pollutants for Source Categories: Aerospace Manufacturing and Rework Facilities, Vol. 60 (170), September 1995, p. 45947
2. S. Xianglin, N.S. Dalal, Environ. Health Perspect. 102 (3) (1994) 231.
3. European community legislation EC 1907/2006.
4. Lisa project. Light-Weight Low-Cost Surface Protection for Advanced Aircraft Structures, EU GROWTH Program, contract G4RD-CT-2002-00691.
5. International Aluminium Institute http://www.world-aluminium.org
6. www.geology.com
7. F.M. Mazzolani. Aluminium alloy structures. 2nd ed. 1995 Chapman & Hall, London p 13.
8. D. Talbot, J. Talbot. Corrosion, Science and Technology. 1st ed. 1999 CRC Press LLC, Boca Raton, chapter 10.
9. M. Pourbaix, Atlas of Electrochemical Equilibria in Aqueous Solutions, Pergamon Press, 1966, p 171.
10. J.E. Hatch (Ed). Aluminum: Properties and Physical Metallurgy, American Society for Metals, 1984, chapter 7.
11. C. Vargel. Corrosion of aluminium. 1st ed. 2004 Elsevier Ltd, Oxford, p 115.
12. G.M. Scamans, M.P. Amor, B.R. Ellard, J.A. Hunter. Proc. Of Int. Symposium on Aluminium Surface Science and Technology, Antwerp, 229 (1997).
13. C. Vargel. Corrosion of aluminium. 1st ed. 2004 Elsevier Ltd, Oxford, p 136.
14. K. Nisencioglu, H. Leth-Olsen, O. Lunder, Corrosion Protection by Organic Coatings, Cambridge, 40 (1994)
15. J. Snodgrass. Corrosion Resistance of Aluminum Alloys, Corrosion: Fundamentals, Testing, and Protection, Vol 13A, ASM Handbook, ASM International, 2003, p 689 –691
16. R.L. Twite, G.P. Bierwagen, Prog. Org. Coat., 33 (1998) 91
17. K. Shimizu, G.M. Brown, H. Habazaki, K. Kobayashi, P. Skeldon, G.E. Thompson, G.C. Wood, Electrochim. Acta, 44 (1999) 2297
18. N.F. Jackson, D.S. Campbell, Thin Solid Films 36 (1976) 331.
19. A. Delong, V. Kolarik, J. Vac. Sci. Technol. B 7 (1989) 1442.
20. P.E. Troyan, R.B. Lubsanov, G.A. Vorobyev, S.A. Ghyngazov, I.V. Lakstroem, S.S. Kramor, J. Vac. Sci. Technol. B 11 (1993) 514.
21. T. Kusunoki, M. Suzuki, S. Sakai, J. Yamaguchi, T. Aida, Jpn. J. Appl. Phys. 22 (1993) L1695.
22. G.E. Thompson, Thin solid films 297 (1997) 192
23. F. Keller, M.S. Hunter, And D.L. Robinson, J. Electrochem. Soc., 100 (1953) 411
24. H. Masuda, F. Hasegwa, S. Ono, J. Electrochem. Soc., 144 (1997) L127
25. British anodising association Architectural anodising: sulphuric acid anodic film quality, 1981
26. Ministry of Defence DEF STAN 03-24/3 (1996)
27. Kaiser Aluminium and Chemical Corp. Brit. Pat. 820583 (1959)
28. J.M. Kake, Electroplat. Met. Finish. 14 (1961) 407
29. J.M. Kake, Electroplat. Met. Finish. 45 (1967) 34
30. U.S. Pat. 0,157,961 2001
31. L. Iglesias-Rubianes, S.J. García-Vergara, P. Skeldon, G.E. Thompson , J. Feruson, M. Beneke, Electrochim. Acta 52 (2007) 7148

32. M. Curioni, P. Skeldon, E. Koroleva, G.E. Thompson, J. Ferguson, J. Electrochem. Soc. 156 (2009) C147
33. Boeing Co. U.S. Pat. 4,894,127 (1990)
34. G.E. Thompson, L. Zhang, C.J.E. Smith, P. Skeldon, Corrosion 55 (1999) 1053
35. L. Domingues, J.C.S. Fernandes, M. Da Cunha Belo, M.G.S. Ferreira, L. Guerra-Rosa, Corros. Sci. 45 (2003) 149
36. Boeing Co., U.S. Pat. 4,127,451 (1978)
37. Rohr Inc., U.S. Pat. 5,486,283 (1996)
38. Airbus U.S. Pat.2005/0150771 A1
39. K. Shimizu, K. Kobayashi, G.E. Thompson, G.C. Wood, A.J. Forty, Thin solid films 173 (1991) 345
40. P. Skeldon, K. Shimizu, G.E. Thompson, G.C. Wood, Philos. Trans. Roy. Soc. A347 (1994) 295
41. C. Cherki, J. Siejka, J. Electrochem. Soc. 120 (1973) 784
42. J.S.P. Pringle J. Electrochem. Soc. 119 (1972) 482
43. G. Amsel, D. Samuel, J. Phys. Chem. Solids 23 (1962) 1707
44. G.E. Thompson, Thin solid films 297 (1997) 192
45. Y. Xu, Ph.D. Thesis, Unversity of Manchester, 1983
46. K. Shimizu, K. Kobayashi, G.E. Thompson, G.C. Wood, Philos. Mag. A 66 (1992) 643.
47. A.M. Etheridge, J.M. Sykes, J.D.B. Sharman, E. McAlpine, Mater. Sci. Forum 192 (1995) 345.
48. W. Zhang, B. Hurley, R.G. Buchheit, J. Electrochem. Soc., 149 (2002) B357.
49. M. Kendig, S. Jeanjaquet, R. Addison, J. Waldrop, Surf. Coat. Tech., 140 (2001) 58
50. L. Xia, E. Akiyama, G. Frankel, R. McCreery, J. Electrochem. Soc., 147 (2000) 2556
51. Hashimoto, U.S. Patent 2007/0089808 A1
52. Navair U.S. Patent
53. H. Yu, B. Chen, X. Shi, X. Sun, B. Li, Matter. Lett., 62 (2008) 2828.
54. J. Bibber, Aluminium finishing. Dec 2001, 15.
55. P.G. Sheasby, R. Pinner. The surface treatment and finishing of aluminium and its alloys, 6th ed. Vol. 2 Finishing publications Ltd. 2001, chapter 11.
56. T.P. Hoar, G.C. Wood, Electrochim. Acta 7, (1962) 333.
57. W. Vedder, D.A. Vermilyea, Trans. Inst. Metal Finishing, 45 (1967) 17.
58. W. Vedder, D.A. Vermilyea, Trans. Inst. Metal Finishing, 45 (1967) 107.
59. K. Wefers, Aluminium, 49 (1973) 553.
60. K. Wefers, Aluminium, 49 (1973) 622.
61. G.E. Thompson, R.C. Furneaux, G.C. Wood, Trans. Inst. Metal Finishing, 53 (1975) 97.
62. M.B.H. Ahmadun, J.L. Dawson, G.E. Thompson, Trans. Inst. Metal Finishing, 68 (1990) 109.
63. G.E. Thompson, G.C. Wood, Anodic Films on Aluminium in Corrosion: Aqueous Processes and Passive Films. J.C. Scully ed, 1983 Academic Press.
64. V. López, M.J. Bartolomé, E. Escudero, E. Otero, J. A. González, J. Electrochem. Soc., 153 (2006) B75.
65. H.S. Hunter, P.F. Turner, D.L. Robinson, Proc. American Electroplaters Society, 40 (1959) 220.
66. P.G. Sheasby, R.D. Guminski, T.K. Castle, Trans. Institute Metal Finishing, 44 (1966) 50.
67. N.D. Tomashov, A. Tyukina, Light Metals, 9 (1946) 22
68. L.W. Owen, H.G. Cole, Trans. Institute Metal Finishing, 52 (1974) 177.
69. G.P. Bierwagen, D.E. Tallman, Prog. Org. Coat., 41 (2001) 201.
70. P.T. LaPuma, J.M. Fox, E.C. Kimmel, Regulatory Toxicology and Pharmacology, 33 (2001) 343.

71. Z.W. Wicks jr. and others. Organic coatings, science an technology 3rd ed. John Wiley & Sons. Inc. Hoboken, New Jersey 2007, ch. 7 p 150.
72. S.A. Furman, F.H. Scholes, A.E. Hughes, D. Lau, Prog. Org. Coat 56 (2006) 33
73. J. Sinko, U.S. patent 5,378,446.
74. J. Sinko, U.S. patent 5,176,894.
75. J. Sinko, Prog. Org. Coat., 42 (2001) 267.
76. J. Sinko, U.S. patent 6,139,610 (2000).
77. J. Sinko, U.S. patent appl. 20020197468.
78. J. R. Davis & Associates, Aluminum and aluminum alloys. ASM International.
79. Airbus Spain Patent EP 2055 810A2, 2009.
80. J. Falbe, M. Riregitz (ed.) Römpp Chemie Lexikon 9th ed. Vol 2 1990 George Thiem Verlag, Stuttgart.
81. J.J. Bozzola and L.D. Russell. Electron microscopy: principles and techniques for biologists 2nd ed. 1992 Jones and Bartlett Publishers, Inc. chapter 3 p 207.
82. R.C. Furneaux, G.E. Thompson, G.C. Wood, Corros. Sci. 18 (1978) 853.
83. R.K. Marcus, J.A.C. Broekaert (ed.). Glow Discharge Plasmas in Analytical Spectroscopy. John Wiley & Sons Ltd. 1st ed. 2003.
84. Nuclear methods in science and technology Y. M. Tsipenyuk, D.A. Bradley 1997 Institute of Physics Publishing, Bristol, chapter 7 p286.
85. M. Mayer, SIMNRA
86. User's Guide, IPP 9/113, 1997
87. A.J. Bard, L.R. Faulkner. Electrochemical Methods J. Wiley & Sons, New York, 1980
88. David Loveday, Pete Peterson, and Bob Rodgers- Gamry Instruments. Evaluation of Organic Coatings with Electrochemical Impedance Spectroscopy Part 1: Fundamentals of Electrochemical Impedance Spectroscopy. JCT Coating Tech. August 2004.
89. David Loveday, Pete Peterson, and Bob Rodgers- Gamry Instruments. Evaluation of Organic Coatings with Electrochemical Impedance Spectroscopy Part 2: Application of EIS to Coatings. JCT Coating Tech. October 2004
90. David Loveday, Pete Peterson, and Bob Rodgers- Gamry Instruments. Evaluation of Organic Coatings with Electrochemical Impedance Spectroscopy Part 3: Protocols for Testing Coatings with EIS. JCT Coating Tech. February 2005.
91. J.P. Hoar, G.C. Wood, Electrochim. Acta, 7 (1962) 33.
92. M. Koda, H. Takahashi, M. Nagayama, Paper no. 0803, 34th Meeting Int. Soc. Electrochem., Erlangen, Germany, 1983.
93. J. Hitzig, K. Jüttner, W. J. Lorenz, W. Paatsch, Corros. Sci., 24, (1984) 945.
94. J. Hitzig, K. Jüttner, W. J. Lorenz, W. Paatsch, J. Electrochem. Soc., 133 (1986) 887.
95. G.J. Brug, A.L.G. Van Den Eeden, M. Sluyters-Rehbach, J.H. Sluyters, J. Electroanal. Chem,., 176 (1984) 275.
96. G.C.Wood, A.J. Brug, Trans. Inst. Met. Finish. 84 (1966) 189.
97. S. Feliú Jr., M.J. Bartolomé, J.A. González, V. López, S. Feliú, Appl. Surf. Sci. 254 (2008) 2755.
98. J.A. González, V. López, A. Bautista, E. Otero, X.R. Novoa, J. Appl. Electrochem. 29 (1999) 229.
99. F. Mansfeld, M. W. Kendig, S. Tsai, Corrosion, 38 (1982) 556
100. M.W. Kendig, F. Mansfeld, S. Tsai, Corros. Sci. 23 (1983) 317
101. F. Mansfeld, M.W. Kending, ASTM STP 866 (1985) 122
102. S. Haruyama, M. Asari, T. Tsuru, Proc. Electrochem. Soc. 87-2 (1987) 197
103. J. Titz, G.H. Wanner, H. Snaehn, M. Ebert, K. Juttner, W. J. Lorenz, Proc. Electrochem. Soc. 89-13 (1989) 261.
104. M. B. Vukmirovic, N. Dimitrov, K. Sieradzki, j. Electrochem. Soc. 149 (2002) B428.

105. T. Ramgopal, P. Schmutz, G.S. Frankel, J. Electrochem. Soc. 148 (2001) B348.
106. J. Hitzig, K. Juttner, W.J. Lorenz, W. Paatsch, Corros. Sci. 24 (1984) 945.
107. X. Zhou, G.E. Thompson, P. Skeldon, G.C. Wood, K. Shimizu, H. Habazaki, Corr. Sci., 41 (1999) 1599.
108. A.C. Crossland, H. Habazaki, K. Shimizu, P. Skeldon, G.E. Thompson, G.C. Wood, X. Zhou, C.J.E. Smith, Corr. Sci., 41 (1999) 1945
109. K. Shimizu, G. E. Thompson, G. C. Wood, Thin Solid Films, 85 (1981) 53.
110. X. Zhou, H. Habazaki, K. Shimizu, P. Skeldon, G.E. Thompson, G.C. Wood, Corr. Sci., 38 (1996) 1563.
111. Y. Liu, M.A. Arenas, P. Skeldon, G.E. Thompson, P. Bailey, T.C.Q. Noakes, H. Habazaki, K. Shimizu, Corros. Sci. 48 (2006) 1225.
112. S. Feliú Jr., J. A. González, V. López, M. J. Bartolomé, E. Escudero, E. Otero, J. Appl. Electrochem. 37 (2007) 1027.
113. G. D. Sulka, V. Moshchalkov, G. Borghs, J. P. Celis, J. Appl. Electrochem. 37 (2007) 789.
114. G. Boisier, N. Pébère, C. Druez, M. Villate, S. Suel, J. Electrochem. Soc. 155 (2008) C521.
115. J. Murray, Prog. Org. Coat., 31 (1997) 375
116. A.S. Castela, A.M. Simoes, M.G. Fereira, Prog. Org. Coat 38 (2000) 1
117. L. Hartshorn, N.J.L. Megson, E. Rushton, J. Soc. Chem. Ind 56 (1937) 266r
118. D.M. Brasher, A.H. Kingsbury; J. Appl. Chem. 4 (1954) 62
119. J.A. Bishopp, M.J. Parker, T.A. O'Reilly, International Journal of Adhesion & Adhesives 21 (2001) 473
120. B. del Amo, R. Romagnoli, C. Deyá, J.A. González, Prog. Org. Coat., 45 (2002) 389.
121. T. Fletcher, Polymers Paint Colour Journal, March 1992.
122. R.L. Twite, V. Balbashyev, G.P. Bierwagen, D. Tallman, in: S.R. Taylor, E. Brooman, H. Isaacs (Eds.), Special Publication of the Electrochemical Society, Proceedings, Vol. 95-16, Chicago, IL, 1995.
123. 219 4.7 Comprehensive coordination chemistry
124. W.S. Li, L.P. Tian, Q.M. Huang, H. Li, H.Y. Chan, X.P. Lian, J. Power Sources 104 (2002) 281.
125. V. Moutarlier, M.P. Gigandet, J. Pagetti, S. Linget, Thin Solid Films 483 (2005) 197.
126. A.M.V.S.V. Cavaleiro, V.M.S. Gil, J.D. Pedrosa de Jesus, R.D. Gillard P.A. Williams, Transition Met. Chem. 9 (1983) 62.
127. H. Habazaki, X. Zhou, K. Shimizu, P. Skeldon, G.E. Thompson, G.C. Wood, Electrochim. Acta 42 (1997) 2627.
128. S.J. Garcia-Vergara, K. El Khazmi, P. Skeldon, G.E. Thompson, Corros. Sci. 48 (2006) 2937.
129. E. Zhuravlyova, L. Iglesias-Rubianes, A. Pakes, P. Skeldon, G.E. Thompson, X. Zhou, T. Quance, M.J. Graham, H. Habazaki, K. Shimizu, Corros. Sci. 44 (2002) 2153.
130. G. C. Wood, P. Skeldon, G. E. Thompson, K. Shimizu, J. Electrochem. Soc. 143 (1996) 74.
131. C.V. Cáceres, J.L.G. Fierro, J. Lázaro, A.L. Agudo, J. Soria, J. Catal. 122 (1990) 113.

8. Annex

8. Annex

The following documents are annexed

1. **M. García-Rubio**, P. Ocón, A. Lavía, I. García "Anodising proceeding for aluminium or aluminium alloys" European patent EP2055810A2
2. **M. García-Rubio**, M.P. de Lara, P. Ocón, S. Diekhoff, M. Beneke, A. Lavía, I. García, "Effect of postreatment on the corrosion behaviour of tartaric-sulphuric anodic films" *Electrochimica* Acta 54 (**2009)** 4789.

3. **M. García-Rubio,** P. Ocón, A. Climent-Font, R. W. Smith, M. Curioni, G.E. Thompson, P. Skeldon, A. Lavía, I. García, "Influence of molybdate species on the Tartaric acid/ Sulphuric acid anodic films grown on AA2024 T3 aerospace alloy" *Corrosion Science* 51(**2009)** 2034.

4. M. García-Rubio, P. Ocón, M. Curioni, G.E. Thompson, P. Skeldon, A. Lavía, I. García, "Degradation of the corrosión resitance of anodic oxide films through immersion in the anodising electrolyte" *Corrosion Science submitted* **2009.**